# Evaluation and Analysis of the Erosion Performance of Flame Spray-Coated Polyurethane Liners

by

Sayed Hossein Ashrafizadeh

A thesis submitted in partial fulfillment of the requirements for the degree of

Doctor of Philosophy

Department of Mechanical Engineering

University of Alberta

# Abstract

Evaluation and Analysis of the Erosion Performance of
Flame Spray-Coated Polyurethane Liners

Sayed Hossein Ashrafizadeh
Doctor of Philosophy
Department of Mechanical Engineering
University of Alberta
2016

Polyurethane has excellent wear resistance and is an effective protective liner against erosion caused by the impact of solid particles. However, similar to most polymeric materials, polyurethane has low thermal and electrical conductivity, and this limits its applicability for use in environments where the operating temperatures are high or where electrical conductivity is required. One of the solutions to overcome such problems is metallization of polymeric materials by thermal spraying processes. Due to the thermal sensitivity of polymer materials and the high temperatures that are typical of thermal spraying processes, prediction of the temperature distribution in the polymer material substrate during spraying is considered to be a key factor in the selection of appropriate coating materials and control of spray process parameters. The first phase of this PhD project focused on deposition of metallic conductive coatings on polyurethane substrates. A mathematical model for determination of the temperature distribution within polymeric substrates during flame spraying was developed to allow for monitoring of the temperature during the spraying process. The effect of air pressure and the stand-off distance of the flame spray torch on the temperature distribution, characteristics of the deposited coatings and electrical resistance were also studied. An analytical heat transfer model based on Green's functions was developed and validated with experimental data. It was found that the temperature distribution, coating porosity, and electrical resistance decreased by increasing the pressure of the air that was injected into the flame spray torch during deposition. The injection of air also allowed for a reduction of the stand-off distance of the flame spray torch to deposit coatings with higher electrical conductivity. Dynamic mechanical analysis was performed to investigate the effect of the increase in temperature within the substrate on its dynamic mechanical properties. It

was found that the spraying process did not significantly change the storage modulus of the polyurethane substrate material. The deposited coating may function: a) to distribute heat to avoid excessive local temperature increases in the polyurethane liner during practical applications that involve erosion and b) for use as a heating element. To that end, the second phase of this PhD thesis research focused on studying the effect of temperature on the wear resistance of polyurethane. A test assembly capable of conducting erosion testing at controlled temperatures was designed and developed. The temperature distribution within the samples during the erosion tests was determined by a three-dimensional finite element model and the velocity of the erodant particles was estimated by a mathematical model based on the principles of supersonic compressible fluid flow through a converging-diverging nozzle. The results that were obtained showed the effect of temperature on the erosion resistance of PU elastomers. The stress-strain behavior of the polyurethane elastomers was characterized at room and at elevated temperatures up to 100ºC by conducting tensile tests and cyclic loadings. Comparison of stress-strain behavior of the polyurethanes with their erosion resistance at controlled temperatures revealed that the residual strain as a result of plastic deformation, stress softening, ultimate failure stress and final elongation at break were the key parameters affecting the erosion resistance of polyurethane elastomers. Evaluation of the surface morphology of the worn samples confirmed the importance of the residual strain and elongation at break on the erosion resistance of polyurethane elastomers. In order to study the effect of temperature on the stresses and strains that were generated during the erosion testing, the impact of erodant particles on the elastomer surface was modeled by using the finite element technique. The model that was developed allowed for better understanding of the mechanism of material removal during solid particle erosion of PU elastomers. The results obtained by the finite element model showed that the ultimate strength and elongation at break have the most significant influence on the erosion rate at velocities higher than a critical value. Residual strain as a result of plastic deformation and stress softening caused by Mullins damage and PU softness were found as other parameters that can affect the erosion rate.

# Preface

Some of the sections presented in this thesis document have been or will be published in peer reviewed journal revues or conference proceedings as follows:

- Some sections of the work presented in Chapter 1 of this thesis document have been or will be published in peer reviewed journals or conference proceedings of Paper No. 1 - Paper No. 9 as shown below.
- Some sections of the work presented in Chapter 2 of this thesis document have been published in peer reviewed journal Paper No. 3 and conference proceedings Paper No. 4.
- Some sections of the work presented in Chapter 3 of this thesis document have been published in peer reviewed journal Paper No. 5 and conference proceedings Paper No. 6.
- Some sections of the work presented in Chapter 4 of this thesis document have been or will be published in peer reviewed journal Paper No. 7 and conference proceedings Paper No. 8.
- Some sections of the work presented in Chapter 5 of this thesis document will be published in conference proceedings Paper No. 9.

Paper No. 1: H. Ashrafizadeh, G. Fisher, A. McDonald, "Applications and Future Developments of Thermal Spray Technology for the Oil & Gas Industry", J. Therm. Spray Technol., *Under Review*, 2016.

Paper No. 2: R. Gonzalez, H. Ashrafizadeh, A. Lopera, P. Mertiny, A. McDonald, "A Review of Thermal Spray Metallization of Polymer-based Structures", J. Therm. Spray Technol., (25-5) 897-919, 2016.

Paper No. 3: H. Ashrafizadeh, P. Mertiny, A. McDonald, "Determination of Temperature Distribution within Polyurethane Substrates during Deposition of Flame-sprayed

Aluminum-12Silicon Coatings Using Green's Function Modeling and Experiments", Surf. Coat. Technol., (259) 625-636, 2014.

Paper No. 4: H. Ashrafizadeh, P. Mertiny, A. McDonald, "Analytical and Numerical Determination of Transient Temperature within a Polyurethane Substrate during a Flame spraying Process", Proceedings of The Canadian Society for Mechanical Engineering (CSME) International Congress, Toronto, ON, Canada, June 1-4, 2014.

Paper No. 5: H. Ashrafizadeh, A. McDonald, P. Mertiny, "Deposition of Electrically Conductive Coatings on Castable Polyurethane Elastomers by the Flame Spraying Process", J. Therm. Spray Technol., (25-3) 419-430, 2016.

Paper No. 6: H. Ashrafizadeh, P. Mertiny, A. McDonald, "Evaluation of the Influence of Flame Spraying Parameters on Microstructure and Electrical Conductivity of Al-12Si Coatings Deposited on Polyurethane Substrates", International Thermal Spray Conference (ITSC), Long Beach, CA, USA, May 11-14, 2015.

Paper No. 7: H. Ashrafizadeh, P. Mertiny, A. McDonald, "Evaluation of the Effect of Temperature on Mechanical Properties and Wear Resistance of Polyurethane Elastomers", Wear, *Under Review*, 2016.

Paper No. 8: H. Ashrafizadeh, P. Mertiny, A. McDonald, "Development of a Test Assembly for Evaluating the Erosion Resistance of Polyurethane Elastomers at Controlled Temperatures", First Pacific Rim Thermal Engineering Conference (PRTEC), Hawaii's Big Island, HI, USA, March 13-17, 2016.

Paper No. 9: H. Ashrafizadeh, P. Mertiny, A. McDonald, "Development of a Finite Element Model to Study the Effect of Temperature on Erosion Resistance of Polyurethane Elastomers", 21st International Conference on Wear of Materials, Long Beach, California, USA, March 26-30, 2017, *Abstract Accepted*.

All the authors contributed to the preparation of the listed papers. I conducted the research work under the guidance of Dr. Andre McDonald and Dr. Pierre Mertiny in their roles

as research supervisors. I collaborated with Dr. Gary Fisher, Alberta Innovates - Technology Futures, to draft a short paper on the applications of thermal spraying in the oil and gas industry. Paper No. 2 was prepared through research collaboration with Dr. Raelvim Gonzalez Henriquez and Mr. Adrian Lopera-Valle, producing a review article on the thermal spray metallization of polymer-based materials.

# Acknowledgments

First and foremost, I wish to express my sincerest gratitude to my supervisors, Prof. A. McDonald and Prof. P. Mertiny for their guidance, continuous support and excellent supervision throughout the course of my doctoral program. Completion of this research program would have been impossible without their support, hard work, and encouragement. I would like to thank the member of my doctoral supervisory committee, Prof. M. Lipsett for his time, valuable advice and suggestions. I am also thankful to the members of the examining committee, Prof. K. Sridharan and Prof. H. J. Chung and the examining committee chair Prof. C. Dennison.

I would like to thank technical support from the machine shop technicians. In particular, I am thankful to Mr. B. Faulkner for his assistance in assembly of some of the experimental equipment needed for my doctoral program. I would like to thank Mr. E. Sullivan for assisting me with the heat flux measurements and Mr. M. Ivey for helping me with the tensile tests. I would also like to acknowledge the support from Natural Sciences and Engineering Research Council of Canada (NSERC) and Syncrude Canada Limited.

Last, but certainly not the least, I would like to thank my parents, Prof. F. Ashrafizadeh and Ms. F. Kashefipoure-Dezfouli, for their encouragement and support for my studies towards graduate degree and all accomplishments that I have made. Finally, I am indescribable grateful to my wife, Niaz Ghomeshi, for her love, patience and continuous support during my PhD study over the past few years.

# Table of Contents

# List of Tables

# List of Figures

# Chapter 1

# Introduction

## 1.1 Background

Corrosion and wear of components used in the oil and gas industry is one of the main causes of failure and leakage [1]. This is due mainly to the corrosive nature of the fluids that are transported and the low corrosion resistance of carbon steel. Carbon steel is the material of choice in the oil and gas industry because of its ability to withstand high pressures and the relatively low cost to purchase and install the material in comparison to other highly alloyed materials [2]. On the other hand, some extraction processes in the petrochemical industry may involve the processing of multi-phase solid-liquid mixtures. These mixtures will contain hard-face erodant particles such as sand, which may lead to solid particle erosion in addition to corrosion. The combination of wear and corrosion can extensively reduce the lifetime of equipment, parts, and pipelines [3]. Solid particle erosion is a process in which the material is removed from the target surface by the impact of a stream of particles [4]. This type of wear affects many components in the oil and gas industry including pipelines, drill bits, pump casing and impellers, valves, gas turbines, boilers, and compressors [5]. The adverse effects of this type of wear mode is not limited to the oil and gas industry and reduced longevity of parts caused by solid particle impact has been reported in other industries such as aerospace, marine, mining, and wind energy [4, 6, 7].

Protective coatings can be employed to increase the lifespan of the equipment exposed to erosive environments. Among all the types of protective coatings and liners, soft elastomeric liners have been found to be effective for industrial use owing to their excellent erosion

resistance and comparatively low cost [8, 9]. The excellent erosion resistance of elastomers is a result of their high resilience and propensity to elastic deformation that allow for absorption of impact energy with minimal plastic deformation [8, 10]. Among all the types of elastomeric materials, polyurethane (PU) elastomers have received particular attention given that they can be processed by methods typically used for polymers while still having the superior mechanical properties of vulcanized rubber such as high elasticity, high load capacity, and resistance to tear [11]. PUs are organic polymers with urethane group in their chemical structure that can be synthesized by the reaction of a diisocyanate and a polyol [12]. The relatively low cost of PU elastomers [11] and the fact that their resistance to wear is greater than that of most polymers [13], rubbers [14], stainless steels, [13] and even hard-faced tungsten carbide-cobalt (WC-Co) coatings [15] has made PU an attractive option for use as protective coatings and liners in large scale applications involving pipelines [16].

On the other hand, the low thermal and electrical conductivity of PU, as is similar to most polymers, have limited its functionality for use in environments with high temperature or where high electrical conductivity is required. Metallization of polymeric materials by the deposition of conductive thermal-sprayed coatings is a possible means to augment the effective thermal and electrical conductivity of a polymeric material, but it has proved to be challenging [17-21]. Firstly, the standard surface preparation of the polymeric substrate prior to spraying by using grit blasting may not be feasible due to the fragile nature of some of the polymer-based structures and the damage that can be induced in the substrate by grit blasting. Secondly, the soft nature of some of the polymeric substrates such as PU may not allow for appropriate deformation of powder particles upon impact. The third, and the main, challenge with thermal spray deposition on polymeric materials is difficulty in controlling the substrate temperature during the deposition

process. This is problematic since even the most thermally resistant polymers have a thermal decomposition temperature of less than 470°C [22]. It should be noted that, even though alternative surface metal deposition techniques, such as physical vapor deposition (PVD) [23, 24], chemical vapor deposition (CVD) [25], and plasma-enhanced CVD (PECVD) [26], may be applied to polymer-based structures, these techniques are relatively expensive to use and are not suitable to fabricate thick metallic coatings (over 100 μm) at high deposition rates [27, 28], which is feasible by thermal spray metallization. In addition, the thermal spray process allows the deposition of coatings onto various substrate geometries and the ability to recoat damaged coatings [29].

The deposited conductive coatings on PU substrates can allow for its wider adoption in engineering applications. The deposited coating can function as a health monitoring device in fiber-reinforced polymer composite (FRPC) pipes. The usual monitoring techniques applicable to steel pipes may not be applicable for FRPC pipes. Thus, alternative techniques for development of a health monitoring device in polymer structured pipelines are of interest. It has been shown in previous studies that the fabricated metallic coatings on the surface of the FRPC pipes can be used as a health monitoring device for detection of leakage and failure of the pipe [18]. This health monitoring system detects damage based on the variation of the electrical impedance as a result of localized fracture of the metallic coating in cases of damage or leakage of the pipe. Figure 1-1 shows a schematic of the metallic coating deposited on the outer surface of a FRPC pipe. The main drawback of this health monitoring technique is that the failure will be detected after the leakage or burst of the pipe. On the other hand, by the use of a system of PU liners and thermally sprayed coatings, such as the one shown schematically in Fig. 1-2, pipe

failure can be detected prior to leakage. In addition, the data from the deposited metallic coating can be used to estimate the integrity of the pipe at different locations.

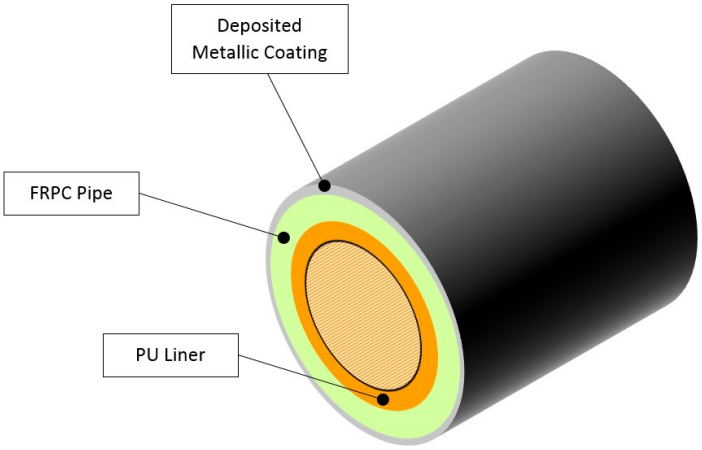


Figure 1-1 Schematic of the metallic coating deposited on the outer surface of the FRPC pipe

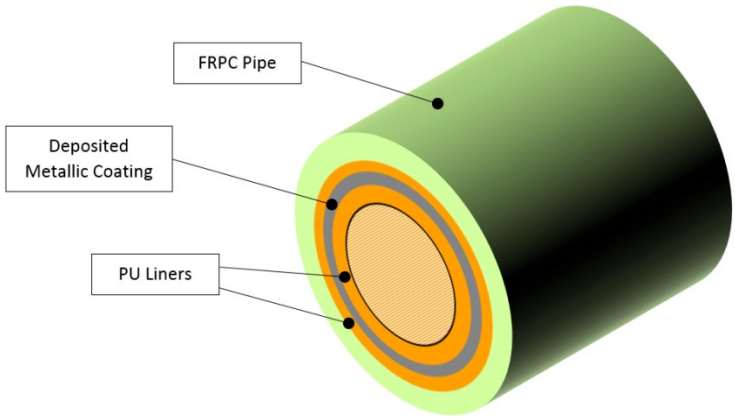


Figure 1-2 Schematic of deposited metallic coating and PU liners in the inner diameter of a FRPC pipe

Improvement in heat transfer of the coated PU can be considered as the second application for thermal spray metallization of PU substrates. Coating materials with high thermal

conductivity such as copper or aluminum may allow for improved heat transfer from areas where localized high temperatures are expected to develop. The localized high temperatures can be a result of heat generation during solid particle impact or heat transfer from the surrounding ambient. Another potential application of the deposited coating on polymeric materials is its use as a heating element for Joule heating of the polyurethane-coating structure. De-icing and heating the polymer-coating structure or the flowing fluid are the possible benefits of the use of the fabricated coatings as heating elements [30, 31].

## 1.2 Thermal Spraying Process

Thermal spraying is a material deposition process whereby a heat source is used to melt or increase the temperature of feedstock particles that are accelerated in a fluid stream through a spray nozzle or torch, for consolidation upon impact on a substrate. Figure 1-3 [32] shows a schematic of the coating build-up process during thermal spray deposition of powder materials. The thermal spray deposition process is characterized by heat, mass, and momentum transfer phenomena [33-35]. These phenomena are functions of the thermal spray process parameters [34] and affect the properties and structure of the resulting thermal-sprayed coatings [33]. Thermal energy is transferred from the thermal spray gas, flame, or plasma to the substrate by gas convection and the impingement of solid or molten particles [29]. The kinetic energy of the impacting particle is used to overcome surface tension energy, deform the particles, and/or is converted to heat due to viscous dissipation or plastic strain energy during flattening to form a splat [36-38]. As a result of the thermal spray deposition onto the substrate, a lamellar structure of splats develops into a coating layer, which exhibits different physical properties from those of the feedstock bulk material of the coating [33]. These differences in properties can be the result of phase changes during the deposition process, residual stresses in the solidified splats, and the

presence of porosities and other microstructural defects within the coating [39]. Thermal spray deposition has been performed using different particle-substrate material systems, including metal particle and polymer-based substrates [29, 34, 40-43].

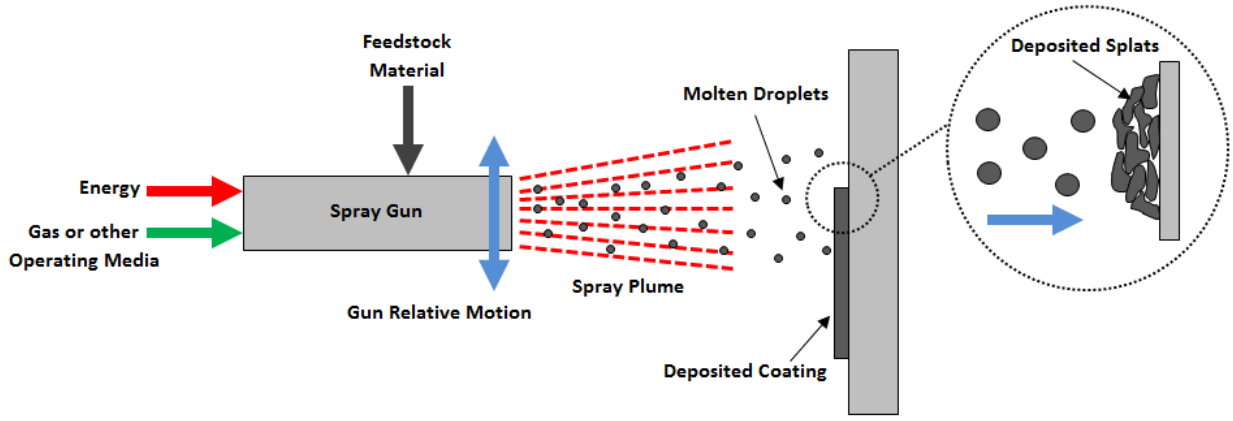


Figure 1-3 Schematic of the thermal spray process [32]

## 1.3 Thermal Spray Metallization of Polymer-Based Structures

Thermal spray metallization of polymer-based structures is defined as the application of thermal spray processes to deposit metals onto a polymer substrate. The deposition of the metal splats is affected by the velocity and temperature of the impacting particles, the roughness and temperature of the substrate surface, and the relative angle between the particle trajectory and the substrate [29, 39]. The deposited metal particles may embed into relatively softer polymer substrates, such as nylon, PU, and polyethylene (PE) [44-46]. Alternatively, the particles may deform and interlock upon contact with the polymer substrate surface, as shown in previous studies involving basalt and glass fiber-reinforced epoxy thermosets [17, 18]. Current thermal spray metallization processes of polymer-based substrates can be classified into four categories according to the primary energy source used for particle acceleration and heating [34, 35, 47]. They are (i) cold spraying, which consists of kinetic-based deposition of metal or metal alloy

particles at relatively lower temperatures, (ii) flame spraying, comprising particle deposition using a combustion flame jet, (iii) electric arc wire spray, which utilizes an electric discharge from electrodes around a carrier gas stream to generate a thermal jet, and (iv) plasma spraying, involving ionized gas jets generated by either direct current (DC) or radio-frequency (RF) current. Each of the thermal spray processes will generate different magnitudes of energy in the fluid heat source that is used to heat and accelerate the particles for deposition. Figure 1-4 shows the approximate range of gas temperature and particle impact velocity of different thermal spray metallization processes [29, 34]. A brief review on the possible use of these four thermal spraying techniques for metallization of polymer-based substrates is provided in the subsequent sections.

### 1.3.1 Cold Spraying

Cold spraying is a relatively low-temperature thermal spray process where solid-state particles are accelerated through a convergent-divergent nozzle to high velocities (300 m/s – 1200 m/s), and the coating is formed as a result of extensive plastic deformation and interlocking of the deformed particles upon impact [34, 39]. The impacting particles may be heated, but their temperature remains below the melting point of the feedstock material. Consequently, cold spraying is subject to lower process temperatures compared to thermal spraying. The process parameters of the cold spray process include nozzle geometry, nozzle stand-off distance (distance between the nozzle and the substrate surface), feedstock material, and carrier gas temperature and pressure.

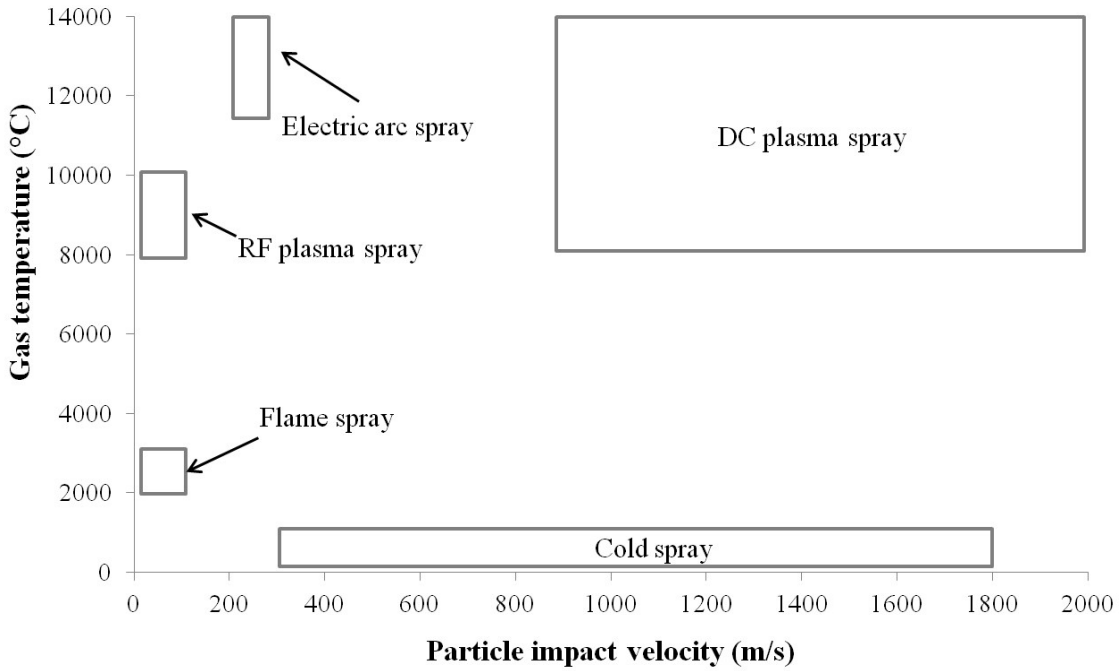


Figure 1-4 Gas temperature and particle impact velocity map of different thermal spray processes [29, 34]

The possibility of employing cold spraying for depositing of metallic coatings on polymeric substrates has been the topic of active research in some previous studies. The main advantage of the cold spraying for metallization of polymer-based substrates is its lower process temperatures compared to those of other thermal spraying processes. Gansen *et al.* [48] studied the feasibility of the cold spraying process for depositing copper on polyvinyl chloride (PVC) substrates. It was shown that the gas temperature had a strong effect on the deposition efficiency, possibly due to the heat sensitivity of the PVC substrate and it's softening during the deposition process. In a study by Zhou *et al.* [49], it was shown that under precise process control the polymeric substrate softened so that aluminum particles could penetrate into the substrate to form a mechanical bond. Copper was subsequently sprayed on the deposited aluminum to form a coating with low electrical resistance. Robitaille *et al.* [19] suggested the addition of a bond coat

on the substrate surface during the curing process of the polymeric material can protect the substrate from the high kinetic energy of cold-sprayed metal particles and prevent the substrate from structural damage to the polymer-based material. Even though the deposition of dense conductive coatings on stiff polymeric substrates by cold spraying is possible as reported in previous studies [19, 48, 49], the number of studies that succeeded in depositing a metallic coating with low electrical resistance on soft elastomeric substrates is rather limited. The reason for this limitation is that particles with high velocity are likely to either rebound or penetrate into the substrate without producing a continuous coating on the substrate surface [44]. Rebound or penetration of the particles depends, in part, on the mechanical properties of the elastomeric substrates and the cold spraying deposition parameters.

### 1.3.2 Flame Spraying

Flame spraying is a thermal spray process in which the combustion of fluid fuels produces a flame jet that melts and accelerates the feedstock material for deposition onto the substrate. The combustion gases are usually acetylene and oxygen, though air may also be added for cooling purposes [42]. The feedstock particles are propelled toward the substrate through a nozzle by the flow of a carrier gas, which is usually an inert gas such as argon. The feedstock material can be in the form of powder, wire, rod, or cord. The flame temperature should be sufficiently high to ensure the melting of the feedstock material [34]. The flame spray process usually exhibits gas temperatures between 2000°C and 3000°C [29, 50], whereas the particle impact velocity is usually below 100 m/s [34].

In flame spraying, the particles reach a temperature that is close to or in excess of their melting point upon impact. Thus, they are softer and deform easily to produce a continuous

coating. In particular, this is beneficial for deposition on soft elastomeric substrates. Conversely, the main challenge of flame spraying on polymeric materials is to control the substrate temperature during the deposition process since even the most thermally resistant polymers have a thermal decomposition temperature of less than 470°C [22]. Accordingly, process parameters play an important role on the level of damage that polymeric substrates may experience during the spraying process. For that reason, flame spray deposition of metal coatings onto polymer-based substrates is constrained by the sensitivity of the substrate to the impact of high-temperature, semi-molten, and molten particles [20]. Voyer *et al.* [20, 21] employed air in a flame spraying process to cool the polymer-based substrate during deposition. It was shown that by using cooling air and optimizing the spraying parameters, the distance between the torch and the substrate could be decreased without producing any thermal damage to the substrate, as confirmed through visual inspection. Therefore, flame-sprayed coatings can be used to modify the electrical properties of the polymer substrate, provided that the deposition process does not compromise the structural integrity of as-sprayed structures. Huonnic *et al.* [17] studied the effect of flame-sprayed Al coatings deposited onto grit-blasted basalt and glass fiber composite tubes. Significant damage to the FRPC structure was reported as a result of the grit blasting and flame spray metal deposition processes. Subsequent studies [18, 51] utilized a garnet sand interlayer between the FRPC substrate and the flame-sprayed metal particles to protect the thermally sensitive substrate from the flame and particle impingement forces.

### 1.3.3 Electric Arc Wire Spraying

Electric arc wire spraying is a thermal spray process whereby the heat generated in an electric arc discharge melts feedstock wires to form droplets, which are accelerated in a gas stream produced through a nozzle, for deposition onto the substrate [34, 52]. Two feedstock

wires with opposing polarity converge at the nozzle outlet at a constant speed to generate the electric arc discharge. The electric arc wire spray process can generate gas temperatures in excess of 5000°C [52], whereas particle impact velocities are usually below 300 m/s [34]. Feedstock wires can be made of metals or metal-cored wires [34]. The electric arc wire spray process has been utilized to deposit Zn and Al particles onto polymer-based substrates. Liu *et al.* conducted two studies [53, 54] on the arc wire spray deposition of Zn and Al bond-coats onto polymer matrix composite (PMC) substrates. In these studies, it was found that the metal bond-coat allowed the deposition of a harder and more thermally resistant top coating. Compared to other thermal spraying processes, limited research is available on electrical arc metallization of polymer-based substrates, and recent studies have focused on the fabrication and characterization of bond-coats using low melting temperature materials such as Al and Zn. Liu *et al.* [54] showed that the arc spraying process is not suitable for metal coating deposition onto graphite fiber-reinforced polyimide substrates given that the tip of the feeding wire must be heated beyond its melting point to form droplets for deposition. As a result of overheating of Al droplets by arc spraying, the formation of thermal damage regions on the substrate have been reported. Therefore, control of the temperature of the arc-sprayed particles is limited compared to that of other thermal spraying processes such as flame spraying, in which the temperature of the flame can be controlled independently to avoid over-heating the impinging metal particles.

### 1.3.4 Plasma Spraying

Plasma spraying is a thermal spray process in which an ionized gas jet melts and propels the feedstock powder for deposition onto the substrate. The plasma jet consists of a carrier gas that is expanded through a nozzle to create a sub- or supersonic flow [35, 55] while being heated to the ionized gas state by DC arc or RF discharges [35]. Argon, nitrogen, helium, and hydrogen

may be used to produce the plasma jet, which reaches temperatures up to 14,000°C [32, 47]. Particle impact velocities associated with the plasma spray process are usually between 160 and 2000 m/s [29, 34]. Plasma spraying is a unique process compared to the other thermal spray processes due to the higher gas temperatures achieved by the plasma jet, which allow the deposition of materials with high melting temperatures. Although the plasma spraying process has relatively high temperatures, metallization of polymers has been performed using air plasma spraying (APS). The APS process has been used to deposit Al, Zn, and Cu coatings onto PMC parts [54, 56-59]. Beydon *et al.* [58] and Ganesan *et al.* [57] reported the APS deposition of Cu layers onto carbon fiber-reinforced thermosets. Alternatively, Huang *et al.* [56] and Guanhong *et al.* [59] studied the deposition of thin Al bond-coats onto FRPCs. In these studies, the research focus was on the fabrication, thermal expansion, and mechanical characterization of the metal deposits, as opposed to the investigation of the electrical properties of as-sprayed parts. On the other hand, Affi *et al.* [60] reported the deposition of electrically conductive plasma-sprayed Al coatings onto carbon fiber-reinforced epoxy (thermoset) substrates. Although successful deposition of metallic coatings by plasma spraying on polymer-based substrates has been reported, it has been noted that the high thermal load exerted by the plasma spray process on the polymer-based substrates can degrade the substrates [54]. Therefore, careful execution of plasma spray metallization of polymer-based parts should be considered to avoid structural degradation of the substrate.

### 1.3.5 Surface Preparation of Polymer-Based Substrates

Preparation of the substrate for thermal spraying is essential to promote the adhesion of the impacting particles. The surface preparation process should increase the roughness of the substrate surface to promote the formation of a mechanical bond between the impacting particles

and the substrate [61]. Grit blasting is one of the most common methods for roughening the substrate prior to thermal spray deposition. During the grit blasting process, the roughness of the surface increases as a result of the erosion and material removal caused by the impact of high velocity hard grit medium such as alumina or glass. The application of grit blasting as a pre-treatment technique for thermal spraying is not limited to metal substrates and has been employed to roughen polymer-based substrates. Liu *et al.* [53] grit-blasted PMC substrates made from graphite fiber-reinforced thermo-setting polyimide prior to plasma spray deposition, in order to promote the adhesion and fabrication of Zn coatings. Huonnic *et al.* [17] used grit-blasted glass and basalt FRPC tubes to promote the formation of Al coatings. Guanhong *et al.* [59] grit-blasted PMC (carbon fiber-reinforced unsaturated polyester) substrates to promote the deposition of Al bond-coats using APS. Although grit blasting allowed the successful deposition and adhesion of metal coatings in previous studies, this process may not be a suitable method for brittle polymer substrates that are susceptible to cracking and localized fracture under the impact of high-velocity grit media.

Damage induced in the substrate by grit blasting can adversely affect the mechanical properties of polymer-based structures. The results of the study by Huonnic *et al.* [17] suggested that grit blasting of FRPC tubes can decrease the burst pressure of composite pipes by compromising the integrity of the reinforcing fibers of the composite. The degree of damage is dependent on the velocity of the blasting media, which is a function of the control parameters of the grit blasting unit and physical properties of the blast medium. Liu *et al.* [53] showed that the level of damage in a graphite fiber-reinforced thermoset polyimide substrate is likely to increase at higher pressures of the carrier air of the blasting medium due to the higher velocity of the impacting particles. On the other hand, difficulties associated with the grit blasting of

polymer-based substrates are not limited to the risk of structural damage. Soft and flexible elastomers, such as PU that exhibit high elongation at yield may cause the grit medium to rebound from the surface as it deforms elastically under the load of the impinging medium.

During grit blasting, the roughness of the substrate surface increases as a result of the erosive wear caused by the impact of hard particles. The roughness of the substrate surface can also be increased via abrasive wear (i.e., grinding) of the substrate surface [53, 56, 62]. Huang *et al.* [56] showed that grinding of the surface of quartz fiber-reinforced polyimide (thermoset) substrates using abrasive paper (mesh size 240) can increase the surface roughness through abrasion of the substrate resin and exposure of the fibers. Liu *et al.* [53] roughened the surface of graphite fiber-reinforced thermo-setting polyimide substrates by both grinding and grit blasting. The grinding was conducted by using a range of sandpaper mesh sizes from 60 to 1000. The maximum shear adhesion strength of the coating was obtained by using mesh size 100, which was still lower than that of samples roughened with grit blasting at pressures higher than 0.2 MPa. This suggests that irregular surface asperities caused by the impact of high-velocity grits can result in mechanical bonds of higher strength between the surfaces and the deposited splats compared to those of abraded surfaces produced by grinding. On the other hand, due to the mechanical damage caused by the grit blasting and grinding, these methods may not be suitable for surface pre-treatment prior to the thermal spray process and alternative methods may be warranted.

The deposition of thermally sprayed coatings onto polymer-based substrates without surface preparation has also been reported in literature [48, 49, 63, 64]. In cold spraying, the sprayed particles are heated to temperatures below the melting temperature of the powder

material. Thus, the metal particles are stiffer and may penetrate into the soft polymeric substrates when accelerated to high velocities. Also, process parameters can allow the hot carrier gas to soften the polymer-based substrate beyond the threshold of penetration for impinging metal particles, resulting in particle penetration into the substrate and ultimate adhesion. The sprayed particles would form a mechanical bond with the deposited metal particles already attached to the polymer-based substrate.

The incorporation of a granular material on the surface of the polymer substrate is an alternative method that has been used to increase the roughness of the substrate surface, in lieu of grit blasting. Gonzalez *et al.* [18] roughened the surface of glass-fiber-reinforced epoxy tubes by the addition a layer of garnet sand during the curing process prior to the flame spray deposition of Al-12Si coatings. In contrast to results reported by Hounnic *et al.* [17], where the grit blasting process was employed, this technique did not alter the strength of the FRPC tubes and the internal pressure required to cause fracture and damage of the coated FRPC specimens remained unchanged from that of the uncoated FRPC specimens. The addition of a ceramic granular material, with its low thermal conductivity, also provided a barrier to heat transfer from the high-temperature flame and particles, protecting the polymer substrate from high-temperature degradation during the thermal spray process [18]. Also, Robitaille *et al.* [19] suggested that the granular metal layer can be added to the substrate surface during the curing process of the polymer substrate to promote thermal spray deposition. In this study, a layer of Cu particles were added onto the unidirectional/weave carbon-fiber-reinforced epoxy (thermoset) substrate during the curing process to enable the deposition of cold-sprayed Zn coatings without inducing any damage to the substrate fibers. Deposition on the substrate with no surface pre-treatment led to erosion of epoxy and exposure and damage of the carbon fibers. In another study by Lopera-

Valle *et al.* [30, 31], it was shown that the layer of granular sand material can also be added to the thermosetting substrate (glass fiber-reinforced epoxy composite) surface by applying a layer of adhesive after the curing process, which allowed the deposition of coatings consisting of 80 wt.% nickel and 20 wt.% chromium (Ni-20Cr). Figure 1-5 shows a cross-section image of the deposited Ni-20Cr coating and the sand layer added onto the FRPC substrate [31]. As evidenced by Fig. 1-5, the metal coating and the granular particles used for roughening the polymer-based substrate are bound by mechanical interlocking.

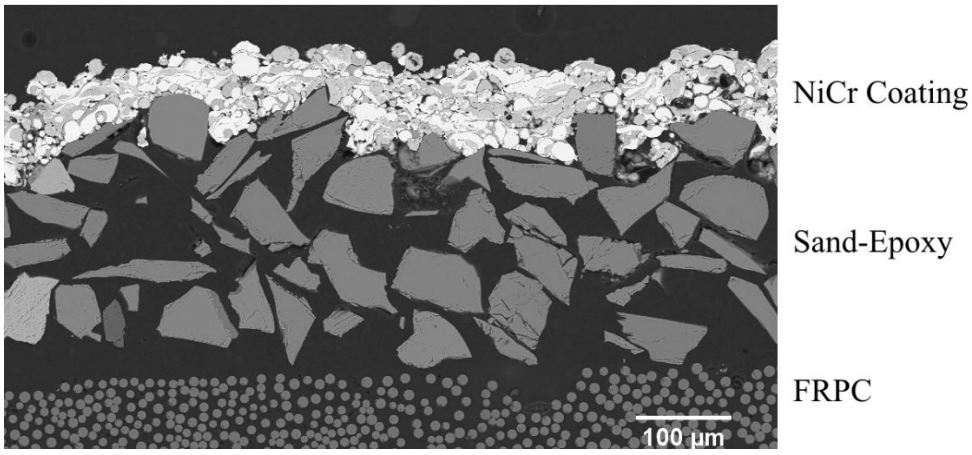


Figure 1-5 Backscattered scanning electron microscope (SEM) image of the cross section of a flame-sprayed Ni-20Cr coating deposited onto a FRPC substrate [31]

## 1.3.6 Deposition of Metal Bond-Coat

In the case of deposition of powder particles with high melting temperatures, regardless of the heat produced by the spray plume, localized degradation of the polymer substrate can occur as a result of the impact of high-temperature particles. Under these circumstances, fabrication of an intermediate metal coating with lower melting temperature particles can be advantageous. Guanhong *et al.* [59] deposited an Al bond-coat onto carbon fiber-reinforced unsaturated polyester (thermoset) substrate prior to deposition of the final aluminium oxide

($Al_2O_3$) coating by APS. This technique allowed for enhanced protection of the polymer substrate from the high temperatures of the molten and semi-molten $Al_2O_3$ particles and the high temperature of the plasma spray deposition process. Aluminium bond-coats deposited at shorter stand-off distances and higher plasma currents were found to have higher adhesion strength. This was due to the greater deformation exhibited by splats and the overall improvement in morphology that led to a denser structure of the coating. Huang *et al.* [56] deposited Al as a bond-coat prior to spraying the final yttria-stabilized zirconia (YSZ) coating in an effort to protect the fiber-reinforced polyimide substrate from the high temperature of the plasma-sprayed YSZ deposition particles. Alternatively, it was further shown by Huang et al., [62] that the use of Zn as a bond-coat provided better thermal protection for the polymer substrate. This was likely due to the lower thermal conductivity of Zn of approximately 116 W/m-K in comparison to that of Al of approximately 237 W/m-K [65]. As a result of the deposition of the Zn bond-coat, the final deposited coating had higher thermal shock resistance compared to that of the Al bond-coat. Thus, deposition of a suitable bond-coat can reduce the adverse thermal effects of thermal spray metallization of polymer-based substrates. Liu *et al.* [54] studied the effect of the bond-coat material on the microstructure and shear adhesion strength of plasma-sprayed coatings deposited onto graphite fiber-reinforced polyimide substrates. It was found that materials with higher melting temperature, such as Cu (melting temperature of 1083°C) and nickel (melting temperature of 1453°C), produced thermal damage on the polymer-based substrate (polyimide) upon deposition. This thermal damage affected the bond strength between the carbon fibers and the polyimide matrix, which led to separation of some fibers and a weak bonding at the coating-substrate interface. The bond-coats of materials with lower melting temperature, such as Al

(melting temperature of 660°C) and Zn (melting temperature of 418°C), did not delaminate from the substrate.

### 1.3.7 Thermal Spray Process Parameters

The properties of thermal-sprayed coatings are a function of the spraying parameters. Thermal spray parameters can be considered as the process inputs that affect the particle velocity, particle temperature, and substrate temperature distribution. The substrate temperature distribution is of particular importance when depositing on substrates with a low heat capacity, such as polymer-based materials. In this case, the spraying parameters not only affect the morphology of the final deposited coating, they also affect the level of damage that the substrate might experience during the thermal spraying process. Accordingly, the parameters should be selected based on the physical properties of the sprayed particles and the substrate heat capacity. Consequently, spraying parameters such as the electric current input in plasma and arc spraying, and fuel and oxygen feeding rates in flame spraying should be apt to ensure that the produced thermal load will not compromise the integrity of the polymer substrates. To that end, Guanhong *et al.* [59] studied the effect of the plasma spray current on the quality of the coatings deposited onto polymer substrates. It was shown that the use of high currents and long spraying times during plasma spraying of $Al_2O_3$ introduced thermal damage to carbon fiber-reinforced polyester substrates even with pre-deposition of Al as bond-coat. Other spraying parameters such as air cooling and varying the stand-off distance between the thermal spray heat source and the substrate can be employed for further process control. It has been found that the stand-off distance influences the metal coating deposition onto polymer-based substrates [20, 21]. Shorter stand-off distances led to shorter in-flight time of the metal particles and, therefore, they had higher impact velocity and temperature and reduced oxide content. On the other hand, shorter

stand-off distances produce a higher heat flux into the substrate, increasing the temperature within that substrate [66]. This increased the risk of imposing excessive thermal load onto heat sensitive substrates such as polymer-based materials. Thus, although shorter stand-off distance can lead to higher deformation of splats and improved coating morphology, setting the stand-off distance to very low values is not recommended for thermal spray deposition onto polymer-based materials, unless temperature control methods such as air cooling are used.

The injection of compressed air during the thermal spraying process is an effective method to cool the substrate and limit thermal damage induced by the thermal spray deposition process. As shown by Floristan *et al.* [67], air cooling was utilized to reduce the thermal load on the substrate and prevent the coating from cracking during plasma spraying of $TiO_2$ coatings onto glass substrates. The addition of compressed air can protect the substrate from residual-stress induced cracking by reducing the thermal load and temperature within the substrate and allow thermal spray deposition at shorter stand-off distances. As a result of shorter stand-off distances, coatings with lower electrical resistance were deposited due to the reduction in oxidation, higher deformation and improved interlocking of splats and lower porosity of the $TiO_2$ coating [67]. In another study, Voyer *et al.* [20, 21] utilized air cooling of the substrate during the deposition of flame-sprayed Al coatings onto substrates made of polyester woven fabric (thermoset). It was shown that by introducing cool air and optimizing the spraying parameters, the stand-off distance could be reduced without imposing any evident thermal damage to the polymer-based substrate. This technique allowed for the fabrication of metal coatings with improved morphology.

Similar to other thermal spray metallization processes, cold spray parameters play an important role on determining the final characteristics of the deposited coating and possible mitigation of damage of the polymer-based substrate. Ganesan *et al.* [48] explored the feasibility of the cold spray process for the deposition of Cu and Sn coatings onto PVC substrates. It was shown that the gas temperature affects the coating deposition efficiency, possibly due to the thermal softening of the PVC substrate. Thermal softening of the substrate occurred under conditions in which the gas temperature exceeded the glass transition temperature of the PVC substrate (353 K) and changed the condition of the substrate from a rigid to a rubbery state. It was further shown that Sn powder particles had higher deposition efficiency than Cu particles due to the soft nature of Sn and its lower impact energy compared to that of Cu. In a subsequent study, Ganesan *et al.* [64] evaluated the effect of substrate type on the deposition efficiency of cold-sprayed Cu and Sn particles, using thermoset epoxy and thermoplastic PVC substrates. It was found that brittle epoxy substrate exhibited a lower coating deposition efficiency compared to that of PVC. Fracture of the epoxy substrate was observed during cold spray deposition, whereas the soft PVC substrate allowed the penetration of impacting particles, which resulted in higher deposition efficiency [64]. Thermal softening of carbon fiber-reinforced PEEK450CA30 substrates caused by the high temperature of gas during cold spray deposition of Al powder has also been reported by Zhou *et al.* [49]. The softening of the PEEK450CA30 matrix was found to be responsible for the penetration of Al particles into the FRPC material and the formation of a mechanical bond between Al particles and the polymer-based substrate [49]. Thus, depending on the mechanical properties of the substrate and the cold spray parameters, particles with high velocity either rebound from or penetrate into the substrate [44]. In a comprehensive study by King *et al.* [44], the embedment of copper particles into a series of substrates, namely polyamide

(nylon), PU, HDPE, PTFE, PC, and polypropylene (PP) was investigated. The Cu particles were embedded into the polymer substrates by increasing the gas temperature from 150ºC to 350ºC. The maximum penetration depth occurred in the PU (softest material) and HDPE (lowest melting temperature). However, due to the softening of the substrates that were studied, the Cu particles did not deform properly to form a continuous electrically conductive coating. Similarly, in a study conducted by Gardon *et al.* [68], it was found that due to the softening of the substrate (bio-compatible PEEK), the cold-sprayed titanium particles penetrated into the substrate in the absence of coating build-up. A balance between the carrier gas temperature and the thermal softening of the polymer substrate was experimentally found to permit the deposition of titanium coatings. Another study conducted by Lupoi *et al.* [63] showed that Cu and Al powder particles are not suitable for cold spray metallization of polymer-based substrates such as PC/ABS blend, polystyrene, polyamide-6, and PP substrates. The high density of Cu particles led to high impact energy and erosion of the polymer substrates with higher erosion rates at higher gas pressure. Fabrication of Al coatings was unattainable since the required critical velocity for cold spray deposition of Al particles was not achieved for the given substrates and process parameters. On the other hand, Sn, with lower specific weight and melting temperature was successfully deposited onto all tested polymer-based substrates of the same study [63]. Therefore, along with the carrier gas temperature, the feedstock particle material properties have a significant effect on the deposition of cold-sprayed metal coatings onto polymer-based substrates. If the gas temperature is not sufficiently high so as to soften the impacting particles, the high velocity, rigid particles may either penetrate or erode the substrate upon impact. However, introducing excessive heat during the cold spray deposition process can soften the substrate and limit the particle impact energy that remains available for particle deformation, adiabatic shear instability

heating, and ultimate adhesion. In general, knowledge of the particle velocity and substrate temperature distribution during the thermal spray deposition process can facilitate the experimental approach to find the optimum spray parameters for the deposition of metal coatings onto polymer-based substrates.

## 1.4 Temperature Distribution within Substrates during the Thermal Spraying Process

Damage caused by the high temperature of the thermal spraying process is one of the main concerns in thermal spray metallization of polymer-based substrates. Accordingly, a model that can predict the temperature distribution in the substrate during the spraying process will be useful to ensure that the substrate temperature is kept below critical values. In addition, knowledge about the effect of spraying parameters such as cooling air pressure and stand-off distance on the substrate temperature distribution would facilitate the optimization process.

To determine the temperature distribution within substrate during spraying, a transient heat conduction problem should be solved. A number of previous studies have focused on development of analytical and numerical models for determination of the temperature distribution during the thermal spraying process. Pawlowski [66] developed an analytical model based on the assumption that the coated substrate is a semi-infinite body. The model was then employed to study the influence of spraying distance and initial temperature of the substrate on temperature distribution within the coating [66]. Hugot *et al.* [69] used a 2D finite element (FE) model to determine the temperature distribution within substrate and resulting residual stresses. Good agreement between the numerical model and the experimental data was obtained for the preheating stage [69]. FE modeling has also been used to model electric arc spraying for

determination of temperature distribution during spraying [70]. There was good agreement between the experimental and computed temperatures [70]. Finite difference method is another numerical technique that has been found to be reliable for the simulation of thermal spraying processes [71-73]. Zhu *et al.* [71] have modeled electric arc spraying by using the finite difference method while in another study by Bao *et al.* [72, 73] the flame spraying process was modeled by using the finite difference method. To avoid the disadvantages of methods that involve meshing, Wu *et al.* [74] have developed a model based on a meshless local Petrov-Galerkin method to simulate the plasma spraying process. The model was verified experimentally and a strong influence of the spraying stand-off distance on the substrate temperature was shown [74]. On the other hand, Green's functions have been shown to be powerful and efficient tools to obtain analytical solutions for transient heat conduction problems [75-79]. Monds *et al.* [76] have employed the Green's function method to determine the temperature distribution in skin when exposed to simulated fire by developing a finite-length scale heat conduction model. Good agreement between the mathematical model results and experimental results was reported [76]. Grine *et al.* [77] used a Green's function methodology to identify temperature distribution in a flat plate exposed to convective heat transfer and a known heat flux, which is the amount of heat energy transferred per unit area of surface. Again, good agreement between the experimental findings and the results of the theoretical model was found [77]. Fernandes *et al.* [78] have shown that the Green's function method will reduce the computational time that is required to execute the mathematical models, in comparison to that which is required for models based on full numerical methods. Wang *et al.* [80] also showed that the Green's function approach requires lower computational time since the value of each time step is not subjected to instabilities, which may be typical of the FE method.

## 1.5 Wear Resistance of Polyurethane

The main application of PU liners is to protect the component substrate material from erosion caused by solid particle impact. Metallization of the PU by thermal spraying processes can influence its wear resistance by affecting the temperature distribution within the PU during service. Therefore, knowledge regarding the effect of temperature on wear resistance of PU elastomers can provide insight on the possible effects of the deposited metallic coatings on the erosion resistance of PU. Although the relationship between the wear resistance of elastomers and their mechanical properties has been the subject of previous studies, their wear phenomena has been found to be a complex process involving many parameters that affect the final wear performance [8, 9]. Ping *et al.* [15] showed that two PU samples with similar tensile and tear strengths had different erosion rates, which was probably due to differences in elongation at break of the two samples. Beck *et al.* [81] showed that PU samples with similar hardness had different erosion rates. Variation of hysteresis of the samples was presupposed to be the factor affecting the erosion rate of the PU. Hysteresis of a polymer represents the fractional energy lost in a deformation cycle. Samples with higher hysteresis had higher erosion rates. Temperature rise caused by the hysteresis of PU samples was suggested to have an effect on the erosion rate of the PU. This would indicate that the variation in temperature due to the higher heat generation could have adversely affected the wear rate of PU elastomers. In a comprehensive study by Li *et al.* [8], the erosion resistance of a series of castable PU elastomers with almost the same rebound resilience was investigated. A trend of increase in erosion rate with increasing hardness, tensile modulus, and tensile strength was observed. The softest material with the lowest tensile strength produced the maximum resistance to erosive wear. On the other hand, Hutchings *et al.* [82] showed that there was no simple relation between the wear rate of rubber elastomers and

material and mechanical properties such as Shore hardness, ultimate tensile elongation, and tensile strength. Rebound resilience was found to be the most dominant factor affecting the wear resistance of rubber elastomers in which the rubber with higher rebound resilience had the highest erosion resistance.

The mechanical properties of PU elastomers are sensitive to temperature and may vary significantly even by changing the temperature by only approximately 50°C. Thus, the temperature rise during a wear experiment may affect the erosion resistance of PU adversely, and this has been reported in fact in previous studies [7, 11, 14, 81, 83-86]. However, the number of studies that have focused on designing a test assembly for studying the effect of working temperature on erosion resistance of PU and, in general, elastomers are limited. Zuev *et al.* [87] studied the effect of slurry temperature on the erosion rate of rubber elastomers. The erosion rate decreased when the temperature was increased from 20°C to 70°C. The increase in elasticity at higher temperatures of the rubber was suggested as the parameter that caused the reduction in the erosion rate. Marei *et al.* [88] reported similar phenomenon when evaluating the erosion of rubber in an air blasting test scheme at elevated air temperatures. It was found that the higher the difference between the testing temperature and the glass transition temperature of the rubber, the lower the erosion rate. It should be noted that neither of the aforementioned studies of Zuev *et al.* [87] and Marei *et al.* [88] focused on determining the actual temperature distribution within the samples during the erosion test. Hill *et al.* [83] evaluated the wear performance of PU by employing an abrasion testing procedure based on ASTM Standard G65 [89]. The temperature rise during the abrasion test improved the wear resistance of the elastomer and that outcome was attributed to the softening of PU and its lower hardness at elevated temperatures. On the other hand, in other studies, a decrease in the erosion resistance of PU has been reported at elevated

temperatures [7, 14]. Zhang *et al.* [14] found that the temperature rise caused by the hysteresis decreased the erosion resistance of the PU during the erosion test. Due to the low thermal conductivity of PU, the heat generated by hysteresis caused a temperature rise in the layer beneath the surface. This higher temperature decreased the cohesive energy between the surface layer and the substrate, finally leading to lower erosion resistance. Zhang *et al.* [7] showed that the erosion rate increased by increasing the PU thickness beyond a threshold level. The heat generated that was caused by hysteresis and subsequent temperature rise was found to be responsible for the increase in erosion rate.

## 1.6 Finite Element Modeling of Wear Processes

Erosion caused by solid particle impact is a complicated process due to the high number of factors that affect the wear mechanism and final erosion rate. The wear resistance is a function of a) the properties of the erodant particles, their shape, density, size, and hardness, b) the properties of the target material, including Young's modulus, plastic behavior and failure behavior, and c) wear testing parameters, such as velocity of erodant particle, angle of impacts, testing temperature, and flow rate of the erodant particles [90]. Accordingly, experimental study of the wear phenomenon to investigate all the influencing parameters is time consuming and costly. To that end, a number of analytical and numerical models have been developed to date for a wide range of erosion conditions to study the wear phenomenon [91]. The models developed can assist with understanding the fundamental principles of the wear mechanisms and after verification can be used as predictive tools to study the effect of different parameters on the wear rate. Through different models developed to date, the finite element (FE) technique has received much attention for simulating the solid particle erosion both for fundamental study of the erosion phenomenon and also as a tool for prediction of the effect of testing conditions on the wear

resistance of the target material. Eltobgy *et al.* [90] developed a 3D FE model to simulate the erosion caused by solid particle impact of Ti–6Al–4V substrate material. The model developed enabled the study of the residual stresses produced during the erosion process. The effect of particle size, velocity, and impact angle on the erosion rate was also studied [90]. Balu *et al.* [91] developed a FE model to study the erosion behavior of AISI 4140 steel and nickel (Ni) - tungsten carbide (WC) metal matrix composites (MMC). The model was verified by comparing the computed data with data obtained from experiments. The model was further employed to study the effect of impingement angle, velocity, and the shape of erodant particles on the erosion rate and produced stresses. FE modeling of the erosion process caused by solid particle impact of both ductile and brittle materials have been the subject of some previous studies. Examples of ductile materials that were the subject of modelling included Steel, Al6061-T6 [92], Ti-6Al-4V [90] while the examples for modeling of erosion of brittle materials included cermets such as $Cr_3C_2$/NiCr [93] and Silicon carbide [94]. Furthermore, FE modeling of erosion caused by solid particle impact can also be extended to simulate the machining processes that involve material removal caused by solid particle impact such as water jet machining [95, 96].

Although numerous studies have focused on development of FE models for modeling the erosion caused by solid particle impact of ductile metals and brittle cermet materials, a limited number of studies have focused on modelling the solid particle erosion of soft elastomeric materials such as PU. Martinez *et al.* [97] developed a 2D FE model for an in depth analysis of the wear phenomenon as a result of sliding and contact of PU over rough metal surfaces. The Yeoh strain energy potential function was chosen to describe the hyperelastic behavior of PU. Compression tests were conducted for data fitting of the chosen material model formulation. FE simulation allowed for micro level evaluation of the contact between the PU and rough metal

surface. The calculated stresses from the FE model supported the hypothesis that there was a possibility of crack formation below the worn surface. In a recent study by Zhang *et al.* [7], a FE model based on an elastic-plastic constitutive law with linear isotropic hardening for material formulation was developed to simulate the impact of a single particle on PU liners with different thicknesses. The results obtained were validated with experimental temperature measurements. The element removal criterion was defined to model the material removal and calculate the wear rate as a result of impact of a single particle. The FE model predicted improvement in erosion resistance by increasing the coating thickness similar to data obtained from experiments. However, the FE model failed to predict the increase in erosion rate at larger film thicknesses due to the effect of temperature rise in thicker PU liners. In another study by Gong *et al.* [98], a 3D combined FE-mesh free model was developed to simulate the solid particle erosion of PU liners. The use of the mesh free formulation was chosen to eliminate the adverse effects of element distortion in FE model. In mesh free techniques, there is no connection between the nodes, and the model is discretized with scattered particles. The Johnson-Cook model, a viscoplastic material model, was used to develop the FE model. The area impacted had large deformations and was discretized by smoothed hydrodynamics (SPH) particles, a classic meshfree model, and the remaining section was modeled by FEM meshes. The obtained results by the combined FE-mesh free and FE model were compared in terms of the stresses produced. The results obtained show that the difference between the calculated stresses at the impact point by the two models were negligible [98]. However, the computation time by the FE model was approximately four times shorter. Although in a few studies the FE technique has been employed to simulate the wear phenomenon of PU elastomers, the number of developed models that take

into account the effect of some of the mechanical properties of PU elastomers such as stress softening and/or the effect of repeated impact of particles is limited.

## 1.7 Summary

Among all elastomeric materials, PU elastomers have received particular attention given that they can be processed by methods typically used for polymers while still having the superior mechanical properties of vulcanized rubber such as high elasticity, high load capacity, and resistance to tear. The relatively low cost of PU elastomers and the fact that their resistance to wear is greater than that of most elastomers and even some of the hard-faced coatings has made PU an appropriate option for use as protective liners in large scale applications such as pipelines. However, low thermal and electrical conductivity of PU similar to most polymers have limited its functionality for use in environments with high temperature or where high electrical conductivity is required. Metallization of polymeric materials by the deposition of conductive coatings is a possible technique to augment the effective thermal and electrical conductivity of a polymeric material, but it has proven to be challenging. Review of thermal spray metallization of polymeric substrates revealed that although the working temperature of cold spraying process is comparatively lower than other thermal spraying processes, it is not an appropriate method for deposition of continues conductive coatings on soft elastomeric materials such as PU. Alternatively, the flame spraying process allows for better control of spraying parameters and has a lower working temperature than plasma spraying and arc spraying. This suggests that employing the flame spraying process may be a more pragmatic choice for deposition of metallic coatings on heat sensitive polymers such as PU. Surface pretreatment prior to thermal spraying is mandatory to facilitate the adhesion of the impacting powder particles. In contrast to metallic substrates, the grit blasting is not the ideal option for roughening the surface of polymer-based

substrates. Breakage and localized fracture of hard polymer-based substrates can occur during grit blasting. Alternatively, the grit media may rebound or penetrate into the soft polymeric elastomers without formation of substantial roughness on the substrate surface. Thus, alternative methods for pretreatment of the surface of polymer-based substrates such as the addition of granular material during the curing process are of interest. The thermal spray process parameters have a significant influence on the morphology of the deposited coatings and also the thermal and mechanical damage that the polymeric substrate may experience during the spraying process. The thermal load can be controlled by adjustment of spraying parameters such as the temperature of the plume and stand-off distance. Techniques such as substrate air cooling has been shown to be effective in cooling the substrate during the spraying process. Knowledge about the temperature distribution within the substrate during the spraying process can allow to study the effect of process parameters on the temperature distribution and facilitate the sensitivity analysis.

Thermal spray metallization can improve the heat transfer rate of the polymeric material. Thus, the metallization of polymers such as PU can affect the in service temperature distribution and, therefore, its wear resistance. Although several studies have addressed the effect of temperature on the wear performance of PU elastomers, the literature is inconclusive about the effect of temperature on wear resistance of PU. Further research to study the effect of heat and temperature on wear properties of PU is essential to gain knowledge and greater understanding about the erosion mechanisms of the material at elevated temperatures and identify the key parameters that affect the wear resistance. The wear phenomenon has been found to be a complex process involving many parameters that affect the final wear performance. For that reason, simulating the erosion process by techniques such as FE formulation can allow for closer

study of the wear phenomenon and deeper understanding of the material removal mechanism during erosion caused by solid particle impact.

## 1.8 Objectives

The objectives of this doctoral research project were to:

i) Investigate the possibility of deposition of continuous conductive metallic coatings on PU substrates.

ii) Develop a robust analytical model for determination of temperature distribution within the substrate during the flame spraying process.

iii) Study the effect of flame spraying parameters of air pressure and stand-off distance on the temperature distribution within the substrate, the electrical resistance and the characteristics of coatings deposited on PU substrates.

iv) Study possible changes in dynamic mechanical properties of PU substrates due to the exposure to heat from the flame spray torch.

v) Design and develop an erosion test assembly capable of wear testing at controlled temperatures to study the effect of temperature on wear resistance of PU elastomers.

vi) Find the mechanical properties that best correlate with the erosion resistance of PU elastomers at controlled temperatures.

vii) Develop a numerical model based on the FE technique to simulate the solid particle erosion process of PU elastomers at controlled temperatures.

## 1.9 Thesis Organization

The present thesis document has several Chapters with the following structure: Chapter 2 focuses on the development of a novel heat transfer model for prediction of the temperature distribution within PU substrates during flame spraying process. The experimental setup that was employed for fabrication of metallic coatings and further verification of the developed models have also been included in this Chapter. In Chapter 3 of this thesis document, the microstructure and electrical properties of the flame sprayed metallic coatings is studied. Discussion about the effect of flame spraying process parameters on temperature distribution and its corresponding effect on coating characteristic is also discussed in this Chapter. Chapter 4 presents the novel testing assembly that was developed to study the effect of temperature on erosion resistance of PU elastomers. Evaluation of the worn surfaces and studying the relation between the mechanical properties of PU elastomers and the erosion rates at set temperatures are other subjects that will be discussed in this Chapter. In Chapter 5, details about the developed FE model for simulating the erosion of PU elastomers is provided. The obtained results from the simulation and the effect of material properties such as ultimate strength, elongation at break and softness on produced stresses and strains are discussed in this Chapter. Chapter 6 summarizes the conclusions from this thesis. Finally, Chapter 7 provides the suggestions for future work as for extension and modification of this research work.

# Chapter 2

# Determination of Temperature Distribution within Polyurethane Substrate during Flame Spraying Process

The deposition of metallic coatings on polymer-based substrates by using a thermal spraying process is a challenging task due to the thermal sensitivity of polymeric materials and the high temperatures that are typical of thermal spraying processes. Thus, predicting the temperature distribution in the substrate during spraying is considered a key factor in the selection of appropriate coating materials and control of process parameters. Analytical and numerical models for the prediction of the temperature distribution within polyurethane substrate during flame spraying was developed. An experimental setup was developed to generate data as for the verification of the developed models. In addition to validating the model with experimental results, it was also verified by comparing its predictions with those of an established model. The model was further utilized to study the effect of air pressure and the stand-off distance of the flame spray torch on the temperature distribution in the substrate.

Some sections of the work presented in this chapter have been published in Surface and Coatings Technology, (259) 625-636, 2014, and proceedings of The Canadian Society for Mechanical Engineering (CSME) International Congress, Toronto, ON, Canada, June 1 4, 2014.

## Nomenclature

| | |
|---|---|
| $T$ | temperature (°C) |
| $x$ | $x$ coordinate (m) |
| $y$ | $y$ coordinate (m) |
| $z$ | $z$ coordinate (m) |
| $x'$ | $x$ coordinate dummy variable (m) |
| $x^*$ | non-dimensionalized x coordinate |
| $t$ | time (sec) |
| $t_l$ | time duration that takes the torch to scan each horizontal line (s) |
| $t_p$ | time duration that takes the torch to scan the whole rectangular area in each pass (s) |
| $t_s$ | total spraying time (s) |
| $t^*$ | non-dimensionalized time |
| $k$ | thermal conductivity ($Wm^{-1}K^{-1}$) |
| $G$ | Green`s function (°C) |
| $F$ | function in Green`s functions equation (°C) |
| $Fo$ | Fourier number, Fo = $\alpha t L^{-2}$ |
| $f$ | function in Green`s functions equation ($Wm^{-2}$) |
| $f'$ | function in Green`s functions equation (°C) |
| $V$ | transverse velocity of the torch ($ms^{-1}$) |
| $W$ | width of the area scanned by the torch in each pass (m) |
| $L$ | thickness of the substrate (m) |
| $d$ | displacement from the center of torch (m) |
| $q''$ | heat flux ($Wm^{-2}$) |
| $Q''_{total\text{-}p}$ | heat per unit area absorbed by the substrate in each pass ($Jm^{-2}$) |
| $q''_{AVG\text{-}p}$ | average heat flux of each pass ($Wm^{-2}$) |
| $q''_{AVG}$ | average heat flux for $n_p$ number of passes ($Wm^{-2}$) |
| $n_p$ | number of passes |
| $n$ | summation index |
| $m$ | increment number |
| $m_p$ | total number of increments |

*Greek Symbols*

| | |
|---|---|
| $\alpha$ | thermal diffusivity ($m^2s^{-1}$) |
| $\lambda$ | eigenvalue ($m^{-1}$) |
| $\tau$ | time dummy variable (s) |
| $\eta'$ | vector normal to the surface pointing outward |
| $T^*$ | non-dimensionalized temperature |
| $\infty$ | infinity |

## 2.1 Experimental Method

The operation of a flame spray torch over PU substrate samples was used as the basis to generate experimental data to validate the model that was developed in this study. In particular, the experimental study consisted of PU substrate preparation, flame spray deposition of coatings onto PU, and the measurement of heat flux and transient temperatures.

### 2.1.1 Flame Spraying

A flame spray torch (6PII, Oerlikon Metco, Westbury, NY, USA) was used to deposit conductive coatings on PU substrates. The torch was operated by a programmable robot (HP-20, Motoman, Yaskawa Electric Corp., Waukegan, IL, USA). The combustion of oxygen and acetylene was utilized to generate a flame to melt and accelerate aluminum alloy powder particles for coating fabrication. Air was added to the flame through the air cap that was located on the tip of the flame spray gun to shape the flame and to provide cooling to mitigate damage to the polymer substrate. The powder material was fed through a volumetric powder feeder (5MPE, Oerlikon Metco, Westbury, NY, USA) with argon as the carrier gas. Three sets of spraying parameters, subsequently denoted S1, S2, and S3 spraying conditions, were explored in this study, as presented in Table 2-1. In Table 2-1, the stand-off distance (SOD) is defined as the distance between the torch and the substrate surface, the increment size represents the vertical height that the torch moves after completely traversing the substrate surface after each pass, argon is the carrier gas for the feedstock powder, and Flow Meter Reading (FMR) is a unitless parameter representing the relative powder feed rate as measured by the volumetric powder feeder.

Table 2-1: Flame spraying parameters (NLPM: normal liters per minute, SOD: stand-off distance)

| **Set No.** | **S1** | **S2** | **S3** |
|---|---|---|---|
| Oxygen flow rate (NLPM) | 15 | 15 | 15 |
| Acetylene flow rate (NLPM) | 6 | 6 | 6 |
| Air pressure (gage pressure, kPa) | 34.5 | 68.9 | 103.4 |
| Argon pressure (gage pressure, kPa) | 482.6 | 482.6 | 482.6 |
| Argon flow rate for powder (NLPM) | 9.4 | 9.4 | 9.4 |
| Flow meter reading (FMR) of powder | 120 | 120 | 90 |
| Powder feed rate (g/min) | 84 ± 2 ($n$ = 3) | 84 ± 2 ($n$ = 3) | 51 ± 2 ($n$ = 3) |
| SOD (mm) | 215 | 215 | 150 |
| Torch velocity (mm/s) | 500 | 500 | 500 |
| Increment size (mm) | 4 | 4 | 4 |

A spherical gas-atomized powder of aluminum with 12 wt % silicon (Al-12Si) (52C-NS, Oerlikon Metco, Westbury, NY, USA) with a size distribution of 45 to 90 μm (-90+45 μm) was used in this study. This eutectic material has a lower melting temperature (577°C) than pure aluminum (660°C). Figure 2-1 shows that the morphology of the powder particles was predominantly spherical.

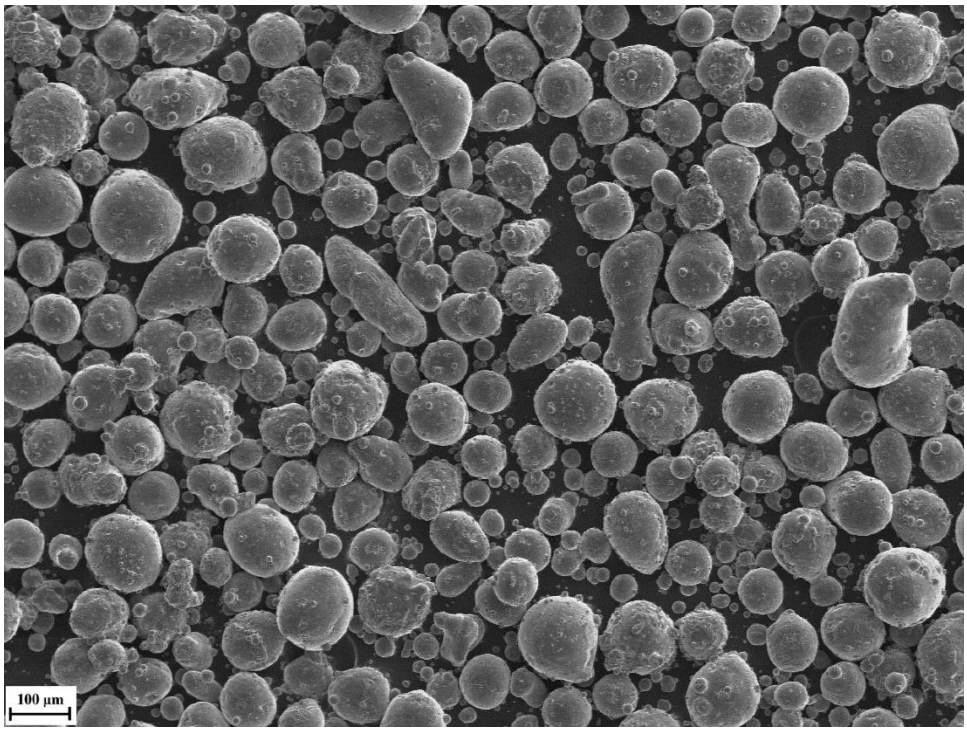


Figure 2-1 Morphology of Al-12Si powder particles

### 2.1.2 Polyurethane Substrate Preparation

The PU material that was selected as the substrate for this study was fabricated from 100% solid toluene di-isocyanate (TDI) ether castable PU (NR 606, Normac Adhesives Products Ltd., Burlington, ON, Canada). This castable PU consisted of two parts: a resin (Part A) and a hardener (Part B). In the preparation of the PU samples, 80 g of resin was mixed with 12 g of hardener and the mixture was blended mechanically for two minutes. The mixture was degassed in a vacuum chamber at -85 kPa of vacuum pressure for five minutes in order to extract any entrapped air. The PU was poured gently into a steel mold that was coated with a release agent (Frekote 700 NC, Henkel Corporation, Rocky Hill, CT, USA) and placed in an oven that was preheated to 50°C to allow for curing. After 40 minutes of curing Al-12Si powder particles were distributed uniformly over the PU surface to act as a roughening agent in preparation for the deposition process. At this stage of the curing process the PU substrates were sufficiently soft to

allow for penetration of the Al-12Si powder particles onto the surface, while avoiding complete immersion of the particles into the surface. The curing process was continued for an additional 4 hours at 82°C. Upon completion of the curing and cool-down process, the samples were cut into 100 mm x 10 mm x 2.9 mm sections and rinsed with acetone to remove unattached particles. A stream of air was also blown over the surface of the samples prior to spraying to ensure that all unattached Al-12Si particles were removed. The thermal properties of the fabricated PU substrates are shown in Table 2-2.

Table 2-2 Thermal properties of the PU substrate [7, 99]

| **Thermal property** | **Value** |
|---|---|
| $k$ (W/m-ºC) | 0.2 |
| $\alpha$ ($m^2/s$) | $1.08 \times 10^{-7}$ |

### 2.1.3 Heat Flux and Temperature Measurements

The heat flux from the flame of the torch and the temperature distribution along the surface of the PU substrate that was directly exposed to the flame was measured in this study. The heat flux was measured by using a heat flux sensor that was developed by Sullivan *et al.* [100]. The heat flux sensor uses measured transient temperatures at the front and rear surfaces of an aluminum block as inputs into an equation for the heat flux that was derived from a heat conduction governing equation. Details of the development of the sensor and heat flux equation are presented elsewhere [100].

Two J type thermocouples (Gage 30, Thermo Electric Ltd., Brampton, ON, Canada) were inserted into the PU substrate as shown schematically in Fig. 2-2 in order to measure the transient temperature. A data acquisition system (SCXI 1600, National Instruments, Austin, TX, USA) was used to collect the data of transient temperatures during the heating and spraying processes. The data collection rate was 100 Hz. The data obtained from thermocouple $T_1$ (see Fig. 2-2) was used as the transient temperature boundary condition in the mathematical model for the temperature distribution in the PU substrate. The data from thermocouple $T_2$ was used to validate the mathematical model. The thermocouples were press-fitted into orifices that were made in the PU substrate. This ensured a near perfect contact between the thermocouples and the PU substrate to mitigate thermal contact resistance.

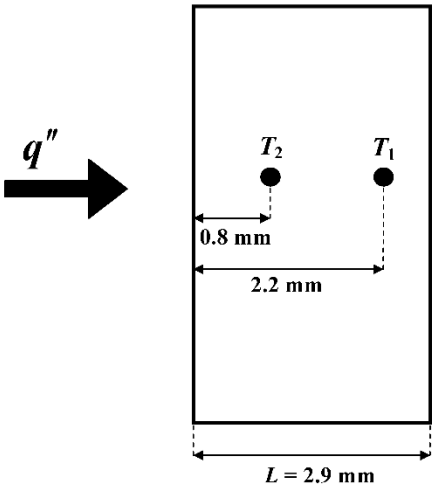


Figure 2-2 Schematic of the position of thermocouples inserted into the PU substrate

## 2.2 Heat Transfer Model for Determination of Temperature Distribution

In the flame spray deposition process, the torch traverses the substrate surface and, depending on parameters such as the number of layers and the speed of the torch, the amount of heat absorbed by the substrate from the torch during the heating and deposition processes will

vary. The amount of energy absorbed by the substrate, in particular, polymer-based substrates, will result in a temperature distribution that may have an adverse impact on the chemistry, microstructure, and/or integrity of the material [17, 18, 54]. To that end, a transient, one-dimensional (1D) heat conduction model was developed to estimate the temperature distribution in a PU substrate during the heating and deposition processes of flame spraying. Figure 2-3 shows a schematic of the problem. Heat flux from the torch and powders was applied uniformly across the surface of the substrate. In this study, it was assumed that heat conduction through the PU substrate was one dimensional since the thickness, $L$, was much smaller than the other dimensions of the sample. The thermal properties of the PU substrate were assumed to be constant. The governing heat conduction equation is

$$\frac{\partial^2 T}{\partial x^2} = \frac{1}{\alpha}\frac{\partial T}{\partial t},\ 0 < x < L\,. \tag{2-1}$$

The boundary and initial conditions are

$$-k\frac{\partial T(0,t)}{\partial x} = q''(t)\,, \tag{2-2}$$

$$T(L,t) = T_1(t)\,, \tag{2-3}$$

$$T(x,0) = T_0\,. \tag{2-4}$$

The boundary condition at the front surface ($x = 0$) of the PU substrate is a boundary condition of the second kind, where a prescribed heat flux is known. Since the torch will move across the surface of the PU substrate, the heat flux observed for a given location over the substrate surface is specified generally as a function of time, $t$. At $x = L$ (see Fig. 2-3), a boundary condition of the first kind is given for a known transient temperature at the boundary. In order to solve the partial differential equation of Eq. (2-1) with the boundary and initial conditions described in Eqs. (2-2) to (2-4), two approaches were employed: a) an analytical approach based on the Green's function

and b) numerical approach based on the controlled volume method. The approach on development of the analytical and numerical solutions are described in Sections 2.2.1 and 2.2.2, respectively.

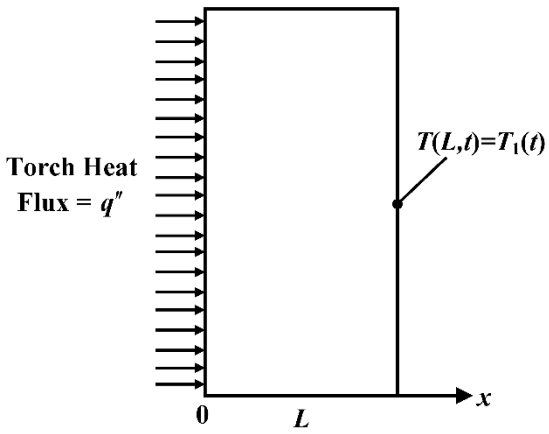


Figure 2-3 Schematic of the heat conduction model

## 2.2.1 Analytical Solution

The simplified Green's function solution for boundary conditions of the first and second kinds, with no heat generation is given by Eq. (2-5) [101] as

$$T(x,t)=\int_{x'}^{L} G(x,t\mid x',0)F(x')dx'+\alpha\int_{\tau=0}^{t} d\tau\sum_{i=1}^{2}\left[\frac{f_i(\tau)}{k_i}G(x,t\mid x_i',\tau)\right] \\ -\alpha\int_{\tau=0}^{t} d\tau\sum_{i=1}^{2}\left[f_i'(\tau)\frac{\partial G}{\partial \eta_i'}\mid_{x'=x_i}\right] \tag{2-5}$$

The Green's function was found by solving the homogeneous problem that is governed by Eq. (2-1), in which the boundary conditions of Eqs. (2-2) and (2-3) were set to zero. Through use of the separation of variables method, the Green's function is [101]

$$G(x,t\mid x',\tau)=\frac{2}{L}\sum_{n=1}^{\infty}\cos(\lambda_n x)\cos(\lambda_n x')\exp(-\lambda_n^2\alpha(t-\tau)). \tag{2-6}$$

The eigenvalues, $\lambda_n$, were determined by using the homogeneous form of the boundary condition of Eq. (2-3), and is given by [101]

$$\lambda_n = \frac{(2n-1)\pi}{2L} \quad \text{for} \quad n = 1, 2, 3,\ldots. \tag{2-7}$$

Substitution of Eq. (2-6) into Eq. (2-5) produced the temperature distribution function as

$$\begin{aligned} T(x,t) = {} & \frac{2T_0}{L}\sum_{n=1}^{\infty}\left[\frac{1}{\lambda_n}(-1)^{(n+1)}\exp(-\alpha\lambda_n^2 t)\cos(\lambda_n x)\right] \\ & + \frac{2\alpha}{kL}\sum_{n=1}^{\infty}\left[\exp(-\alpha\lambda_n^2 t)\cos(\lambda_n x)\int_{\tau=0}^{t} q''(y,z,\tau)\exp(\alpha\lambda_n^2\tau)d\tau\right] \\ & - \frac{2\alpha}{L}\sum_{n=1}^{\infty}\left[\lambda_n(-1)^n\exp(-\alpha\lambda_n^2 t)\cos(\lambda_n x)\int_{\tau=0}^{t}\exp(\alpha\lambda_n^2\tau)T_1(\tau)d\tau\right] \end{aligned} \tag{2-8}$$

Equation (2-8) is the analytical solution for the temperature distribution within the PU substrate during the heating and spray deposition processes. The transient temperature at the boundary where $x = L$ (see Fig. 2-3) will be measured experimentally in this study. The expression for this temperature trace will be substituted into Eq. (2-8) and the integration will be executed in order to find the temperature distribution. The heat flux as a transient variable, $q''(t)$, may complicate the integration of Eq. (2-8). Therefore, an average heat flux over the surface will be determined and employed.

The average heat flux was derived by calculating the total amount of heat that the substrate absorbed while the torch moved across it. This heat flux was normalized based on the spray time duration. In each pass, the torch scanned a rectangular area by moving on horizontal lines and moved up to the next horizontal line after reaching the end of each line. The velocity of the torch was constant when traversing the PU substrate on horizontal lines due to the existence of a three-inch point of departure distance between the start point of the torch and the edge of the

substrate over which the torch accelerated from rest to a constant velocity. The amount of heat flux that was absorbed at a given point (for example, at the origin in Fig. 2-4) was a function of time and position of the torch ($z$, $y_m$). The total heat absorbed by the substrate at the origin is equal to the sum of the heat that is absorbed at the origin as the torch moved on the horizontal lines. The total heat absorbed is

$$Q''_{total-P} = \sum_{m=1}^{m_p} \int_0^{t_l} q''(t)dt \,. \tag{2-9}$$

The average heat flux per pass was derived by normalizing $Q''_{total-P}$ with the time duration for each pass as

$$q''_{AVG-P} = \frac{1}{t_p} \sum_{m=1}^{m_p} \int_0^{t_l} q''(t)dt \,. \tag{2-10}$$

Given that the velocity of the torch is $V = \frac{dz}{dt}$, $dt = \frac{dz}{V}$. At time $t = 0$, the torch is at location $z = \frac{-W}{2}$ and at time $t = t_l$, it is at location $z = \frac{W}{2}$ (see Fig. 2-4). Also at time $t = t_l$, $q''(t) = q''(\sqrt{z^2 + y_m^2})$. The average heat flux per each pass of Eq. (2-10) can be rewritten as

$$q''_{AVG-P} = \frac{1}{t_p} \sum_{m=1}^{m_p} \int_{\frac{-W}{2}}^{\frac{W}{2}} \frac{q''(\sqrt{z^2 + y_m^2})}{V} dx \,. \tag{2-11}$$

The total spraying time for $n_p$ number of passes is higher than that of the summation of spraying times of each pass since there exists a rest time that the torch requires for motion from each subsequent horizontal line of each pass. Consequently, the average heat flux for $n_p$ number of passes can be calculated as

$$q''_{AVG} = \frac{t_p n_p q''_{AVG-P}}{t_s}. \tag{2-12}$$

Equation (2-12), coupled with Eq. (2-11), was employed to calculate the average heat flux of the torch flame onto the substrate.

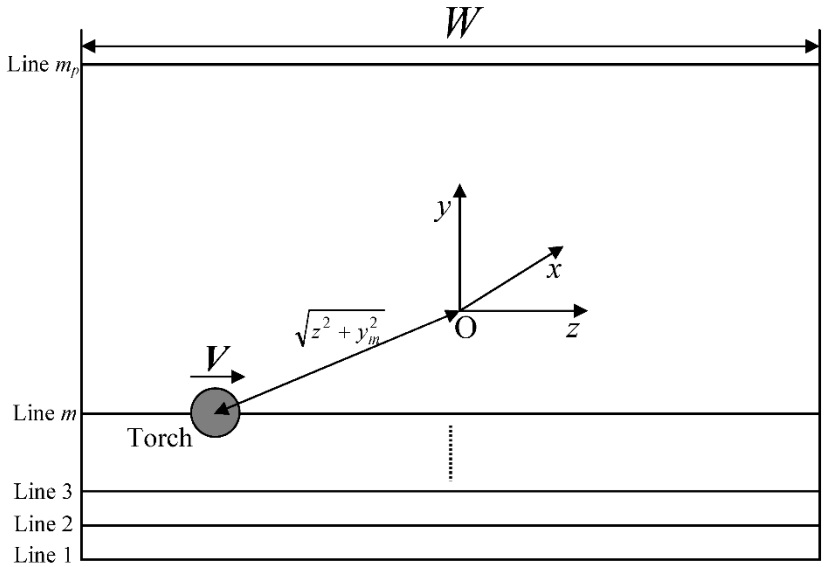


Figure 2-4 Schematic of the flame spray torch motion over the substrate

In this study, validation of the model was accomplished primarily by comparison with experimentally measured data. Further validation of the model was conducted in which it was simplified by making the assumption of the existence of an insulated surface on the back of the substrate. This assumption will hold true when the duration of heating of the substrate is low and/or the thermal diffusivity ($\alpha$) of the substrate is small. The validity of this assumption and its effect on the predicted temperature distribution in the polymeric substrate during the flame spraying process was studied. The assumption of an insulated back surface will yield a simpler mathematical model than that of Eq. (2-8).

The governing equation and the initial condition for the simplified model is the same as those given in Eqs. (2-1) and (2-4), respectively. The boundary conditions for this model are given by Eq. (2-2) and

$$\frac{\partial T(L,t)}{\partial x} = 0 . \tag{2-13}$$

The solution for the temperature distribution function with the insulation boundary condition is available elsewhere [102], and is given by

$$T(x,t) = \frac{q''_{AVG}}{k}\left[\frac{L}{3} + \frac{\alpha t}{L} + \frac{x^2}{2L} - x - \frac{2L}{\pi^2}\sum_{n=1}^{\infty}\frac{\cos(\frac{n\pi x}{L})}{n^2}\exp(-\frac{n^2\pi^2}{L^2}\alpha t)\right] + T_0 . \tag{2-14}$$

Further details of the derivation of Eq. (2-14) are also presented by Faghri *et al.* [102].

## 2.2.2 Numerical Solution

The numerical solution was determined based on a control volume approximation. Figure 2-5 shows a schematic of the continuous medium divided into *N* control volumes. The energy balance for each control volume was determined and the set of equations was solved by using Euler's method of numerical integration. The final solution was obtained as [103]

$$T_{node=1,j+1} = T_{node=1,j} + \left[\frac{2k}{\Delta x^2 \rho c}\left(T_{node=2,j} - T_{node=1,j}\right) + \frac{2q''_{AVG}}{\Delta x \rho c}\right]\Delta t , \tag{2-15a}$$

$$T_{node=i,j+1} = T_{node=i,j} + \frac{k}{\Delta x^2 \rho c}\left(T_{node=i-1,j} + T_{node=i+1,j} - 2T_{node=i,j}\right)\Delta t , \tag{2-15b}$$

for $i = 2...(N-1)$ and $T_{node=N,j+1} = T_1(t = (j+1)\times\Delta t)$.

In this equation, $\Delta t$ and $j$ represent the time step and iteration step, respectively. To ensure convergence of the numerical solution, the value of each time step was smaller than the critical time step. The critical step is defined as [103]

$$\Delta t_{crit} = \frac{\Delta x^2 \rho c}{2k}. \tag{2-16}$$

In this study, the time step was chosen to be equal to the inverse of the frequency of acquisition of the temperature data (100 Hz). The control volume length ($\Delta x$) was defined as 0.05 mm and required a critical time step of 0.012 second, which was higher than the chosen time step of 0.01 second. This ensured stability of the solution.

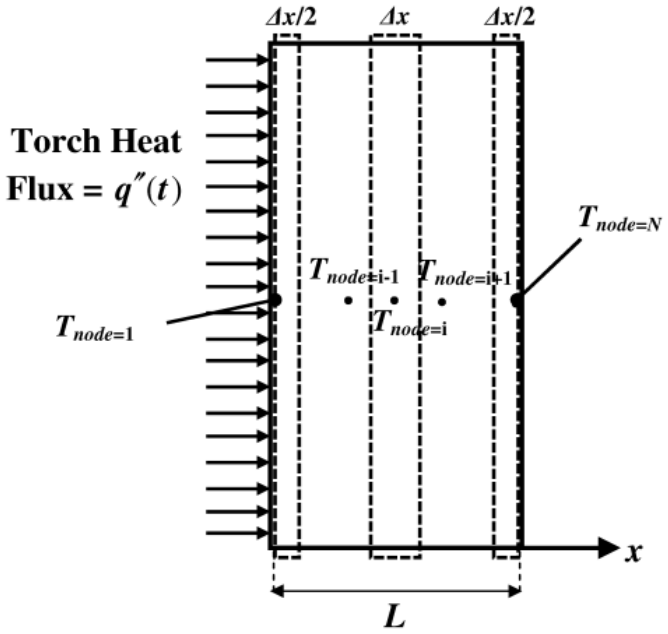


Figure 2-5 Schematic of the finite volume heat conduction model

## 2.3 Results and Discussion

### 2.3.1 Average Heat Flux

The heat flux of three spraying parameters (S1, S2 and S3) at four positions (given by $d = \sqrt{z^2 + y_m^2}$) from the torch was measured by using a heat flux sensor. Figure 2-6 shows a typical graph of the measured transient heat flux for the S1 spraying condition for four positions

with respect to the torch. The largest heat flux value shown in the figure (45 kW/m$^2$) indicates that the torch was positioned directly in front of heat flux sensor, at the center. As the torch moved away from the center of the heat flux sensor, the measured heat flux decreased. The lower heat fluxes with values of 37, 23, and 16 kW/m$^2$ represented positions of 25.4, 50.8, and 63.5 mm, respectively. The procedure of measuring the heat flux for each set of spraying parameters was repeated three times. Table 2-3 shows the average values and the standard deviations of the heat fluxes for each position in front of the sensor. In order to find the relation between the heat flux and position from the torch, a second order polynomial was fitted to the data of heat flux as a function of position from the torch. Figure 2-7 shows the data points of heat flux versus position from the torch for the S1 spraying conditions that have been fitted with a polynomial. The equation for the polynomial is given as

$$q''(d) = Ad^2 + Bd + C\,. \tag{2-17}$$

The quadratic function was chosen based on its excellent fit with the data points obtained from experiments. Table 2-4 shows the values of the curve fit parameters (A, B, C) and the regression value ($R^2$) for the curve fits. The $R^2$ value is very close to unity and, therefore, the fitted curve has good correlation with the experimental data. A similar trend was observed for the S2 and S3 spray conditions. Equation (2-17) was substituted into Eq. (2-12), and with $d = \sqrt{z^2 + y_m^2}$, the average heat flux was determined to be

$$q''_{AVG} = \frac{n_p}{Vt_s}\sum_{m=1}^{m_p} By_m^2 \ln\left(\frac{\sqrt{W^2 + 4y_m^2} + W}{2y_m}\right) + \frac{BW}{4}\sqrt{W^2 + 4y_m^2} + \frac{AW^3}{12} + W\left(Ay_m^2 + C\right). \tag{2-18}$$

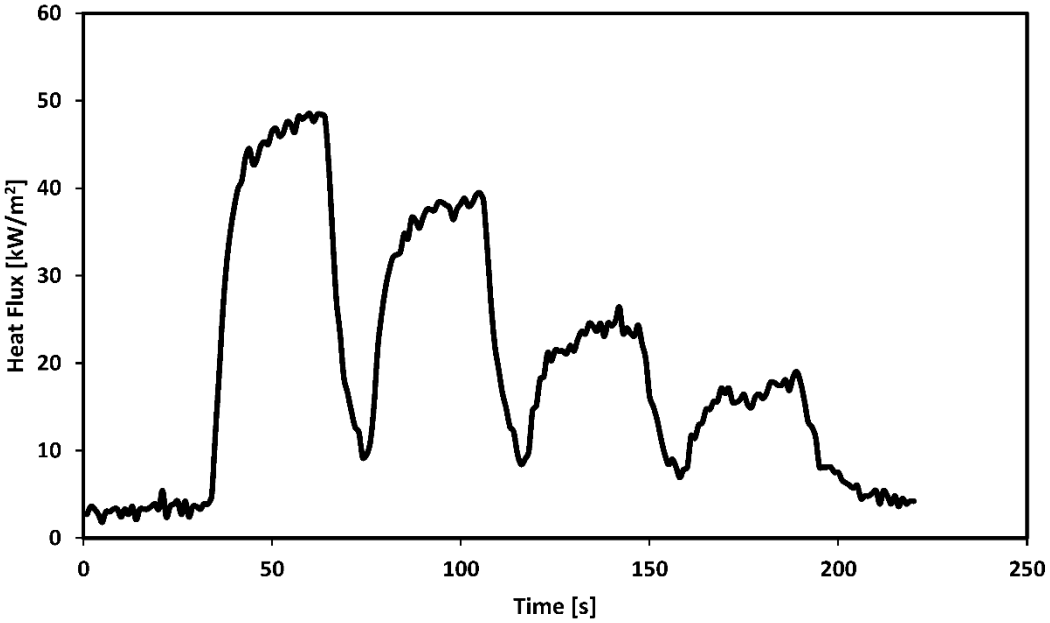


Figure 2-6 Measured heat flux as a function of time for the S1 spray conditions

Table 2-3 Heat flux at four torch-to-substrate distances

| **Distance from the torch (mm)** | **Heat flux: S1 spraying parameters ($kW/m^2$)** | **Heat flux: S2 spraying parameters ($kW/m^2$)** | **Heat flux: S3 spraying parameters ($kW/m^2$)** |
|---|---|---|---|
| 0 | 45 ± 0.7 ($n$ = 3) | 30 ± 1.2 ($n$ = 3) | 39 ± 2.6 ($n$ = 3) |
| 25.4 | 37 ± 1.2 ($n$ = 3) | 25 ± 1.1 ($n$ = 3) | 30 ± 2.4 ($n$ = 3) |
| 50.8 | 23 ± 0.9 ($n$ = 3) | 17 ± 0.6 ($n$ = 3) | 20 ± 1.1 ($n$ = 3) |
| 63.5 | 16 ± 0.3 ($n$ = 3) | 13 ± 1 ($n$ = 3) | 15 ± 0.7 ($n$ = 3) |

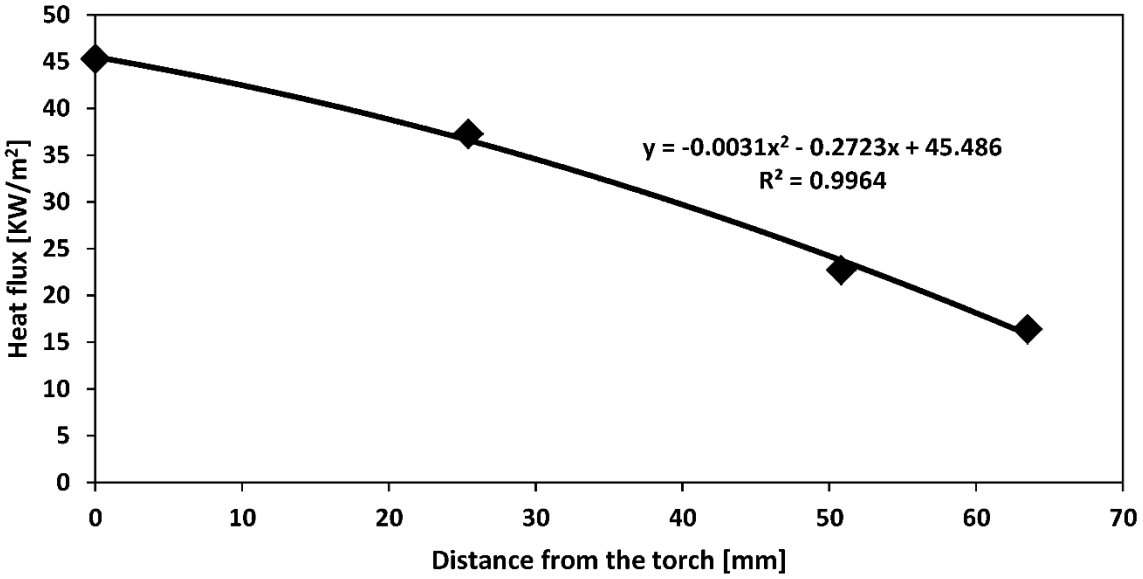


Figure 2-7 Heat flux as a function of distance from the center of torch for S1 conditions

Table 2-4 Curve fit coefficients of Eq. (2-17) for each set of spraying parameters

| **Set No.** | ***A*** | ***B*** | ***C*** | $R^2$ |
|---|---|---|---|---|
| S1 | $-3.066 \times 10^{-3}$ | $-2.723 \times 10^{-1}$ | $4.549 \times 10$ | 0.996 |
| S2 | $-2.062 \times 10^{-3}$ | $-1.521 \times 10^{-1}$ | $3.033 \times 10$ | 0.998 |
| S3 | $-2.264 \times 10^{-4}$ | $-3.707 \times 10^{-1}$ | $3.955 \times 10$ | 0.998 |

The average heat flux after three passes of the torch was calculated by employing Eq. (2-18), and the results are shown in Table 2-5. The table also shows the values of $t_p$ and $t_s$ for each spraying condition. Given the average heat fluxes for the three spraying parameters, it may be concluded that the air that was added to the torch had a significant effect on the value of average heat flux. The average heat flux decreased by approximately 2 $kW/m^2$ due to the increase of air pressure from 135 kPa to 170 kPa (5 psig to 10 psig) for the S1 and S2 spray

conditions, respectively. This is expected since excess air will cool the flame of a combustion reaction. In addition, it was found that further increase of the air pressure in the S3 spray conditions, coupled with a reduction in the stand-off distance to 150 mm produced an increase in the average heat flux to a value that was close to that of the S1 spray conditions.

Table 2-5 Average heat fluxes of the S1, S2, and S3 conditions after three passes of spraying

| **Set No.** | $t_p(s)$ | $t_s(s)$ | **Average heat flux for three passes (kW/m$^2$)** |
|---|---|---|---|
| S1 | 12.5 | 48.4 | 7.3 |
| S2 | 12.5 | 48.4 | 5.2 |
| S3 | 12.5 | 45.2 | 7.0 |

### 2.3.2 $T_1$ Transient Temperature

The transient temperature that was measured by thermocouple $T_1$ was used to find a function that could properly describe the temperature at the boundary where $x = L$. A simple linear curve and a fourth-order polynomial curve were fitted with the experimental data, and the regression values for these two curve fits were determined to find the curve with closer correlation. Equations (2-19) and (2-20) show the expressions of the linear and fourth-order polynomials as

$$T_1(\tau) = A\tau + B, \tag{2-19}$$

$$T_1(\tau) = A\tau^4 + B\tau^3 + C\tau^2 + D\tau + E. \tag{2-20}$$

Figure 2-8 presents the experimental data obtained from the $T_1$ thermocouple for the S1 spray conditions. The linear and fourth-order polynomial curve fits are also presented. The regression values were 0.993 and 0.999, respectively. Accordingly, the fourth-order polynomial correlated closer with the experimental data and described the behavior of the $T_1$ transient temperature more accurately. A similar trend was observed for the S2 and S3 spray conditions. The values of the coefficients in Eqs. (17) and (18), coupled with the regression values ($R^2$) for the fitted curves are shown in Tables 2-6 and 2-7, respectively.

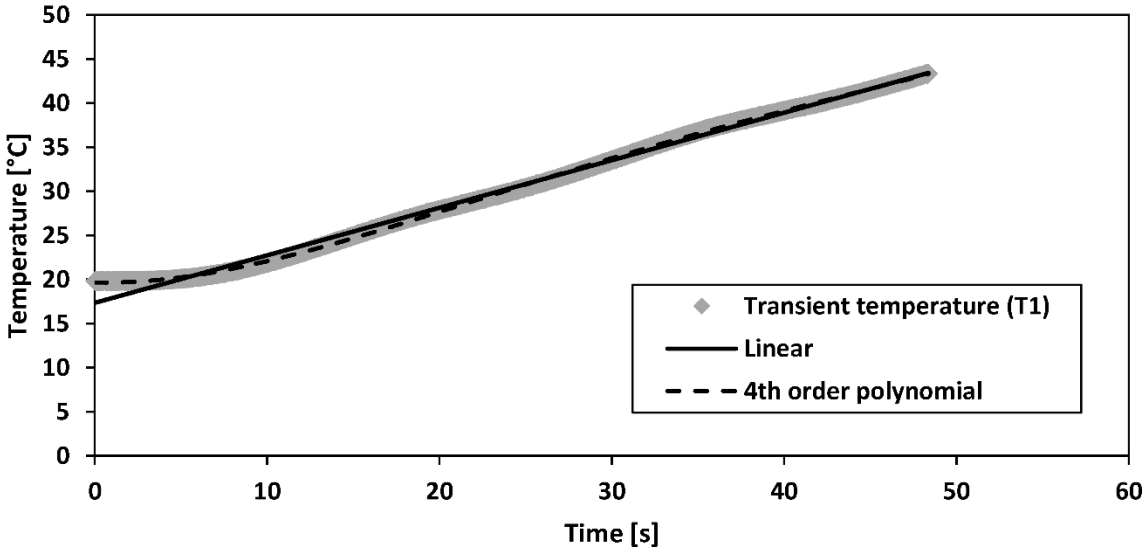


Figure 2-8 $T_1$ transient temperature trace

Table 2-6 Curve fit coefficients of Eq. (2-19) for each set of spraying parameters

| Set No. | *A* | *B* | $R^2$ |
|---|---|---|---|
| S1 | $5.392 \times 10^{-1}$ | 1.734 x 10 | 0.994 |
| S2 | $4.662 \times 10^{-1}$ | 1.769 x 10 | 0.993 |
| S3 | $6.016 \times 10^{-1}$ | 1.716 x 10 | 0.994 |

Table 2-7 Curve fit coefficients of Eq. (2-20) for each set of spraying parameters

| **Set No.** | ***A*** | ***B*** | ***C*** | ***D*** | ***E*** | $R^2$ |
|---|---|---|---|---|---|---|
| S1 | $6.419 \times 10^{-6}$ | $-8.37 \times 10^{-4}$ | $3.656 \times 10^{-2}$ | $-4.767 \times 10^{-2}$ | 1.967 x 10 | 0.999 |
| S2 | $7.077 \times 10^{-6}$ | $-8.963 \times 10^{-4}$ | $3.707 \times 10^{-2}$ | $-8.029 \times 10^{-2}$ | 1.96 x 10 | 0.999 |
| S3 | $1.152 \times 10^{-5}$ | $-1.328 \times 10^{-3}$ | $5.124 \times 10^{-2}$ | $-1.24 \times 10^{-1}$ | 1.97 x 10 | 0.999 |

### 2.3.3 Verification of the Developed Model

The constant value of the average heat flux ( $q''_{AVG}$ ) and Eq. (2-19) were substituted into Eq. (2-8) to give the temperature distribution in the PU substrate as

$$T(x,t) = \frac{2T_0}{L}\sum_{n=1}^{\infty}\left[\frac{1}{\lambda_n}(-1)^{(n+1)}\exp(-\alpha\lambda_n^2 t)\cos(\lambda_n x)\right]$$
$$+\frac{2\alpha}{kL}\sum_{n=1}^{\infty}\left[\frac{q''_{AVG}}{\alpha\lambda_n^2}(1-\exp(-\alpha\lambda_n^2 t))\cos(\lambda_n x)\right]$$
$$-\frac{2\alpha}{L}\sum_{n=1}^{\infty}\left[\lambda_n(-1)^n\frac{1}{\alpha^2\lambda_n^4}\left[\left(A\alpha\lambda_n^2 t + B\alpha\lambda_n^2 - A\right) - (B\alpha\lambda_n^2 - A)\exp(-\alpha\lambda_n^2 t)\right]\cos(\lambda_n x)\right]. \quad (2\text{-}21)$$

The same procedure was repeated for the fourth-order polynomial function for the transient temperature at $x = L$ (see Eq. (2-20)) and the temperature distribution in the PU substrate was derived to be

$$T(x,t)=\frac{2T_0}{L}\sum_{n=1}^{\infty}\left[\frac{1}{\lambda_n}(-1)^{(n+1)}\exp(-\alpha\lambda_n^2 t)\cos(\lambda_n x)\right]+\frac{2\alpha}{kL}\sum_{n=1}^{\infty}\left[\frac{q''_{AVG}}{\alpha\lambda_n^2}(1-\exp(-\alpha\lambda_n^2 t))\cos(\lambda_n x)\right]$$
$$-\frac{2\alpha}{L}\sum_{n=1}^{\infty}\left[\lambda_n(-1)^n\frac{1}{\alpha^5\lambda_n^{10}}\cos(\lambda_n x)\left[\begin{array}{l}At^4\alpha^4\lambda_n^8+t^3\alpha^3\lambda_n^6\left(B\alpha\lambda_n^2-4A\right)\\+t^2\alpha^2\lambda_n^4(C\alpha^2\lambda_n^4-3B\alpha\lambda_n^2+12A)\\+t\alpha\lambda_n^2\left(D\alpha^3\lambda_n^6-2C\alpha^2\lambda_n^4+6B\alpha\lambda_n^2-24A\right)\\+E\alpha^4\lambda_n^8-D\alpha^3\lambda_n^6+2C\alpha^2\lambda_n^4-6B\alpha\lambda_n^2+24A\\-\left(E\alpha^4\lambda_n^8-D\alpha^3\lambda_n^6+2C\alpha^2\lambda_n^4-6B\alpha\lambda_n^2+24A\right)\exp(-\alpha\lambda_n^2 t)\end{array}\right]\right].$$

(2-22)

It can be seen that the final solution of the temperature distribution of Eq. (2-22) through use of the fourth-order polynomial for the transient temperature, $T_1$(t) has led to a more complex solution that requires a higher level of computation compared to that of Eq. (2-21).

Three sets of spraying parameters (S1, S2, and S3) were used to provide data to verify the proposed model. Figure 2-9 shows the experimental results of thermocouple $T_2$, after three passes of spraying that were compared with the results of the mathematical model. The results obtained from Eqs. (2-21) and (2-22) overlapped with no noticeable variation. Consequently, the linear function describing the transient temperature behavior at the boundary condition at $x = 0$ ($T_1$) was chosen due to its simplicity. In addition, the results obtained from the numerical solution overlapped with the data obtained from the mathematical model similar to graphs presented in Fig. 2-9. Although the analytical and numerical solutions predicted the $T_2$ temperature with no noticeable difference, the analytical solution appears to be more efficient since the numerical solution is restricted to a finite number of specific positions (nodes) within the substrate and for any given time, the numerical solution has to solve the problem step by step from the beginning ($t = 0$) to find the temperature of a specific location at the desired time.

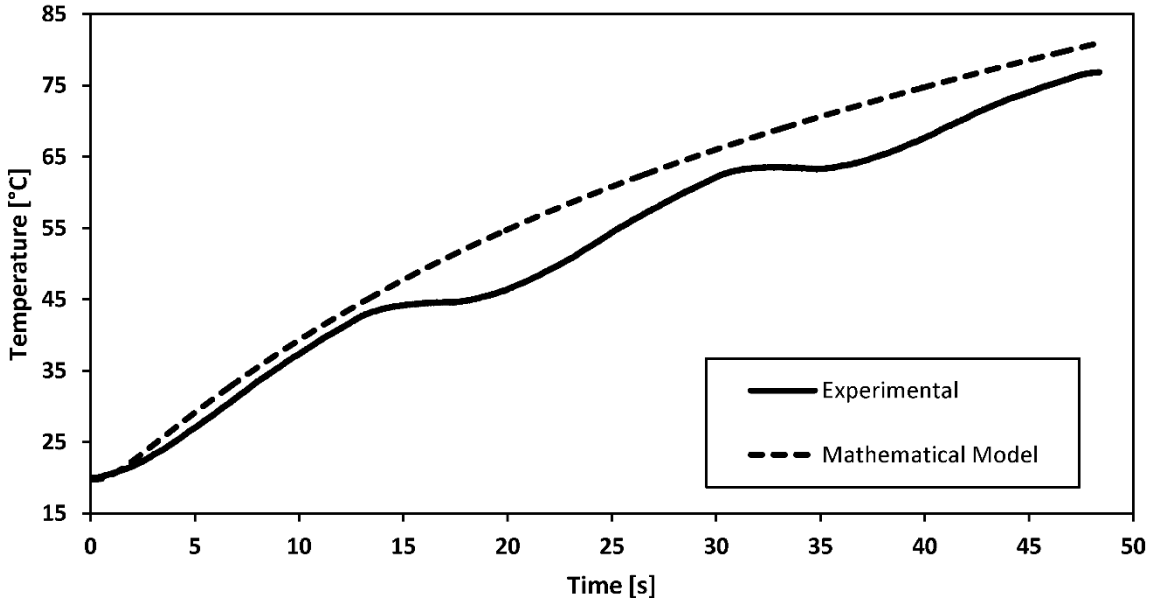
Temperature [°C]
85
75
65
55
45
35
25
15
0
5
10
15
20
25
30
35
40
45
50
Time [s]
Experimental
Mathematical Model

(a)

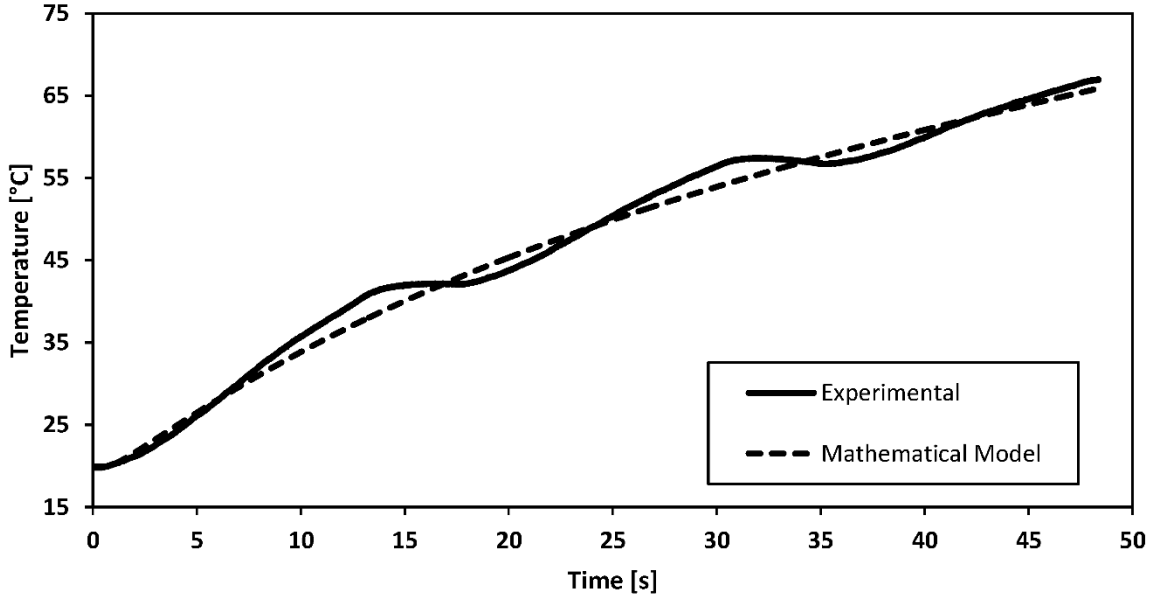
Temperature [°C]
75
65
55
45
35
25
15
0
5
10
15
20
25
30
35
40
45
50
Time [s]
Experimental
Mathematical Model

(b)

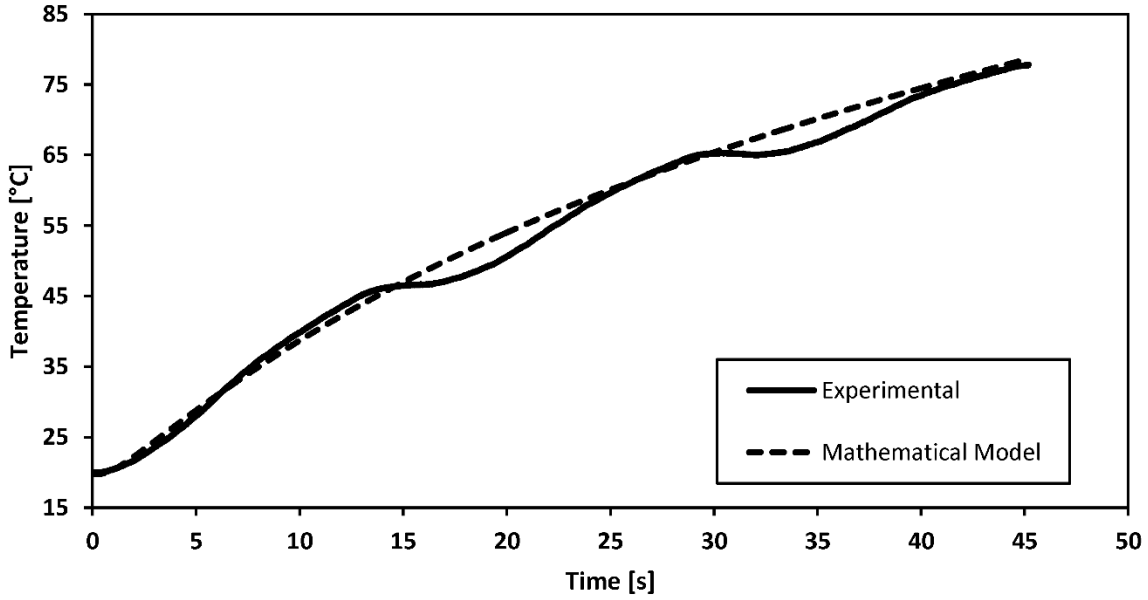


(c)

Figure 2-9 Curves of the $T_2$ transient temperature trace at $x$ = 0.8 mm in the PU substrate for the *a*) S1, *b*) S2, and *c*) S3 spraying conditions

Figure 2-9a shows that for the S1 spray conditions, there exist approximately a 5% difference between the experimental results and the results of the model. Improved agreement was obtained for the S2 (Fig. 2-9b) and S3 (Fig. 2-9c) spray conditions. This was likely due to the higher air pressure that was employed in S2 and S3 spray conditions that made the flame of the torch accumulated and more stable. For each spray condition, an average heat flux with a constant value was utilized in the proposed model of Eq. (2-21). However, the flame spray torch was brought to a complete stop after each pass to return to its initial position before proceeding to the next pass. In this short period of time, the torch and flame do not traverse the substrate. The fluctuation of the transient temperatures in the curves of the experimental results in Fig. 2-9 is a result of the short period of time when the torch ceased to traverse the substrate between the passes. In addition, due to the use of average heat fluxes, rather than transient heat fluxes in the

model, the curves from the mathematical model intersect those of the experimental results as shown in Fig. 2-9.

The model was then employed to study the effect of air pressure on the temperature distribution within the PU substrates. Figure 2-10 shows the temperature distribution within the substrate after three passes of the torch for the S1, S2, and S3 spraying conditions were executed. The maximum temperature occurred at the exposed surface of the substrate where $x = 0$ in the mathematical model (see Fig. 2-3). The maximum temperature decreased when the air pressure was increased (from the S1 to the S2 spray conditions) due to the reduced heat flux from the cooler torch flame. Thus, the temperature distribution within the substrate can be controlled by the amount of air that is added to the flame. Figure 2-10 also shows that the increased heat flux in the S3 spray conditions (see Table 2-5) due to the decrease in the stand-off distance to 150 mm produced a temperature distribution profile that was nearly similar to that of the PU substrate that was exposed to the S1 spray conditions, where the stand-off distance was larger (215 mm), but the air pressure to the flame was lower. In thermal spraying, shorter stand-off distances lead to higher impact velocity of the droplets and improved coating quality [20, 21]. On the other hand, shorter stand-off distances lead to higher temperatures within the substrate that can have adverse effects on heat sensitive substrate materials. According to Fig. 2-10, the temperature increase within the substrates for shorter stand-off distances can be controlled by increasing the amount of air that is added to the flame of the torch.

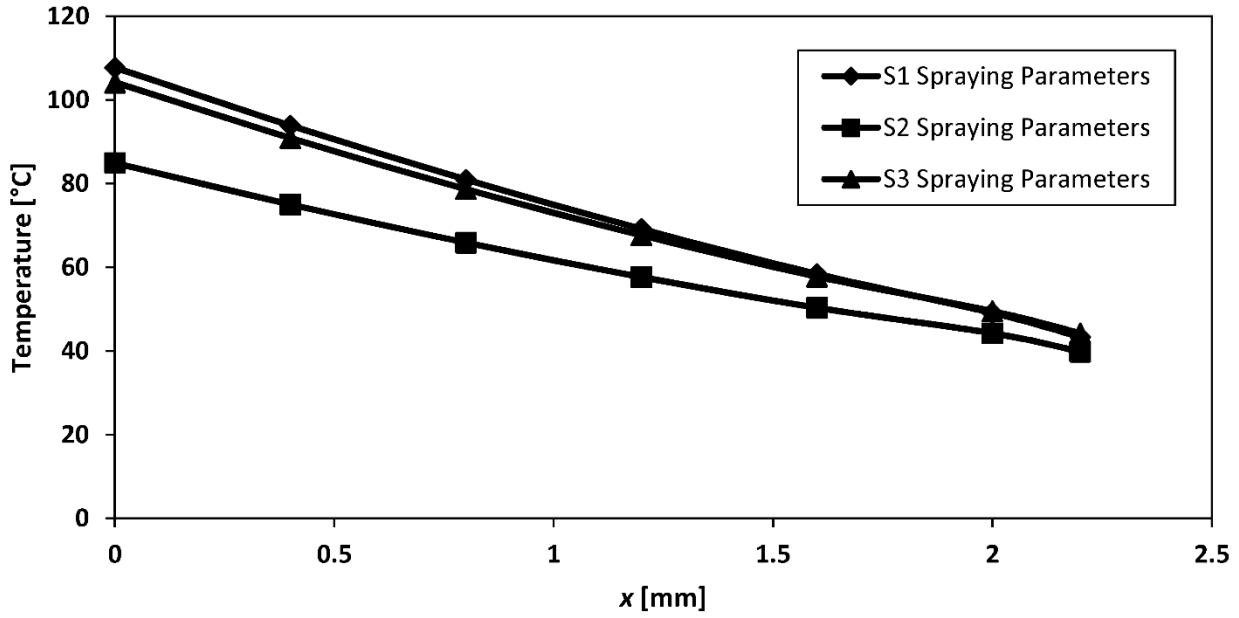


Figure 2-10 Temperature distribution within the PU substrate after three passes for the S1, S2, and S3 spraying conditions

### 2.3.4 Verification of the Model with the Assumption of an Insulated Back Surface

Another approach for prediction of the temperature distribution within the substrate was based on solving the model with the assumption of an adiabatic surface on the back of the substrate. The main advantage of this model is its simplicity in the mathematical formulation. In addition, the results of this simplified model can be non-dimensionalized easily and represented in graphs for further use in a wide range of spraying conditions.

The temperature at the position of the $T_2$ thermocouple that was calculated by using the model of Eq. (2-14) and shown with the corresponding experimental results for the three spraying conditions is presented in Fig. 2-11. It can be seen in Fig. 2-11a (S1 spray conditions) that the deviation between the computed temperatures and the experimentally measured

temperatures has increased in comparison with the results shown in Fig. 2-9a for the model of Eq. (2-21). In the S2 spraying condition (see Fig. 2-11b), a good agreement is observed between the calculated temperatures and experimental results until the end of the second pass at approximately 32 second. From this point to the end of the third pass, the difference between the results calculated by the model and those of the experiment increases. The same trend is observed for S3 spraying conditions (Fig. 2-11c). After the thermal wave has traversed the thickness of the substrate, heat will be lost from the back of the substrate. In this case, the back of the substrate cannot be considered to be adiabatic or insulated. Since the model does not account for energy loss from the back of the substrate, the temperature predicted by the model would be higher than that found by experiment as observed in Fig. 2-11. This indicates that the model of Eq. (2-14) is only valid for the period of time before the thermal wave arrives at the back surface of the substrate.

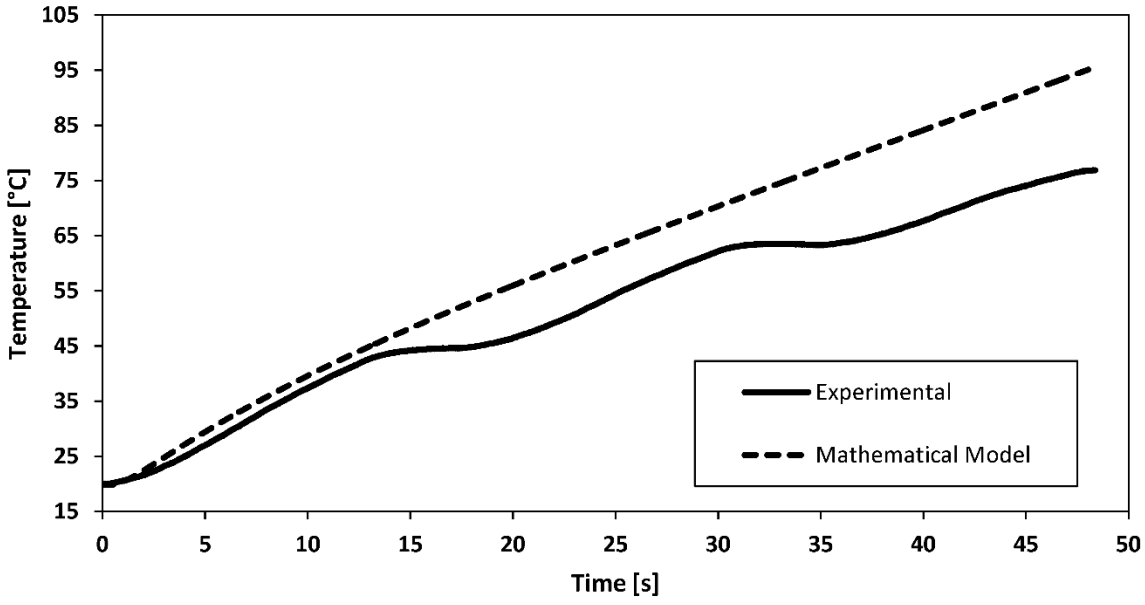


(a)

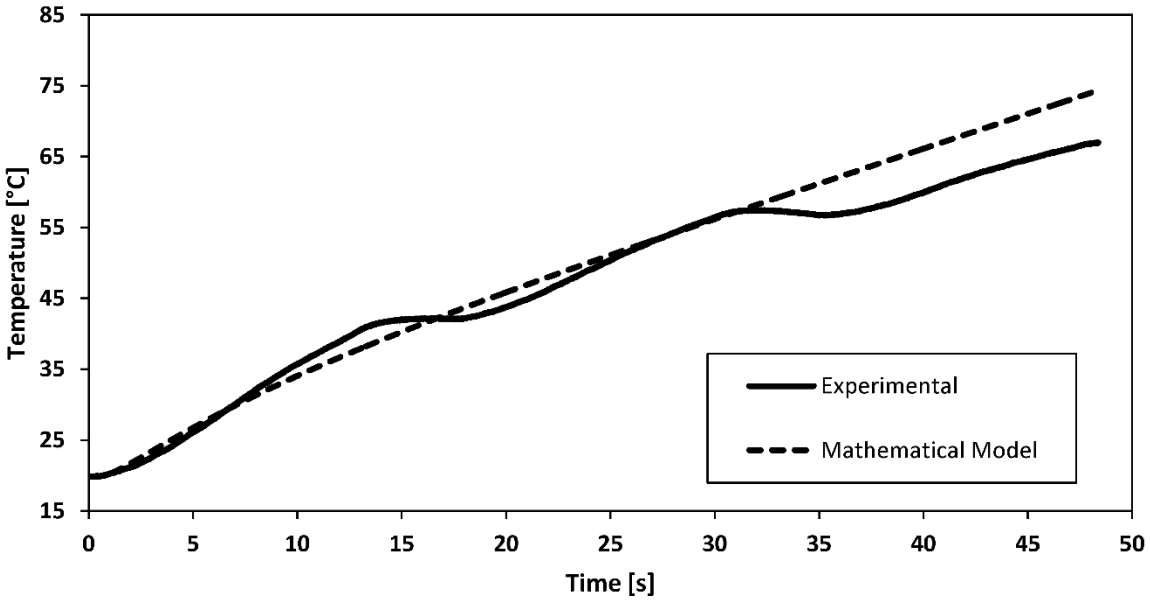


(b)

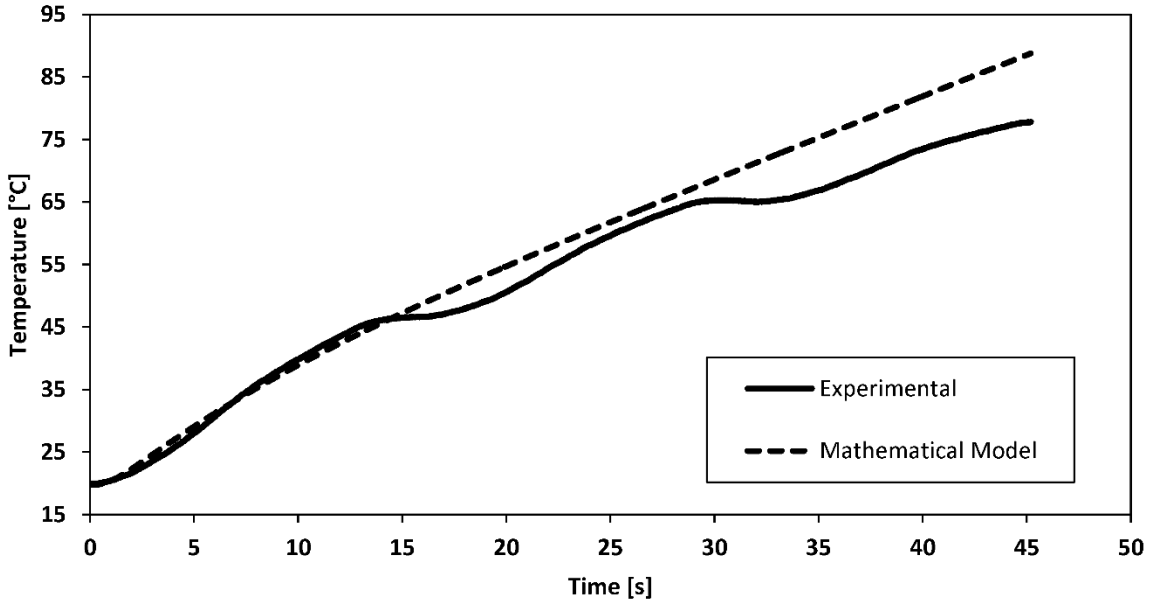


(c)

Figure 2-11 Curves of the $T_2$ transient temperature trace at $x$ = 0.8 mm in the PU substrate from the model of Eq. (2-14) for the *a*) S1, *b*) S2, and *c*) S3 spraying conditions

In order to interpret the results of the model of Eq. (2-14) more generally and find a parameter that can describe the time period for which the model is applicable, non-dimensional parameters were used and defined as

$$T^* = \frac{T - T_0}{\frac{q''L}{k}}, \tag{2-23}$$

$$t^* = \mathrm{Fo} = \frac{\alpha t}{L^2}, \tag{2-24}$$

$$x^* = \frac{x}{L}. \tag{2-25}$$

Curves of the non-dimensional temperature traces for the $T_2$ thermocouple from both the experiments and the model of Eq. (2-14) for the S1, S2 and S3 spraying conditions are shown in Fig. 2-12. According to Nellis and Klein [103], for the thickness and properties of the PU substrate, the thermal wave will arrive at the back of the substrate when the Fourier number is approximately 0.25 ($t^* = 0.25$). However, according to the results shown in Fig. 2-12, the model of Eq. (2-14) shows good agreement with experimental results up to a Fourier number of 0.4 ($t^* = 0.4$). The Fourier number is considered conceptually as the ratio of the diffusive rate of heat transport to the heat storage rate in a material. Therefore, low values of the Fourier number ($t^*$) will indicate low rates of heat conduction through the material, and, in this study, the assumption of an insulated back surface will be valid until heat moves completely through the thickness of the material to induce temperature changes on the back of the substrate. As the Fourier number increases, the validity of the model of Eq. (2-14) decreases. Therefore, it can be concluded that the model of Eq. (2-14) in this study is capable of predicting the temperature distribution within the substrate, provided that the Fourier number, $t^*$ is less than 0.4.

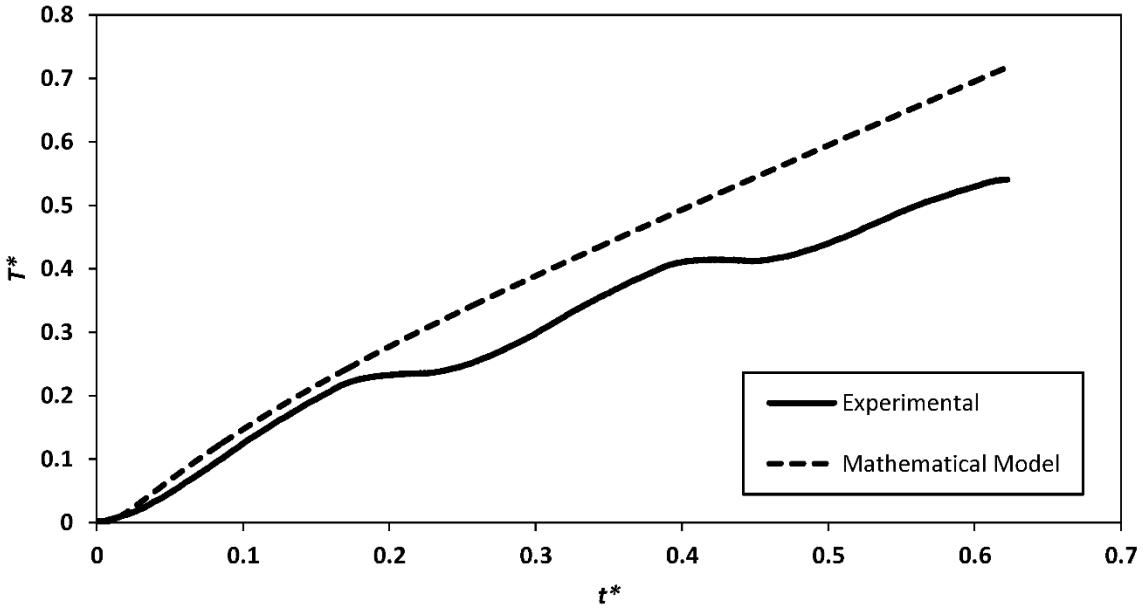
0.8
0.7
0.6
0.5
0.4
0.3
0.2
0.1
0
T*
0
0.1
0.2
0.3
0.4
0.5
0.6
0.7
t*
Experimental
Mathematical Model

(a)

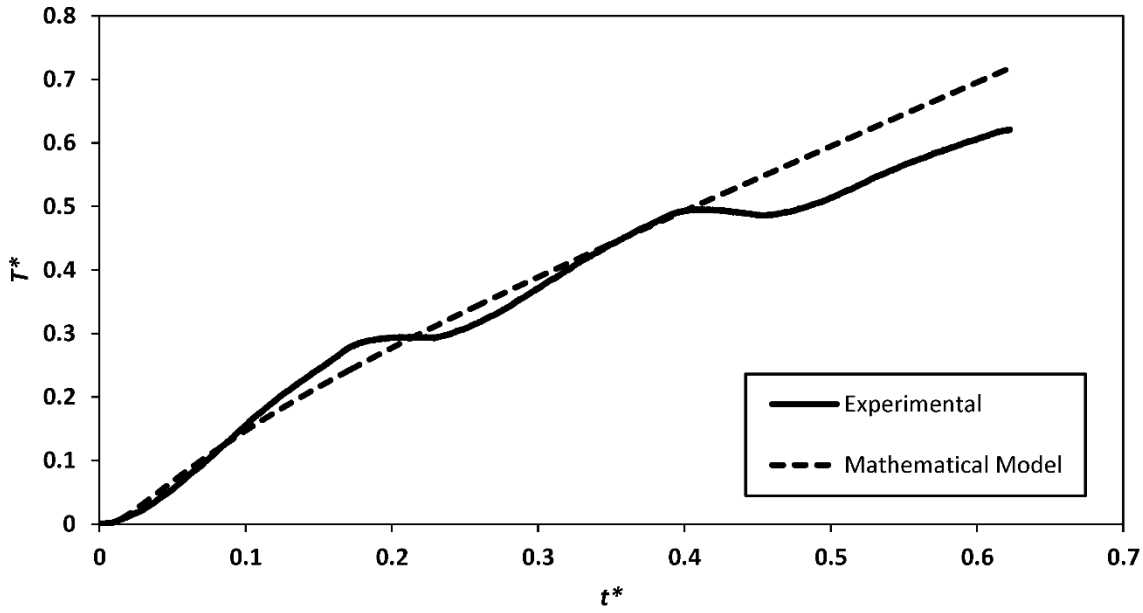
0.8
0.7
0.6
0.5
0.4
0.3
0.2
0.1
0
T*
0
0.1
0.2
0.3
0.4
0.5
0.6
0.7
t*
Experimental
Mathematical Model

(b)

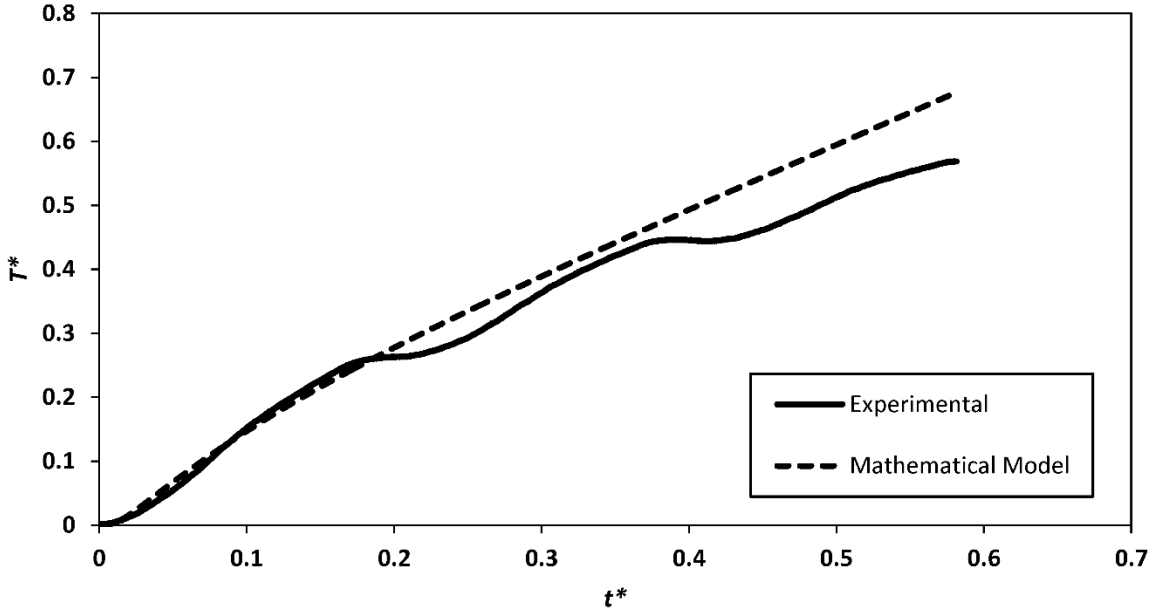


(c)

Figure 2-12 Curves of the non-dimensionalized experimental and Eq. (2-14) model results for the $T_2$ transient temperature at $x$ = 0.8 mm for the *a*) S1, b) S2 and *b*) S3 spraying conditions

Figure 2-13 shows the non-dimensionalized temperature as a function of non-dimensionalized time for various non-dimensionalized positions in the substrate. Since the curves are non-dimensionalized, they can be used to predict the temperature distribution within the substrate for a variety of thermal spraying conditions, provided that $t^*$ is smaller than 0.4.

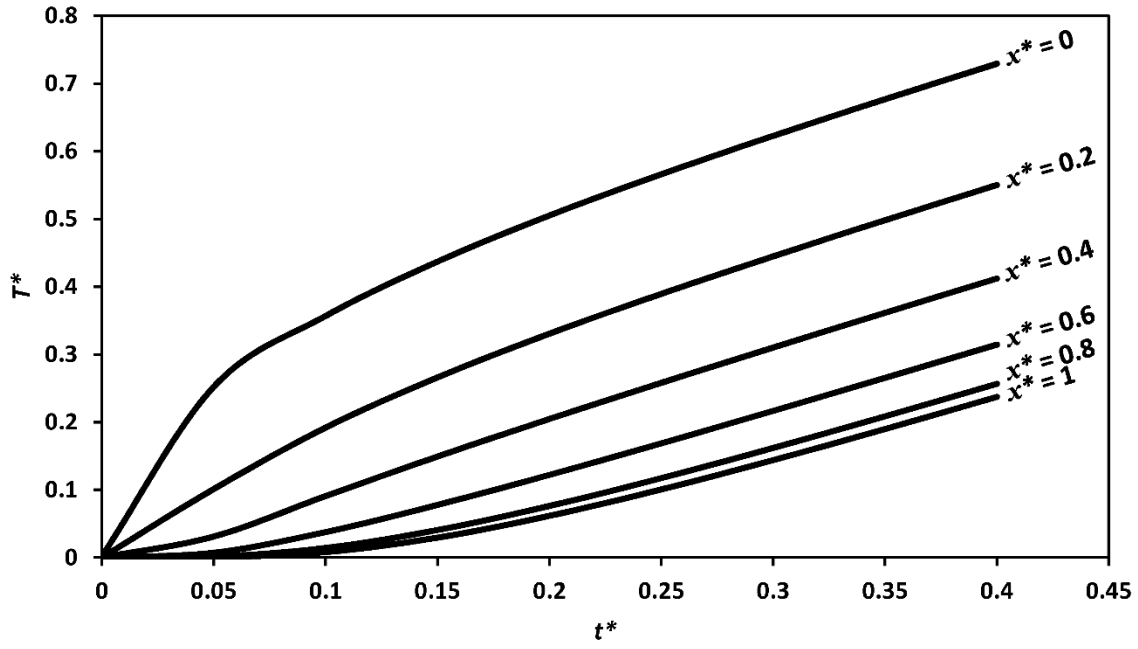


Figure 2-13 Curves of the non-dimensionalized temperature as a function of non-dimensionalized time for different positions within substrate

### 2.3.5 Effect of Deposition of Al-12Si Powder

In the development and validation of the proposed model of Eq. (2-21) for the S1, S2, and S3 spraying conditions, no Al-12Si powder was deposited. The S3 spraying condition was used to deposit powder and the temperature in the PU substrate at the $T_2$ thermocouple was measured experimentally. Figure 2-14 shows the transient temperatures at the $T_2$ thermocouple with and without the deposition of powder. As expected, the temperature in the PU substrate with the deposition of powder was larger due to the additional heat input from the molten and partially molten Al-12Si particles. However, the difference between the temperatures for any given time was less than 15%, suggesting that the energy input of the deposited powder was much less than that of the flame of the torch. It should be noted that for the case of deposition of powders with high melting temperatures, this difference might become higher. Although powders with high melting temperatures require higher torch heat fluxes, the amount of heat

input from molten and partially molten particles might not be negligible when compared to the heat flux from the torch. To that end, further investigation is required to determine if the error induced by the assumption of negligible impact of the powder on the temperature distribution of the proposed heat transfer model is reasonable when depositing powders with high melting points.

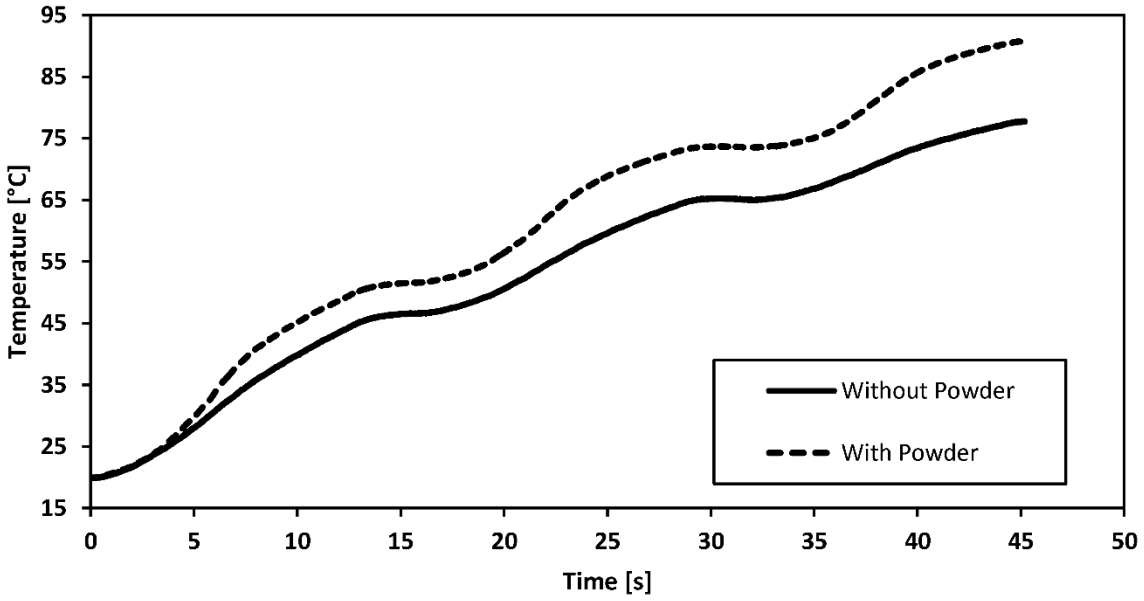


Figure 2-14 Curves of the $T_2$ transient temperature as a function of time during the spraying process with and without deposition of powders

# Chapter 3

# Evaluation of the Morphology and Electrical Resistance of Metallic Coatings Deposited on Polyurethane Elastomers

Flame spraying process was employed to deposit conductive coatings of Al-12Si on polyurethane elastomers. The effect of process parameters, i.e., stand-off distance and air added to the flame spray torch, on temperature distribution and corresponding effects on coating characteristics, including electrical resistivity were investigated. It was found that the coating porosity and electrical resistance decreased by increasing the pressure of the air injected into the flame spray torch during deposition. The latter also allowed for a reduction of the stand-off distance of the flame spray torch and deposition of denser metallic coating with lower electrical resistance. Dynamic mechanical analysis was performed to investigate the effect of the increase in temperature within the substrate on its dynamic mechanical properties. It was found that the spraying process did not significantly change the storage modulus of the polyurethane substrate material.

Some sections of the work presented in this chapter have been published in Journal of Thermal Spray Technology, (25-3) 419-430, 2016, and proceedings of the International Thermal Spray Conference (ITSC), Long Beach, CA, USA, May 11-14, 2015.

## 3.1 Experimental Method

Details about the flame spraying process parameters for deposition of metallic coatings, spraying powder and substrate preparation were discussed in Sections 2.1.1 and 2.1.2 of Chapter 2 of this dissertation. Experimental procedure that was employed to study the properties of the deposited coatings, measurement of the electrical resistance and evaluation of the dynamic mechanical properties of the PU substrates are discussed in the following sections.

### 3.1.1 Electrical Resistance Measurement

The electrical resistance of the deposited coatings was measured using a four-point method with a 6.5 digit precision multimeter (Fluke 8846A, Fluke Electronics Canada LP, Mississauga, ON, Canada). Silver epoxy (Chemtronics CW2400J, Allied Electronics Inc., Ottawa, ON, Canada) with a low electrical resistivity, $\rho$ ($\rho < 0.001$ Ω.cm), was used to attach two thin copper sheets with dimensions of 10 mm x 10 mm x 0.8 mm on the top of the coatings at the two distal ends (see schematic in Fig. 3-1). After attaching the copper sheets, the epoxy was cured in an oven for 15 minutes with the temperature set to 90°C. The wires connecting the multimeter were attached to the copper sheets using alligator clips.

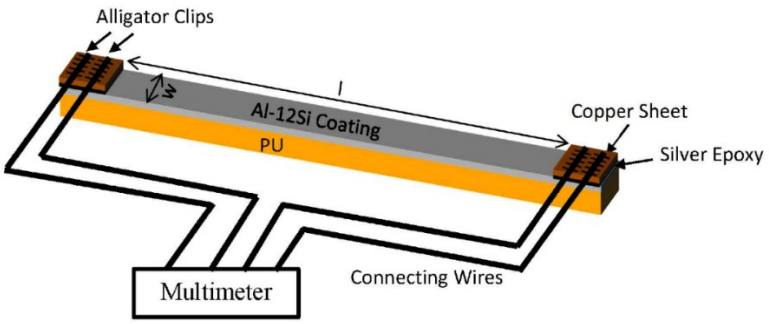


Figure 3-1 Schematic of the assembly used to measure electrical resistance of the deposited coatings

### 3.1.2 Coating Morphological Characterization

The mass of the substrate was measured before and after spraying by using a balance with an accuracy of ±1 mg (Acculab VI Balance, Sigma-Aldrich Canada Co., Oakville, ON, Canada) in order to determine the mass of the coating. The coated samples were then cut and cold-mounted in an epoxy resin for microstructural examination. The sections were ground using 240, 320, 400, 600, 800, and 1200 grit silicon carbide paper and further polished using 3 μm and 1 μm diamond slurry suspension (LECO, Mississauga, ON, Canada).

The surface topography and the cross sections of the coatings were examined by using a scanning electron microscope (EVO LS15 EP, Carl Zeiss Canada Ltd., Toronto, ON, Canada) in the secondary electron mode and the backscattered electron (BSE) mode, respectively. A thin film of carbon was deposited onto the cold-mounted samples by using a carbon evaporation system (EM SCD 005, Leica Baltec Instrument, Balzers, Liechtenstein) to avoid surface charging during scanning electron microscopy (SEM). SEM micrographs obtained from the BSE detector were analyzed with image analysis software (ImagePro, Media Cybernetics, Bethesda, MD, USA) to calculate the average thickness, porosity, and roundness of the splats of the deposited coatings. At least seven images for each coating were used to determine the average coating porosity. In order to ensure consistency among the porosity measurements, the image analysis threshold was chosen close to the "automatic bright object" setting of the software in which the dark and bright objects were separated by defining a threshold based on the histogram shape method. Due to the non-uniform thickness of the deposited coatings, the average coating thickness was measured by performing image analysis on cross sections at a magnification of 200X. Separation lines that enveloped the coating were drawn manually, and the average coating thickness, in pixels, was measured by normalizing the area of the drawn curve by the image

width in pixels. Equation (3-1) shows the expression that was used to estimate the thickness of the coating as

$$t = \frac{1}{w}\sum_{i=1}^{n} h_i \,, \tag{3-1}$$

where $t$, $w$, $n$, and $h_i$ represent the average coating thickness, width of the image in pixels, number of pixels within the width and height of the $i_{th}$ pixel, respectively. The pixel value for the average coating thickness was then converted into micrometers by using the scale on the image. The roundness of the deposited splats was calculated by manually drawing separation lines that covered each splat and the roundness of each splat was calculated with

$$R = \frac{P^2}{4A\pi}, \tag{3-2}$$

where $A$ and $P$ represent the area and perimeter of the splat, respectively.

### 3.1.3 X-ray Diffraction Analysis

X-Ray diffraction (Rigaku Ultima IV XRD, Rigaku, Texas, USA) was used to identify the phase composition of the coatings. XRD was carried out with a copper anode operated at 40 kV and 44 mA. The 2θ diffraction angles ranged from 10º to 110º in continuous mode with a scan rate of 2º per minute.

### 3.1.4 Dynamic Mechanical Analysis

In order to determine the effect of the flame temperature on the dynamic mechanical properties of coated PU substrates, a DMA apparatus (DMA 8000, PerkinElmer, Woodbridge, ON, Canada) was used. Samples having dimensions of 10 mm x 5 mm x 2.9 mm were subjected to oscillation in a single-cantilever beam assembly at an amplitude of 0.05 mm. Three sets of

experiments were performed: a) temperature scans from 30°C to 100°C at a heat-up rate of 3°C/min and frequency of 1 Hz, and b) logarithmic frequency scans from 0.02 Hz to 30 Hz for three points per decade at a fixed temperature of 30°C.

### 3.1.5 Shore A Hardness Measurement

In order to determine the effect of the temperature on the hardness of the PU substrates, the Shore A hardness of the PU samples was measured according to ASTM Standard D2240 [104]. PU samples of size 50 mm x 50 mm x 2.9 mm were tested at both room temperature (22°C) and elevated temperatures of up to 185°C. The PU samples were heated in an oven for one hour at the set temperatures before conducting the hardness testing at elevated temperatures.

## 3.2 Results and Discussion

### 3.2.1 Splat Morphology and Coating Microstructure

The coating morphology and microstructure is expected to have an impact on the electrical and thermal properties of the coatings. Figure 3-2 shows SEM images of the top surface of the coatings that were deposited under the S1, S2, and S3 spraying conditions. Figure 3-2a shows that the impacting particles that were deposited under the S1 condition were not significantly deformed, i.e., some particles remained un-deformed as indicated by the arrows in the micrograph. Low particle deformation led to the formation of cavities that can be observed on the top surface. The splats of the coating deposited with the S2 spraying parameters (see Fig. 3-2b) shows a higher level of deformation compared to that of S1 spraying conditions. The difference between the S1 and S2 conditions was that air at a higher pressure was added to the flame produced by the torch, which cooled the flame and produced a jet and powder particles with higher velocities. Gas-particle momentum transfer is typical in two-phase flow with

dispersed particles, resulting in changes in particle velocities. Given that a cooler flame will result in lower temperatures of the impacting particles, the improved droplet deformation under the S2 condition was due to the higher velocity of the impacting droplets and the stiffer substrate, the latter being a result of lower temperatures within the PU substrate (as shown in Fig. 2-10) due to reduced heat transfer from the cooler flame. A softer substrate absorbs the kinetic energy of impacting particles to a greater extent, and hence, a lower amount of energy is available for plastic deformation of the impacting droplets. As shown in Table 3-1, a reduced thickness and mass of coatings sprayed under the S2 condition was ascertained, which is the result of a stiffer substrate and harder powder particles upon impact, leading to an increased amount of rebounding of the impacting particles.

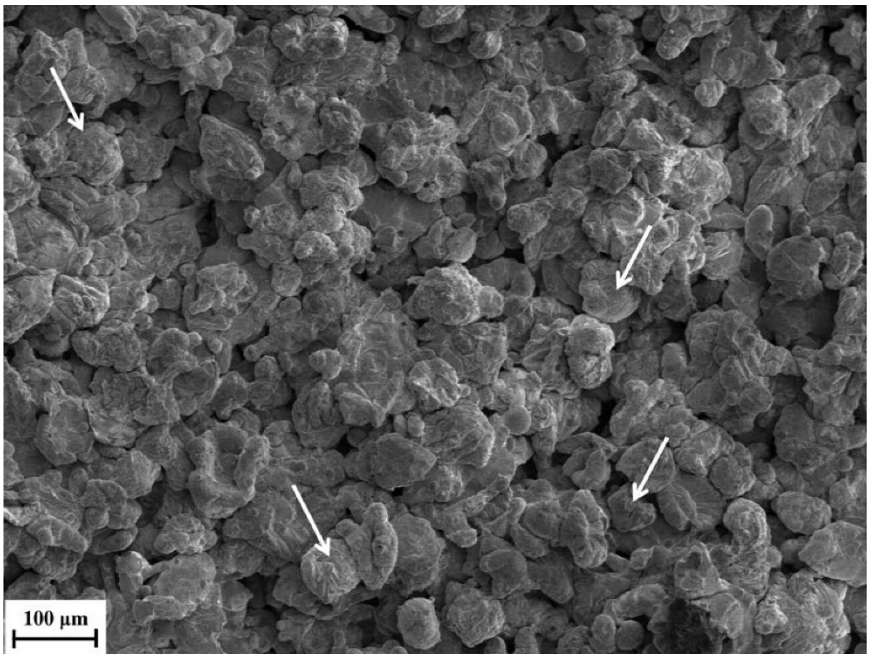


(a)

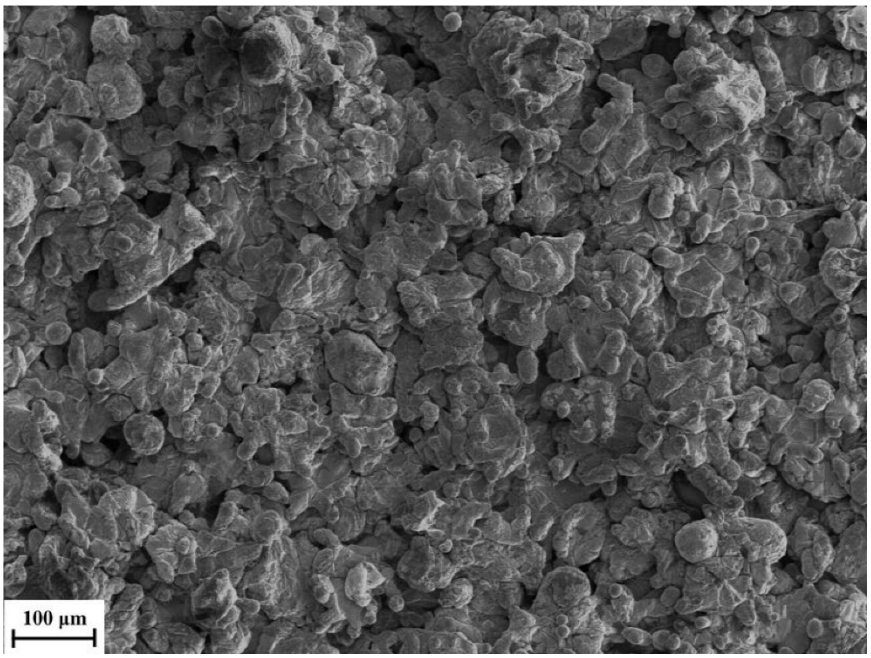


(b)

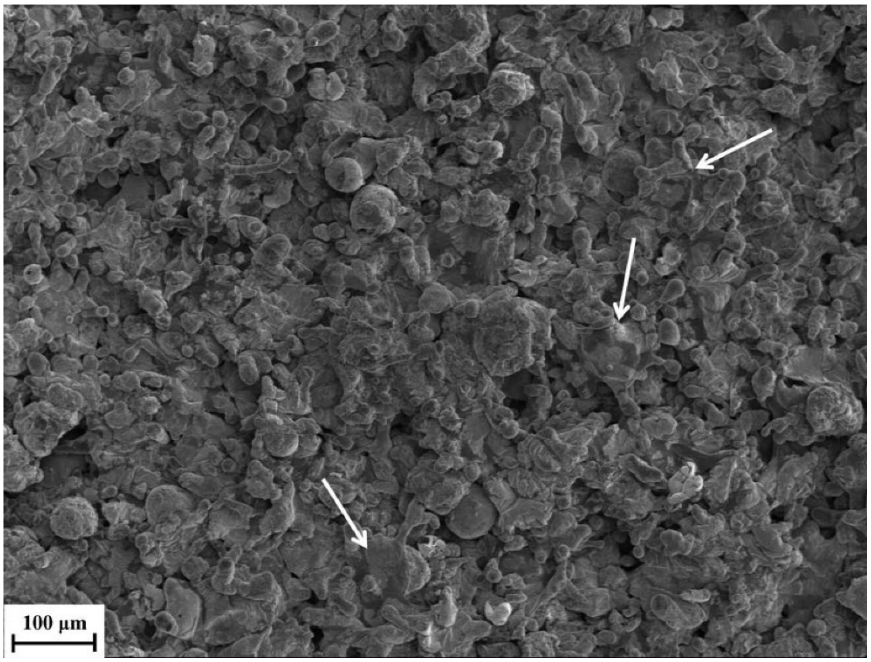


(c)

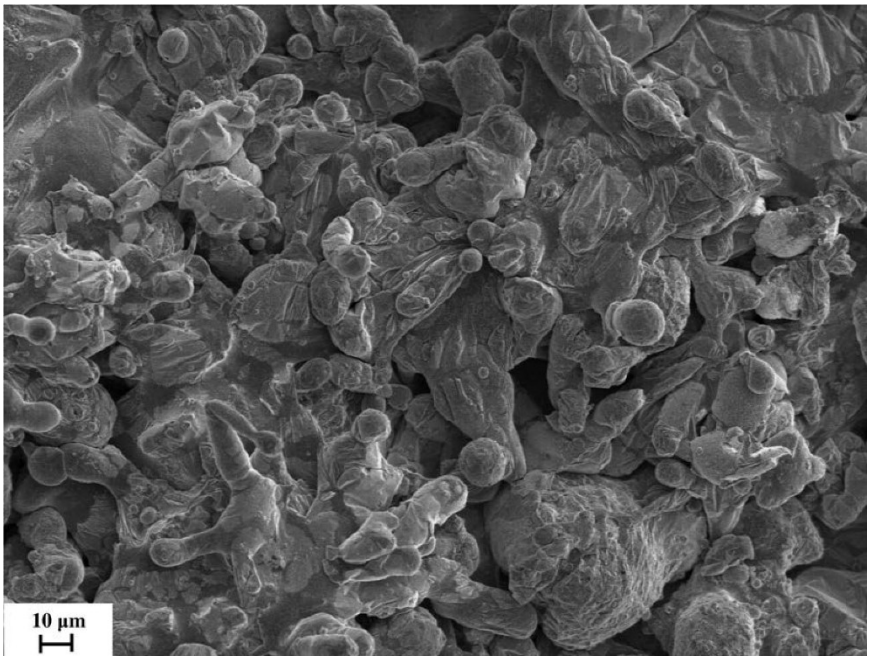


(d)

Figure 3-2 Typical SEM images of coating top surfaces after three flame spray passes for the a) S1, b) S2, and c) S3 spraying parameters. A higher magnification image is shown in (d) for the S3 spraying conditions

Table 3-1 Thickness and weight of deposited coatings after three passes of spraying for the S1, S2, and S3 spraying conditions

| **Set No.** | **Coating thickness (µm)** | **Coating weight (mg/cm$^2$)** |
|---|---|---|
| S1 | 95.8 ± 7.1 ($n$ = 7) | 20.8 ± 0.1 ($n$ = 3) |
| S2 | 82.2 ± 3.4 ($n$ = 7) | 17.0 ± 1.6 ($n$ = 3) |
| S3 | 53.6 ± 3.1 ($n$ = 8) | 11.8 ± 0.3 ($n$ = 3) |

According to Fig. 2-10, the higher air pressure of 103.4 kPa in the S3 spraying conditions made it possible to reduce the stand-off distance to 150 mm and maintain a substrate temperature distribution profile that was nearly equal to that of the S1 spraying conditions, where the stand-off distance was 215 mm and the pressure of the air added to the flame was lower. Note

that in thermal spraying, a shorter stand-off distance is often preferable since it results in higher impact velocities and higher temperatures of the droplets, which leads to improved coating quality [20, 21]. For the case of the S3 spraying parameters (Fig. 3-2c and 3-2d), the flattened shape of some of the splats, indicated by arrows, suggests that the droplets were largely fully molten prior to impact and have spread on the surface of the coating. Due to the reduced stand-off distance between the torch and substrate in the S3 condition, a shorter in-flight time of the particles led to higher droplet temperature and velocity prior to impact [21, 67]. It is expected that longer in-flight distances and time will allow for increased cooling of the particles and droplets by forced heat convection.

Figure 3-3 shows cross section images of coatings deposited by the S1, S2, and S3 spraying conditions, respectively. Similar to images obtained on the top surface, low deformation and interlocking between particles (Fig. 3-3a) was noticed when the S1 spraying parameters were employed. Higher droplet deformations can be observed for the S2 condition as shown in Fig. 3-3b. For the case of the S3 condition (Fig. 3-3c), the cross section image indicates that the droplets were largely molten prior to impact since they were highly deformed. The average roundness of splats for each spray parameter set, along with the standard error of the mean are compiled and shown in Table 3-2. Roundness is defined as having the form of a circle. Larger values of roundness would suggest greater deformation of the particles in the coating. The two-sample *t*-test statistical method was employed to verify that the average mean roundness of the splats significantly differ from each other for the S1, S2, and S3 spraying conditions. The *F*-test method was used to investigate the equality of the variances between the groups upon comparison (S1-S2, S2-S3, and S1-S3). The results obtained from the *F*-test revealed that for all the three comparison groups, the variances of the compared groups were unequal. Hence, the

*t*-test that was based on unequal variances of the means was employed. Table 3-3 summarizes the results of the *t*-test. Given that for all comparisons (S1-S2, S2-S3, and S1-S3) the *p*-value is smaller than 0.05, it can be concluded that there was a significant difference between the means of the two groups. The average roundness value of the splats deposited by the S2 spraying set is higher than that of the splats deposited by the S1 condition (see Table 3-2). Similarly, the average roundness of the splats deposited by the S3 spraying condition is higher than that of the S1 and S2 conditions. This is quantitative evidence that there was higher deformation of splats deposited with the S3 spraying parameters than when deposited by using the S1 and S2 conditions. This is expected since the particles sprayed under the S3 spray conditions were likely predominately fully molten due to the lower stand-off distance that was used.

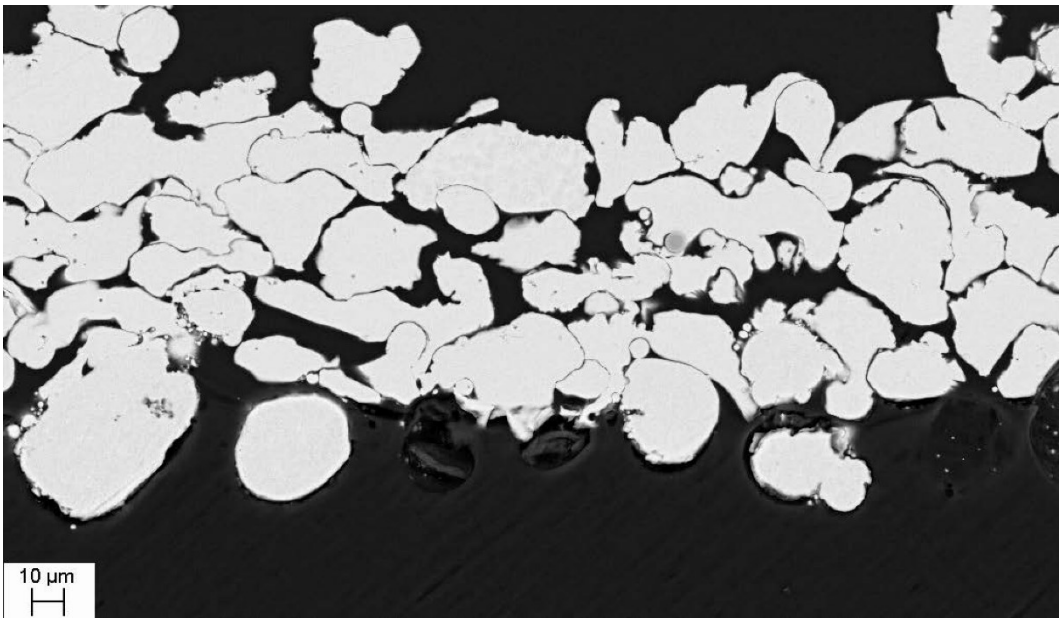


(a)

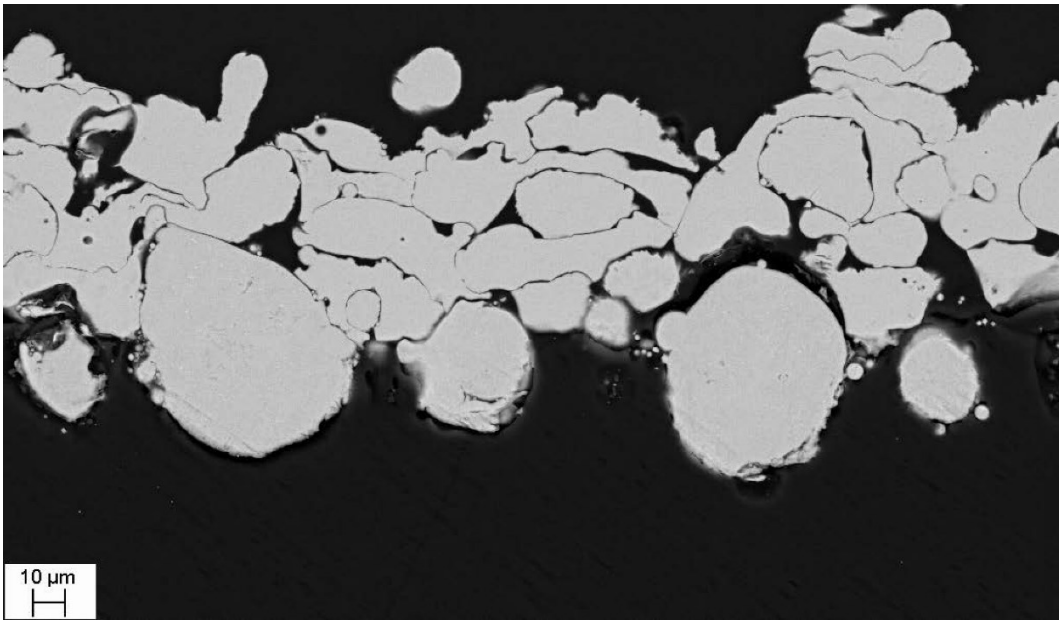


(b)

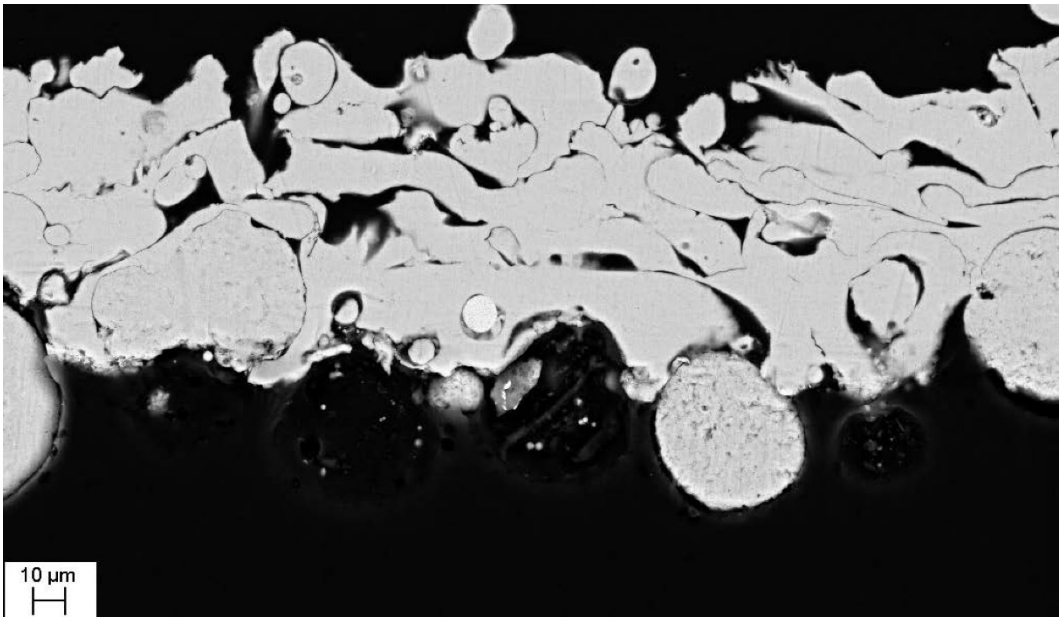


(c)

Figure 3-3 Cross-section micrographs of deposited coatings for the a) S1, b) S2, and c) S3 spraying conditions

Table 3-2 Roundness of the splats and overall porosity of deposited coatings after three passes of spraying for the S1, S2, and S3 spraying conditions

| Set No. | Roundness of the splats | Coating porosity (vol.%) |
|---|---|---|
| S1 | 2.2 ± 0.7 ($n$ = 90) | 20.0 ± 1.2 ($n$ = 7) |
| S2 | 3.1 ± 1.2 ($n$ = 90) | 16.4 ± 2.9 ($n$ = 8) |
| S3 | 3.8 ± 1.6 ($n$ = 90) | 12.1 ± 2.2 ($n$ = 9) |

Table 3-3 *t*-test results for roundness of deposited splats under the assumption of unequal variances

| Compared group | *p*-value |
|---|---|
| S1-S2 | $7.1 \times 10^{-9}$ |
| S2-S3 | $2.5 \times 10^{-4}$ |
| S1-S3 | $1.1 \times 10^{-15}$ |

The measured values of the coating porosities, along with the standard error of the mean, are shown in Table 3-2. The coatings deposited with the S1 spraying parameters had the highest measured porosity as a consequence of the low deformation of the impacting particles. Gaps between the solidified droplets are indicative of high porosity (see Fig. 3-3a). The particles sprayed with the S2 condition impacted a stiffer substrate with higher velocity and experienced improved interconnection with the substrate. This is evidenced from the lower porosity of the coating (16.4 vol %) for the S2 spraying condition. Figure 3-4 shows the Shore A hardness of the PU material with respect to temperature. As can be seen, the PU samples become softer as the temperature increases. Particularly, the Shore A hardness of the PU decreases suddenly when the temperature exceeds 100°C. This is most likely due to the softening of the hard segment and possible reduction in the amount of crosslinking in the polymer structure due to the breakage of

some hydrogen bonds of the PU [12]. This supports the hypothesis that a softer PU substrate results when the S1 spraying condition was employed and when the temperature within the substrate was higher (see Fig. 2-10). For the case of the S3 spray parameters, the porosity decreased further to 12.1 vol %, which likely was a consequence of higher velocity and temperature of the impacting droplets and, therefore, increased droplet deformation. Given these observations, it can be ascertained that the air that was injected into the flame spray torch had a significant influence on the temperature within the substrate and, ultimately, on the quality of the final deposited coating.

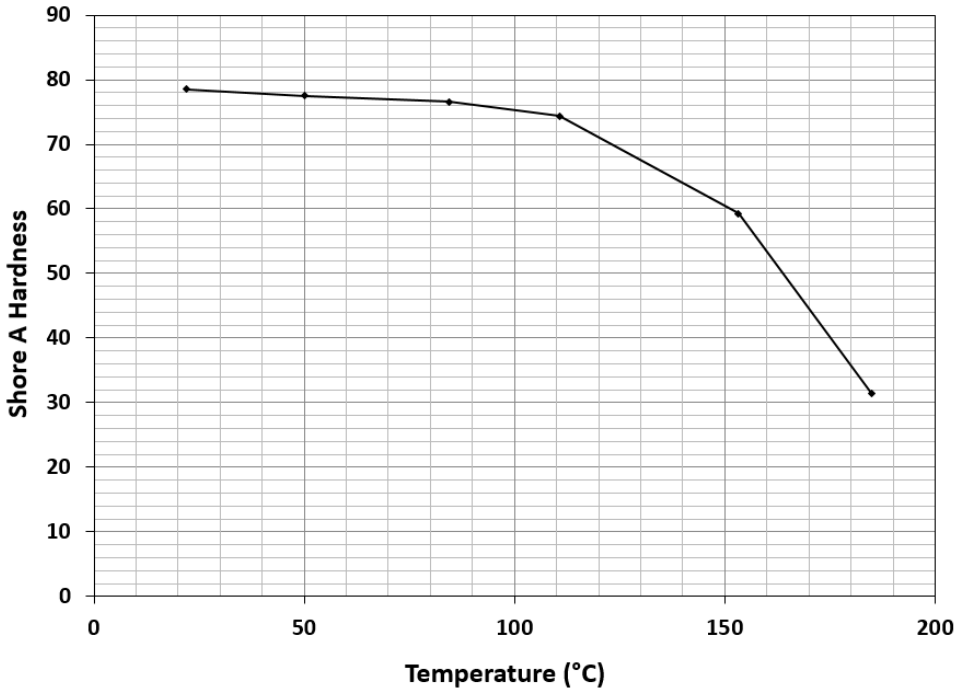


Figure 3-4 Shore A hardness as a function of temperature

### 3.2.2 Coating Electrical Resistance

Deposition of uniform coatings with low electrical resistance on PU substrates was one of the objective of this study. In order to study the effect of flame spraying parameters on the

electrical resistance of the fabricated coatings the electrical resistivity ($\rho$) of the deposited coatings were compared and studied. Electrical resistivity is a material property of the coating and is not a function of the physical dimensions of the coating. Consequently, assessing the electrical resistivity of the coating can provide useful information for comparison of the electrical properties of coatings deposited under different spraying conditions. The electrical resistivity of the coatings was calculated according to Eq. (3-3):

$$\rho = R\frac{wt}{l}, \tag{3-3}$$

where $R$, $w$, $l$, and $t$ are electrical resistance, width, length, and thickness of the coating, respectively.

Table 3-4 summarizes the electrical resistivity of coatings deposited by three passes of the flame spray torch, employing the S1, S2, or S3 spraying conditions. Three passes were chosen to ensure that the deposited coatings were continuous and uniform. A comparison of the values of coating porosity (Table 3-2) and electrical resistivity (Table 3-4) shows that electrical resistivity decreases with decreasing porosity. The minimum electrical resistivity of $0.9 \times 10^{-3}$ Ω-cm was obtained by employing the S3 spraying parameters. For comparison, the electrical resistivitites of pure aluminum and Al-12Si were determined as $2.71 \times 10^{-6}$ Ω-cm and $4.25 \times 10^{-6}$ Ω-cm [105], which are three orders of magnitude lower than the lowest measured electrical coating resistivity. Porosity and possible oxides within the deposited coating are considered to be the cause of the elevated coating resistivity. Powder particles oxidize during the flame spraying process and, since the electrical resistivity of oxides is very high, they act as barriers to the conduction of charge. In order to investigate the possibility of oxidation of the Al-12Si powder during the flame spraying process, XRD analysis was performed on a coating

that was deposited using the S3 spray parameters. As shown in Fig. 3-5, only two phases of aluminum and silicon were identified in the XRD pattern, which suggests that the amount of oxide within the coating was insufficient (less than 10%) to produce detectable diffraction peaks. The results of the XRD pattern would indicate that, while some small content of oxides may be present in the coating, the predominant factors that account for the increased electrical resistivity of the coating, in comparison to that of the base Al-12Si material, is likely the presence of pores in the coating as well as its lamellar microstructure.

Table 3-4 Electrical resistivity of deposited coatings after three passes of spraying for the S1, S2, and S3 spraying conditions

| **Set No.** | **Electrical resistivity (Ω-cm x $10^{-3}$)** |
|---|---|
| S1 | 397.9 ± 56.0 ($n$ = 3) |
| S2 | 14.8 ± 8.4 ($n$ = 3) |
| S3 | 0.9 ± 0.2 ($n$ = 3) |

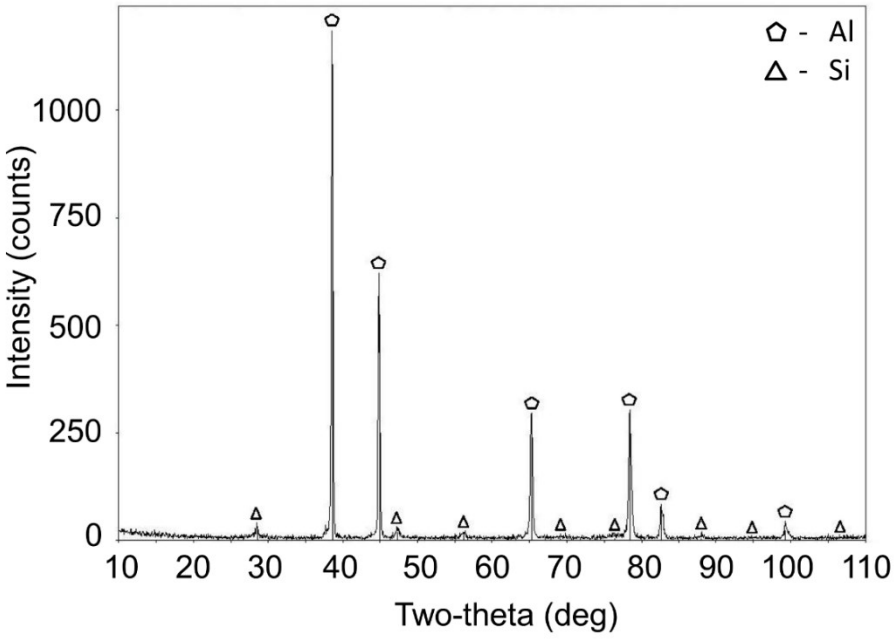


Figure 3-5 XRD pattern of an Al-12Si coating deposited under the S3 spraying conditions

### 3.2.3 Effect of Spray Torch Passes on Coating Characteristics

The S3 spraying parameters were chosen to study the effect of the number of flame spray torch passes on coating thickness, porosity, and electrical resistivity. Figure 3-6 shows low magnification cross section images of coatings deposited after two, three, and four passes of the flame spray torch. As depicted in Fig. 3-7, the coating thickness increased expectedly with an increase in the number of torch passes. However, it can further be observed that the rate of increase in coating thickness with respect to the number of passes was not linear, i.e., the coating thickness increased by 24% from two to three passes whereas the increase was 36% between three and four passes. A congruent behavior can be observed in Fig. 3-8 for the coating mass per unit area, which also increased non-linearly with the number of flame spray torch passes. This may be attributed to a reduction in the number of particles rebounding from the elastomeric sample surface. As is qualitatively observed in Fig. 3-6, after two passes of spraying, the coating

was still non-uniform and there were areas on the PU surface that were not covered with deposited splats. These types of typical areas are indicated in Fig. 3-6a with arrows. The possibility of adhesion of the incoming droplets on these areas was lower than those areas that were covered with deposited splats. The particles impacting the uncoated areas may have experienced direct contact with the PU substrate, resulting in local melting and decomposition of the PU substrate, instead of interlocking with and adhering to the substrate. This phenomenon can lead to weak attachment or rebounding of particles and, therefore, lower deposition efficiency. On the other hand, after three passes of spraying, the coating surface became relatively uniform and continuous (Fig. 3-6b), given that most of the clearances between the Al-12Si particles that were used for roughening the substrate were filled with the deposited splats. This reduced the possibility of direct contact of the in-flight droplets with the PU surface, and allowed for a smoother top surface of the coating with enhanced possibility of adhesion of the droplets upon impact. Also, the substrate temperature increased with increasing number of passes, yielding a softer substrate, which in turn may also have reduced rebounding of the impacting particles.

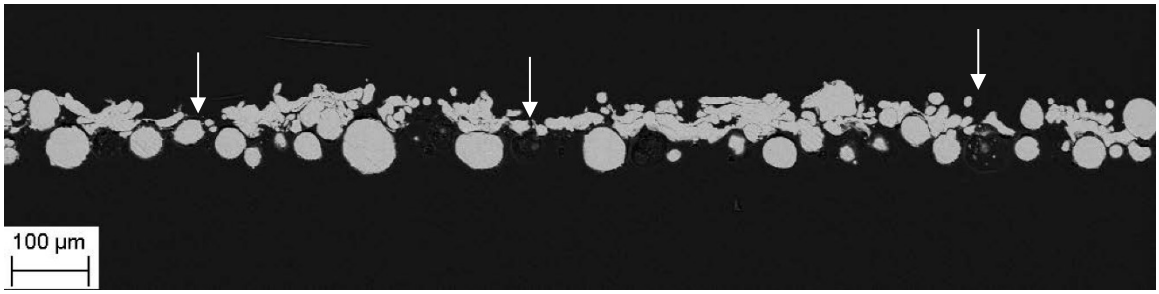


(a)

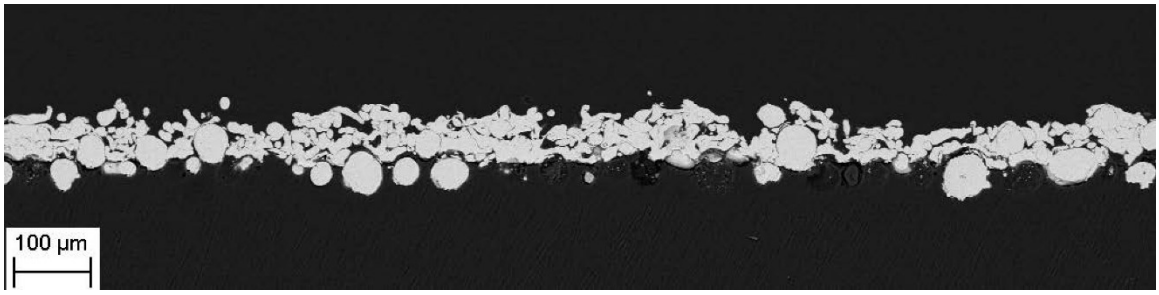


(b)

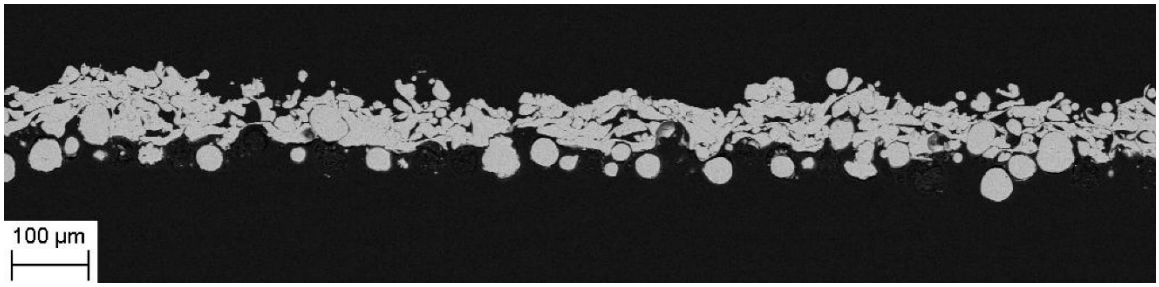


(c)

Figure 3-6 SEM images of coatings deposited by employing the S3 spraying parameters for a) two, b) three, and c) four passes of the flame spray torch

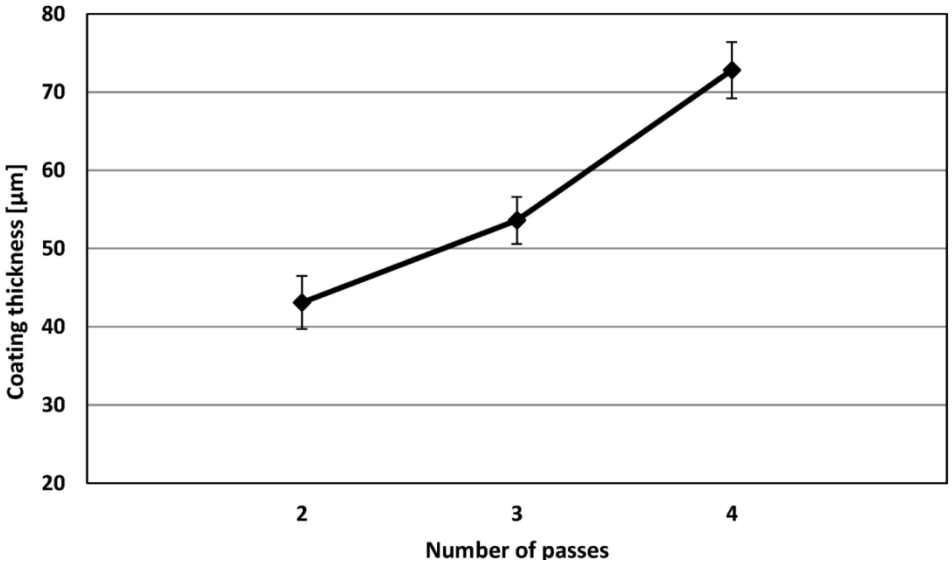


Figure 3-7 Coating thickness as a function of the number of flame spray torch passes

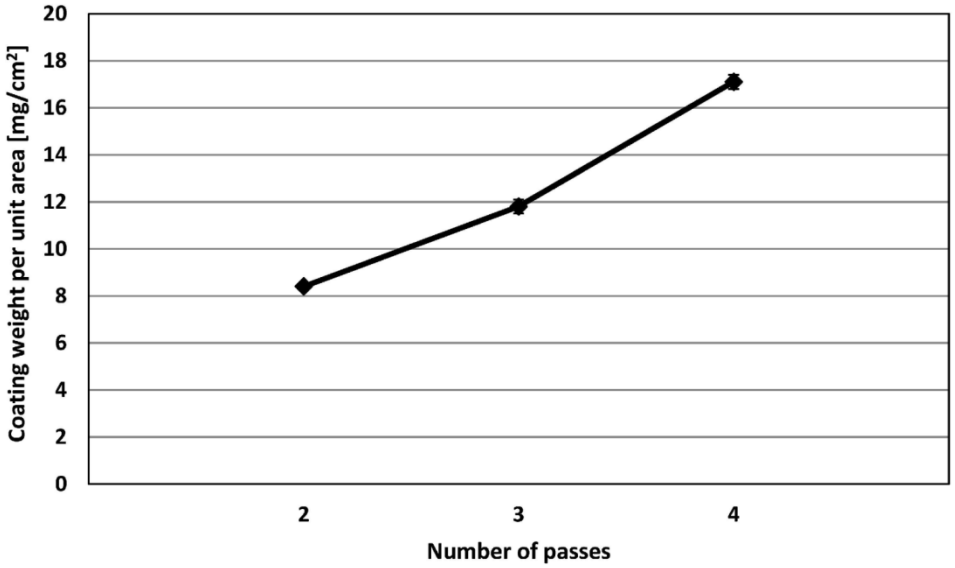


Figure 3-8 Coating weight per unit area as a function of the number of flame spray torch passes

Porosity measurements using SEM micrographs revealed that the porosity of the deposited coatings did not vary significantly with the increase in the number of flame spray torch passes (see Fig. 3-9). However, as shown in Fig. 3-10, the electrical resistivity of the coatings decreased significantly from two to three torch passes, after which it remained approximately constant. An elevated electrical resistivity of the coatings deposited by two passes of spraying is likely to be the result of non-uniformity of the coating, given that the estimated coating porosities for two and three passes of the torch did not deviate significantly. The effect of non-uniformity and non-homogeneity of the coating and its microstructure is to produce large variances in the material properties of the coating. This is evidenced by the large error bar for the average electrical resistivity of the coating after two passes of the flame spray torch (see Fig. 3-10).

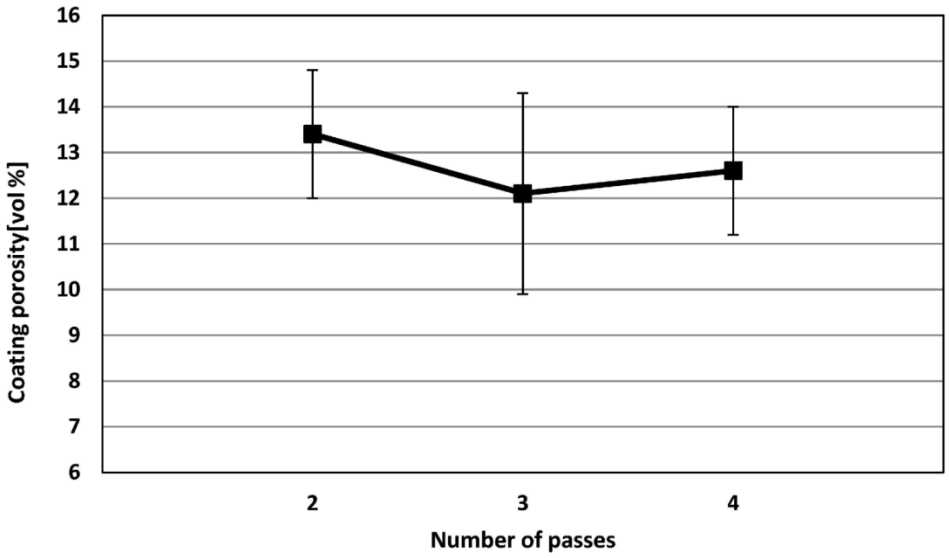


Figure 3-9 Coating porosity as a function of the number of flame spray torch passes

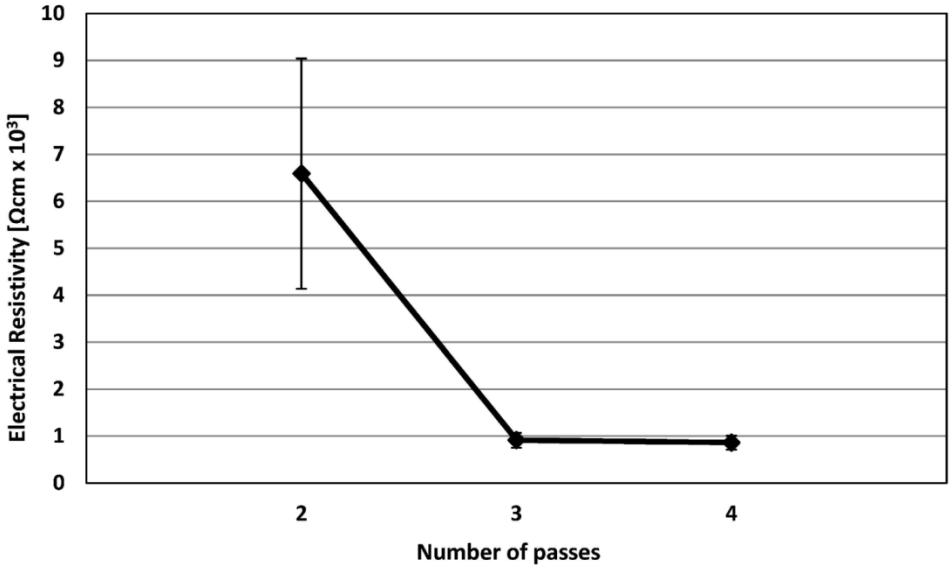


Figure 3-10 Coating electrical resistivity as a function of the number of flame spray torch passes

### 3.2.4 Dynamic Mechanical Analysis

In this study, visual inspection did not reveal any substrate damage for the spraying conditions that were employed. In order to evaluate quantitatively the influence of heat from the flame spray torch on property variation of the PU substrates, dynamic mechanical analysis

(DMA) experiments were performed. As mentioned above, the S3 spraying parameters produced coatings with the lowest porosity and electrical resistance, and hence, corresponding samples were evaluated by DMA. The dynamic mechanical properties of the sprayed samples were studied by testing PU substrates before and after exposure to the high-temperature flame spray process. In these experiments, the flame spraying process was performed without the addition of metal powder to avoid any incidental effects from surface-deposited coatings on the DMA measurements [106]. It was shown that the spray powder would increase the temperature within the substrate only by about 15 % (see Fig. 2-14).

Figure 3-11 shows the measured storage modulus as a function of temperature for a DMA oscillation frequency of 1 Hz. Compared to virgin samples (Fig. 3-11a), only a minor increase in storage modulus was observed for the PU samples exposed to the flame (Fig. 3-11b), over most of the DMA-tested temperature range. This minor increase in storage modulus may be the result of heat input into the PU substrate during the spraying process. It is known that oxidation and other decomposition effects can occur in PU at elevated temperatures, leading to an increase in storage modulus and rigidity. A monotonic increase in storage modulus in PU as a function of time at 70°C and 90°C was reported by Boubakri *et al.* [107]. However, since the sample exposure time to the flame of the spray torch was only 45 seconds, and peak temperatures within the substrate were less than 110°C, the mechanical properties of the PU samples were not changed significantly in the present experiments.

The variation in storage modulus of the virgin and flame-exposed PU samples for DMA oscillation frequencies ranging from 0.02 Hz to 30 Hz at a fixed temperature of 30°C was also examined (see Fig. 3-12). With increasing frequency, the elasticity of the material is expected to

rise [108], which can be observed in Fig. 3-12. A comparison of Figs. 3-12a and 3-12b reveals that a slight increase in storage modulus of the flame-exposed samples occurred. However, similar to the DMA scans based on variations in temperature, this increase in storage modulus with frequency is considered insignificant. Given these observations, it can be concluded that the exposure to flame from the torch does not considerably affect the material properties of the PU elastomer, even though the heat transfer may soften the elastomer.

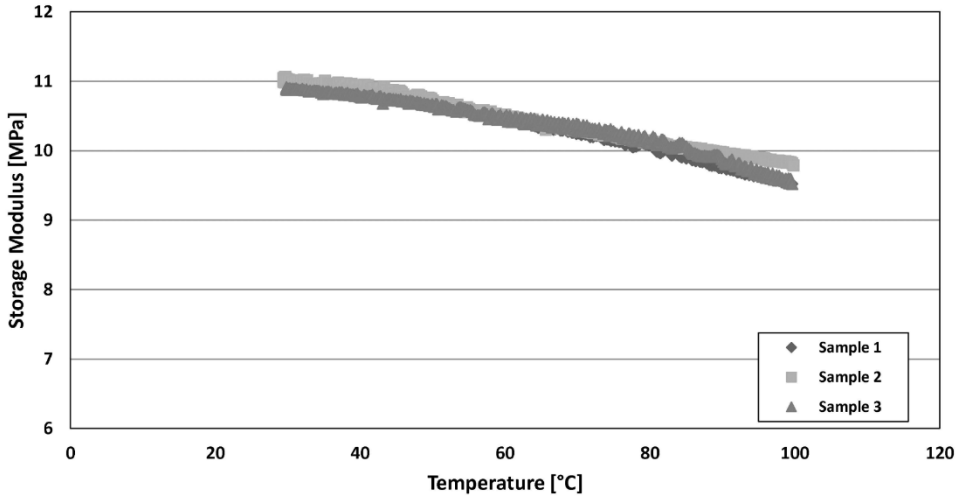


(a)

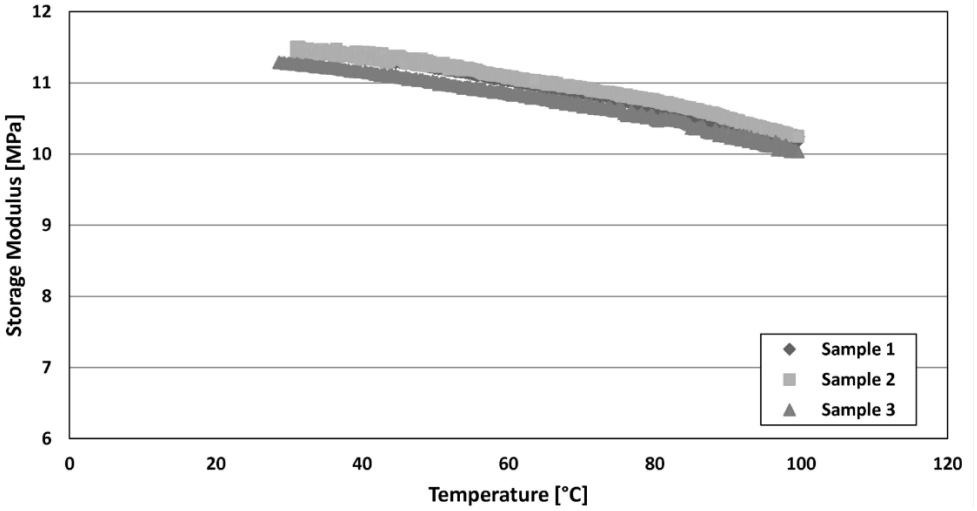


(b)

Figure 3-11 Substrate storage modulus measured at a DMA oscillation frequency of 1 Hz as a function of temperature for a) virgin and b) flame-exposed PU samples

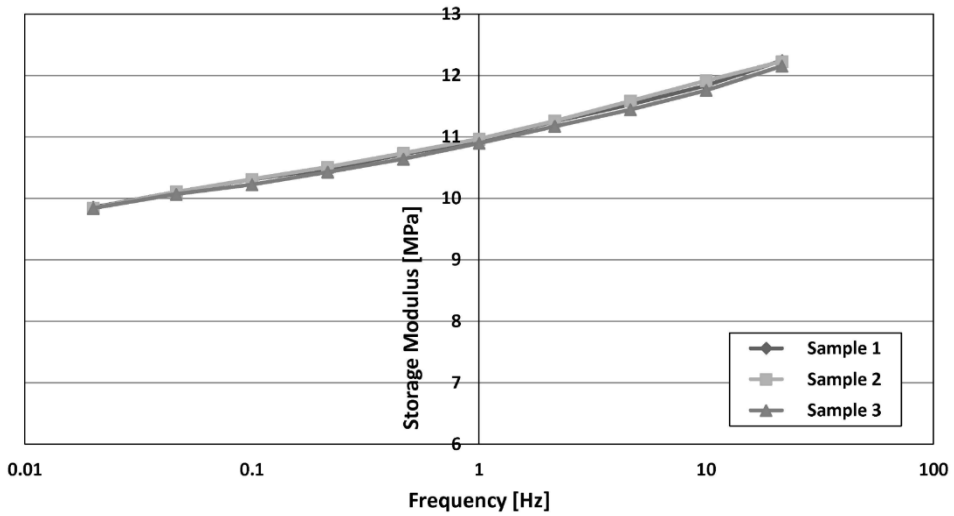


(a)

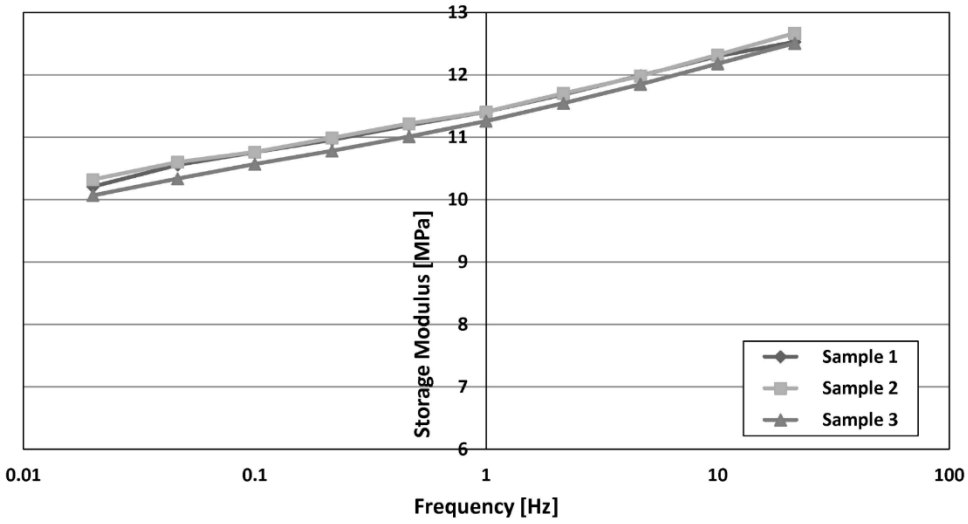


(b)

Figure 3-12 Substrate storage modulus as a function of DMA oscillation frequency at a constant temperature of 30°C for a) virgin and b) flame-exposed PU samples

# Chapter 4

# Evaluation of the Effect of Temperature on Wear Resistance of Polyurethane Elastomers

To evaluate the wear resistance of polyurethane elastomers at controlled temperatures, an erosion test assembly was designed and developed. A cold gas dynamic spray system was used to conduct the erosion tests. The transient temperature distribution within the samples during erosion experiments was determined by the development of a 3D FE model. The velocity of the impacting particles was determined by a model based on the principles of supersonic fluid flow through a converging-diverging nozzle. The stress-strain behavior of the polyurethane elastomers were characterized at room and elevated temperatures by conducting tensile tests and cyclic loadings. The obtained results showed the substantial effect of testing temperature on erosion resistance of PU elastomers. Comparison of stress-strain behavior of the studied polyurethanes with their erosion resistance at controlled temperatures revealed that the residual strain as a result of plastic deformation, stress softening, ultimate strength and elongation at break were the key parameters affecting the wear resistance of polyurethane elastomers. Evaluation of the surface morphology of the worn samples confirmed the importance of the residual strain on the erosion resistance of polyurethane elastomers.

Some sections of the work presented in this chapter have been published in proceedings of the First Pacific Rim Thermal Engineering Conference (PRTEC) 2016, Hawaii's Big Island, HI, USA, March 13-17, 2016, and have been submitted for publication in Wear, 2016.

## Nomenclature

| | | | |
|---|---|---|---|
| $a$ | Acceleration (m/s$^2$) | $V$ | Velocity (m/s) |
| $A$ | Cross section area (m$^2$) | $W$ | Molecular weight (kg/mol) |
| $C_p$ | Specific heat (J/kg.K) | $x$ | Axial distance (m) |
| $C_D$ | Drag coefficient | | |
| $d$ | Diameter (m) | *Greek Symbols* | |
| $F_D$ | Drag force (N) | $\rho$ | Density (kg/m$^3$) |
| $h$ | Convective heat transfer coefficient (W/m$^2$.K) | $\gamma$ | Specific heat rate |
| $l$ | Thickness (m) | | |
| $m$ | Mass (kg) | *Subscripts* | |
| $M$ | Mach number | 0 | Stagnation condition |
| $P$ | Pressure (kPa) | $e$ | Nozzle exit condition |
| $P_s$ | Shock pressure (kPa) | $p$ | Particle condition |
| $q'''$ | Rate of energy generation per unit volume (W/m$^3$) | $g$ | Gas condition |
| $q_s''$ | Surface heat flux (W/m$^2$) | | |
| $R$ | Gas constant (J/mol.K) | | |
| $T$ | Temperature (K) | *Superscripts* | |
| $T_b$ | Back temperature (K) | * | Nozzle throat condition |
| $T_s$ | Surface temperature (K) | | |
| $T_\infty$ | Surrounding temperature (K) | | |
| $t$ | Time (sec) | | |

## 4.1 Experimental Method

### 4.1.1 Polyurethane Material

The erosive wear resistance of four types of PU elastomers (RoPlasthan-1200-55A, RoPlasthan-1200-85A, RoCoat-3000-85A, and RoCoat-3000M-85A (Castable), Rosen Group, Lingen, Germany) with Shore A hardness within the range of 55 to 85 was studied. A PU sheet thickness 7 mm was selected to ensure that the thickness did not influence the erosion results and did not decrease significantly during the test [9]. The PU samples were cut into sections of 48 mm x 36 mm by using a water jet cutter (OMAX 2652 JetMachining Center, OMAX Corporation, Kent, WA, USA). In order to attach the PU samples to the erosion testing equipment, the samples were bonded to aluminum sheets of size 48 mm x 48 mm x 3 mm with a thin layer of adhesive (3M DP460, 3M Scotch-Weld, St. Paul, MN, USA). The glass transition temperature of the tested PU elastomers was determined by differential scanning calorimetry (DSC) analysis for the temperature range of -60°C to 180°C (DSC Q100 V9.8, TA Instruments, New Castle, DE, USA).

### 4.1.2 Erosion Testing Assembly

In order to evaluate the erosion resistance of PU elastomers at controlled temperatures, an erosion test assembly based on ASTM Standard G76 [109] was developed. The testing equipment was slightly modified from the requirements of ASTM Standard G76 to incorporate the effect of the PU temperature during the erosion test. A cold gas dynamic spray system ("cold spray") (SST Series P, CenterLine Ltd., Windsor, ON, Canada) was used to heat and move compressed air at various temperatures, and the gas was used to accelerate the erodant particles to impact on the surface of the PU. The operating parameters of the cold spray system that were

employed for erosion testing are summarized in Table 4-1. The PU sample holder was fabricated from copper and it was equipped with two cartridge heaters (50 Watts Miniature High Temperature Cartridge Heater (D 1/8" x 1 1/4"), McMaster-Carr, Aurora, OH, USA). A temperature controller (CNI8A42, Omega Engineering Inc., Stamford, CT, USA) was used to maintain the temperature of the copper cube at the desired set-point. Figure 4-1 shows a schematic and the assembly of the custom-fabricated erosion testing system.

Table 4-1 Cold spray system parameters

| | |
|---|---|
| Pressure of compressed air (kPa) | 435 |
| Temperature of compressed air (°C) | 25, 75, and 125 |
| Stand-off distance (mm) | 22 |
| Nozzle length (mm) | 70 |
| Nozzle throat diameter (mm) | 2.5 |
| Nozzle output diameter (mm) | 5.4 |

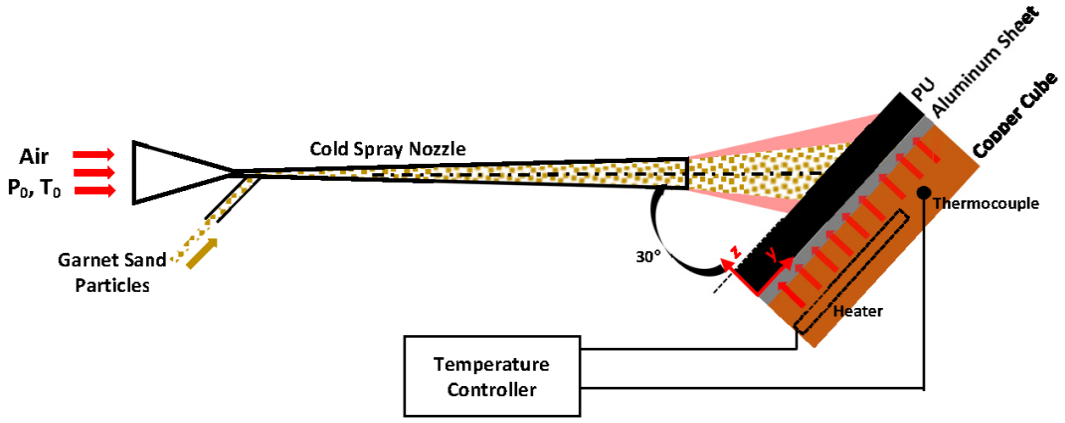


(a)

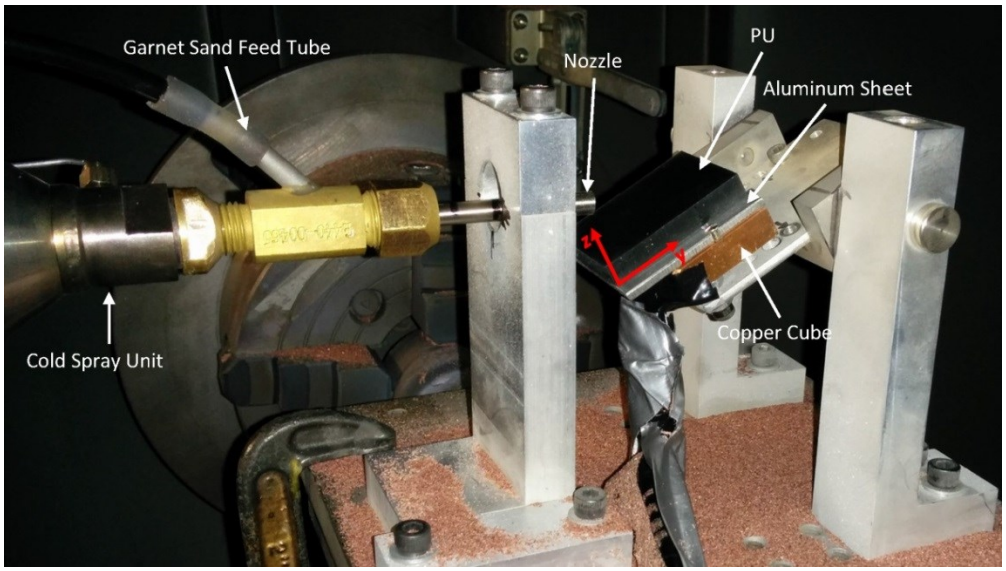


(b)

Figure 4-1 a) Schematic and b) image of the custom-made erosion test assembly

The PU samples were weighed before and after the erosion test by a balance with an accuracy of ±1 mg (Adventurer Pro AV313, OHAUS Corporation, Parsippany, NJ, USA). The wear rate was calculated by normalizing the mass loss of the sample with the mass of the erodant particles. Garnet sand (Super Garnet, V. V. Mineral, Tamil Nadu, India) was chosen as the erodant medium. Figure 4-2 shows the morphology of the garnet sand. As observed in the image, the sand particles are rounded on most of the sides. The average diameter of the garnet sand particles was measured by image analysis (ImagePro, Media Cybernetics, Bethesda, MD, USA). The average diameter was calculated by averaging length of lines passing through the object centroid at 2 degree intervals. The average size of the garnet sand particles was 266 ± 49 µm ($n$ = 159). The average radius of the corners of the erodant particles was also determined by image analysis and was estimated to be 67 ± 26 µm ($n$ = 132).

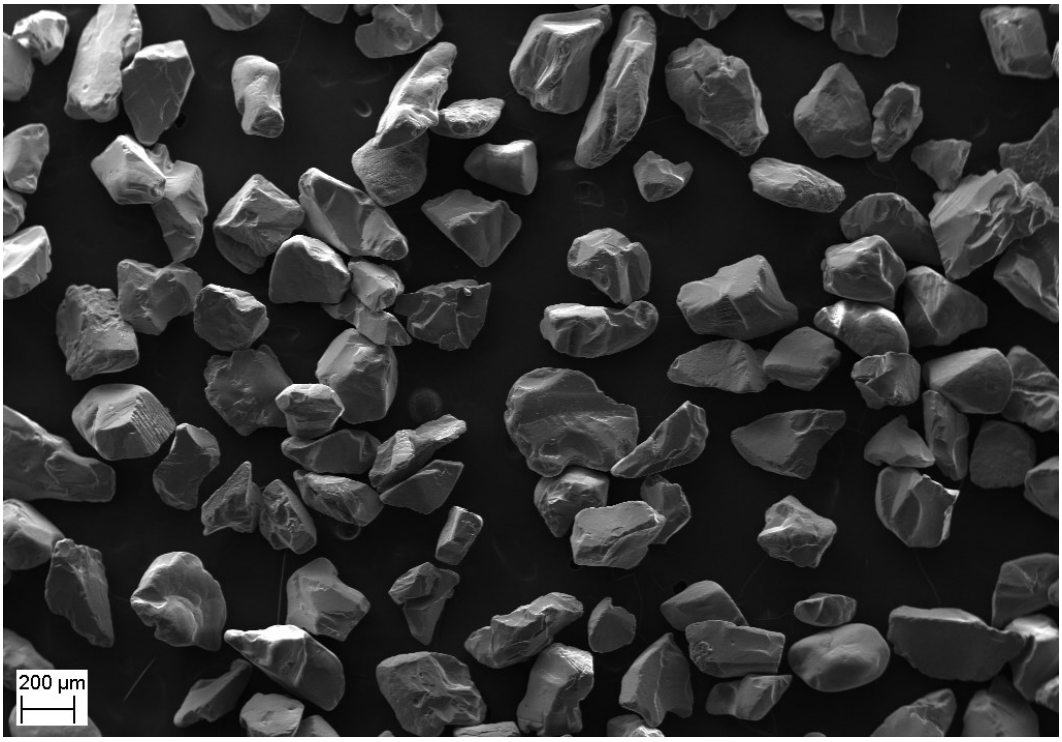


Figure 4-2 Morphology of the garnet sand particles

Each type of PU was tested at three different set-point temperature values for conditions A, B, and C (see Table 4-2). The PU samples were heated by both the hot compressed air from the cold spray system and by the cartridge heaters that were mounted in the copper plate support. Details on the set-point temperatures of the air from the cold spray system and in the copper support plate are summarized in Table 4-2. The PU samples were preheated for 120 seconds from the unexposed surface by the cartridge heaters and copper plate. Then, the samples were heated at the exposed surface with air from the cold spray system (see Fig. 4-1) for 120 seconds, simultaneously with heating from the unexposed surface that was in contact with the copper plate support. This ensured that the temperature was uniform throughout the PU samples prior to initiating the erosion tests.

Table 4-2 Details of parameters for each testing condition of the PU samples

| Test Condition / Parameters | Condition A | Condition B | Condition C |
|---|---|---|---|
| Target PU temperature | 22°C | 60°C | 100°C |
| Pressure of air | 435 kPa | 435 kPa | 435 kPa |
| Set temperature at cold spray console | 25°C | 75°C | 125°C |
| Set temperature at temperature controller | 25°C | 65°C | 105°C |
| Preheating period from the unexposed surface | 120 sec | 120 sec | 120 sec |
| Preheating period from the unexposed and exposed surfaces | 120 sec | 120 sec | 120 sec |
| Erosion test period | 240 sec | 240 sec | 240 sec |

### 4.1.3 Temperature Measurements

A J-type thermocouple (Gage 30, Thermo Electric Ltd., Brampton, ON, Canada) was inserted into the PU substrate at a depth of 1.5 mm below the surface of the center of the area that was to be eroded. A data acquisition system (SCXI 1600, National Instruments, Austin, TX, USA) was used to collect the data of transient temperature that was measured by the inserted thermocouple. The data obtained from this thermocouple were used for the verification of the subsequently presented FE heat transfer model and to study the possible temperature rise caused by friction forces and hysteresis during the erosion process. The temperature at the unexposed surface of the PU samples was measured by second J-type thermocouple (Gage 30, Thermo

Electric Ltd., Brampton, ON, Canada) that was placed below the unexposed surface between the PU and aluminum sheet. An infrared camera (VIR50, Extech Instruments Corporation, Nashua, NH, USA) was employed to measure the temperature of the exposed surface of the PU samples. The exposed surface of the PU was divided into 12 square sections and the temperature at each section was measured by pointing the infrared camera towards the center of a given section. The data obtained was used to formulate boundary conditions for the FE model. The emissivity needed for the setup of the infrared thermometer pointing towards the PU surface was determined by adjusting the emissivity coefficient until approximately the same temperature was measured by the infrared thermometer and the thermocouple that was inserted below the sample surface. The emissivity was determined as 0.99.

### 4.1.4 Materials and Mechanical Testing

The stress-strain behavior of the PU samples at room and elevated temperatures were studied by conducting tensile tests and cyclic loading. PU sheets with a thickness of 1 mm were cut to shape and dimensions based on the ASTM Standard D638-Type V [110] (see Fig. 4-3) by waterjet cutting (OMAX 2652 JetMachining Center, OMAX Corporation, Kent, WA, USA). A dynamic mechanical analyzer (ElectroForce 3200, TA Instruments, Eden Prairie, MN, USA) was employed to conduct the tensile tests and cyclic loadings. The tensile tests were conducted up to a nominal strain of 350% in the PU while cyclic loading was performed for a nominal strain range of 0% to 50%. The tests were conducted at 25°C and at elevated temperatures of 60°C and 100°C at a strain rate of 0.25 $s^{-1}$. In experiments at elevated temperature, the samples were preheated for 4 minutes at the desired temperature to ensure that the temperature within the samples was uniform prior to performing the test.

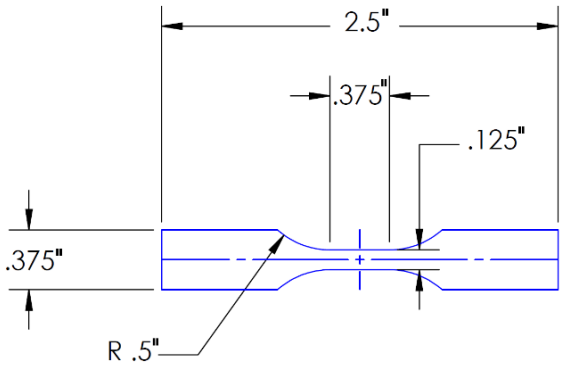


Figure 4-3 Dimensions of the dog-bone shape samples used for the tensile tests

### 4.1.5 Scanning Electron Microscopy

The surface topography of the worn PU elastomers were examined by using a scanning electron microscope (EVO LS15 EP, Carl Zeiss Canada Ltd., Toronto, ON, Canada) in the secondary electron mode with a beam voltage of 5 kV. A thin film of carbon was deposited onto the PU surface by using a carbon evaporation system (EM SCD 005, Leica Baltec Instrument, Balzers, Liechtenstein) to avoid surface charging during scanning electron microscopy (SEM).

## 4.2. Mathematical Model for Determination of Erodant Particle Velocity

The velocity of the erodant particles at the nozzle exit was estimated by employing the mathematical model that was developed by Dykhuizen *et al.* [111]. The model is based on the principles of dynamics and thermodynamics of compressible fluid flow through a converging-diverging nozzle. The geometry and dimensions of the nozzle are shown in Fig. 4-4. The following assumptions were made in order to derive the model:

(a) The gas flow was one dimensional and isentropic (adiabatic and frictionless);

(b) The gas was treated as ideal;

(c) The specific heats of the gas were constant; and

(d) The carrier gas was supplied from a large chamber where its velocity was zero.

Based on the geometry of the nozzle, the Mach number at each point was determined from [111]:

$$\frac{A}{A^*} = \left(\frac{1}{M}\right)\left[\left(\frac{2}{\gamma+1}\right)\left(1+\frac{\gamma-1}{2}M^2\right)\right]^{\frac{\gamma+1}{2(\gamma-1)}}. \tag{4-1}$$

Due to the difficulty associated with solving the non-linear equation of Eq. (4-1), equations developed by Grujicic *et al.* [112] were used to determine the Mach number at each section of the diverging part of the nozzle:

$$M = \left[k_1 \frac{A}{A^*} + (1-k_1)\right]^{k_2}, \tag{4-2a}$$

where $k_1 = 218.0629 - 243.5764\gamma + 71.7925\gamma^2$ and (4-2b)

$$k_2 = -0.12245 + 0.28130\gamma. \tag{4-2c}$$

Once the Mach number was calculated at a given cross-sectional area, pressure, velocity, temperature, and density of the gas at any point was determined by using Eqs. (4-3) to (4-6) as [111, 112]:

$$P_g = P^*\left(\frac{\gamma+1}{2+(\gamma-1)M^2}\right)^{\frac{\gamma}{\gamma-1}}, \tag{4-3}$$

$$T_g = \frac{T_0}{\left(1+\left(\frac{\gamma-1}{2}\right)M^2\right)}, \tag{4-4}$$

$$V_g = M\sqrt{\gamma R T_g}, \text{ and} \tag{4-5}$$

$$\rho_g = \frac{\rho_0}{\left(\left(1+\frac{\gamma-1}{2}\right)M^2\right)^{\frac{1}{\gamma-1}}}. \tag{4-6}$$

The validity of Eqs. (4-3) to (4-6) are based on the assumption that there are no shocks in the nozzle. This condition requires that the shock pressure be higher than that of the ambient pressure. In other words, $P_s$, as determined by Eq. (4-7) should be larger than the ambient pressure [111,112]. This condition was verified in this study based on the chosen spraying parameters and the nozzle geometry. Equation (4-7) for the shock pressure is

$$P_s = P_e\left(\frac{2\gamma}{\gamma+1}M_e^2 - \frac{\gamma-1}{\gamma+1}\right). \tag{4-7}$$

The particle velocity was determined according to the second law of motion by assuming that the drag force was the only force that was applied on the accelerating particles. The second law states:

$$m_p a_p = F_D. \tag{4-8}$$

With $a_p = \frac{dV_p}{dt}$, Eq. (4-8) can be re-written as:

$$m_p \frac{dV_p}{dt} = F_D, \tag{4-9}$$

where

$$F_D = \frac{1}{2}C_D A_p \rho_g \left(V_g - V_p\right)^2, \tag{4-10a}$$

$$m_p = \frac{1}{6}\pi d_p^3 \rho_p, \text{ and} \tag{4-10b}$$

$$A_p = \frac{1}{4}\pi d_p^2. \tag{4-10c}$$

By substituting Eqs. (4-10a) to (4-10c) into Eq. (4-9), the equation of the instantaneous acceleration of the particle is:

$$\frac{dv_p}{dt} = \frac{3}{4}\frac{C_D \rho_g}{d_p \rho_p}(V_g - V_p)^2, \tag{4-11}$$

where the drag coefficient, $C_D$, was determined to be [113]:

$$C_D = \frac{24}{\mathrm{Re}_p}\left[\frac{\left(1+0.15\,\mathrm{Re}_p^{0.687}\right)\left(1+e^{-\left(0.427/M_p^{4.63}\right)-\left(3/\mathrm{Re}_p^{0.88}\right)}\right)}{1+\left(M_p/\mathrm{Re}_p\right)\left(3.82+1.28e^{-1.25M_p/\mathrm{Re}_p}\right)}\right], \tag{4-12a}$$

for

$$\mathrm{Re}_p = \left|V_g - V_p\right|\frac{\rho_g d_p}{v} \text{ and} \tag{4-12b}$$

$$M_p = \frac{\left|V_g - V_p\right|}{\sqrt{\frac{\gamma R T_g}{W}}}. \tag{4-12c}$$

Euler's numerical integration method was used to solve Eq. (4-11) numerically. The chain rule was applied to simplify the acceleration term so that $\frac{dV_p}{dt} = V_p\frac{dV_p}{dx}$ and the final equation for particle velocity was [114]:

$$V_{p,x} = \left(V_{p,x-1}^2 + \frac{1.5\Delta x C_D \rho_A}{d_p \rho_p}\left(V - V_{p,x-1}\right)^2\right)^{0.5}. \tag{4-13}$$

Equation (4-13) was solved at spatial intervals of $\Delta x = 0.1$ mm through the length of the nozzle. The average diameter of the garnet sand particles (266 μm) and a density of 4 g/cm$^3$ [115] was used in conjunction with Eq. (4-13).

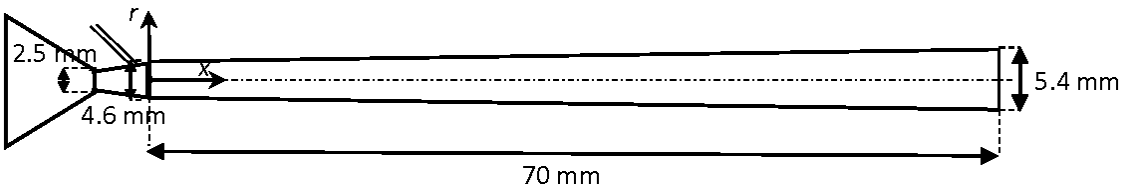


Figure 4-4 Geometry of the converging-diverging nozzle of the cold spray system

## 4.3 Finite Element Model for Determination of Temperature Distribution

In order to determine the transient temperature field within the PU samples during the erosion test, a thermal FE model was developed using the generalized FE software Abaqus/Standard Version 6.13 [116]. The boundary conditions of the model were assigned according to the preheating that was introduced at the exposed and unexposed surfaces of the PU sample. The erosion tests were conducted in a dust collection system that produced airflow with a velocity of approximately 1.4 m/s over the sample surface during the first step of preheating. This flow of air produced forced convection heat transfer from the surface during the initial 120 seconds of preheating where the samples were being heated from the unexposed surface. Thus, for the first 120 seconds of the preheating procedure, the boundary conditions were selected as a transient temperature on the unexposed surface of the samples and forced convection on the top surface. The heat transfer coefficient was determined according to the Newtons' law of cooling under steady-state conditions $\left( h = \frac{k}{l} \frac{T_b - T_s}{T_s - T_\infty} \right)$ [117] as 53 ± 2 W/m$^2$K ($n$ = 3) for three set-point temperatures of 60ºC, 80ºC and 105ºC on the unexposed surface of the samples.

In the second preheating step, the boundary condition on the unexposed surface of the sample was similar to that of the first preheating stage (as transient temperature measured by the thermocouple) while the boundary condition on the exposed surface was changed from a convection boundary condition to a temperature boundary condition, with the temperature being measured with the infrared camera. Given that the effect of heat generation caused by the friction forces of the impacting particles and repeated deformation of PU was neglected, the boundary conditions during the erosion test remained unchanged and were similar to those of the second step of preheating. The validity of this assumption was verified by monitoring the temperature measured by the thermocouple that was inserted 1.5 mm below the PU surface during the erosion test. Constant thermal properties such as thermal conductivity and negligible heat loss due to natural convection from the sides of the sample were the other two assumptions that were made during the development of the FE model. The governing equation that was solved by the FE model was

$$\rho C_P \frac{\partial T}{\partial t} = div(k\ grad(T)) + q''' . \tag{4-14}$$

The Galerkin method was then used to derive the integral form of the heat transfer equation, yielding the FE equations in matrix form [116]. A standard heat transfer protocol in the Abaqus software was chosen for the analysis. In the chosen formulation, the time integration was completed by the backward Euler method (Crank-Nicholson operator) [116]. Three-dimensional eight-node linear heat transfer brick elements (DC3D8 in the Abaqus library) were chosen as the element type [116]. The model was discretized with 13,824 elements. The initial condition and boundary conditions were defined based on the discussed preheating stages as:

$$T(x, y, z, t = 0) = T_{initial}, \tag{4-15}$$

$$T(x, y, z = 0, t) = T_b(t), \tag{4-16}$$

$$q''_s = \left(T_\infty - T(x, y, z = l, t)\right)h \quad for \quad t < 120\,\text{sec}, \tag{4-17a}$$

$$T(x, y, z = l, t) = T_s(x, y, t) \quad for \quad t > 120\,\text{sec}. \tag{4-17b}$$

## 4.4 Results and Discussion

### 4.4.1 Erodant Particle Velocity

Figure 4-5 shows a typical graph of the velocity of the air and the erodant particle through the divergent section of the nozzle. The position at zero meters in the figure refers to the origin as shown in Fig. 4-4. The graph in Fig. 4-5 indicates that the particle velocity is approximately one order of magnitude lower than that of the air due to the relatively high mass of the erodant particles. The velocity of air flowing through the nozzle and, therefore, the particle velocity, is a function of temperature and pressure of the gas as set at the cold spray console. As shown in Table 4-2, for all the testing conditions, the gas pressure was kept constant while the set temperature at cold spray console was increased from 25ºC to 125ºC for Conditions A to C. The gas at higher temperatures has higher kinetic energy and velocity, which affects the velocity of the fed particles. Table 4-3 summarizes the particle exit velocity that was estimated for each temperature set at the cold spray console. As shown in the table, the particle velocity increased when the gas temperature at the cold spray console was increased. To ensure that the small deviation in velocity alone did not significantly affect the erosion rate, the wear performance of a material with erosion resistance that is insensitive to the temperatures in the range explored in this study was tested. Aluminum sheets were selected for that purpose given that the mechanical properties of aluminum do not vary greatly with temperature in the range of 25ºC to 100ºC. The erosion performance of the aluminum samples were tested at 25ºC and 100ºC. The results

revealed that the erosion rate, as expressed as a ratio of mass loss of aluminum to mass of impacting garnet sand particles, did not vary noticeably within the temperature range that was studied (see Table 4-4). The two-sample *t*-test statistical method was employed to verify whether or not the average mean of the two groups shown in Table 4-4 were significantly different. The *p*-value for the *t*-test was based on the assumption of equal variances and was calculated to be 0.34. Given that the calculated *p*-value is higher than 0.05, it cannot be concluded that there is a significant difference between the average values of the two groups. This suggests that while the variation of temperature of the gas as set at the cold spray console affects the temperature distribution within the target samples, its effect on velocity of the garnet sand particle is negligible.

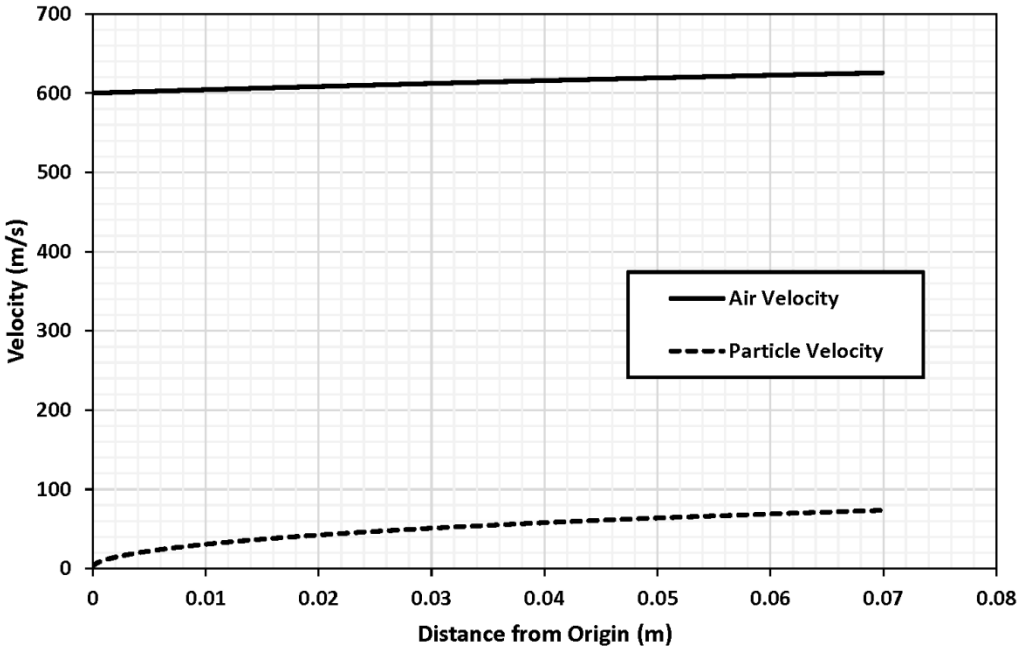


Figure 4-5 Air and particle velocities through the diverging section of the nozzle ($P_0$ = 50 psig and $T_0$ = 25ºC)

Table 4-3 Garnet sand particle velocities at the nozzle exit for different gas temperatures

| Gas set temperature at cold spray console ($T_0$) | Gas set pressure at cold spray console ($P_0$) | Calculated particle velocity and nozzle exit |
|---|---|---|
| 25ºC | 50 psig | 73 m/s |
| 75ºC | 50 psig | 76 m/s |
| 125ºC | 50 psig | 78 m/s |

Table 4-4 Non-dimensional erosion rate of aluminum samples at different air temperatures

| Gas set temperature at cold spray console ($T_0$) | Gas set pressure at cold spray console ($P_0$) | Erosion Rate (mg/g) |
|---|---|---|
| 25ºC | 50 psig | $0.37 \pm 0.01$ ($n = 6$) |
| 125ºC | 50 psig | $0.38 \pm 0.01$ ($n = 5$) |

### 4.4.2 Temperature Distribution within the Polyurethane Samples during Erosion Test

The PU samples that were attached to the aluminum sheet were installed on the copper cube plate that was set to the desired temperatures (see Fig. 4-1). The temperature of the unexposed surface of the PU was monitored by a J-type thermocouple and the temperature data that was obtained was used as one of the boundary conditions in the developed FE model. Figure 4-6 shows the temperature of the unexposed surface of the PU samples upon attachment of the test coupons on the copper cube plate. The fluctuations in the temperature after 120 seconds are a result of the introduction of air from the nozzle during the second step of

preheating and the automatic readjustment of the copper cube temperature by the temperature controller.

The experimental data obtained from the J-type thermocouple that was inserted 1.5 mm below the surface, coupled with the temperature calculated by the FE model, is shown in Fig. 4-7. The sudden increase in the temperature after 120 seconds is a result of the introduction of air from the nozzle during the second step of preheating. The difference between the temperature measured by the thermocouple and that obtained from the simulation after 120 seconds is most probably due to inaccuracies in measuring the surface temperature by the infrared camera. The infrared camera measures the average temperature of a surface area with an approximate diameter of 12 mm while the local temperature on the top of the thermocouple could have been higher in value. Irrespective of this deviation, there was good agreement between the simulation and the experimental results, which thus verifies the model. Figure 4-7 also shows that after 240 seconds (end of preheating), a steady-state condition was practically achieved and the temperature did not vary appreciably beyond that time.

The model was then employed to determine the temperature distribution within the PU samples during the erosion tests. Figure 4-8 shows the cross section images of PU samples after preheating under conditions B and C. In Fig. 4-8, the area to be eroded is indicated. As can be seen, the temperature in that area was relatively uniform and close to 60°C and 100°C for conditions B and C, respectively. The temperature distribution within the PU samples during the erosion test was similar to that presented in Fig. 4-8 before the erosion test. This is evidenced by the fact that the data obtained from the thermocouple that was located below the surface confirmed a negligible temperature rise caused by friction and the deformation of PU.

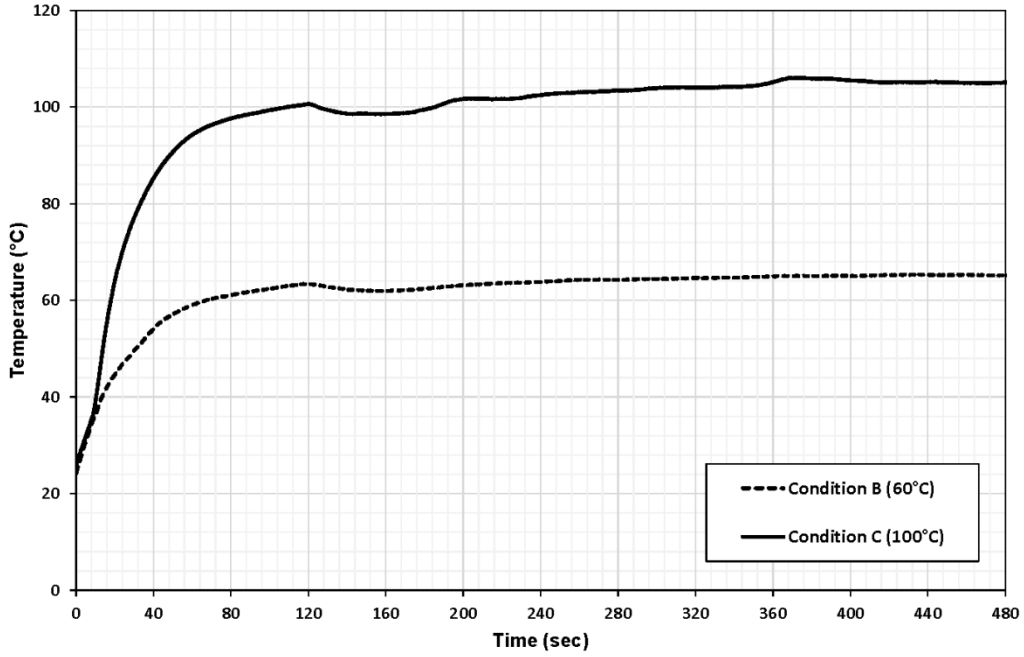


Figure 4-6 Transient temperature of the unexposed surface of the PU samples for the B and C testing conditions

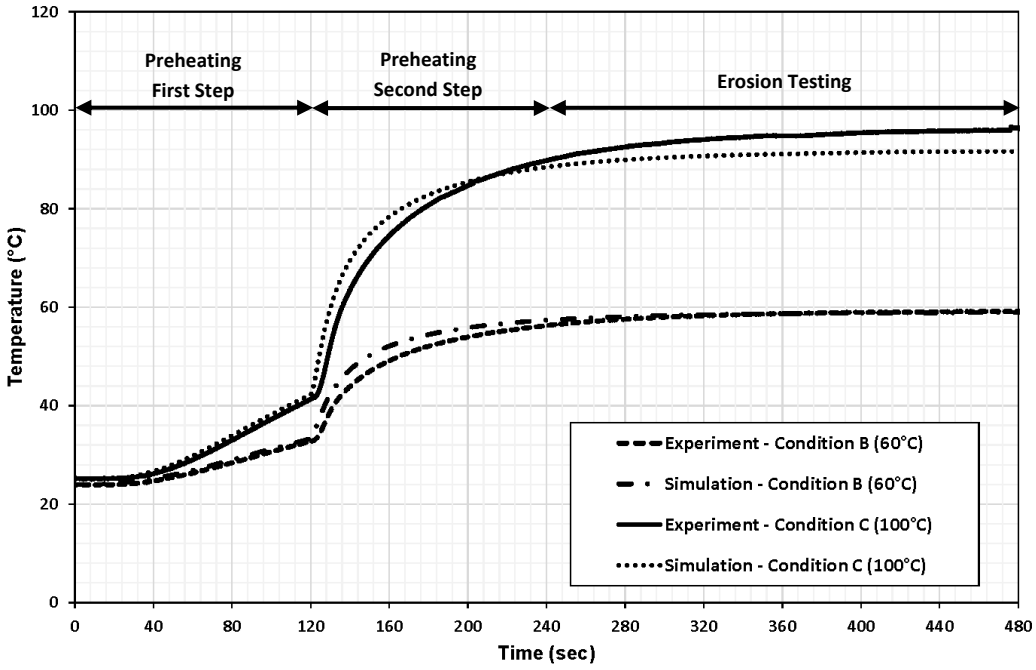


Figure 4-7 Transient temperature at 1.5 mm below the surface of the PU sample - Experiment and model

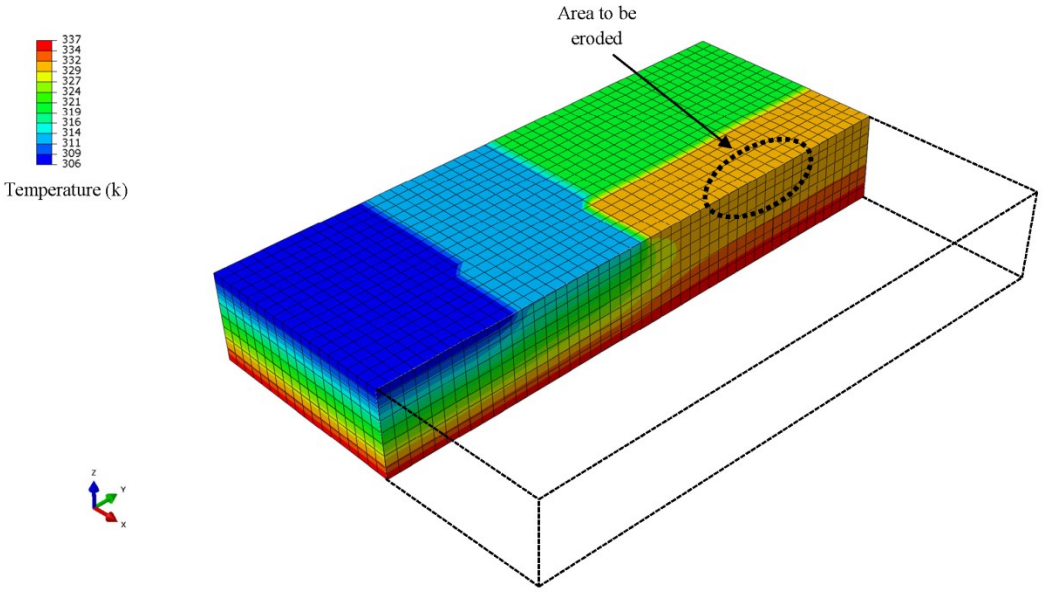


(a)

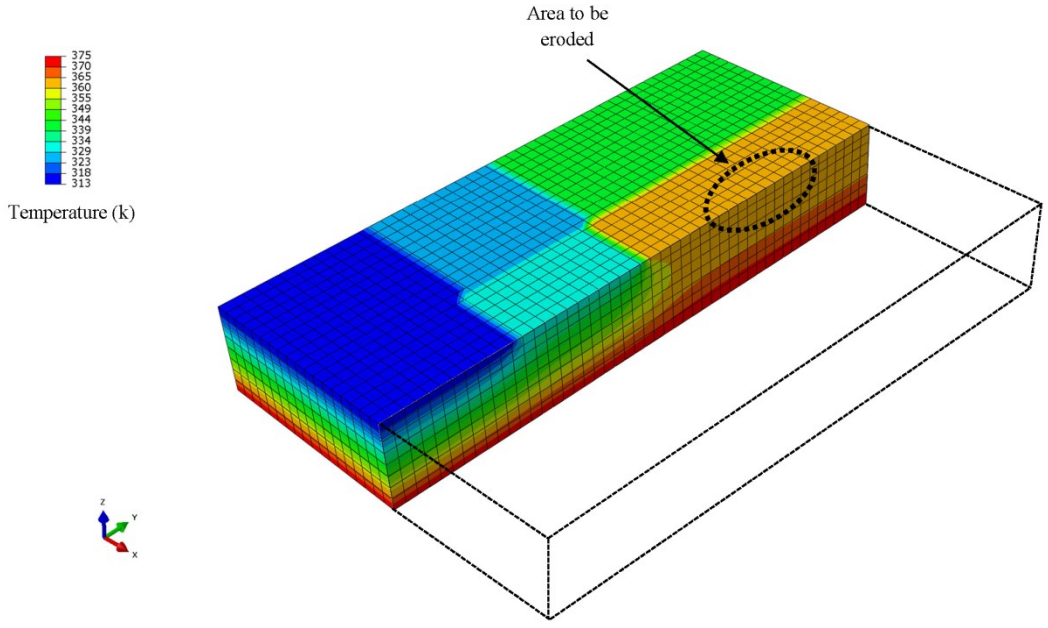


(b)

Figure 4-8 Temperature distribution within PU samples for a) condition B (60ºC) and b) condition C (100ºC) test procedures after preheating and before the erosion tests

### 4.4.3 Erosion Rates of Polyurethane at the Set Temperatures

Table 4-5 summarizes the measured glass transition temperatures of the PU elastomers that were studied. As can be seen, all the PU elastomers were in their rubbery phase at room temperature (25ºC). The erosion resistance of the PU elastomers was evaluated at 25ºC and at other elevated temperatures that are presented in Table 4-2. Figure 4-9 shows the non-dimensional erosion rate for the four types of PU elastomers that were tested at the various temperatures. The erosion rate of 1200-55A and 1200-85A PU elastomers increased continuously from 0.016 to 0.069 mg/g and 0.036 to 0.086 mg/g, respectively, within the range of 25ºC to 100ºC. On the other hand, for the 3000 PU series, 3000-85A and 3000M-85A the trend was different, and an initial improvement of wear resistance, as evidenced by the decrease in erosion rate (see Fig. 4-9), occurred up to 60°C. The erosion rate increased beyond 60°C for all the PU elastomers that were investigated. The results shown in Fig. 4-9 indicate that even with variation of temperature within the range of 20ºC to 60°C, significant changes in erosion resistance of the PU elastomers can occur. The fact that the changes in wear resistance of the PU elastomers that were studied were not similar as the PU temperature was varied emphasizes the influence of the PU temperature on its wear resistance.

Table 4-5 Commercial name and glass transition temperature of PU elastomers

| PU commercial name | Glass transition temperature |
|---|---|
| RoPlasthan-1200-55A | -24°C |
| RoPlasthan-1200-85A | -19°C |
| RoCoat-3000-85A | -6°C |
| RoCoat-3000M-85A | 10°C |

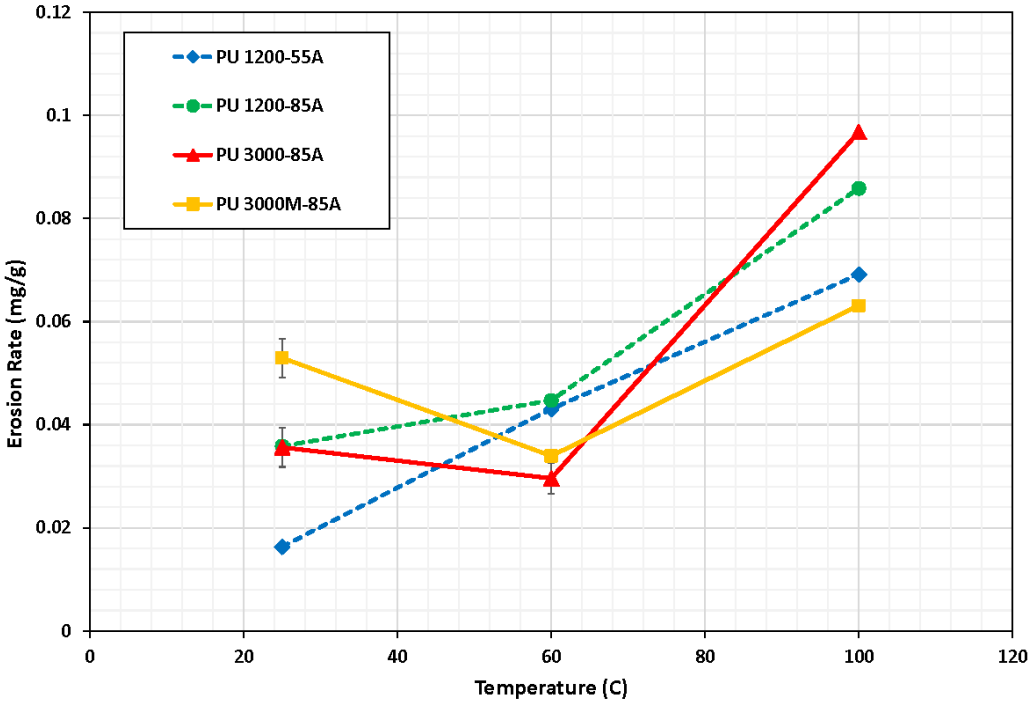


Figure 4-9 Erosion rate as a function of PU temperature

In order to explain the trends observed in Fig. 4-9, tensile tests and cyclic loadings were conducted. The stress-strain curves obtained from these experiments were used to study the alterations in mechanical properties of PU as a result of temperature rise and its corresponding influence on the wear resistance. Figure 4-10 shows the stress-strain curves obtained from tensile

tests of PU elastomers at room and elevated temperatures for strains up to 350%. It should be noted that all stresses and strains in this Chapter represent the nominal stress and strain values. The graph indicates that all the PU elastomers became softer with increasing temperature. This softening was a result of crosslinking disruption and breakage of some hydrogen bonds at higher temperatures and reduction in crosslinking of the polymer structure [118]. A comparison of Figs. 4-9 and 4-10 shows that the softness of the PU elastomer is not the only factor that affects the erosion rate. Although the 1200-55A PU grade is the softest elastomer, the 3000M-85A and 3000-85A elastomers have lower erosion rates at 60ºC. This suggests that another parameter, other than the softness of the PU, has affected the elastomer wear resistance. The data obtained from tensile tests were also used to calculate the ultimate strength and elongation at break of the PU elastomers that failed at strains lower than 350%. Table 4-6 summarizes the measured values of ultimate stress and elongation at break of the tested PU elastomers. The fact that the 3000 PU series have lower elongation at break and lower failure stresses at 60ºC compared to those of the 1200 series suggests that although the final elongation at break and softness may have an impact on the final erosion resistance of the elastomers, they are not the only parameters that affect their wear performance.

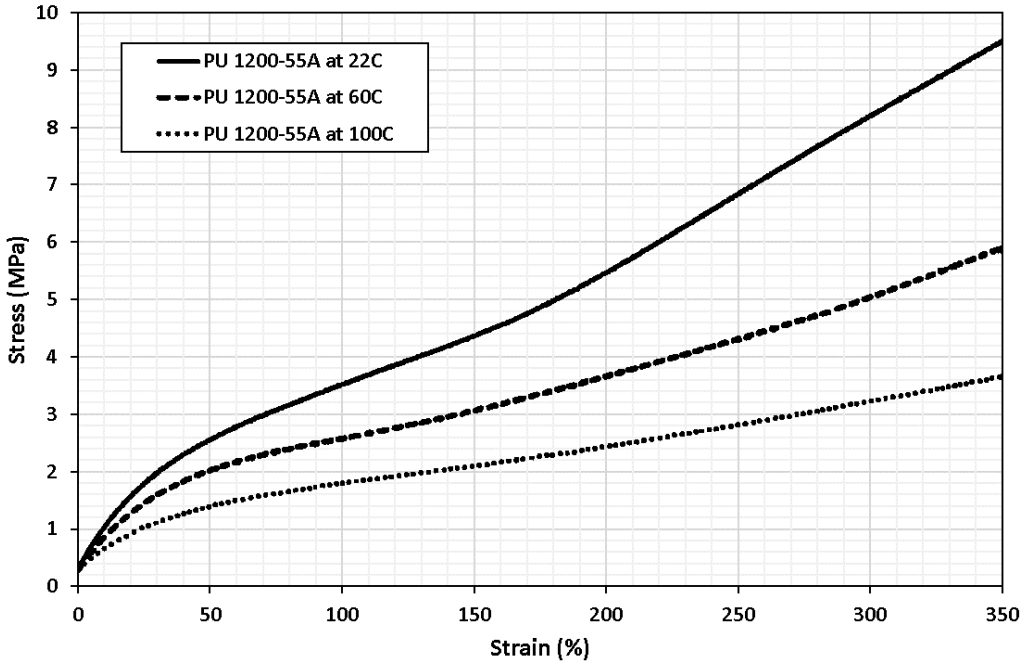
PU 1200-55A at 22C
PU 1200-55A at 60C
PU 1200-55A at 100C
Stress (MPa)
Strain (%)
0
1
2
3
4
5
6
7
8
9
10
0
50
100
150
200
250
300
350

(a)

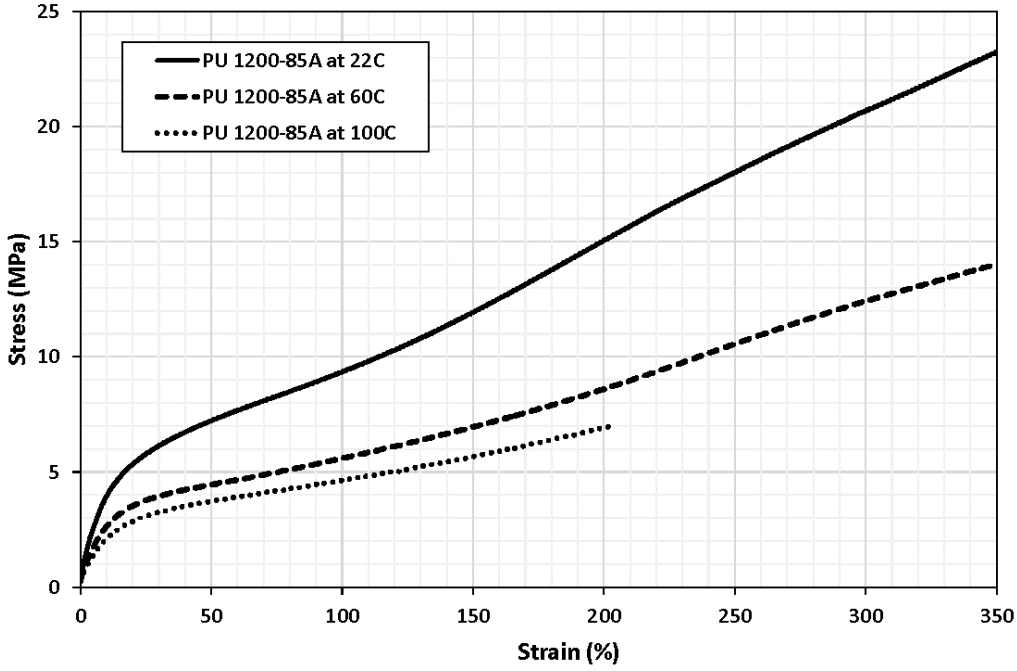
PU 1200-85A at 22C
PU 1200-85A at 60C
PU 1200-85A at 100C
Stress (MPa)
Strain (%)
0
5
10
15
20
25
0
50
100
150
200
250
300
350

(b)

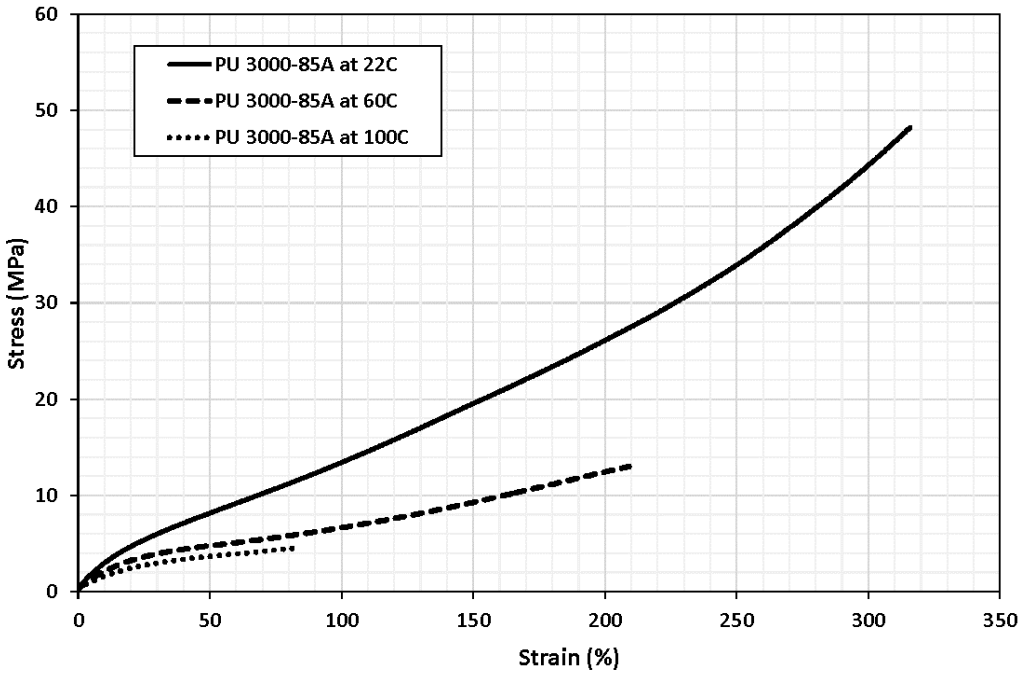


(c)

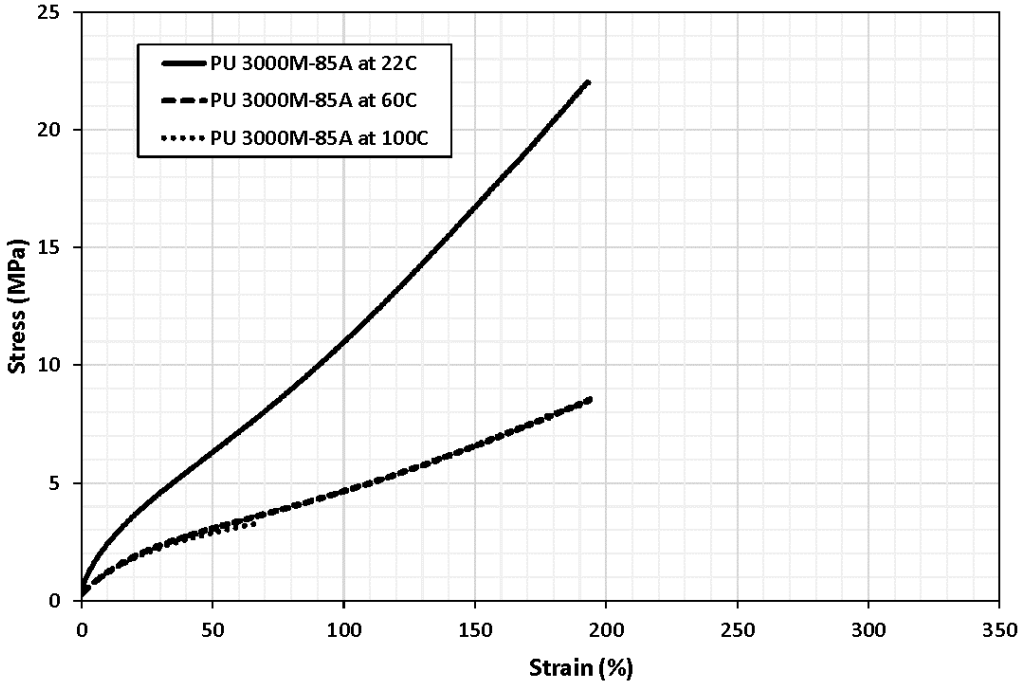


(d)

Figure 4-10 Stress-strain curves obtained at various test temperatures for elongation up to 350% for a) 1200-55A, b) 1200-85A, c) 3000-85A, and d) 3000M-85A PU elastomers

Table 4-6 Nominal stress and strain failure data of PU elastomers up to a nominal strain of 350%

| Temperature / PU type | 25°C | | 60°C | | 100°C | |
|---|---|---|---|---|---|---|
| | Ultimate stress (MPa) | Elongation at break (%) | Ultimate stress (MPa) | Elongation at break (%) | Ultimate stress (MPa) | Elongation at break (%) |
| 1200-55A | NA | NA | NA | NA | NA | NA |
| 1200-85A | NA | NA | NA | NA | 6.4 ± 0.5 ($n$ = 3) | 188 ± 16 ($n$ = 3) |
| 3000-85A | 44.7 ± 3.4 ($n$ = 3) | 304 ± 12 ($n$ = 3) | 13.9 ± 1.8 ($n$ = 3) | 225 ± 30 ($n$ = 3) | 4.2 ± 0.2 ($n$ = 3) | 77 ± 6 ($n$ = 3) |
| 3000M-85A | 24.7 ± 3.0 ($n$ = 3) | 210 ± 18 ($n$ = 3) | 8.8 ± 1.0 ($n$ = 3) | 200 ± 11 ($n$ = 3) | 3.1 ± 0.1 ($n$ = 3) | 58 ± 7 ($n$ = 3) |

Most polymer-based materials, including PU elastomers, experience plastic deformation alongside with elastic behavior upon deformation. This plastic deformation can contribute to the formation of a permanent set (residual strain) upon unloading. The plastic deformation in PU elastomers is a result of the irreversible breakage-disruption of the chemical structure and changes in the orientation of the hard-soft phase [118]. The load induced by the impact of erodant particles during the erosion process is similar to repeated loading-unloading cycles. Consequently, the evaluation of the PU behavior during cyclic loadings can provide important information about the ability of the material to regain its initial condition. Figure 4-11 shows the stress-strain curves of the initial loading-unloading cycle of the PU elastomers that were studied. Qualitatively, for all tests, the PU material became softer and the hysteresis loop decreased at

higher temperatures. However, for the case of the 3000 PU series and, in particular, 3000M-85A, the PU exhibited extensively different behavior; the permanent set and hysteresis loop became smaller as the temperature increased (see Fig. 4-11d). On the other hand, for the 1200-55A and 1200-85A PU samples, the permanent set and material behavior did not greatly vary by increasing the temperature. To obtain a quantitative evaluation of the effect of temperature on the residual strain of PU, the residual strain of at least three samples during a loading-unloading cycle was measured as presented in Table 4-7. The graph shows that the maximum reduction in permanent set occurred in the 3000M-85A and 3000-85A PU. A comparison of the permanent set data shown in Table 4-7 with the erosion results at various temperatures in Fig. 4-9 reveals that there is a relation between the ability of the material to regain its initial condition and the erosion resistance. 3000M-85A and 3000-85A PU elastomers that experienced a reduction in permanent set by increasing the temperature from 25ºC to 60ºC exhibited improved wear resistance at 60ºC (see Fig. 4-9). This behavior is most probably due to the fact that for conditions and PU in which lower permanent set occurred, a higher number of impacts is needed in order to deform the surface up to the threshold strain for final detachment of fragments of material from the surface. On the other hand, at the set temperature of 100°C, although the permanent set tends to decrease further, the significant reduction in material strength (see Table 4-6) has adversely affected the erosion resistance of the PU elastomers.

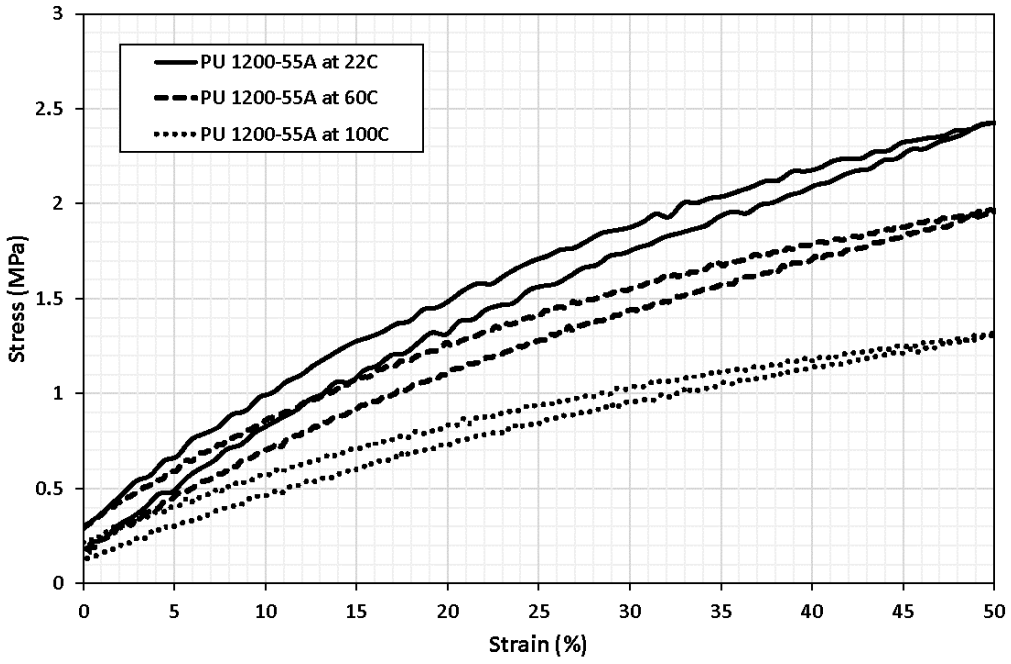
PU 1200-55A at 22C
PU 1200-55A at 60C
PU 1200-55A at 100C
Stress (MPa)
Strain (%)
0
0.5
1
1.5
2
2.5
3
0
5
10
15
20
25
30
35
40
45
50

(a)

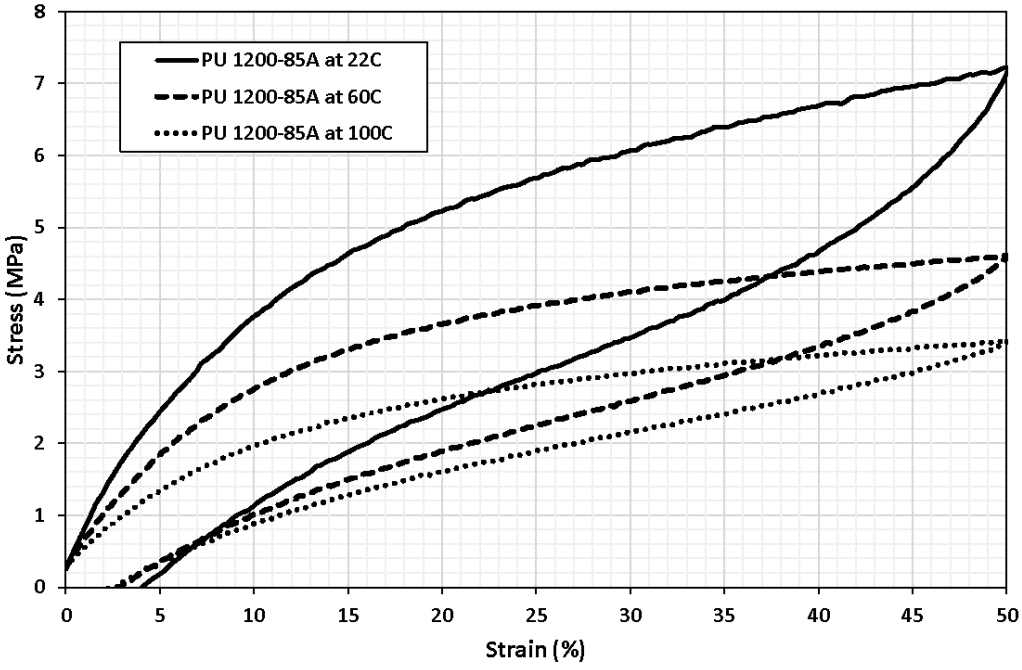
PU 1200-85A at 22C
PU 1200-85A at 60C
PU 1200-85A at 100C
Stress (MPa)
Strain (%)
0
1
2
3
4
5
6
7
8
0
5
10
15
20
25
30
35
40
45
50

(b)

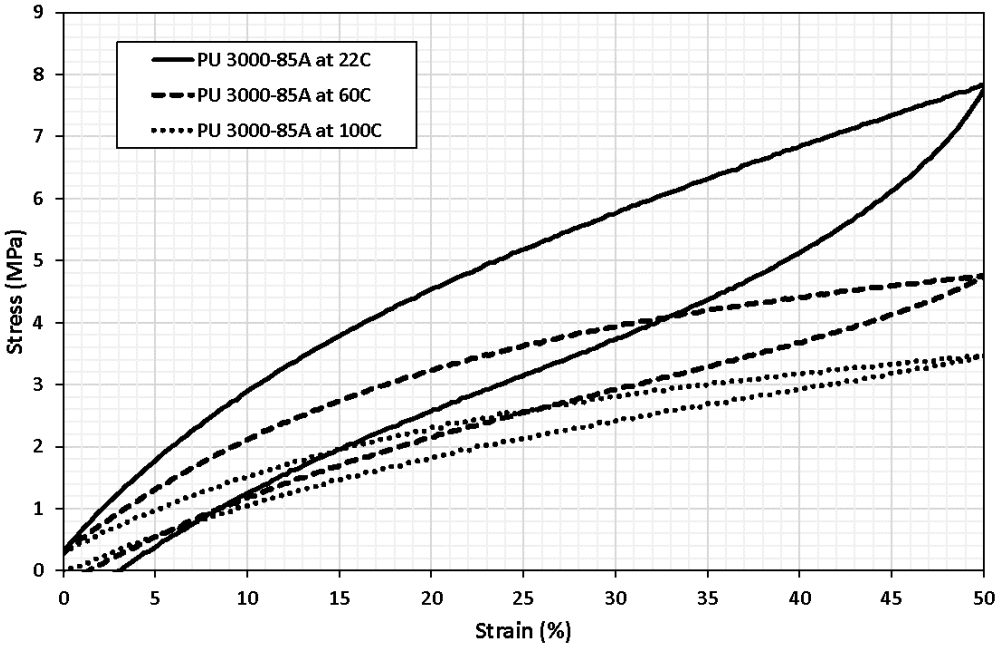


(c)

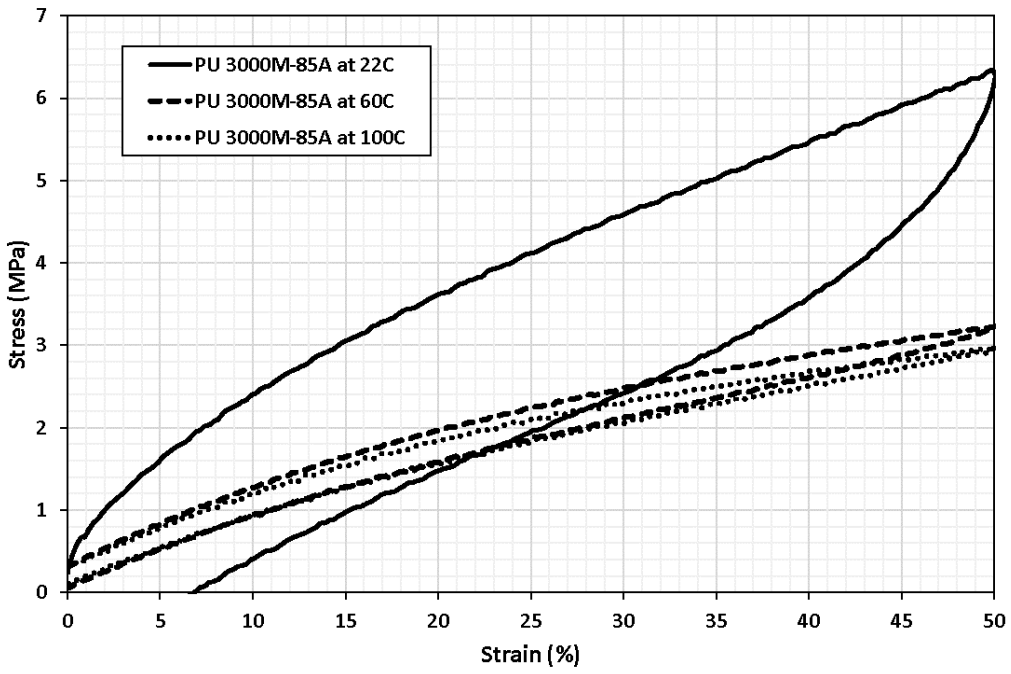


(d)

Figure 4-11 First cycle of loading-unloading at various temperatures for elongation up to 50% for a) 1200-55A, b) 1200-85A, c) 3000-85A, and d) 3000M-85A PU elastomers

Table 4-7 Permanent set of PU elastomers after loading up to 50% nominal strain at various temperatures

| Temperature / PU type | 25°C | 60°C | 100°C |
|---|---|---|---|
| | Permanent set (%) | Permanent set (%) | Permanent set (%) |
| 1200-55A | Less than 0.1% ($n$ = 4) | Less than 0.1% ($n$ = 4) | Less than 0.1% ($n$ = 4) |
| 1200-85A | 4.2 ± 0.1 ($n$ = 3) | 2.9 ± 0.1 ($n$ = 3) | 2.4 ± 0.4 ($n$ = 3) |
| 3000-85A | 3.1 ± 0.1 ($n$ = 3) | 1.4 ± 0 ($n$ = 3) | 0.2 ± 0.2 ($n$ = 4) |
| 3000M-85A | 7.1 ± 0.7 ($n$ = 4) | Less than 0.1% ($n$ = 3) | Less than 0.1% ($n$ = 4) |

In PU elastomers, plastic deformation as a result of irreversible breakage of some crosslinks can occur upon initial loading. Thus, during the first loading cycle, the PU exhibits higher strength to deformation ratio while on the second loading the material will already be permanently deformed due to the damage induced in the microstructure of the PU during the first loading. Evaluation of the second loading cycle of the PU elastomers that were studied (see Fig. 4-12) revealed that irrespective of the residual strain of the material after the first cycle, the PU elastomers became softer and exhibited stress softening. The evaluation of subsequent loading-unloading cycles showed that the material behavior remained similar to that of the second loading cycle given that the irreversible changes occur mostly during the first loading cycle [118]. Thus, the larger difference between the curves that are representative of the stress-strain curve of the first and second loading cycles for a given strain level is representative of greater irreversible damage. This means that the stress softening that occurred would result in the higher strains upon impact of subsequent particles with similar impact force during the

erosion process. Consequently, the level of stress softening of PU can have a direct impact on the erosion resistance of the PU. In fact, the impact of previous erodant particles would weaken the target material by introducing permanent damage into the mechanical structure of the elastomer.

To evaluate qualitatively the level of stress-softening of the PU elastomers that were studied, a parameter known as Mullins factor was calculated [118]. The Mullins factor provides information about how much the second loading deviates from the first loading in terms of hyperelastic response, which is defined as [118]:

$$\text{Mullins factor} = 1 - \frac{\text{Energy loss of second load} - \text{unload cycle}}{\text{work required to extend the PU to the desired strain}}. \quad (4\text{-}18)$$

The energy loss of the second load-unload cycle and the work required to deform the PU to the desired strain are equivalent to the area under the hysteresis loop of the second cycle and the area below the loading curve of the first cycle in the stress-strain curves, respectively. The closer the Mullins factor is to unity, the closer the PU elastomer is to an ideal Mullins response, that is, the reloading stress-strain is closer to the previous unloading path [118]. In this study, numerical integration was employed to calculate the area below the stress-strain curve for determination of the Mullins factor. Figure 4-13 shows the calculated Mullins factor for PU elastomers at the set temperatures. As can be seen, the Mullins factor remained almost unchanged for the 1200-55A PU or increased with temperature for all the other PU elastomers that were studied. The rate of increase of the Mullins factor for the 3000-85A and 3000M-85A PU elastomers was higher from 25ºC to 60ºC. A Mullins factor value that was closer to unity indicates that more damage will be introduced to the PU upon impact of each erodant particles. A comparison of Fig. 4-13 with that of erosion rates of the PU elastomers at various temperatures (see Fig. 4-9)

suggests that the decrease in the erosion rate of 3000-85A and 3000M-85A PU at 60°C is related to the softness and lower plastic deformation (see Table 4-7) of these elastomers at 60°C.

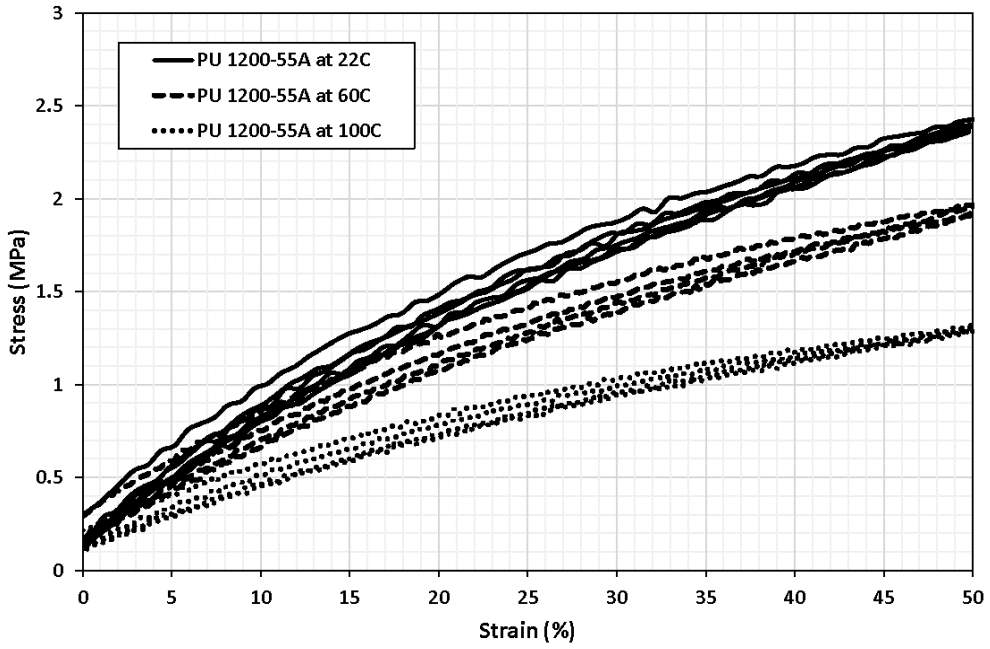


(a)

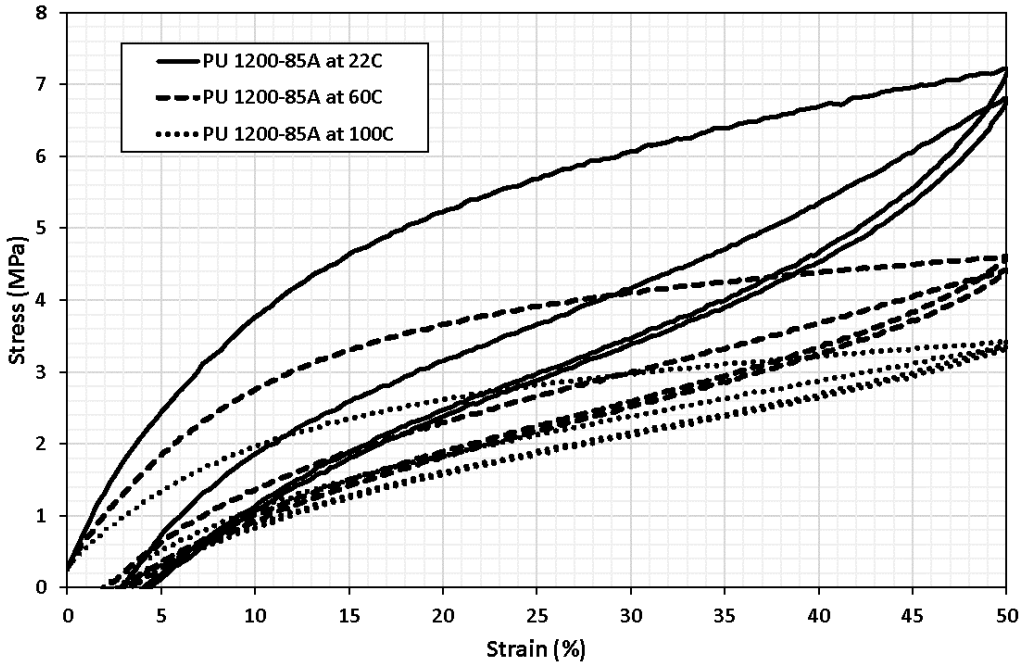


(b)

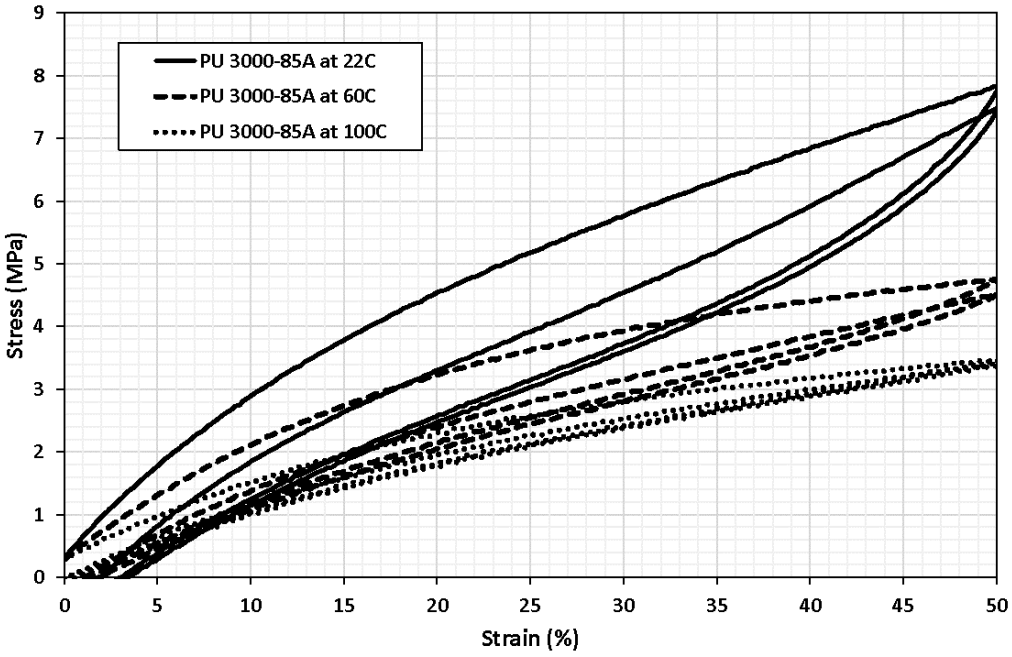


(c)

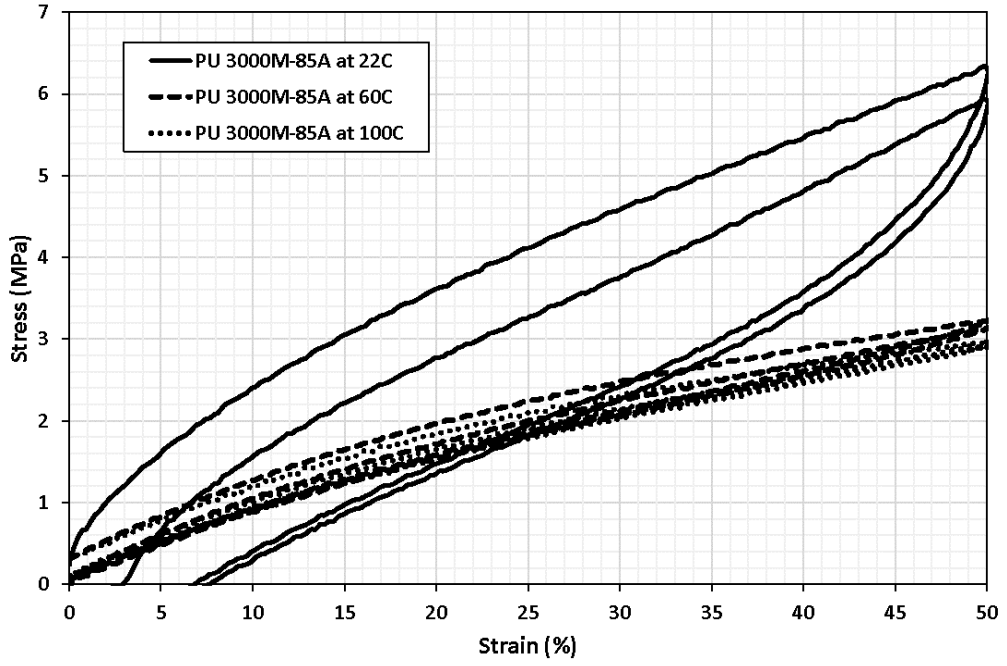


(d)

Figure 4-12 First and second cycles of loading-unloading at various temperatures for elongations up to 50% for a) 1200-55A, b) 1200-85A, c) 3000-85A, and d) 3000M-85A PU elastomers

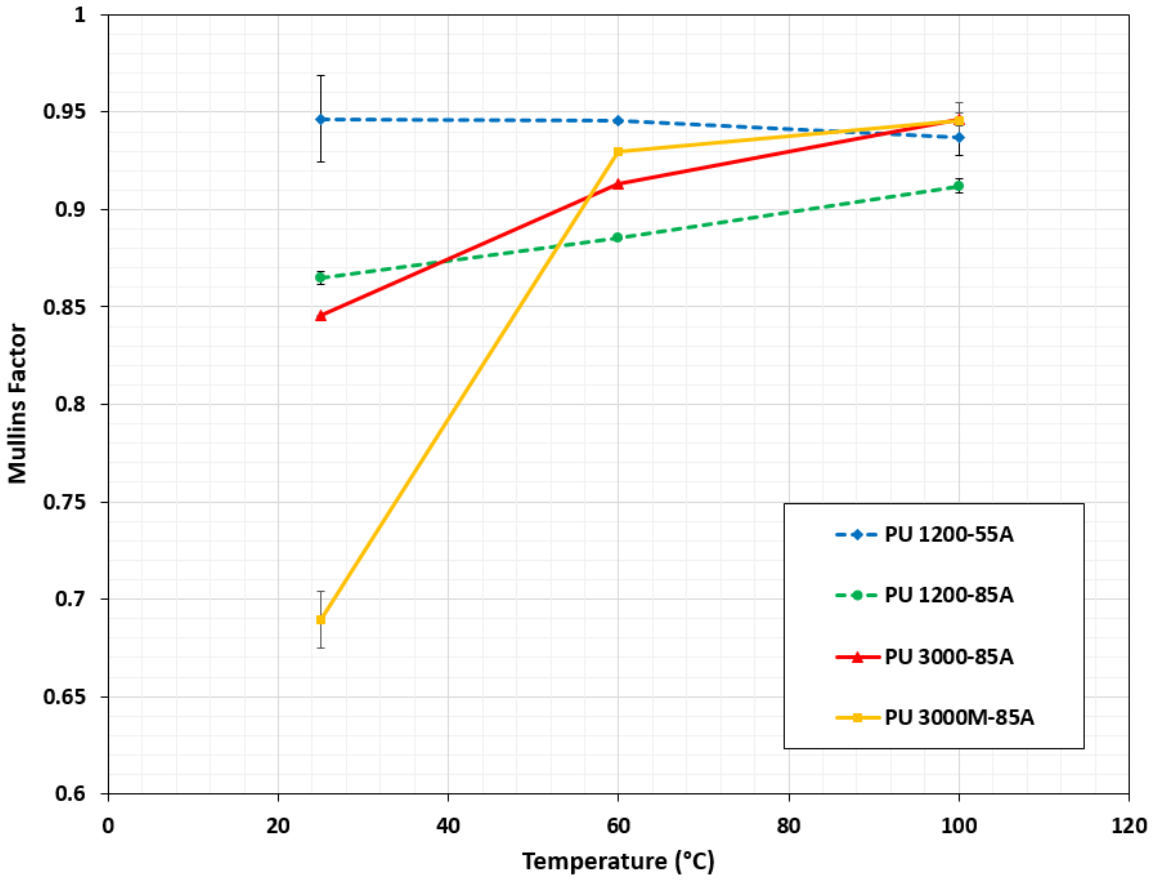


Figure 4-13 Mullins factor of PU elastomers as a function of temperature

### 4.4.4 Evaluation of the Worn Surfaces

The erosion mechanism of elastomers is a function of the wear testing procedure (erosion or abrasion), properties of abrasive media, erodant velocity and mechanical properties of the target material. The wear mechanisms that have been suggested for elastomers are:

a) The formation of cracks below the worn surface due to the tensile, compressive, and shear stresses caused by the impact of particles and final detachment of fragments as a result of the intersection and extension of the formed cracks [7, 11, 14,119];

b) The formation of asperities by plastic deformation to produce ridges perpendicular to the direction of impact and final fracture of the deformed asperities [9, 81-83, 86, 120, 121]; and

c) Random scratches and gouges on worn surfaces due to the cutting and gouging by grit media [81, 122].

Evaluation of the eroded surfaces of PU elastomers suggested that the main erosion mechanism was plastic deformation of the surface and the development of asperities and ridges perpendicular to the direction of impact. Figure 4-14 shows the surface of 1200-55A PU elastomer samples that were eroded at room and elevated temperature. In the PU sample that was held at 25ºC (see Fig. 4-14a), the worn surface showed deformed asperities while at elevated temperatures, where the erosion rate was higher, ridges perpendicular to the impact direction were formed (see Fig. 4-14b and c). A similar behavior was observed for the 1200-85A PU: single asperities emerged at 25ºC and ridges developed perpendicular to the impact direction at elevated temperatures. Although the mechanism of formation of these ridges and subsequent erosion as a result of detachment of these ridges have been discussed in previous studies [9, 83, 120], side view images that can distinctly show the morphology of these ridges are limited. To that end, SEM images were captured for the condition that the PU sample was slightly angled with respect to the SEM detector. These images are shown in Fig. 4-15a, which shows that the asperities that protrude from the surface were formed against the impact direction of the erodant particles (shown by an arrow). The asperities were generated as a result of plastic strain induced by particle impact. The accumulation of strain due to subsequent impact led to the deformation of the asperities to values such that cracks were formed on the bottom of the asperities, followed by the final detachment of the material. A typical crack produced on the base of one of these asperities is indicated in Fig. 4-15a by a circle. On the other hand, the partially detached, but stretched material shown in Fig. 4-15b (marked by circles) provides further support for the proposed erosion mechanism and the importance of elongation at break on the erosion resistance

of PU caused by solid particle impact. In PU elastomers with lower ultimate strength and elongation at break, the deformed asperities on the target surface detached easier from the surface that would lead to higher mass loss and, therefore, higher erosion rate.

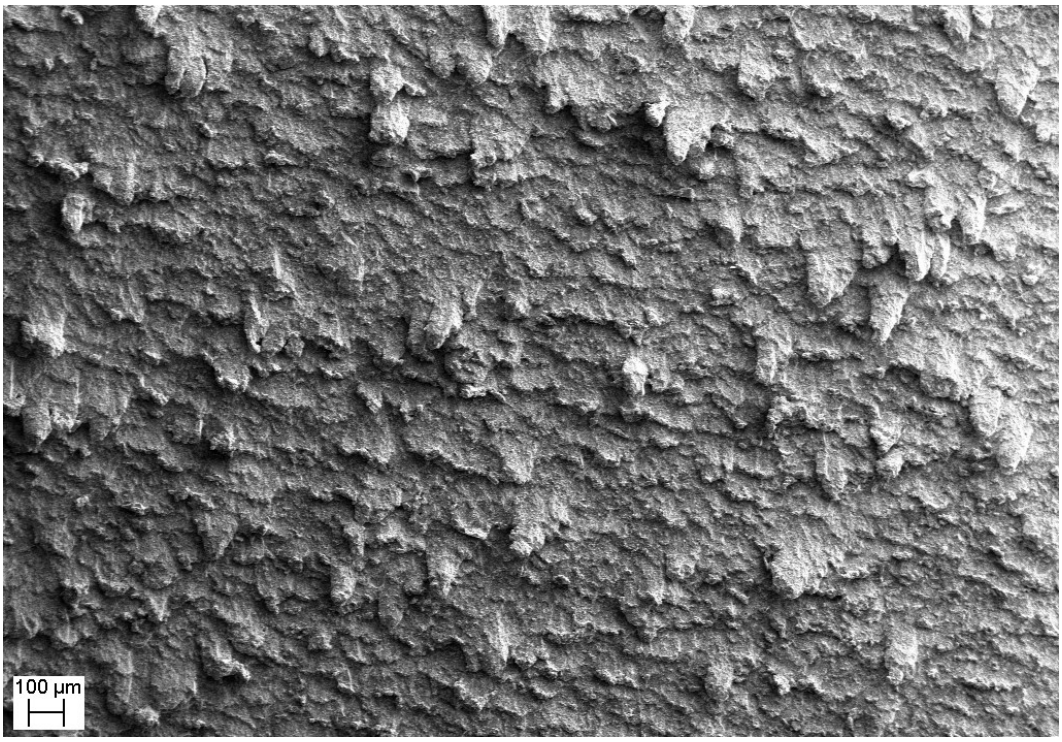


(a)

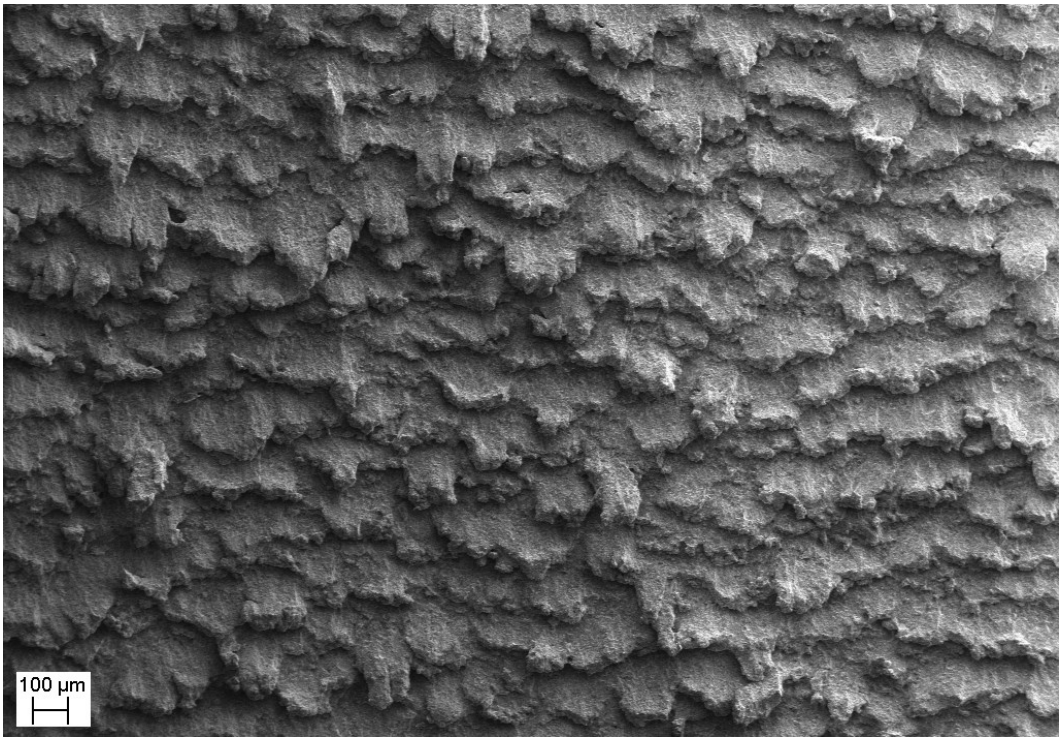


(b)

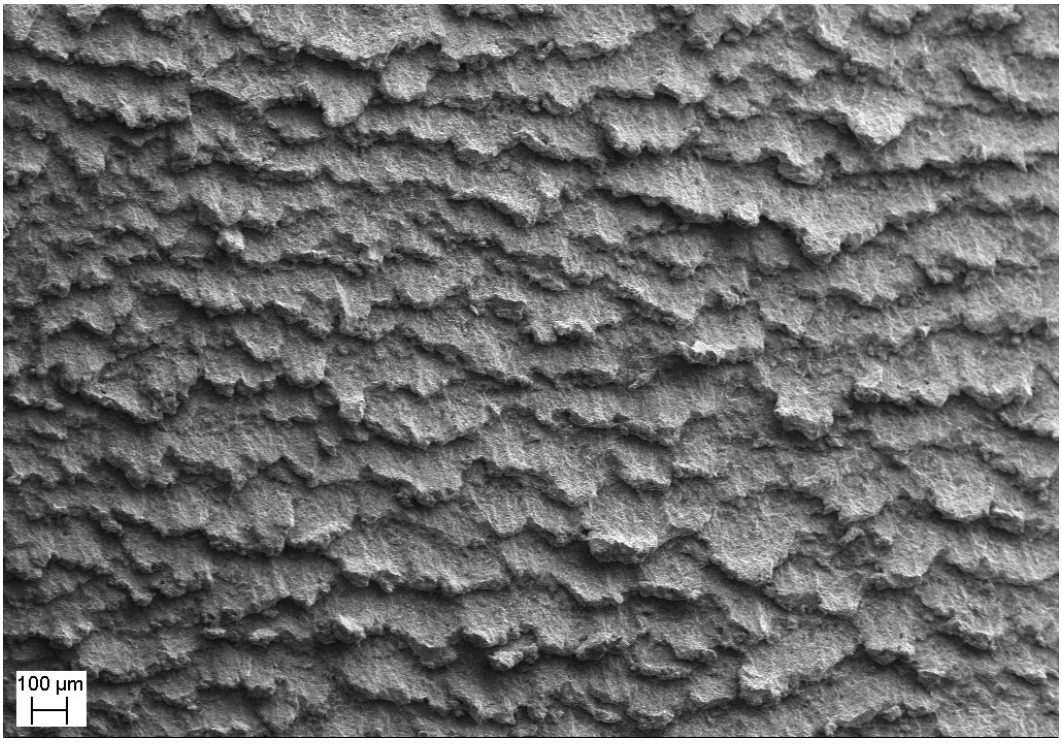


(c)

Figure 4-14 SEM images of eroded 1200-55A PU surface at a) 25ºC, b) 60ºC, and c) 100ºC

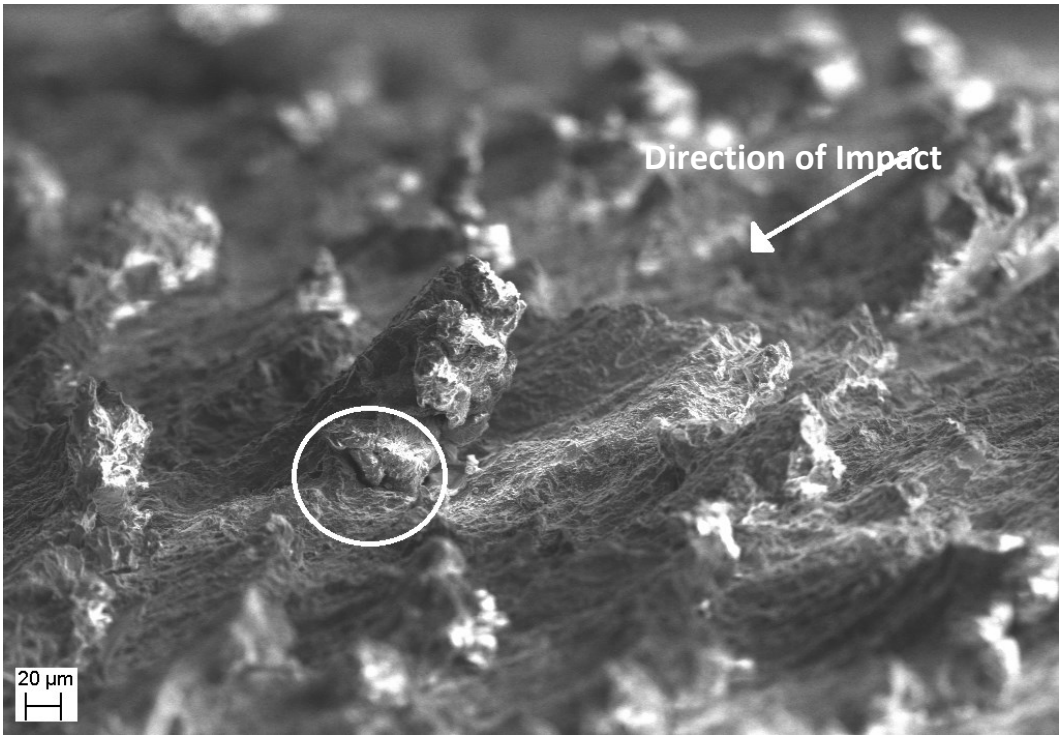


(a)

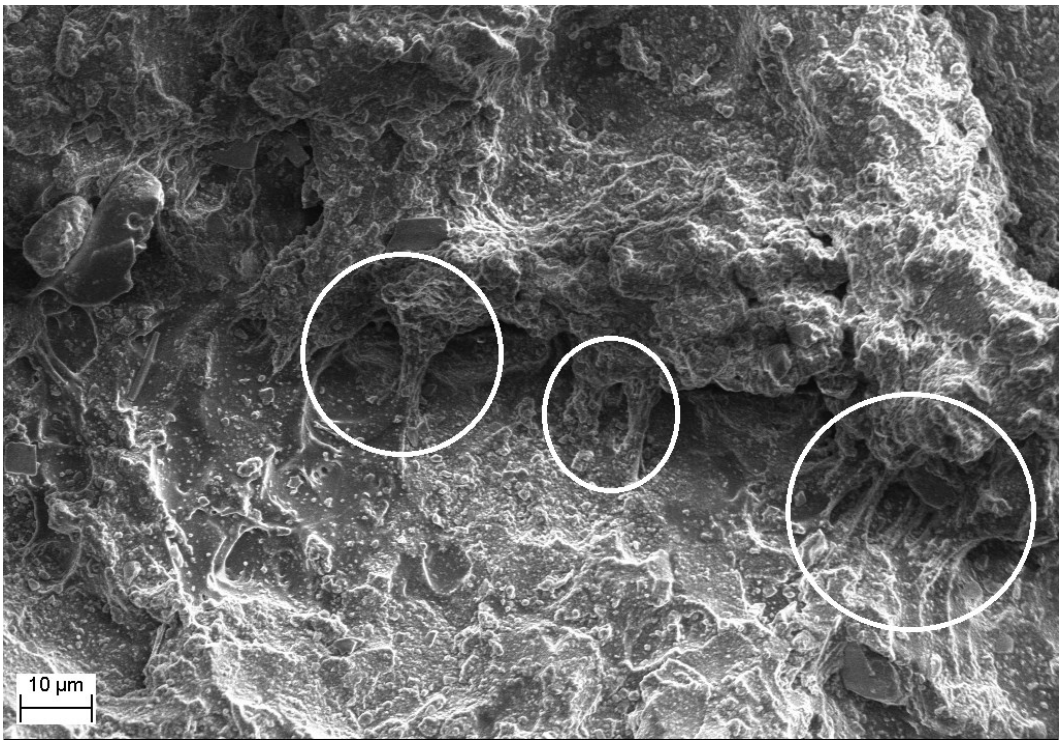


(b)

Figure 4-15 SEM images of eroded 1200-55A PU surfaces tested at 60ºC: a) side and b) top view

The morphology of the eroded surfaces of 3000-85A (see Fig. 4-16) and 3000M-85A PU (see Fig. 4-17) was slightly different from that observed in Fig. 4-14. The asperities that were formed on the 3000 series PU were smaller in size and the ridges were not as continuous and as large as the ones formed on the 1200-55A and 1200-85A PU elastomers. This behavior was due to the smaller elongation at break of the 3000 series (see Table 4-6) which led to the detachment of asperities at lower strain. Thus, the asperities have detached from the surface before extending to large strain values as was observed for the 1200 series PU (see Fig. 4-14). In addition, in contrast to the 1200 series PU, the surface morphology of the 3000 series PU that was tested at 100ºC was different from those samples that were tested at 25ºC and 60ºC. The asperities were smaller compared to those samples held at 25°C and 60°C, and continuous ridges were observed (see Figs. 4-16c and 4-17c). This behavior was most probably due to the significant reduction in elongation at break and ultimate strength of the 3000 series PU elastomers at 100ºC as was shown in Table 4-6. This behavior suggests that although there is no simple relation between elongation at break and the erosion rate, the surface topography and the wear resistance of the PU are dependent on the elongation at break. It should be noted that the spherical shape defects observed in Fig. 4-17 are cavities that were formed in the PU elastomer during its fabrication as a result of possible air entrapment and formation of gases during curing. Two of this typical spherical shape defects on the surface of PU are shown by arrows in Fig. 4-17a.

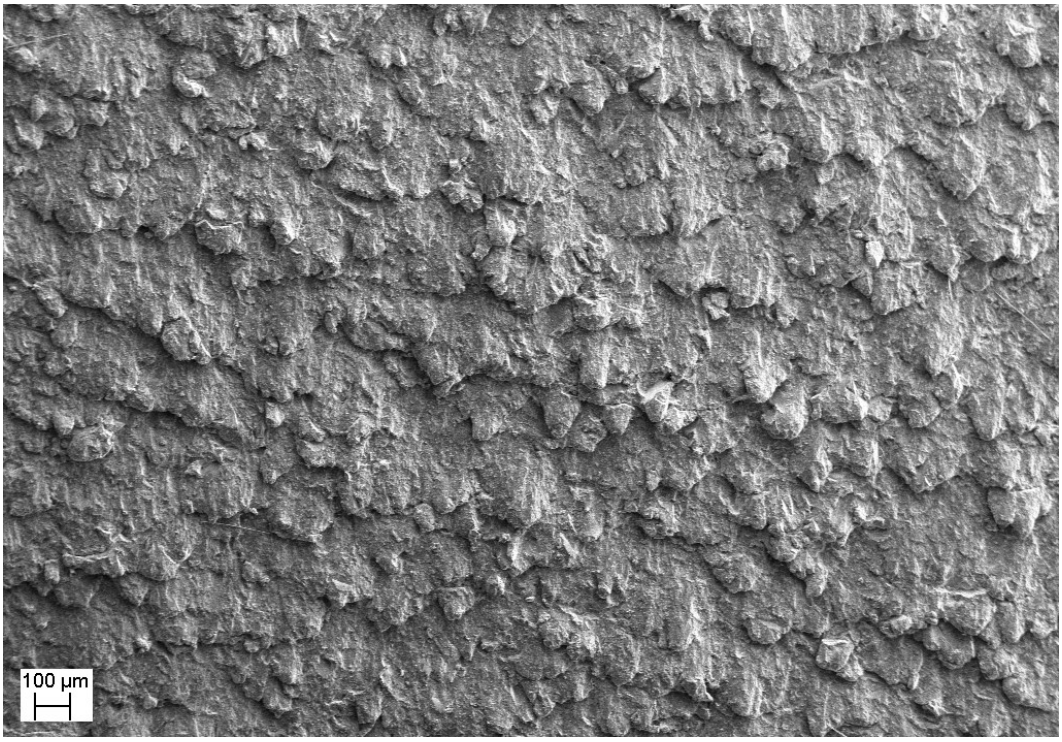


(a)

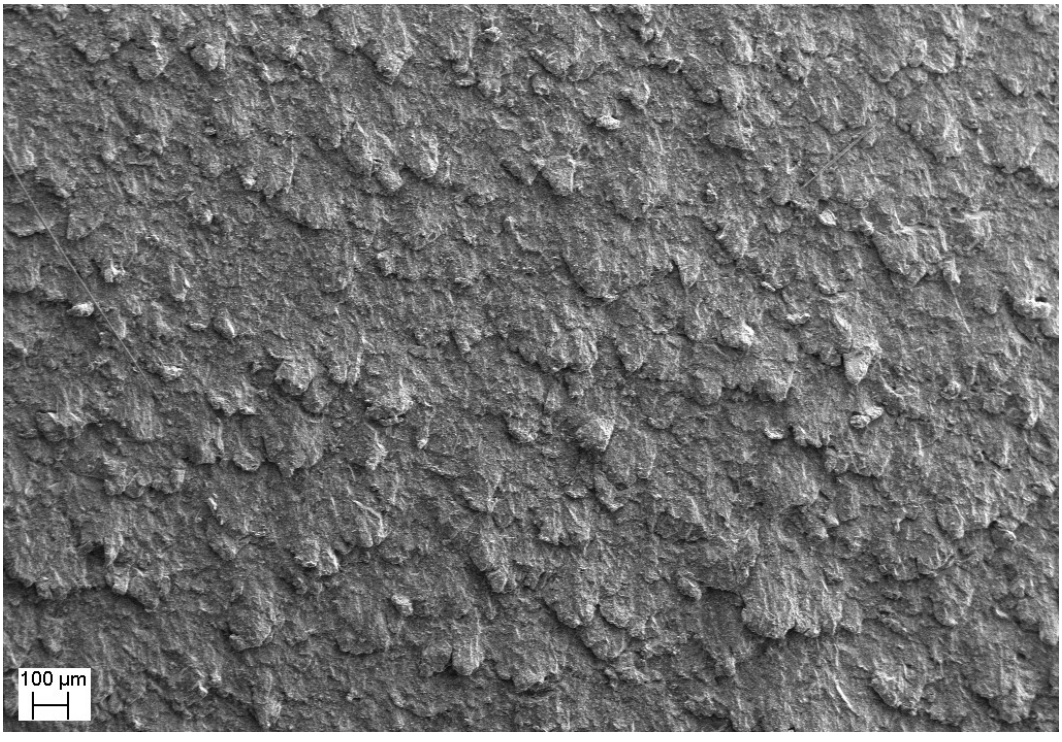


(b)

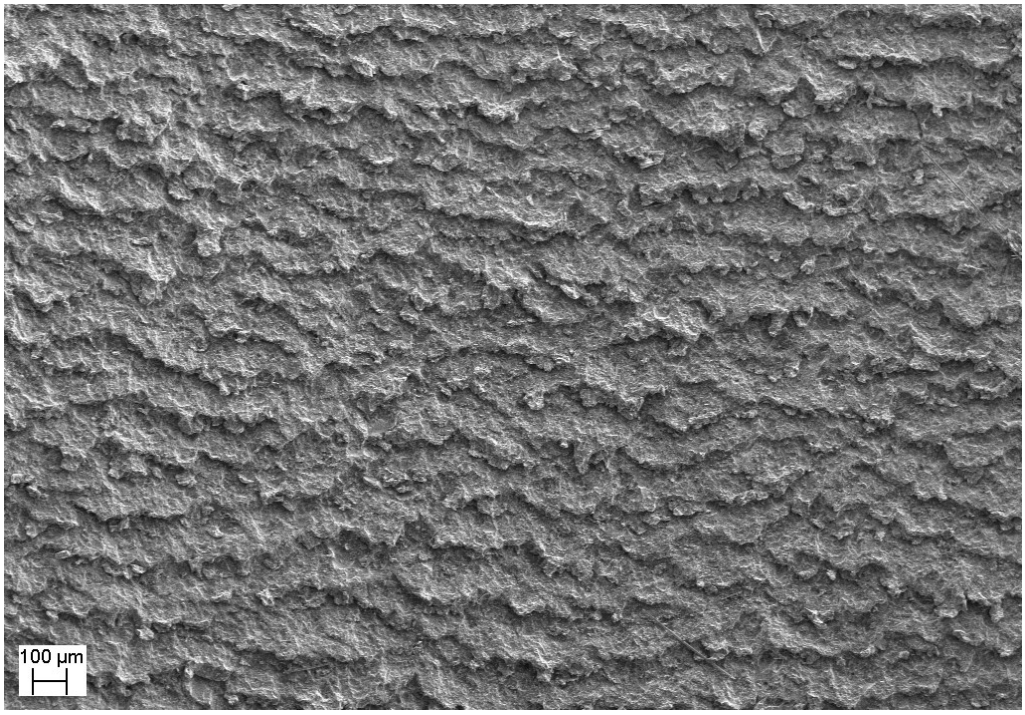


(c)

Figure 4-16 SEM images of the eroded 3000-85A PU surface at a) 25ºC, b) 60ºC, and c) 100ºC

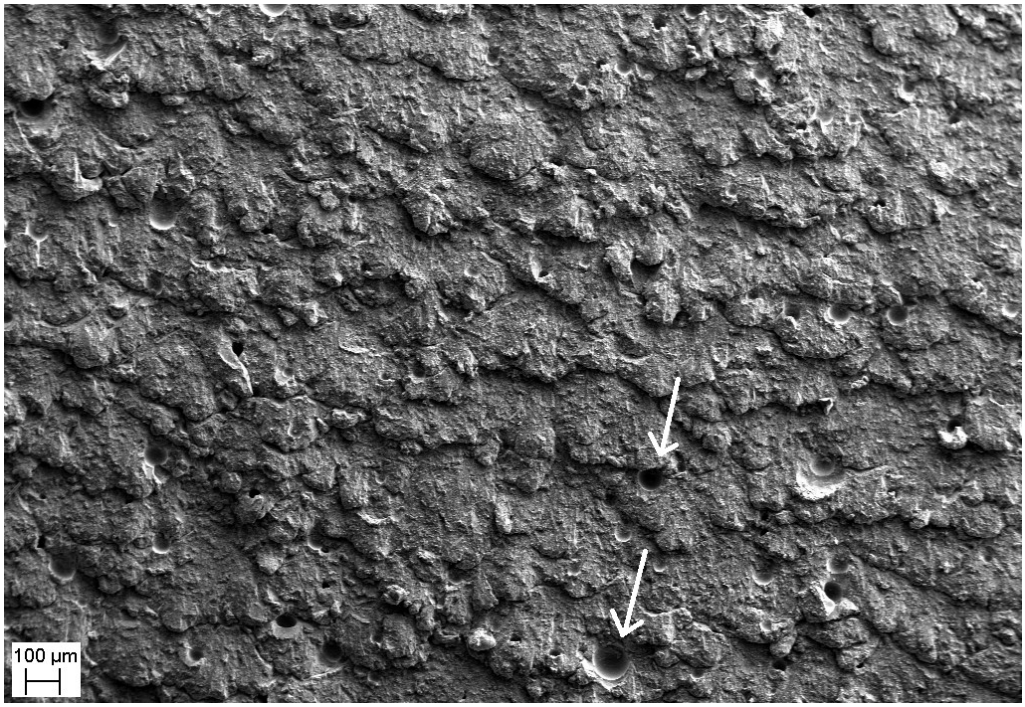


(a)

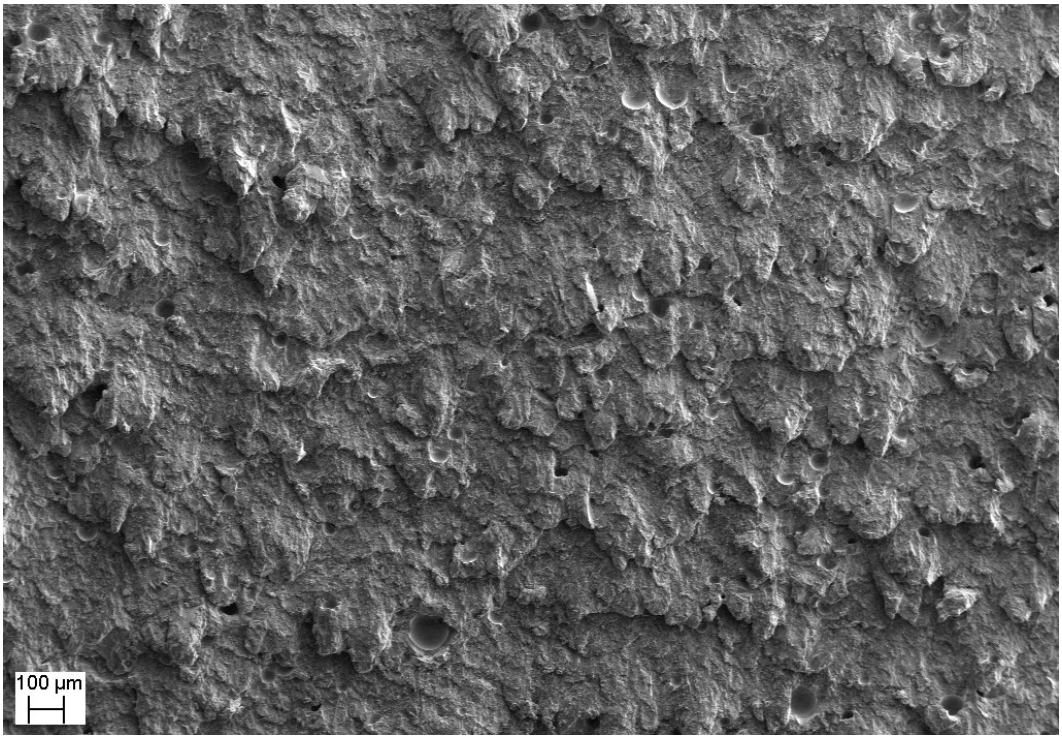


(b)

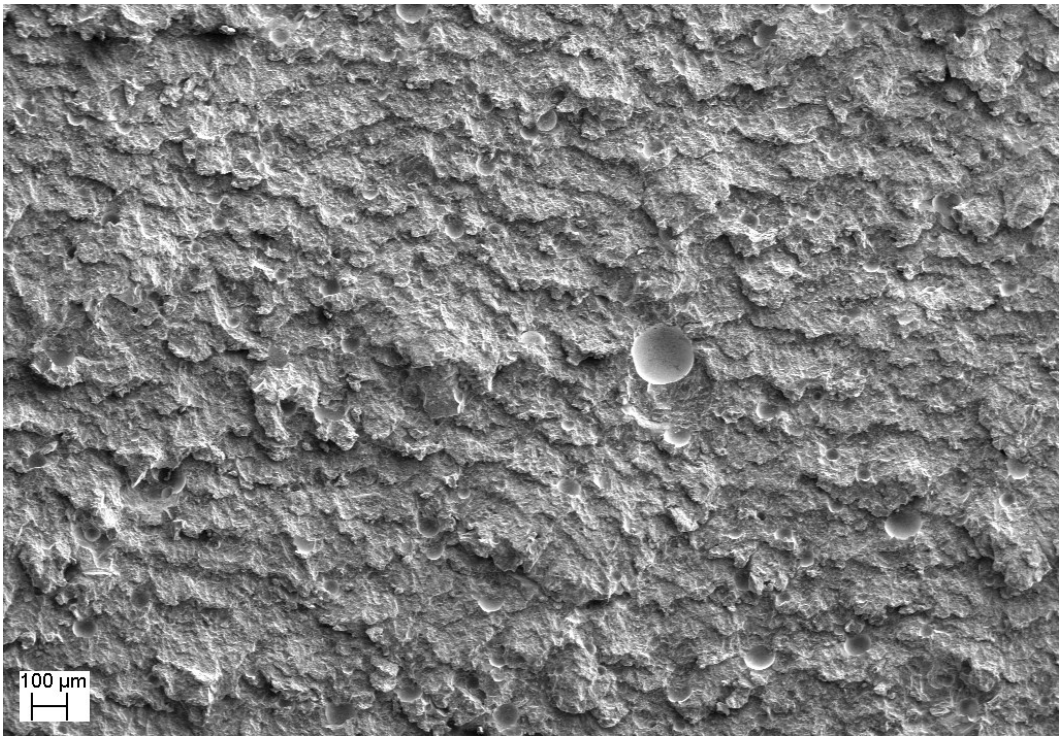


(c)

Figure 4-17 SEM images of the eroded 3000M-85A PU surface at a) 25ºC, b) 60ºC, and c) 100ºC

The evaluation of the erosion mechanism of the PU elastomers that were held at various temperatures and eroded, not only revealed how temperature affects the erosion mechanism, but close evaluation of the worn surfaces also provided further support of the aforementioned effect of the permanent set and elongation at break on the erosion resistance of PU elastomers. The 1200-55A PU exhibited the minimum erosion rate at 25ºC (see Fig. 4-9), which was due to its softness, high elongation at break (higher than 350%), and negligible permanent set upon deformation. In contrast, the 3000M-85A had the maximum permanent set and minimum elongation at break, which caused the 3000M-85A PU to possess the lowest erosion resistance at 25ºC. On the other hand, at the set temperature of 60ºC, the erosion resistance of the 1200 series PU decreased due to the reduction of PU strength as a result of an increase in test temperature. Although the same behavior negatively affected the 3000 PU series, a greater ability to regain an initial state after deformation (smaller residual strain) led to the improvement in erosion resistance at that temperature. Finally, at the test temperature of 100ºC, the erosion rate of the 3000 series greatly increased due to the significant reduction in ultimate stress and elongation at break of these PU elastomers. This reduction in ultimate stress and elongation at break could have allowed for removal of small fragments by gouging and cutting of the PU surface as a result of the impact of erodant particles. On the other hand, given that the permanent set of 3000M-85A at 100ºC was much smaller than the 3000-85A, its erosion resistance was not affected as severely as the 3000-85A PU. This behavior further emphasizes the importance of the ability of a material to regain its initial state (smaller permanent set) on the wear resistance of PU elastomers. It should be noted that the basis for the given discussion is only the relative comparison of the erosion resistance of the studied PU elastomers and how the wear behavior is affected by the test temperature. A more in-depth comparison of the erosion rate of the studied PU elastomers is not

possible given their differences in mechanical properties. To that end, FE model was developed for calculating the generated stresses as a result of impacting erodant particles. The determination of stresses will allow for a more comprehensive comparison and explanation of what was observed for the erosion behavior shown in Fig. 4-9. Details about development of the FE model and the obtained results are discussed in Chapter 5 of this thesis document.

# Chapter 5

# Development of a Finite Element Model to Study the Mechanism of Material Removal during the Erosion Process

A numerical model based on the finite element (FE) technique was developed to better understand the mechanism of material removal during solid particle impact of PU elastomers and to study the effect of erosion testing temperature on the produced stresses. The FE model simulated the impact of 10 erodant particles at a single location on the substrate elastomer at controlled temperatures of 22ºC, 60ºC, and 100ºC. Erosion testing experiments were conducted to provide data for verification of the model. The results obtained by the FE model showed that the ultimate strength and elongation at break have the most significant influence on the erosion rate at velocities higher than a certain threshold. Residual strain as a result of plastic deformation and stress softening caused by Mullins damage and PU softness were identified as other parameters that affect the erosion rate. Evaluation of the surface morphology of the worn samples showed that the model was capable of predicting the morphology of the asperities and they were similar to those observed in scanning electron microscope images. While the model allowed for an in-depth study of the wear mechanisms, the model failed to quantitatively predict the erosion rate, which is most probably due to the assumptions that were made to simplify the model.

Some sections of the work presented in this chapter will be submitted for publication in proceedings of the 21st International Conference on Wear of Materials, Long Beach, CA, USA, March 26-30, 2017.

## 5.1 Finite Element Simulation

The erosion caused by the impact of garnet sand particles on PU elastomers at different temperatures was modelled by the FE numerical technique to study the effect of testing temperature on the produced stresses and to better understand the mechanism of material removal during solid particle impact on PU elastomers. The FE model was developed utilizing a general purpose FE solver, Abaqus Version 6.13 [116]. Details regarding the simulation formulation, material model, contact algorithm, and model boundary conditions are presented in the following.

### 5.1.1 Finite Element Explicit Formulation

Erosion caused by solid particle impact is a high velocity dynamic phenomenon. To that end, a FE explicit dynamic formulation was employed in the simulation to ensure the convergence of the solution. The discretized equilibrium equation for the explicit dynamic formulation is [90]:

$$M\ddot{u} = F^{\text{Ext}} - F^{\text{Int}}, \tag{5-1}$$

where $M$ is the lumped (diagonal) mass matrix, $\ddot{u}$ is the nodal acceleration at each time step, $F^{\text{Ext}}$ is the externally applied force vector at each node, and $F^{\text{Int}}$ is the internal force vector as determined from the element stresses. The nodal acceleration at each time step was calculated as:

$$\ddot{u}_t = M_t^{-1}(F_t^{\text{Ext}} - F_t^{\text{Int}}). \tag{5-2}$$

The central difference explicit time integration method was used to calculate the displacement and velocity at each time step as [116]:

$$\dot{u}_{(t+\frac{1}{2})} = \dot{u}_{(t-\frac{1}{2})} + \frac{\Delta t_{(t+1)} + \Delta t_t}{2}\ddot{u}_t, \tag{5-3}$$

$$u_{(t+1)} = u_t + \Delta t_{(t+1)} \dot{u}_{(t+\frac{1}{2})} . \tag{5-4}$$

In the FE explicit formulation, the displacement, velocity, and acceleration of nodes are integrated and updated step-by-step through time [116]. In central difference method the solution may become unstable and diverge rapidly if incorrect time increment is chosen [116]. Thus, in order to ensure the convergence of the solution, the time increment is automatically determined by the Abaqus solver in each time step based on the material properties and minimum element size in the model. An initial approximation of the time increment is made by [116]

$$\Delta t = \frac{L_{\min}}{C_{\mathrm{d}}}, \tag{5-5}$$

where $L_{\min}$ is the smallest element dimension and $C_{\mathrm{d}}$ is the dilatational wave speed which is a function of the properties of the material. The value determined by Eq. (5-5) is only an estimation for the time increment and in most cases the time increment is less than the value determined by Eq. (5-5) by a factor between 0.7 and 1.0 to ensure the convergence of the solution [116].

### 5.1.2 Material Model

In this FE study, garnet sand particles were the erodant that impacted on a PU substrate. Since the PU was much softer than the garnet sand, the garnet sand particles were modelled as rigid particles rather than deformable objects to reduce the computation effort. In the modelling of rigid particles, no stress field is calculated in each time step of the explicit solution, and consequently, the computation time is reduced. Based on what was observed with regards to the relation between the erosion rate and mechanical properties of PU elastomers in Chapter 4, a

material model that accounts for hyperelastic behavior, plastic deformation, and stress softening was of interest.

The hyperelastic material model that is available in Abaqus was chosen to model the nonlinear elastic response of PU elastomers. The formulation of hyperelastic models available in Abaqus are described by the strain energy potential [116]. In this study, the Marlow model was chosen as representative of the hyperelastic formulation based on the recommendation of the Abaqus solver user manual [116] and the close fit between the mechanical response predicted by this material model and that of experimental data. The Marlow strain energy potential is [116]

$$U = U_{dev}\left(\bar{I}_1\right) + U_{vol}\left(J_{el}\right), \tag{5-6}$$

where $U$ is the strain energy per unit of reference volume, with $U_{\text{dev}}$ as the deviatoric part and $U_{\text{vol}}$ as the volumetric part of the energy, and $I_1$ is the first deviatoric strain invariant. The material coefficients of the hyperelastic model were determined by the Abaqus solver from experimental nominal stress-strain tensile tests data similar to that presented in Section 4.4.3 of Chapter 4.

In order to model the plastic deformation of PU elastomers, the isotropic hardening Mises plasticity material model was employed. The use of this material model is common for modelling of plasticity of ductile materials mainly due to its simplicity in algebraic equations that would allow for easier determination of the explicit equation of the material stiffness matrix [116]. Details on the equations and theory of isotropic hardening plasticity can be found elsewhere [7, 116]. In models where the hyperelastic material model and plastic hardening are defined simultaneously, a softer response compared to that of hyperelastic material model with no hardening will be obtained [116]. The material parameters for the isotropic hardening were

defined as yield stress and plastic strain in tabular data [116]. The yield stress and plastic strain values were approximated from experimental cyclic tensile tests at 20%, 50%, 100% and 200% nominal strain with the same experimental setup as discussed in Section 4.1.4 of Chapter 4.

Mullins stress softening was introduced in the material model by use of the Mullins damage formulation in the Abaqus software. The stress softening is a result of the damage caused by the previous loadings [116]. Similar to the hyperelastic material model, the Mullins damage formulation is defined based on the strain potential energy. However, in contrast to the hyperelastic material model in which the strain potential energy, $U(F)$, is only a function of the deformation gradient tensor ($F$), it is a function of both $F$ and a scalar variable ($\eta$) that describes the damage [116]. Thus, the strain energy potential for the Mullins damage formulation is expressed as $U(F, \eta)$. The damage variable ($\eta$) controls the energy function in a way that differentiates the unloading and subsequent reloading from that of the primary (initial) loading path to reflect the stress softening [116]. In fact, $\eta$ defines what fraction of the energy is stored as strain energy, while the rest is dissipated due to damage based on the elastomer properties [116]. In this study, the Mullins damage parameters were determined from the automatic calibration of the test data parameters by the solver. Experimental loading-unloading stress-strain data similar to those presented in Fig. 4-12 were used as the input to the model. The Abaqus solver computed the material parameters using a nonlinear least-squares curve fitting algorithm [116].

The material removal caused by the solid particle erosion was modelled by defining an element deletion criterion based on the equivalent plastic strain [7, 90, 91]. Once the equivalent plastic strain reached the plastic failure strain, the element was deleted from the model [7, 91]. The plastic failure strain was determined based on the data obtained from the experiments as

shown in Table 4-6. It should be noted that even though the chosen material formulation accounts for the hyperelastic, plastic, and stress softening behavior of the PU elastomer, the model does not account for the viscoelastic and rate dependent behavior of PU elastomers. In this study, the erosion caused by solid particle impact of two PU elastomers of 3000-85A and 3000M-85A at three set temperatures of 25°C, 60°C and 100°C was modelled.

### 5.1.3 Model Description and Parameters

In erosion caused by solid particle impact, damage of the target surface occurs due to the impingement of erodant particles. The repeated impact of erodant particles will finally lead to material removal from the surface. In this study, it was assumed that the erodant particles individually impacted on a single spot on the PU surface, and 10 particles were positioned at a distance of 1.6 mm from each other at the beginning of the simulation similar to what is presented in Fig. 5-1a. The assumption of impact of the erodant particles on a single area on the PU surface, allowed for modeling of a lower number of impacting particles and, therefore, reduced the computational time and need for resources. The 1.6 mm distance between the particles was chosen to ensure that the subsequent, incoming particles do not impact the surface while another particle was in contact with the PU surface. Impact of several particles allows for studying the effect of stress softening and plastic deformation on the erosion phenomenon. Figure 5-1b shows the model assembly. A symmetry boundary condition was employed to permit modelling half of the particle-target configuration to reduce the computation effort. Thus, the model boundary conditions were taken as symmetry with respect to the *xz* plane (see Fig. 5-1b), zero displacement of the bottom face of the PU material and the initial velocity of the eroding particles as follows.

- Symmetry condition: $u_{y-i} = 0$ and $r_{x-i} = r_{z-i} = 0$ at $y = 0$, (5-7)

- Zero displacement on bottom surface of PU material: $u_{x-i} = u_{y-i} = u_{z-i} = 0$ at $z = 0$, (5-8)

- Initial condition of particle nodes: $\dot{u}_{x-i} = v_{ini-x}$, $\dot{u}_{y-i} = 0$, $\dot{u}_{z-i} = v_{ini-z}$ at $t = 0$. (5-9)

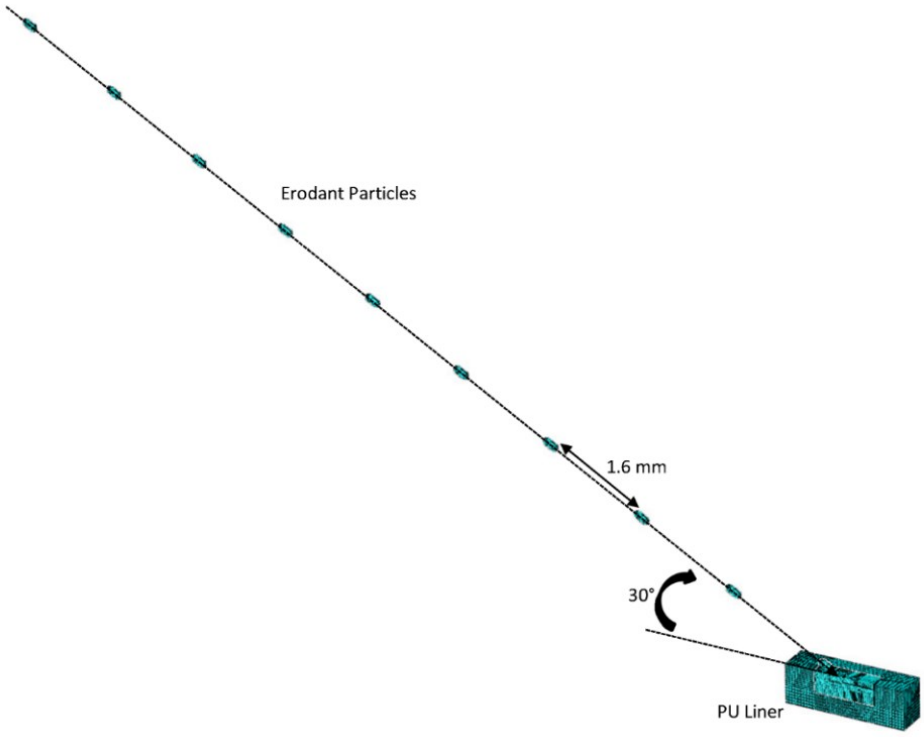


(a)

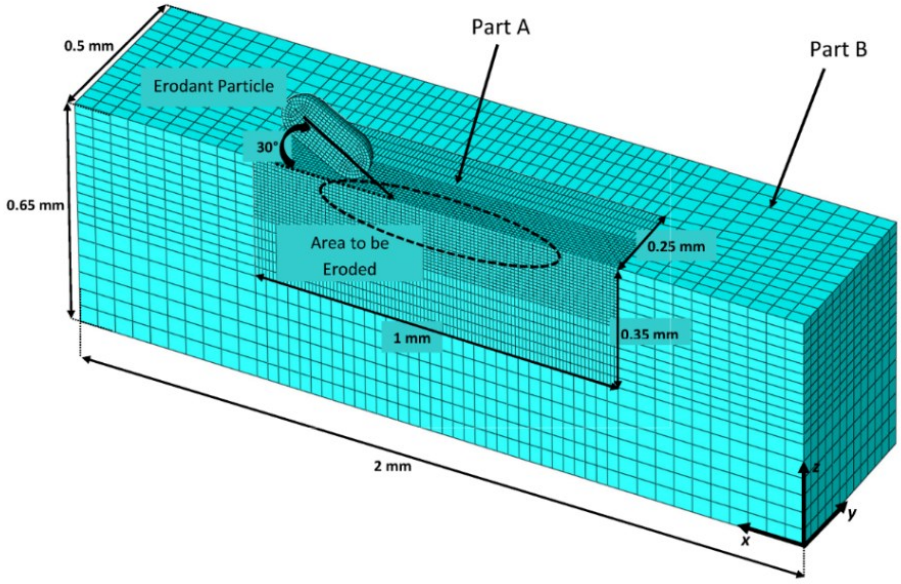


(b)

Figure 5-1 FE model assembly; a) 10 particles arranged in a line to impact the substrate, b) close-up view of the assembly showing one erodant particle and the PU target

The contact between the eroding particles and the PU surface was defined by introducing a general contact with penalty formulation available in Abaqus [116]. For simplicity, it was assumed that the contact was independent of the sliding rate, pressure, and temperature and followed Coulomb's rule of friction as [90]

$$F_t = \mu F_n, \tag{5-10}$$

where $F_t$ is the tangential force, $F_n$ is the normal force and $\mu$ is the coefficient of friction which was assumed to be 0.2 [90]. This value for the coefficient of friction was chosen because in impact problems the dynamic friction coefficients are usually considered to be small [90, 123]. The contact was defined between the outer surface of the erodant particles and the elements of the area to be eroded (see Fig. 5-1b). Upon deletion of the failed elements from the model, the contact algorithm was transferred to the underneath newly exposed elements.

The erodant particles were assumed to be identical in shape and dimensions and similar to the particle shown in Fig. 5-2. This assumption was made based on the measured values of average dimensions of the erodant particles (see Section 4.1.2). The target PU material was modelled as two parts, namely Part A and Part B as shown in Fig. 5-1b. The position of the erodant particles in the model assembly was adjusted so that impact occurred on Part A, which was meshed with refined mesh. Part B was added to the model to provide support for Part A and to ensure that the produced stresses were caused by the impact of erodant particles was not influenced by the discontinuity of the target material. Part B was meshed with larger elements and it was attached to Part A with a tie constraint that enforced zero displacement of the nodes of the two parts that were in contact. An 8-node 3D brick element type was used to discretize Parts A and B. The element size for Part A was chosen as 10 μm for areas to be eroded while the outer areas and Part B were meshed with an element length of 30 μm. Overall, parts A and B were discretized with 40,800 and 9,234 elements, respectively. The erodant particles were meshed with an element length of 10 μm. The garnet sand particles were discretized with both brick and quadrilateral elements due to the complexity of the particle geometry. Each garnet sand particle was meshed with 1,032 elements. It should be noted that a number of trial simulations were performed in a sensitivity analysis to identify the size of the sample that is shown in Fig. 5-1b and to ensure that the results obtained in terms of equivalent plastic strain and equivalent stress were not a function of sample dimensions, constraints, and element sizes.

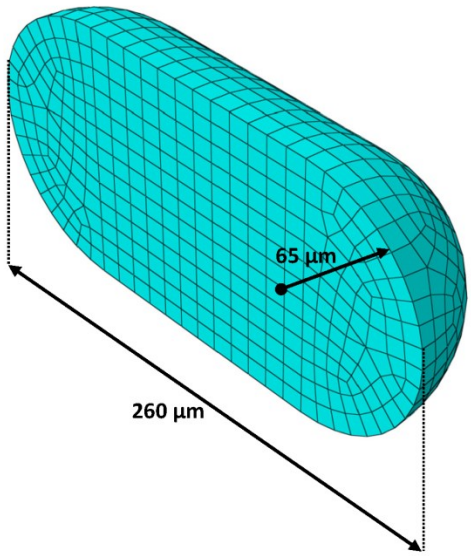


Figure 5-2 Dimensions of the modelled garnet sand particle

## 5.2 Results and Discussion

### 5.2.1 Stress-Strain Response of the Selected Material Model

Cyclic loadings were applied to a single element up to a strain value of 50% to compare the response of the selected material model with that of experiments. Figure 5-3 shows typical stress-strain curves of the 3000M-85A PU at 22ºC that was loaded-unloaded to 50% nominal strain for two cycles. As can be seen, the numerical curve of the first loading predicted similar behavior to that of the experimental graph up to the point where yielding of the PU was initiated (approximately 5 MPa). Beyond that point, the numerical model predicted a softer response compared to that of experiments. This behavior was due to the simultaneous use of isotropic hardening and hyperelastic material models as was pointed out earlier in this chapter [116].

The chosen material model correctly predicted the residual strain upon unloading (see Fig. 5-3). In the second loading cycle, the PU material exhibited a softer response due to the stress softening caused by the Mullins damage as can be seen in Fig. 5-3. The FE simulation

predicted the second loading-unloading curve based on the Mullins damage formulation and the input data from the experimental stress-strain data of the first and the second loading cycles.

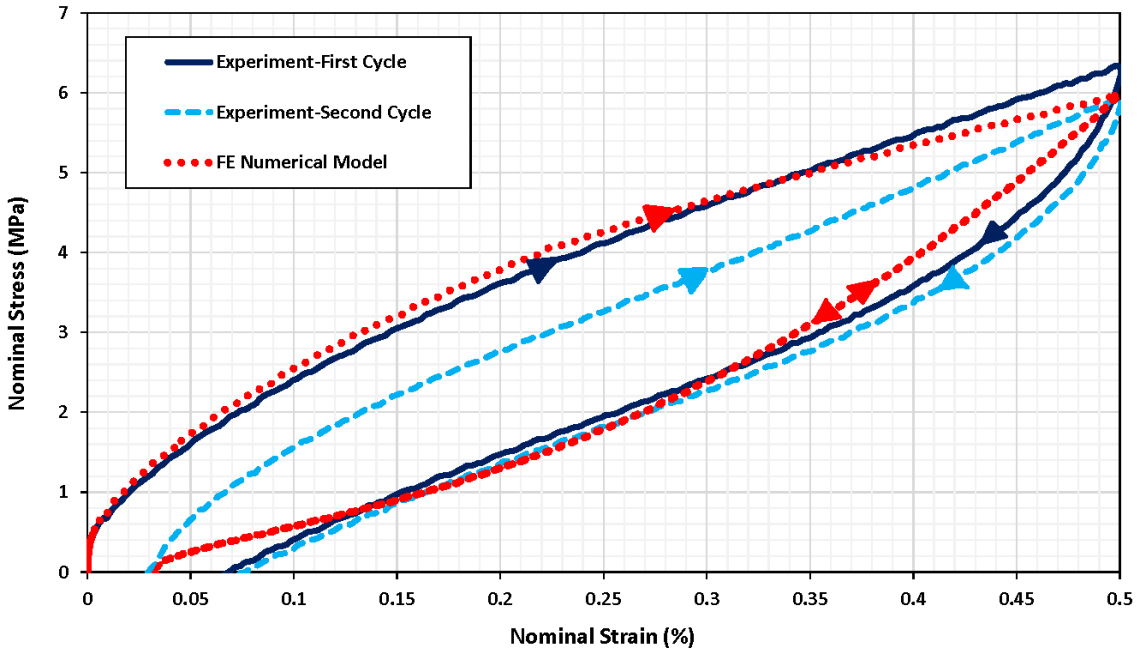


Figure 5-3 Experimental and numerical nominal stress-strain respond of first and second cycles of loading-unloading of 3000M-85A at 22ºC for elongations up to 50%

### 5.2.2 Mechanism of Material Removal

Figure 5-4 shows the impact of a single particle and the stresses that were produced in the PU elastomer from the initiation of impact ($t = 1$ µs) until rebounding of the erodant particle ($t = 10$ µs). The stress values shown in the figure represent the von Mises stress. The PU deformed upon impact of an erodant particle due to the kinetic energy of the impacting particle and the produced impact forces. The PU absorbed the kinetic energy of the particle to reduce its velocity. Based on the mechanical properties of the PU and the impact conditions, the absorbed kinetic energy may be stored partly or in full as potential energy that was released later to facilitate the rebounding of the particle. The impact and further rebounding of the particle is

shown in Fig. 5-4 (a) to (j). As can be seen, within a few initial microseconds of the impact (see Fig. 5-4 (a) to (d)), the erodant particle penetrated into the PU. The stresses produced were smaller than the ultimate failure stress of the PU, and hence, no removal of material from the surface occurred. The maximum stresses were produced within the initial stage of the impact as shown in Fig. 5-4 (c) and (d). Some elements were dragged at the beginning of the impact ($t$ = 1 μs to 2 μs) and were compressed later as the particle penetrated into the PU ($t$ = 3 μs to 4 μs). The elements that represented the PU material close to the surface experienced higher stresses and, therefore, were subjected to plastic deformation and possible damage caused by Mullins stress softening.

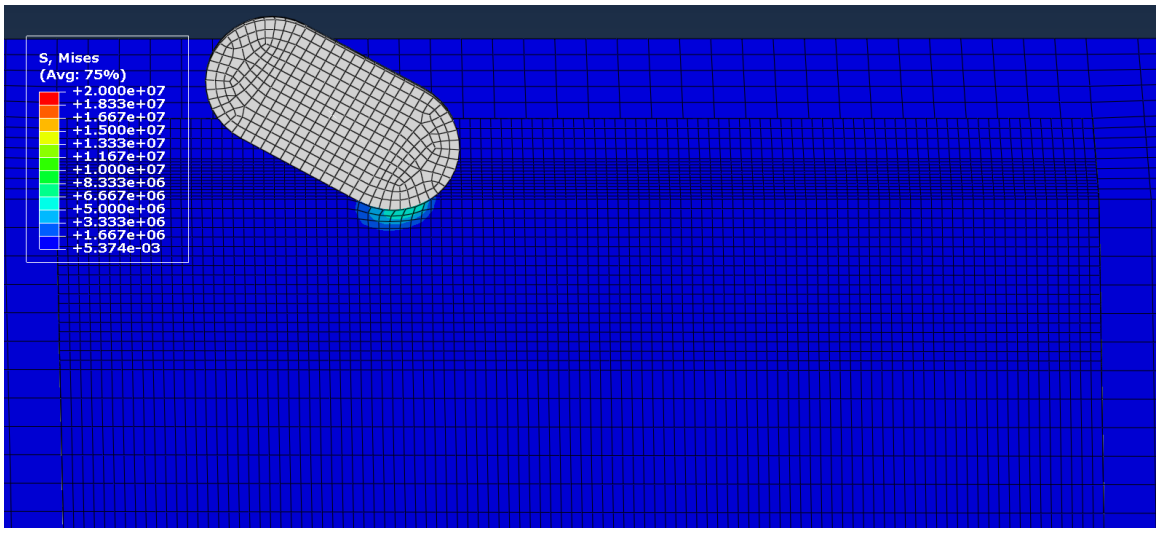


(a)

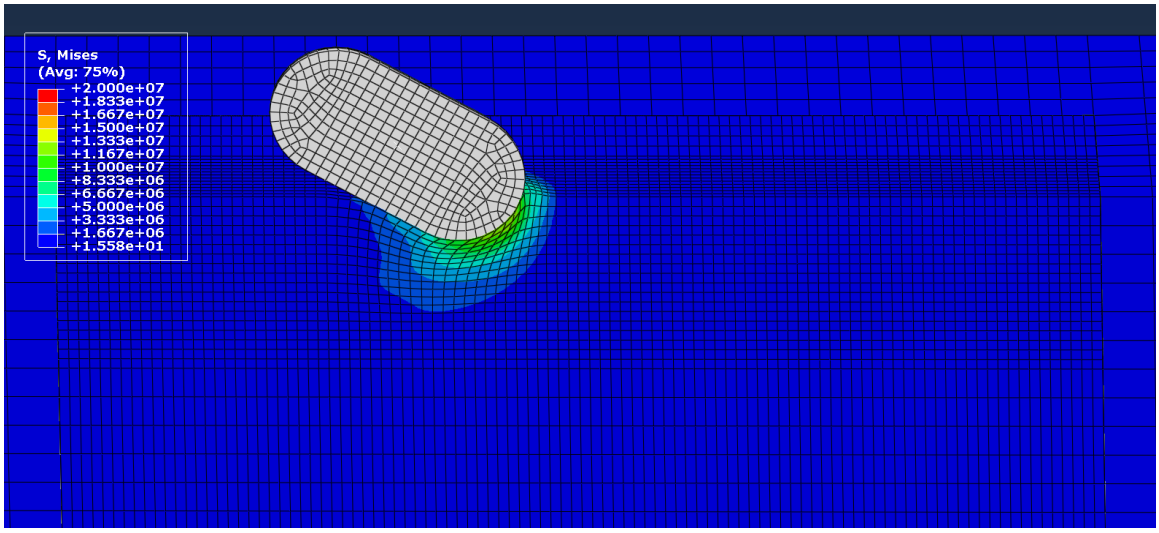
S, Mises
(Avg: 75%)
+2.000e+07
+1.833e+07
+1.667e+07
+1.500e+07
+1.333e+07
+1.167e+07
+1.000e+07
+8.333e+06
+6.667e+06
+5.000e+06
+3.333e+06
+1.667e+06
+1.558e+01

(b)

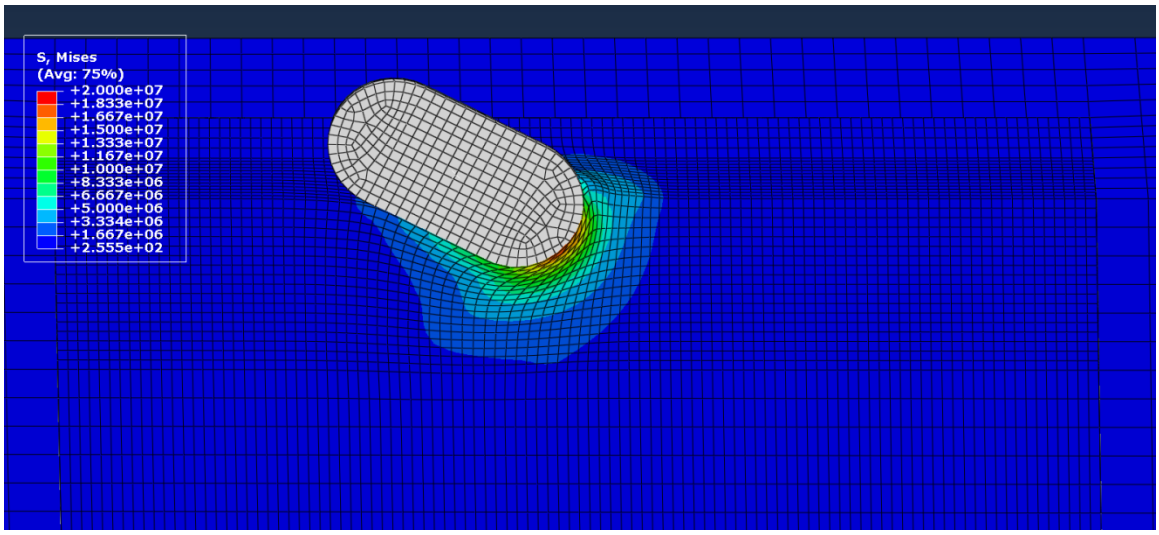
S, Mises
(Avg: 75%)
+2.000e+07
+1.833e+07
+1.667e+07
+1.500e+07
+1.333e+07
+1.167e+07
+1.000e+07
+8.333e+06
+6.667e+06
+5.000e+06
+3.334e+06
+1.667e+06
+2.555e+02

(c)

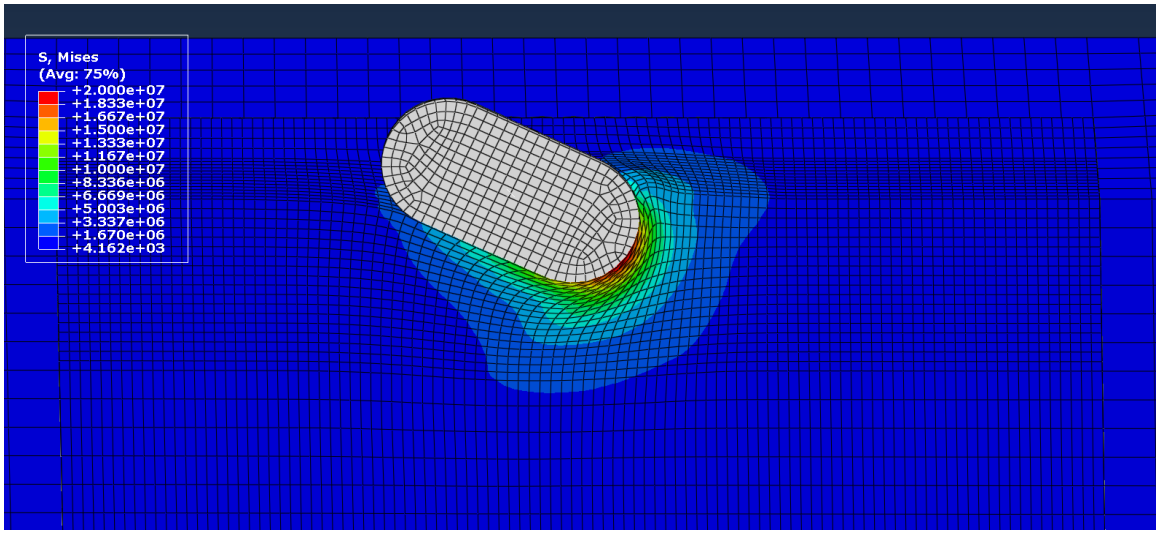
S, Mises
(Avg: 75%)
+2.000e+07
+1.833e+07
+1.667e+07
+1.500e+07
+1.333e+07
+1.167e+07
+1.000e+07
+8.336e+06
+6.669e+06
+5.003e+06
+3.337e+06
+1.670e+06
+4.162e+03

(d)

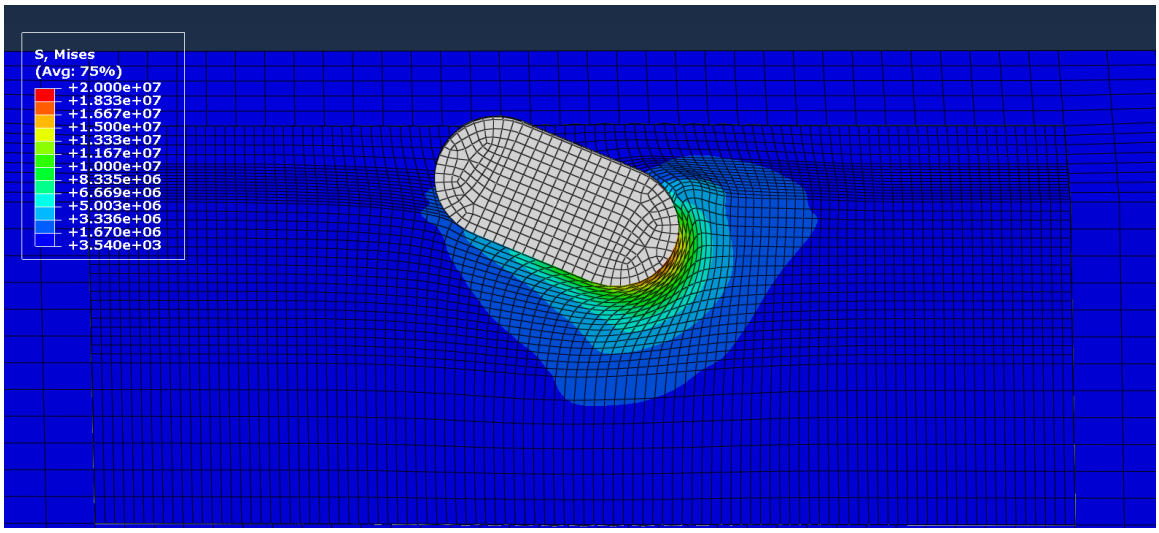
S, Mises
(Avg: 75%)
+2.000e+07
+1.833e+07
+1.667e+07
+1.500e+07
+1.333e+07
+1.167e+07
+1.000e+07
+8.335e+06
+6.669e+06
+5.003e+06
+3.336e+06
+1.670e+06
+3.540e+03

(e)

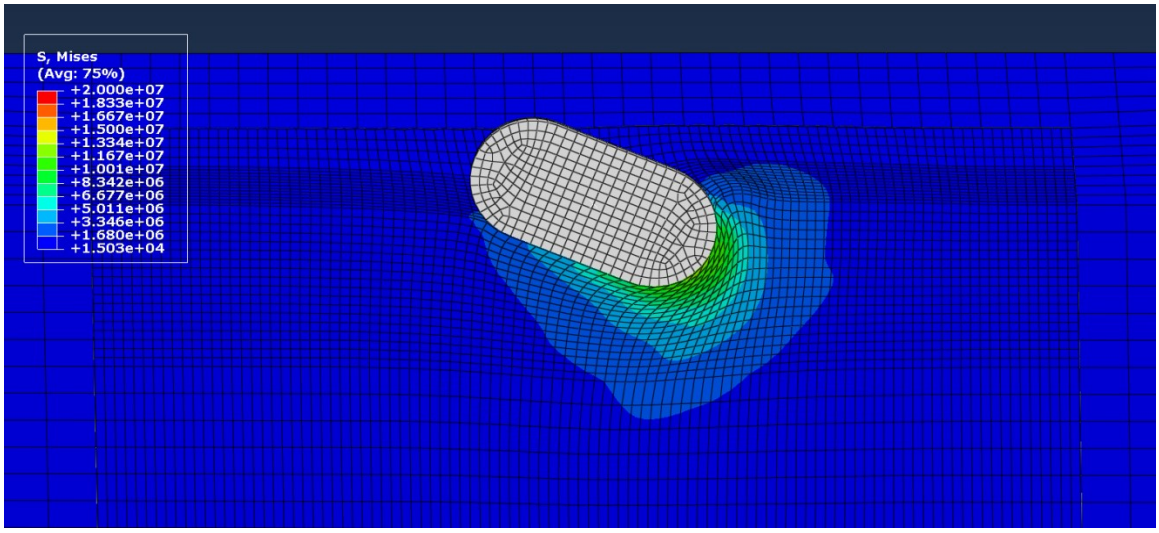
S, Mises
(Avg: 75%)
+2.000e+07
+1.833e+07
+1.667e+07
+1.500e+07
+1.334e+07
+1.167e+07
+1.001e+07
+8.342e+06
+6.677e+06
+5.011e+06
+3.346e+06
+1.680e+06
+1.503e+04

(f)

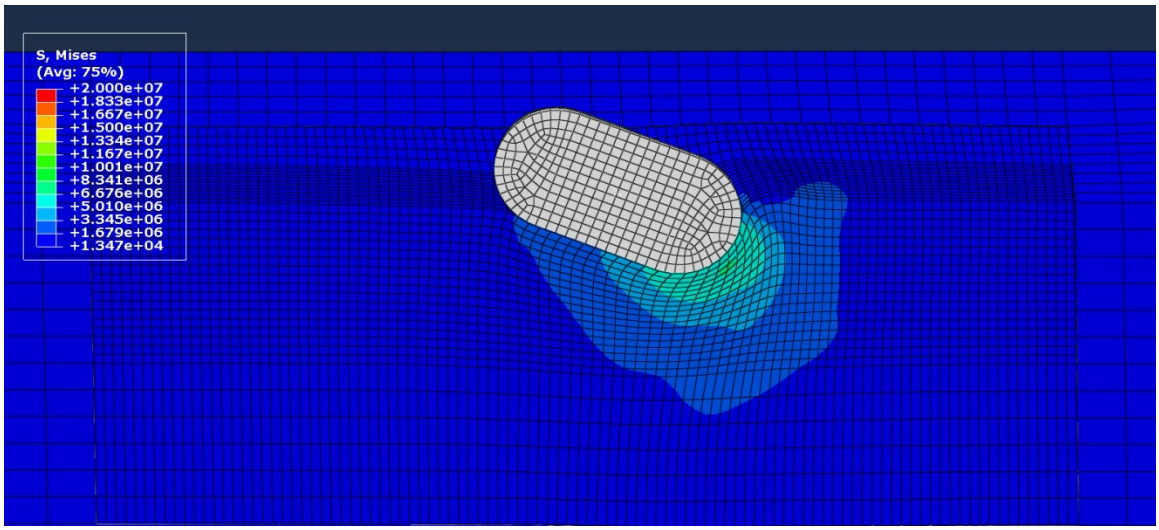
S, Mises
(Avg: 75%)
+2.000e+07
+1.833e+07
+1.667e+07
+1.500e+07
+1.334e+07
+1.167e+07
+1.001e+07
+8.341e+06
+6.676e+06
+5.010e+06
+3.345e+06
+1.679e+06
+1.347e+04

(g)

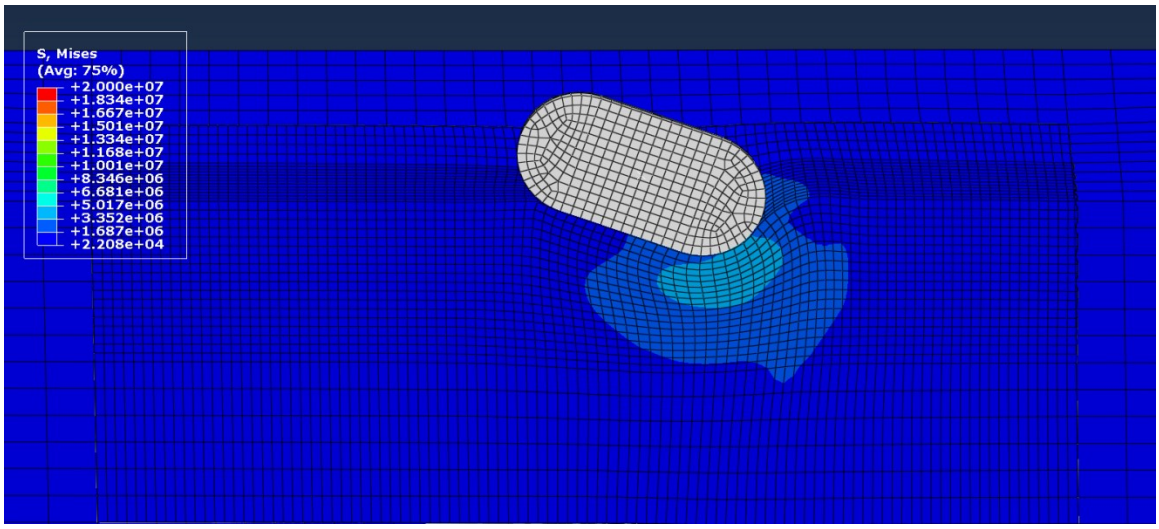
S, Mises
(Avg: 75%)
+2.000e+07
+1.834e+07
+1.667e+07
+1.501e+07
+1.334e+07
+1.168e+07
+1.001e+07
+8.346e+06
+6.681e+06
+5.017e+06
+3.352e+06
+1.687e+06
+2.208e+04

(h)

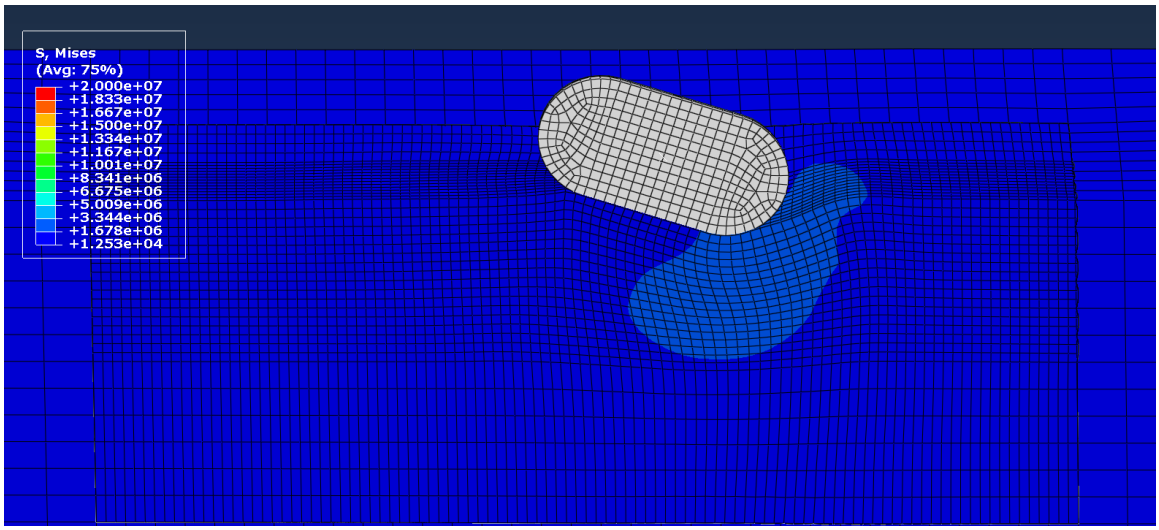
S, Mises
(Avg: 75%)
+2.000e+07
+1.833e+07
+1.667e+07
+1.500e+07
+1.334e+07
+1.167e+07
+1.001e+07
+8.341e+06
+6.675e+06
+5.009e+06
+3.344e+06
+1.678e+06
+1.253e+04

(i)

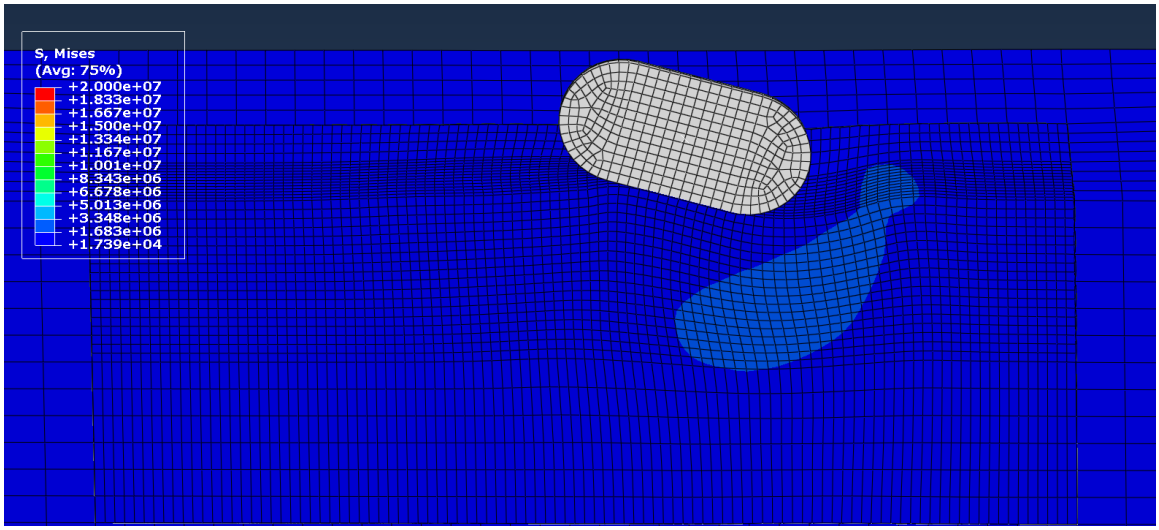


(j)

Figure 5-4 Produced stresses during the impact of a single particle with initial velocity of 73 m/s on 3000M-85A PU at 60ºC; a) $t$ = 1 µs, b) $t$ = 2 µs, c) $t$ = 3 µs, d) $t$ = 4 µs, e) $t$ = 5 µs, f) $t$ = 6 µs, g) $t$ = 7 µs, h) $t$ = 8 µs, i) $t$ = 9 µs, j) $t$ = 10 µs

Figure 5-5 shows the equivalent plastic strain that was produced after the impact of four erodant particles on the surface of 3000M-85A PU at 60°C. It can be seen that after the impact of the first garnet sand particle, the elements on the PU surface did not meet the plastic strain failure criterion and no material removal occurred. However, some parts of the PU deformed plastically as shown in Fig. 5-5a. Upon impact of the second particle (see Fig. 5-5b), the failure criterion was met by a few elements on the top surface upon which these particles were removed from the model. The Mullins stress softening damage during the impact of the first particle enabled the removal of damaged elements during the impact of the second particle. The areas that were removed as a result of localized removal of small fragments were also observed in SEM images taken from the top surface of the eroded surfaces. Those areas are indicated by circles in Fig. 5-6.

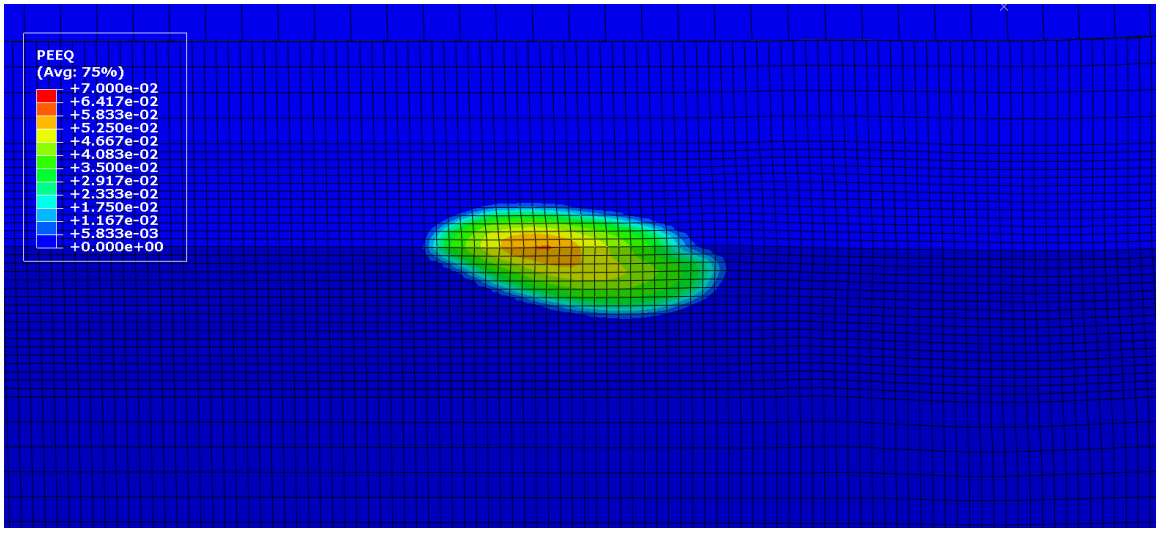
PEEQ
(Avg: 75%)
+7.000e-02
+6.417e-02
+5.833e-02
+5.250e-02
+4.667e-02
+4.083e-02
+3.500e-02
+2.917e-02
+2.333e-02
+1.750e-02
+1.167e-02
+5.833e-03
+0.000e+00

(a)

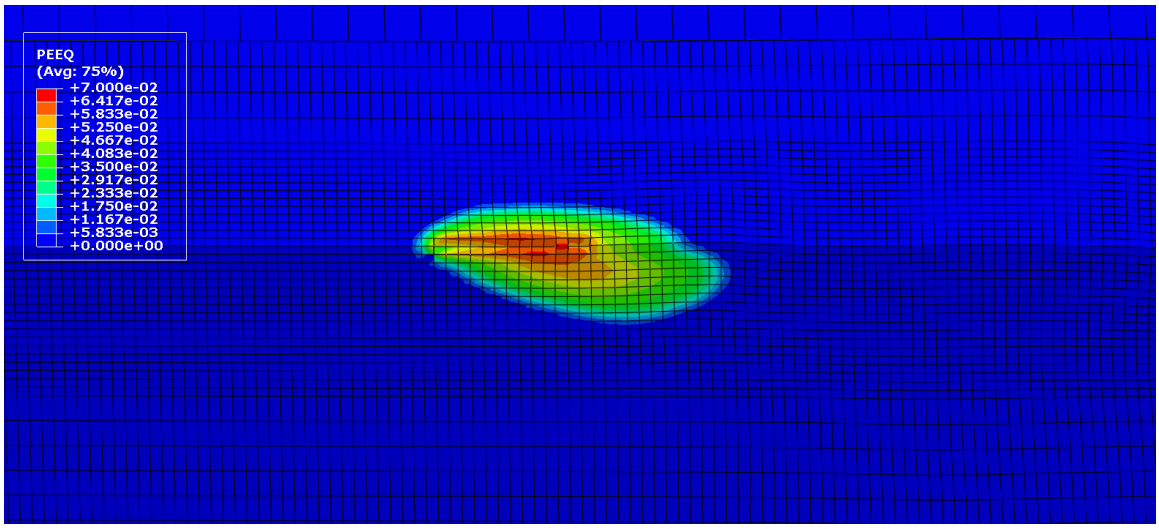
PEEQ
(Avg: 75%)
+7.000e-02
+6.417e-02
+5.833e-02
+5.250e-02
+4.667e-02
+4.083e-02
+3.500e-02
+2.917e-02
+2.333e-02
+1.750e-02
+1.167e-02
+5.833e-03
+0.000e+00

(b)

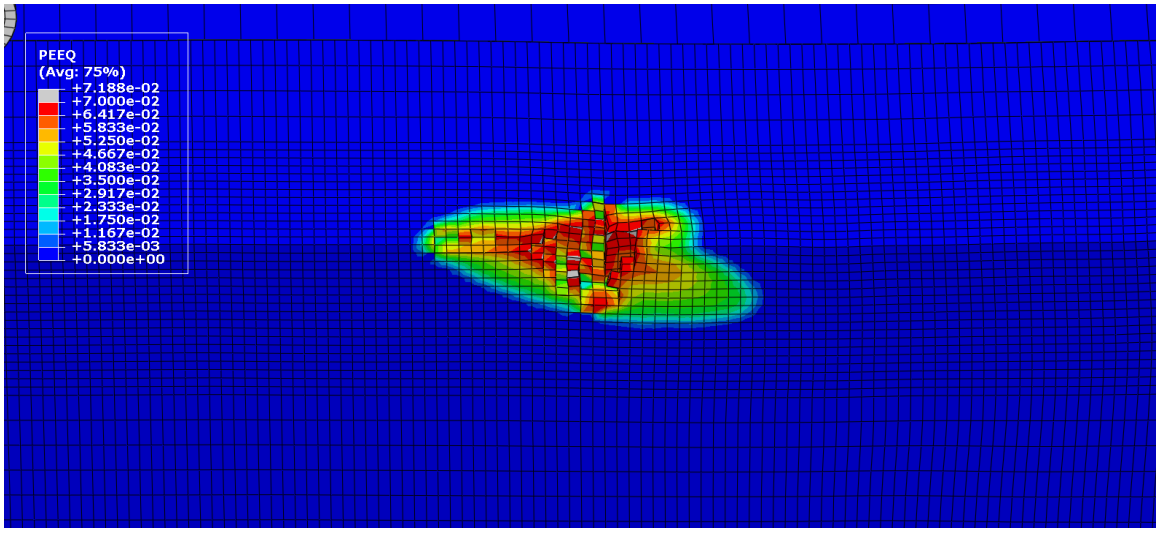


(c)

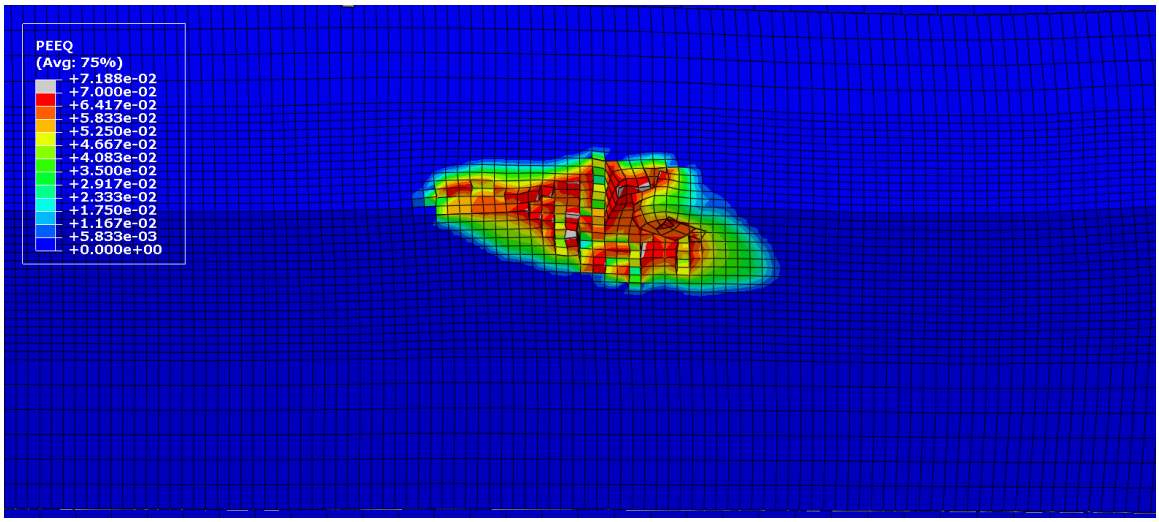


(d)

Figure 5-5 Equivalent plastic strain after impact of erodant particles with initial velocity of 73 m/s on 3000M-85A PU at 60ºC; a) 1 particle, b) 2 particles, c) 3 particles, d) 4 particles

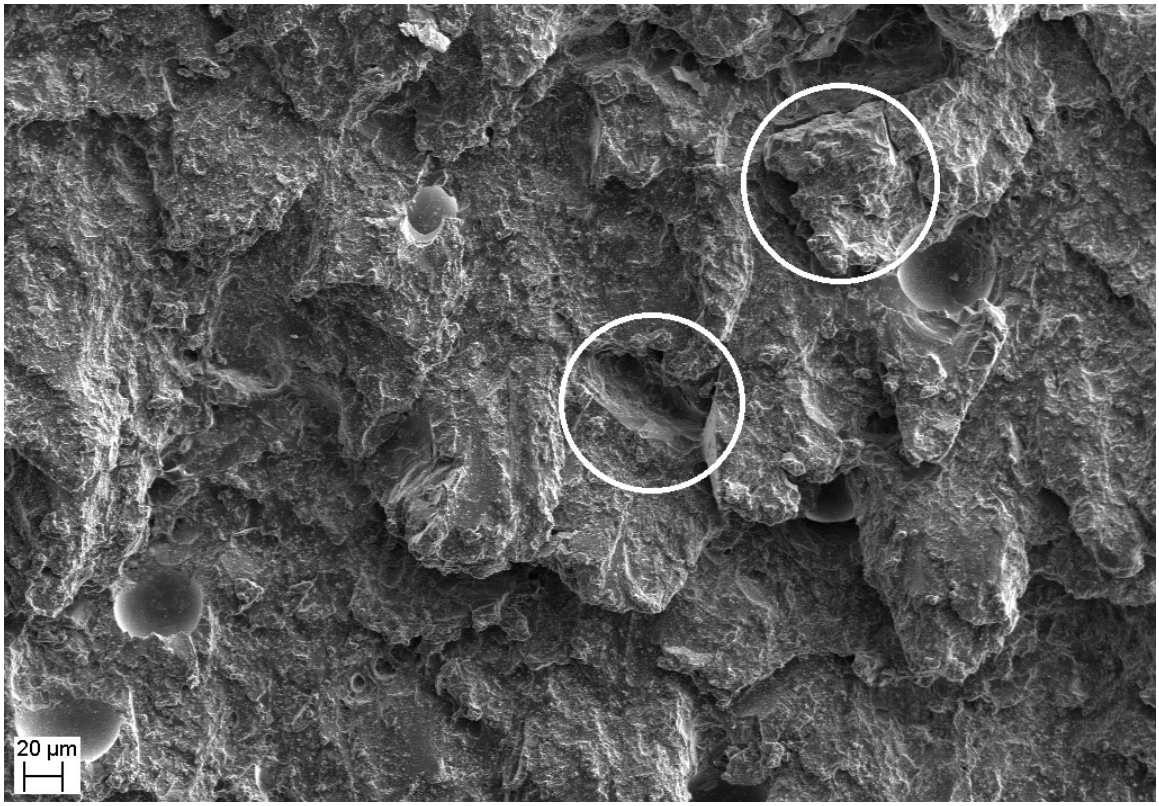


Figure 5-6 SEM images of the eroded 3000M-85A PU surface at 60ºC

The impact of the second particle enlarged the area in which plastic deformation occurred as well increased the maximum value of the equivalent plastic strain as evidenced in Fig. 5-5 (b). The residual strain increased further upon impact of the third and fourth particles (see Fig. 5-5 (c) and (d)), and reached the plastic strain failure criterion of the PU material at the specified temperature. As a matter of fact, upon impact of the third particle, a larger area was subject to failure and was removed from the model. This provides further support for the material removal mechanism that involves the accumulation of residual strains resulting in failure and detachment of material, as discussed in Section 4.4.4 of Chapter 4. Figure 5-7 shows a SEM image taken from the top surface of the eroded samples with areas suspected of removal of material as a result of the accumulation of residual strains. The shape of the asperities in

Fig. 5-5d, as predicted by the FE model, is similar to that indicated in Fig. 5-7 by circles and shown in Fig. 4-15a.

While the model was able to simulate the accumulation of residual strains up to failure and also predict the shape of the asperities that is similar to those observed in experiments, the model overestimated the material removal. It is presumed that this is due to the assumptions that were made in the formulation of the model with respect to the deletion of elements upon reaching the failure criterion. In reality, the failed and separated fragments will remain between the erodant particle and the PU material while in the simulation the material was removed from in front of the erodant particle and, therefore, facilitated the further penetration of the erodant particle into the PU surface.

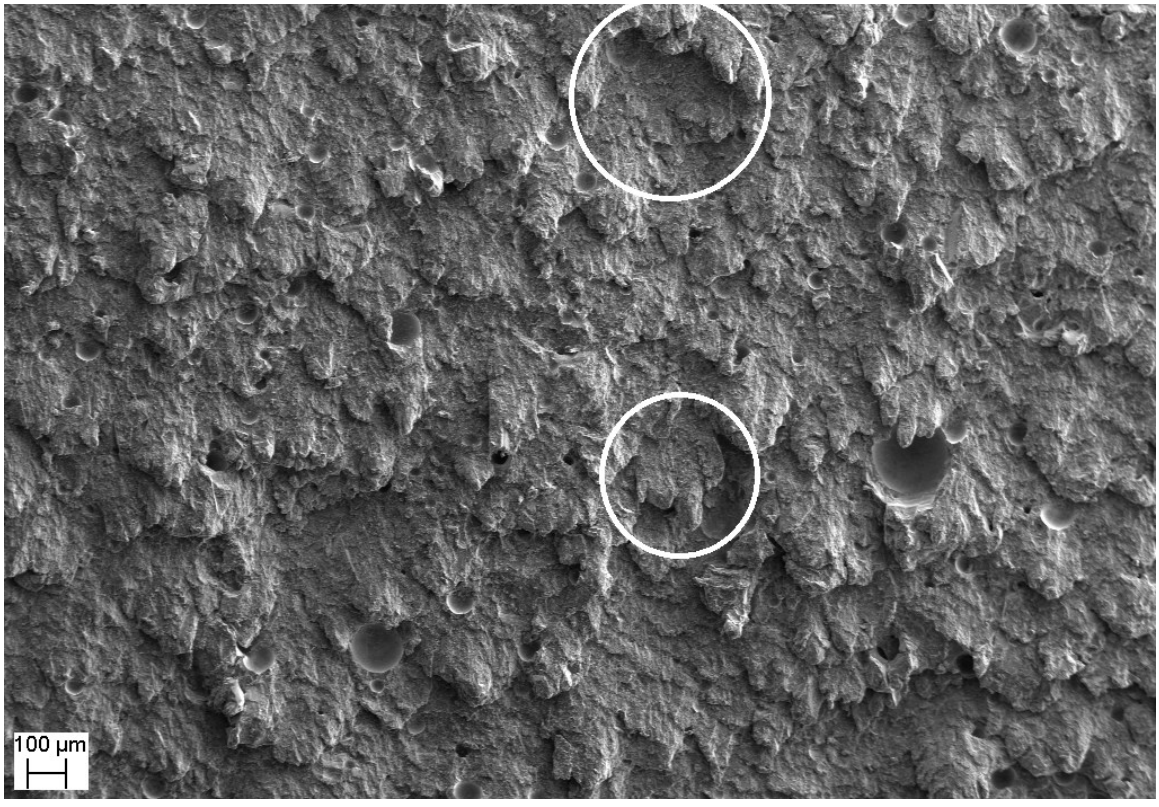


Figure 5-7 SEM images of the eroded 3000M-85A PU surface at 60ºC

The plastic strains produced within the 3000M-85A PU after the impact of 10 particles with initial velocity of 73 m/s at 22ºC is shown in Fig. 5-8. As shown in this figure, the model predicted the area of the PU at 22°C with plastic strain to be larger than that of the PU that was tested at 60ºC (see Fig. 5-5a). This is in agreement with the hypothesis that was discussed in Chapter 4 about the improved ability of PU material at 60°C to revert to its initial condition with less residual strains upon unloading compared to that of PU at 22°C. Similar to the results obtained from the 3000M-85A PU at 60°C (see Fig. 5-5), the repeated impact of subsequent particles led to localized removal of material from the surface most probably due to stress softening caused by Mullins damage (see Fig. 5-8). Even though the value of the equivalent plastic strain and the area with residual strain increased as the number of the impacting particles increased (see Fig. 5-8), a higher number of impacts was required in order to reach the point of detachment of larger fragments from the surface similar to what was observed for the modeled PU at 60°C (see Fig. 5-5).

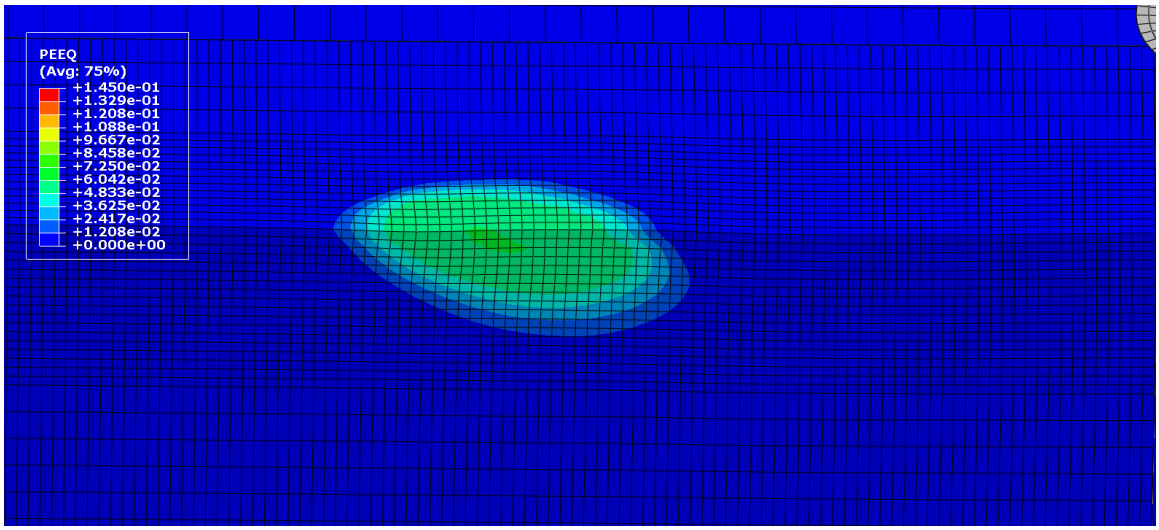


(a)

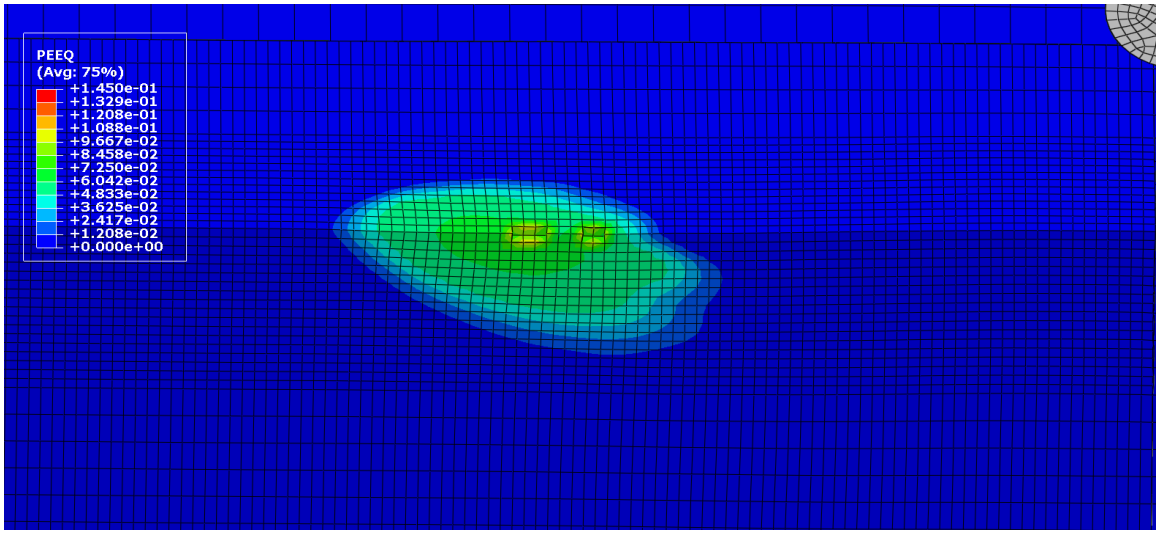
PEEQ
(Avg: 75%)
+1.450e-01
+1.329e-01
+1.208e-01
+1.088e-01
+9.667e-02
+8.458e-02
+7.250e-02
+6.042e-02
+4.833e-02
+3.625e-02
+2.417e-02
+1.208e-02
+0.000e+00

(b)

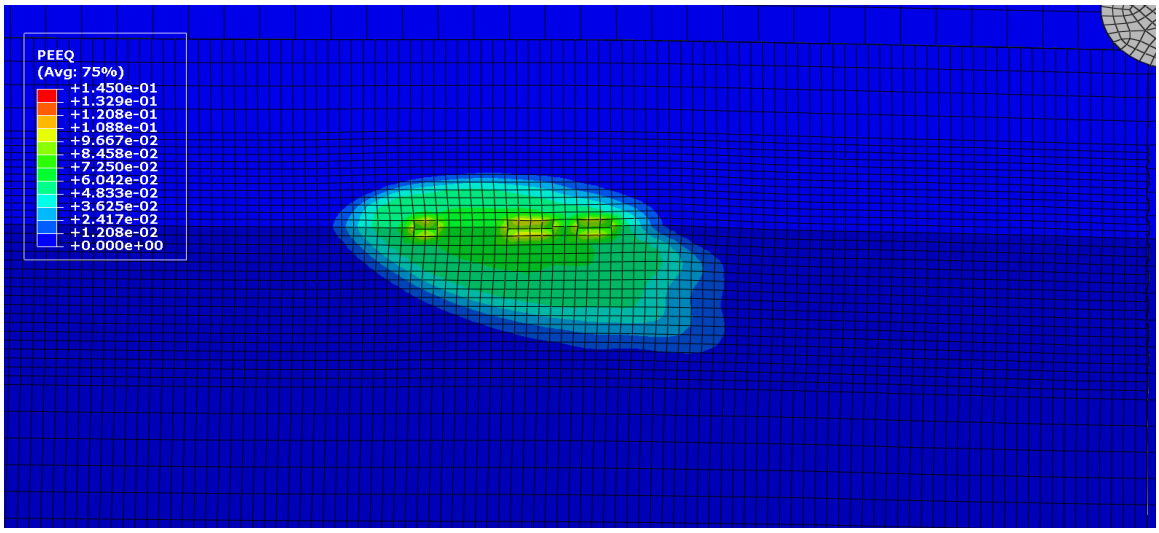
PEEQ
(Avg: 75%)
+1.450e-01
+1.329e-01
+1.208e-01
+1.088e-01
+9.667e-02
+8.458e-02
+7.250e-02
+6.042e-02
+4.833e-02
+3.625e-02
+2.417e-02
+1.208e-02
+0.000e+00

(c)

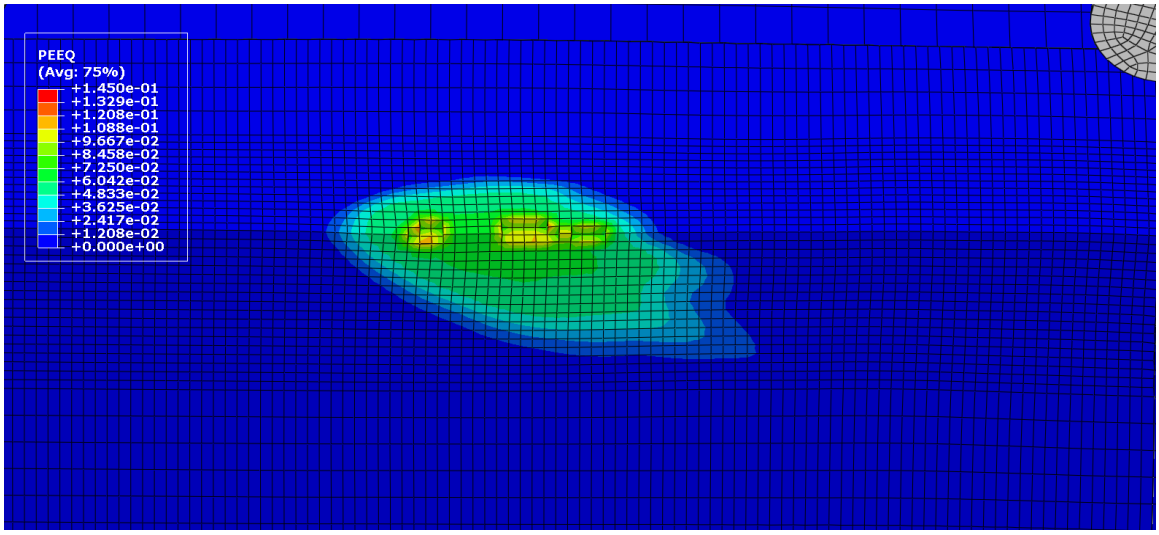
PEEQ
(Avg: 75%)
+1.450e-01
+1.329e-01
+1.208e-01
+1.088e-01
+9.667e-02
+8.458e-02
+7.250e-02
+6.042e-02
+4.833e-02
+3.625e-02
+2.417e-02
+1.208e-02
+0.000e+00

(d)

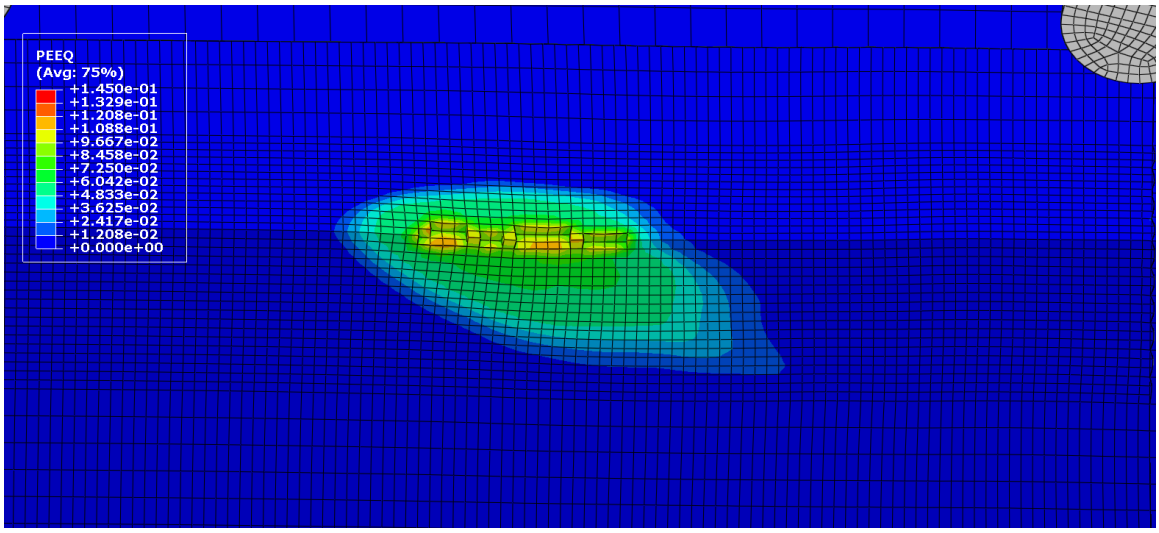
PEEQ
(Avg: 75%)
+1.450e-01
+1.329e-01
+1.208e-01
+1.088e-01
+9.667e-02
+8.458e-02
+7.250e-02
+6.042e-02
+4.833e-02
+3.625e-02
+2.417e-02
+1.208e-02
+0.000e+00

(e)

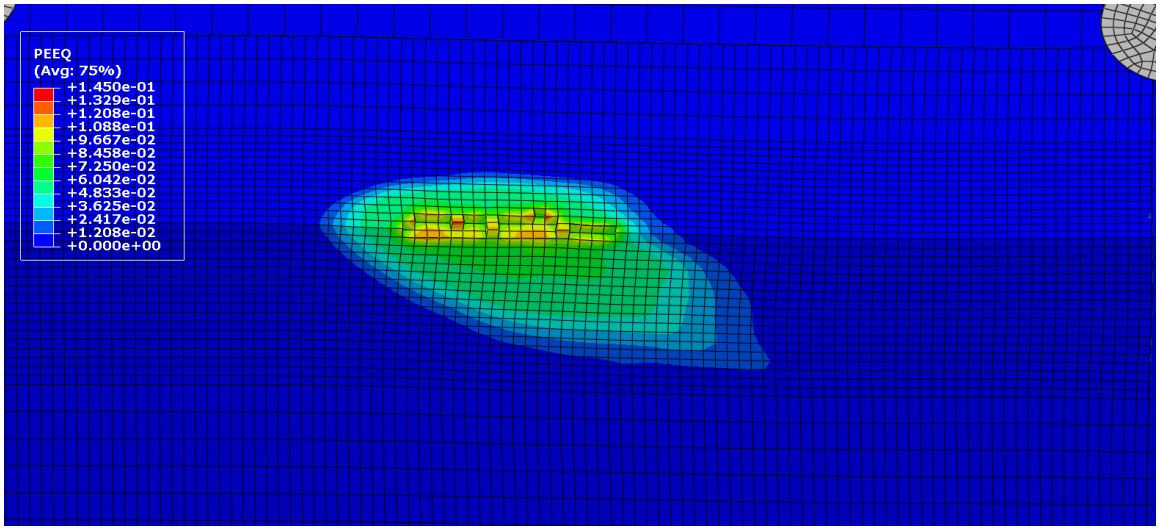
PEEQ
(Avg: 75%)
+1.450e-01
+1.329e-01
+1.208e-01
+1.088e-01
+9.667e-02
+8.458e-02
+7.250e-02
+6.042e-02
+4.833e-02
+3.625e-02
+2.417e-02
+1.208e-02
+0.000e+00

(f)

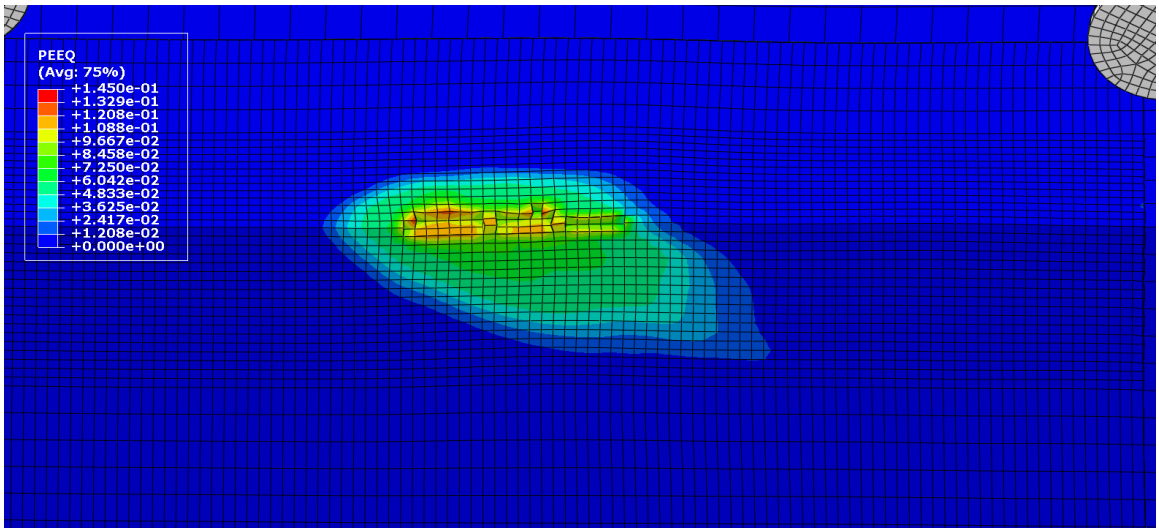
PEEQ
(Avg: 75%)
+1.450e-01
+1.329e-01
+1.208e-01
+1.088e-01
+9.667e-02
+8.458e-02
+7.250e-02
+6.042e-02
+4.833e-02
+3.625e-02
+2.417e-02
+1.208e-02
+0.000e+00

(g)

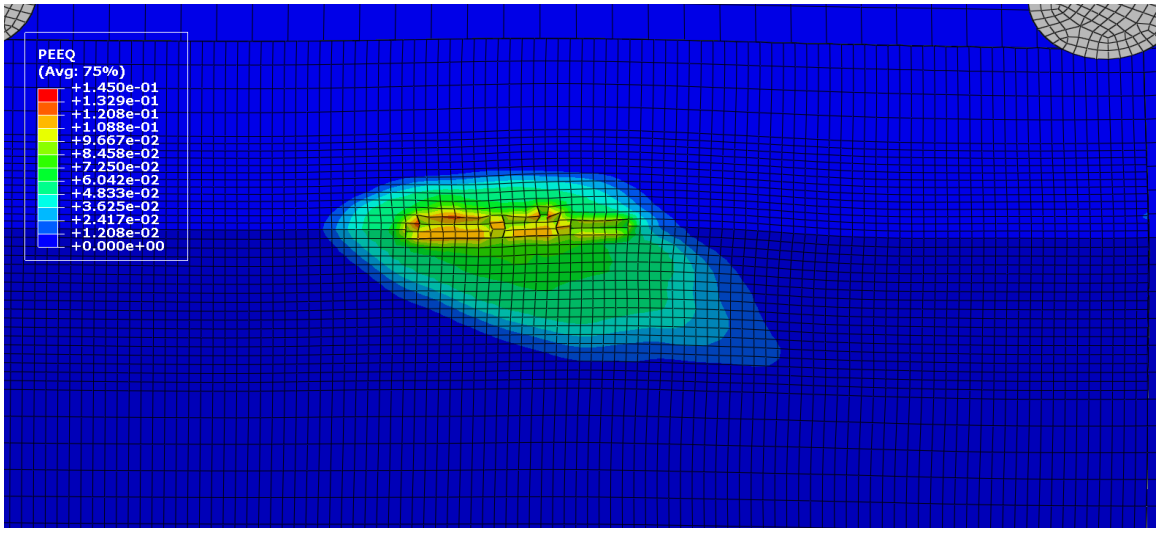
PEEQ
(Avg: 75%)
+1.450e-01
+1.329e-01
+1.208e-01
+1.088e-01
+9.667e-02
+8.458e-02
+7.250e-02
+6.042e-02
+4.833e-02
+3.625e-02
+2.417e-02
+1.208e-02
+0.000e+00

(h)

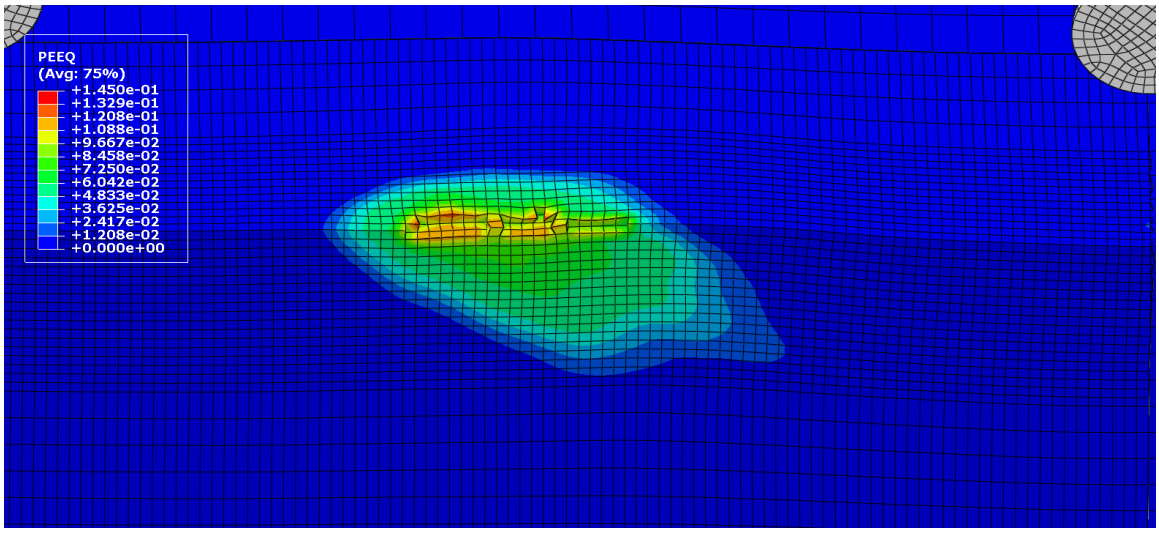
PEEQ
(Avg: 75%)
+1.450e-01
+1.329e-01
+1.208e-01
+1.088e-01
+9.667e-02
+8.458e-02
+7.250e-02
+6.042e-02
+4.833e-02
+3.625e-02
+2.417e-02
+1.208e-02
+0.000e+00

(i)

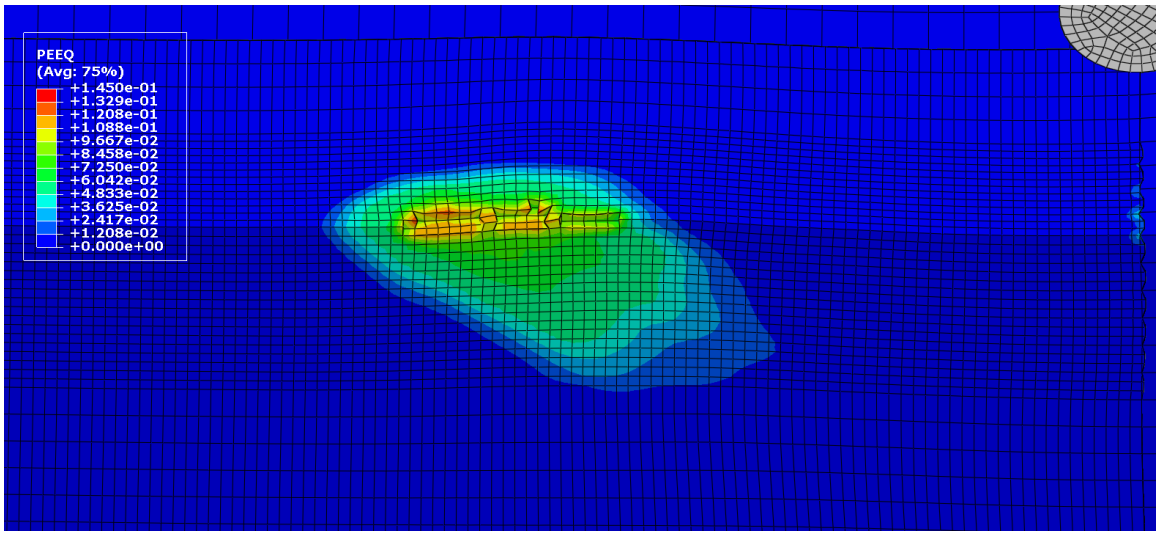


(j)

Figure 5-8 Equivalent plastic strain after impact of erodant particles with initial velocity of 73 m/s on 3000M-85A PU at 22ºC; a) 1 particle, b) 2 particles, c) 3 particles, d) 4 particles, e) 5 particles, f) 6 particles, g) 7 particles, h) 8 particles, i) 9 particles, j) 10 particles

Evaluation of the stresses produced in PU held at 100°C that was impacted by an erodant particle (see Fig. 5-9) revealed that the stresses that were produced upon the initiation of impact was higher than the ultimate stress of the PU material at 100°C, which led to the removal of elements that were in contact with the erodant particle. Although the model successfully indicated the importance of ultimate strength and elongation at break of the material as parameters affecting the erosion rate, it failed to correctly depict the shape of the formed asperities, and the model overestimated the penetration of the erodant particle into the PU. As discussed earlier, this behavior is likely due to the assumption that was made about the removal of failed elements from the analysis. In reality, the detached material will remain between the particle and the PU surface, preventing the impacting particle from excessive penetration into the PU surface. In the present simulation, the erodant particle with initial velocity of 73 m/s penetrated and remained attached to the PU substrate.

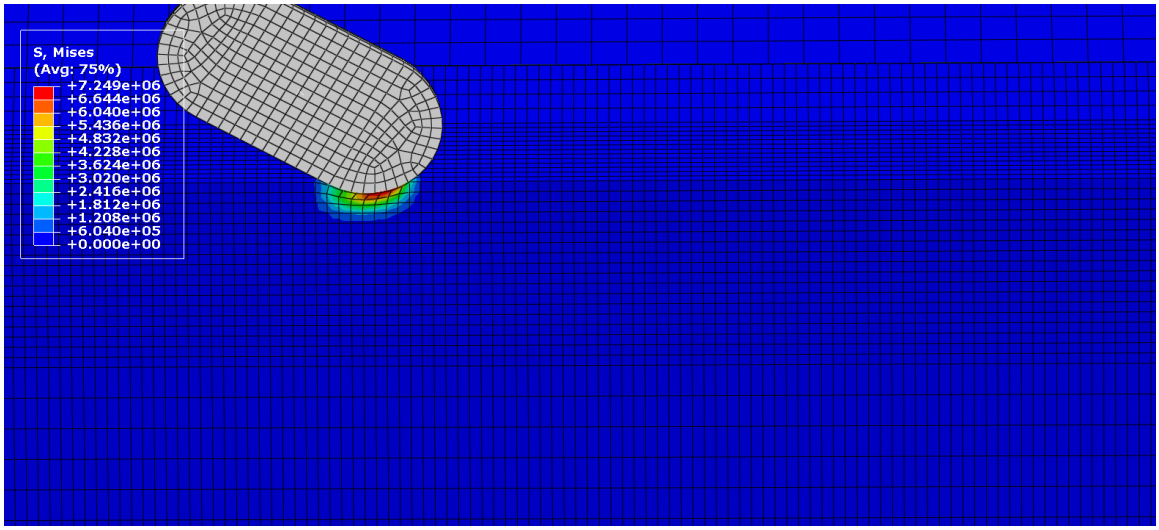
S, Mises
(Avg: 75%)
+7.249e+06
+6.644e+06
+6.040e+06
+5.436e+06
+4.832e+06
+4.228e+06
+3.624e+06
+3.020e+06
+2.416e+06
+1.812e+06
+1.208e+06
+6.040e+05
+0.000e+00

(a)

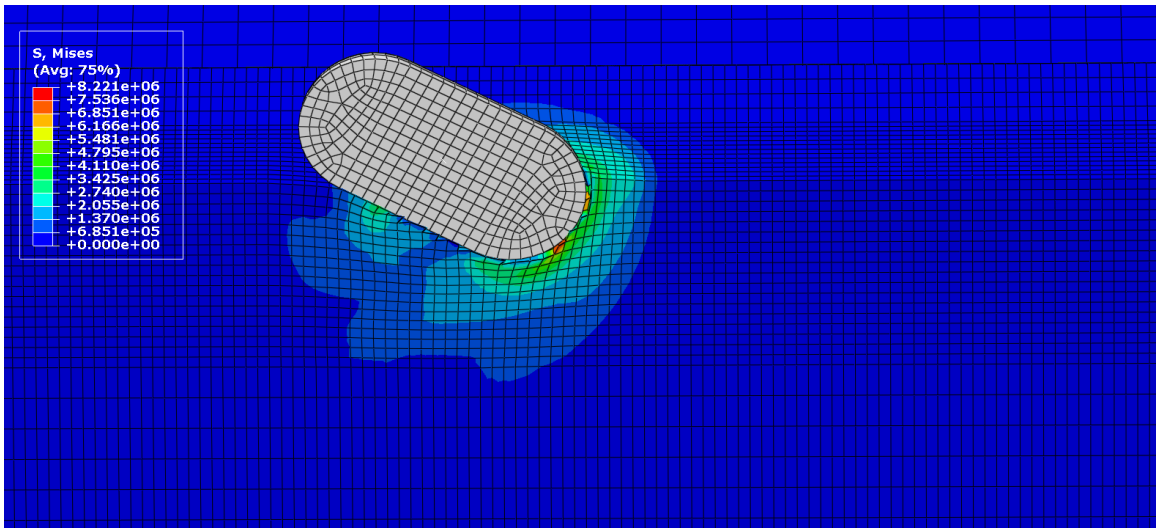
S, Mises
(Avg: 75%)
+8.221e+06
+7.536e+06
+6.851e+06
+6.166e+06
+5.481e+06
+4.795e+06
+4.110e+06
+3.425e+06
+2.740e+06
+2.055e+06
+1.370e+06
+6.851e+05
+0.000e+00

(b)

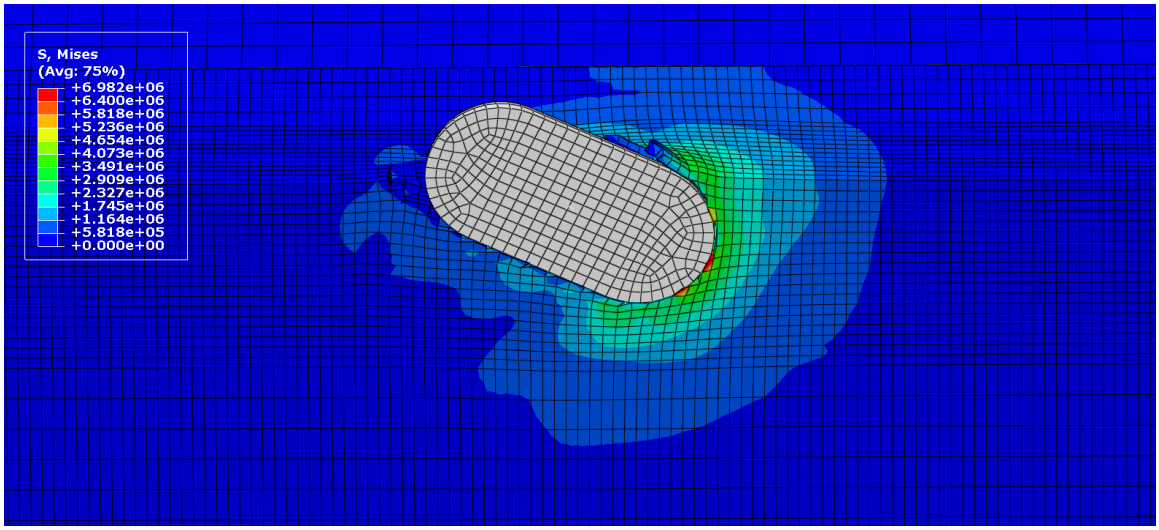


(c)

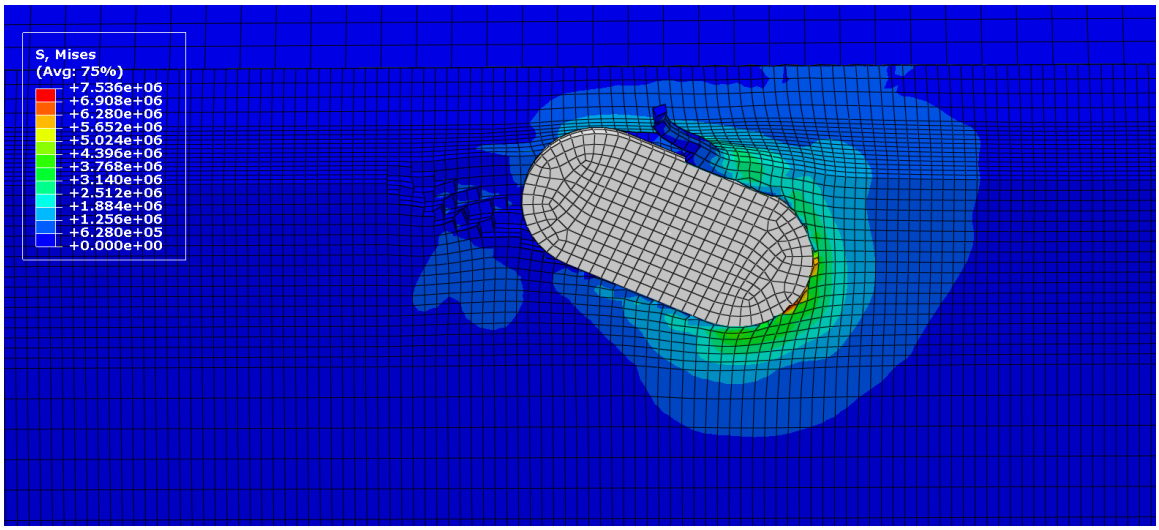


(d)

Figure 5-9 Produced stresses during the impact of a single particle with initial velocity of 73 m/s on 3000M-85A PU at 100ºC; a) $t$ = 1 µs, b) $t$ = 3 µs, c) $t$ = 5 µs, d) $t$ = 7 µs

The modeling of the erosion process of 3000-85A PU at 22°C, 60°C, and 100°C generated similar results to that of 3000M-85A PU. At 22°C, only the detachment of single elements from the surface occurred as a result of stress softening during repetitive impacts. At 60°C, after several impacts, the accumulation of residual strain led to the formation of craters

and removal of a larger number of elements similar to what was presented in Fig. 5-5. Finally, at 100°C, due to the low strength of the PU elastomer, significant damage and failure of the target PU up to the penetration and trapping of the erodant particle was observed.

### 5.2.3 Effect of Particle Velocity on the Predicted Erosion Rate

The numerical model that was used as a predictive tool for estimating the particle velocity (see Section 4.2 of Chapter 4) provided an approximation for the maximum velocity of the erodant particles exiting the nozzle. At the nozzle exit, the high velocity air mixes with the stationary ambient air and that decelerates the air jet. Therefore, the erodant particles are decelerated as well [113]. The deceleration of the gas and erodant particles is a function of stand-off distance and the impingement angle between the air jet and the target surface [113]. The velocity of the erodant particles has a profile that is most probably similar to what is presented schematically in Fig. 5-10. This figure was approximated based on the topography of the worn samples and the relation between the impact velocity and the erosion rate. Particles with higher velocity have higher kinetic energy and can produce additional damage to the substrate upon impact that would lead to higher erosion rates. As seen in Fig. 5-10, the velocity of the erodant particles were within a range from the maximum velocity on the center of impact to lower velocities on areas distal from the center. The FE simulations of the erosion process was conducted for lower velocities of 60 m/s, 50 m/s and 40 m/s to gain knowledge about the erosion mechanism of other areas that have most probably been impacted by erodant particles with lower velocities. The results of these simulations may also provide insight about the effect of velocity on the material removal mechanism.

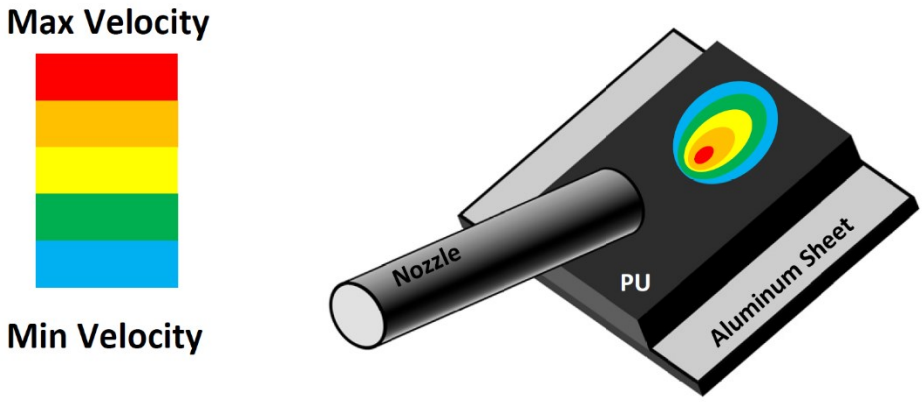


Figure 5-10 Schematic of the erodant particles velocity profile upon impact on the PU surface

Table 5-1 shows the calculated erosion rates of 3000-85A and 3000M-85A PU elastomers at different velocities and temperatures. For velocities higher than 40 m/s, a large number of elements were removed upon impact of the initial erodant particle for both PU types at 100ºC. Although the overestimation of the element removal was one of the disadvantages of the model, the simulation clearly showed the importance of the ultimate strength and elongation at break. In addition, comparison of the erosion behavior of 3000-85A at 100°C for velocities of 40 m/s and 50 m/s emphasizes the fact that, below a critical velocity, a significant difference in wear resistance and material removal mechanism can occur. Figures 5-11 (a) and (b) show the simulated eroded surface of the 3000-85A at 100°C after the impact of the first particle with initial velocities of 40 m/s and 50 m/s, respectively. At an initial velocity of 40 m/s, the stresses that were produced were smaller than the ultimate strength of the material and, thus, no removal of PU material took place.

Table 5-1 Predicted erosion rate of PU elastomers by FE model after impact of 10 erodant particles (NMR: No Element Removal, RLN1: Removal of large number of elements upon initial impact, RLN2: Removal of large number of elements caused by accumulation of residual strains)

| Initial velocity / PU Type | 40 m/s | 50 m/s | 60 m/s | 73 m/s |
|---|---|---|---|---|
| 3000-85A at 22ºC | 0.176 mg/g | 0.33 mg/g | 0.396 mg/g | 0.418 mg/g |
| 3000-85A at 60ºC | 0.05 mg/g | 0.286 mg/g | 0.33 mg/g | RLN2 |
| 3000-85A at 100ºC | 0.231 mg/g | RLN1 | RLN1 | RLN1 |
| 3000M-85A at 22ºC | 0.055 mg/g | 0.187 mg/g | 0.242 mg/g | 0.319 mg/g |
| 3000M-85A at 60ºC | NMR | NMR | 0.176 mg/g | RLN2 |
| 3000M-85A at 100ºC | RLN1 | RLN1 | RLN1 | RLN1 |

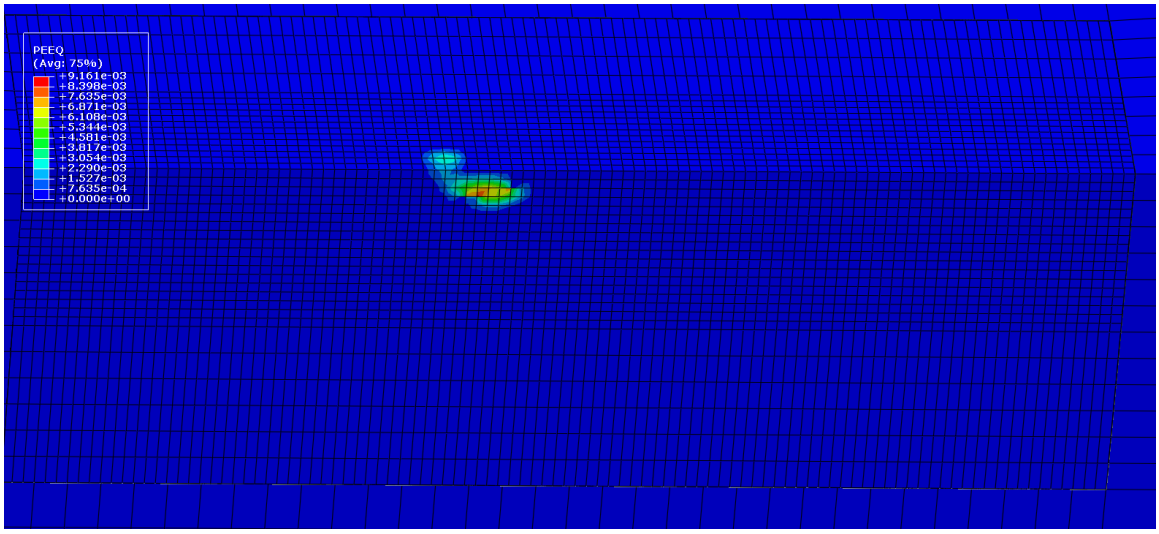


(a)

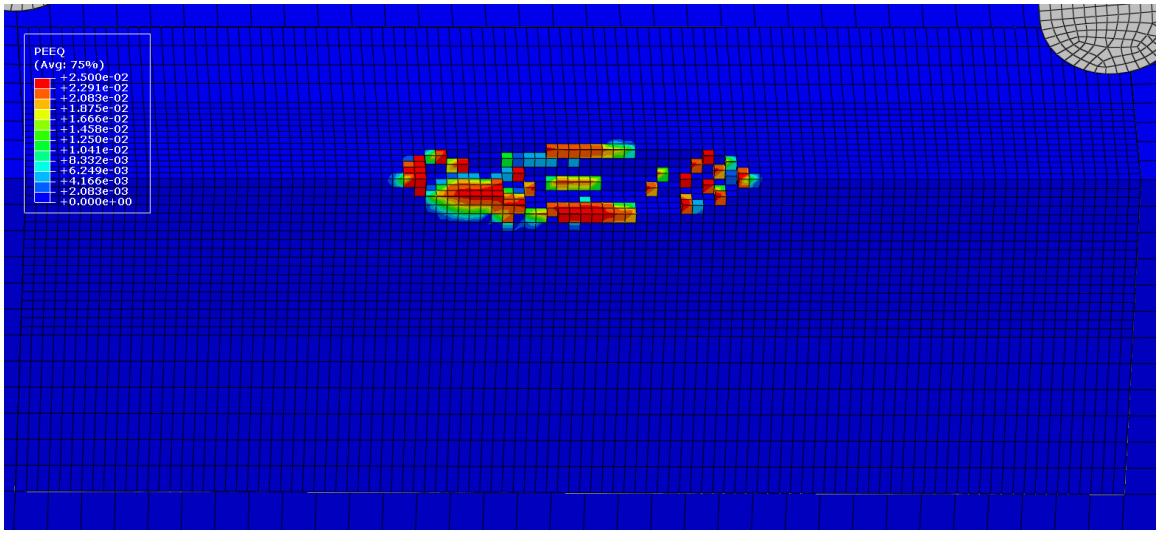


(b)

Figure 5-11 Equivalent plastic strain after impact of one erodant particle on 3000-85A PU at 100ºC with initial velocity of; a) 40 m/s, b) 50 m/s

Evaluation of the erosion rate of both PU types at 22°C and 60°C (see Table 5-1) showed that the 3000M-85A and 3000-85A elastomers had lower erosion rates at 60°C for velocities below 73 m/s and 60 m/s, respectively. In particular, for the case of 3000M-85A at 60°C, no removal of material occurred for erodant particles impacting the PU surface with initial velocities of 40 m/s and 50 m/s. Comparing the results shown in Table 5-1 with those obtained from experiments (Fig. 4-9) suggests that the FE model correctly predicted the trend of erosion rate versus temperature at lower impact velocities. The improvement in wear resistance of PU elastomers at 60°C was most probably due to the softer nature of PU at 60°C and, therefore, longer impact time with smaller impact forces.

The impact time can affect the impact force, stresses produced, and the overall resistance to erosion. As the impact time becomes longer, the impact force decrease accordingly due to the fact that the force is the time derivative of momentum as given by the impulse formula

$$m\Delta v = \int F_{\text{impact}} dt \,, \tag{5-11}$$

where $m$ is the particle mass, $\Delta v$ is variation in particle velocity vector, $F_{\text{impact}}$ is the impact force and $t$ represents time. Thus, the impact force is smaller in softer materials due to the longer impact duration. The evaluation of stress values for the 3000M-85A PU elastomer at 22ºC and 60ºC upon impact of the first erodant particle (see Fig. 5-12 and Fig. 5-13) showed that the stresses produced were higher for the PU at 22ºC due to its higher stiffness compared to the 3000M-85A PU elastomer that was heated to 60ºC (see Fig. 4-10 (d)). Thus, even though the softer substrate would allow for larger deformation of the PU surface, the impact force and, therefore, the generated stresses were smaller. The higher stress values would lead to greater Mullins damage and stress softening that can enable the fulfilment of the failure criterion in subsequent impacts.

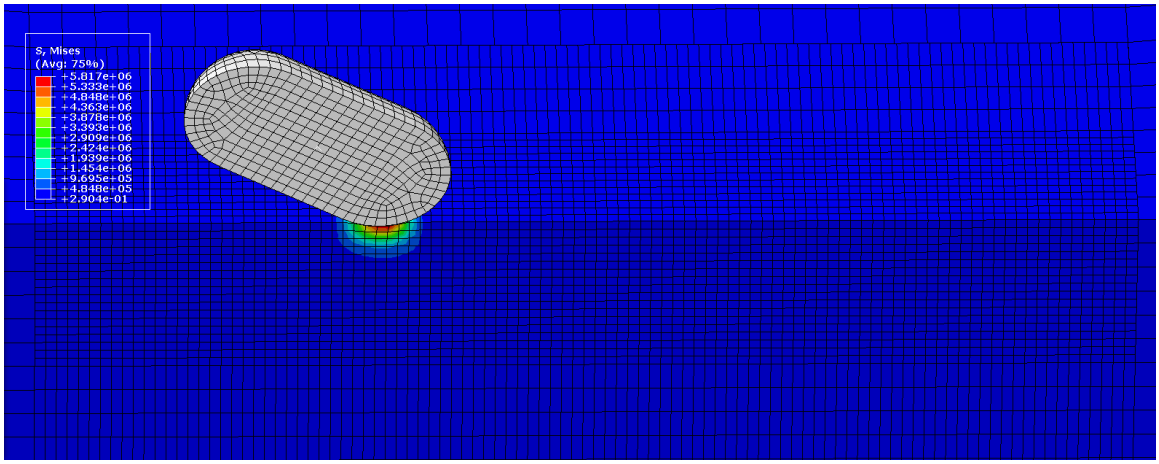


(a)

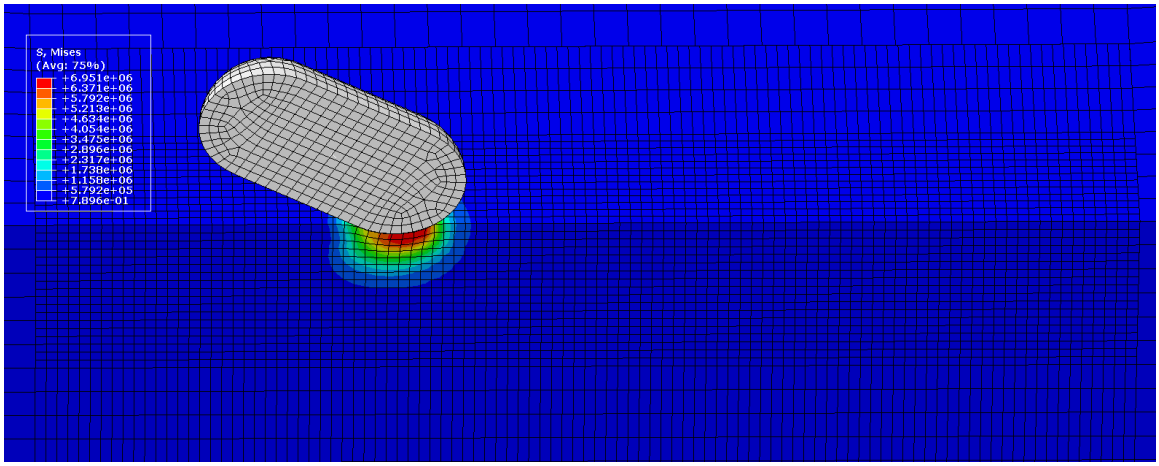
S, Mises
(Avg: 75%)
+6.951e+06
+6.371e+06
+5.792e+06
+5.213e+06
+4.634e+06
+4.054e+06
+3.475e+06
+2.896e+06
+2.317e+06
+1.738e+06
+1.158e+06
+5.792e+05
+7.896e-01

(b)

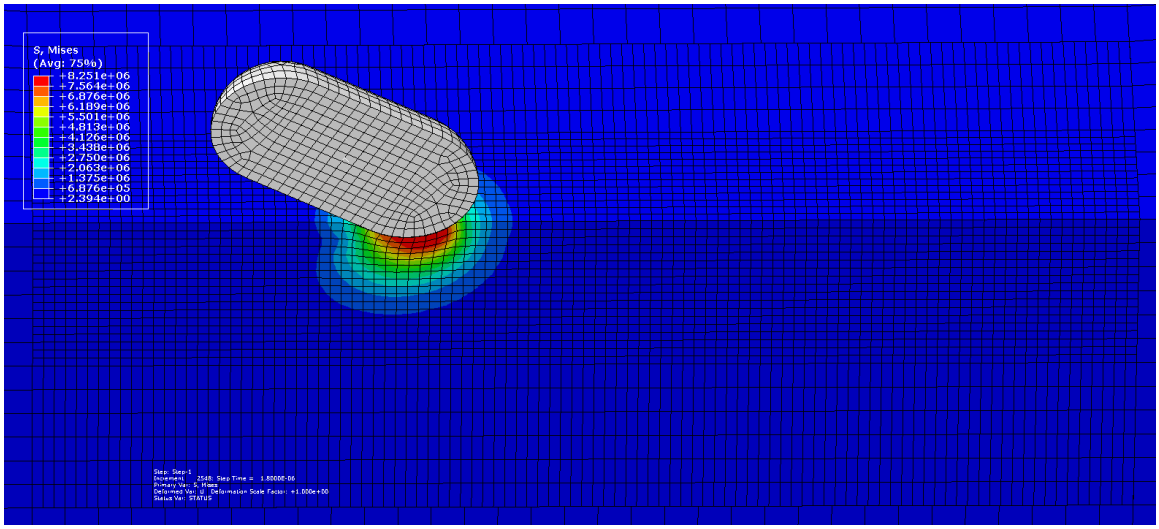
S, Mises
(Avg: 75%)
+8.251e+06
+7.564e+06
+6.876e+06
+6.189e+06
+5.501e+06
+4.813e+06
+4.126e+06
+3.438e+06
+2.750e+06
+2.063e+06
+1.375e+06
+6.876e+05
+2.394e+00

(c)

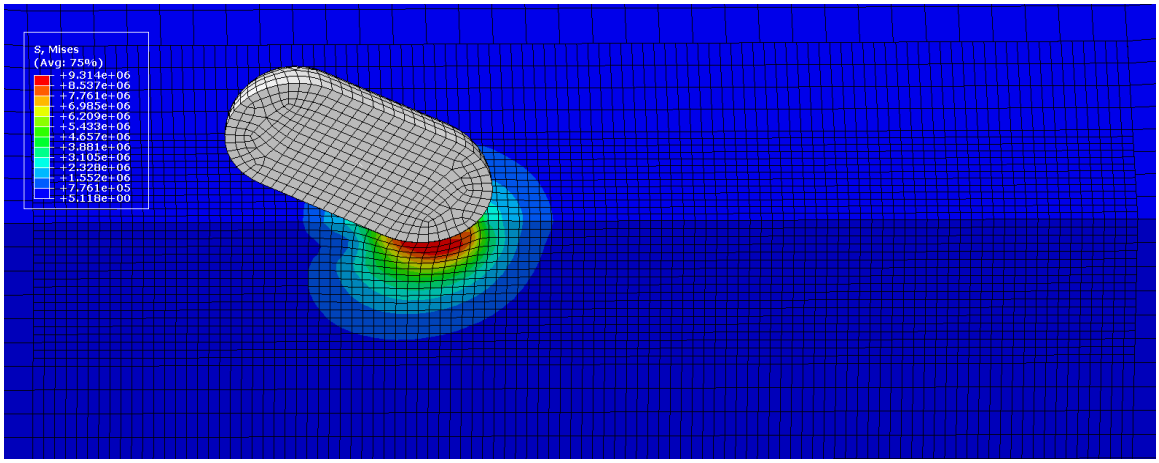
S, Mises
(Avg: 75%)
+9.314e+06
+8.537e+06
+7.761e+06
+6.985e+06
+6.209e+06
+5.433e+06
+4.657e+06
+3.881e+06
+3.105e+06
+2.328e+06
+1.552e+06
+7.761e+05
+5.11e+00

(d)

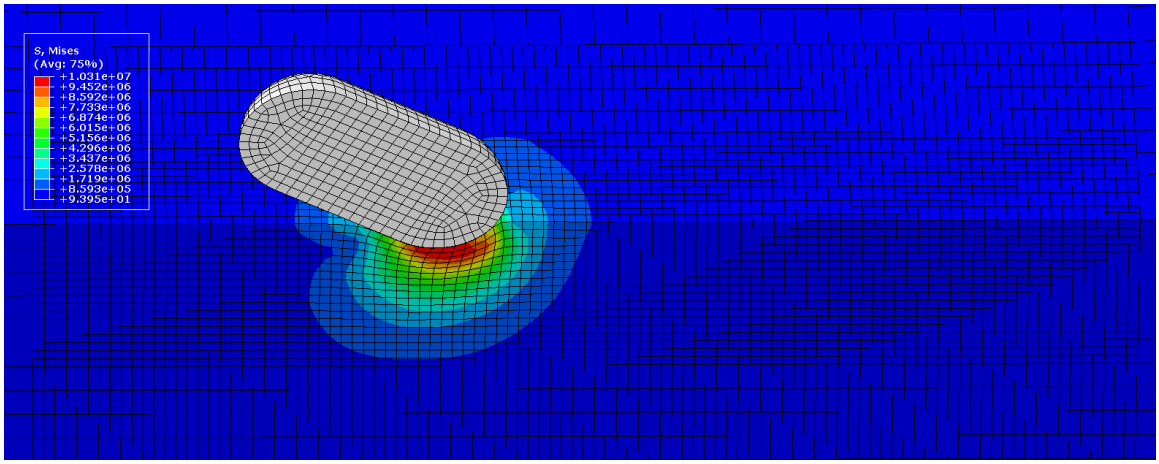


(e)

Figure 5-12 Produced stresses during the impact of a single particle with initial velocity of 50 m/s on 3000M-85A PU at 22ºC; a) $t$ = 1.2 µs, b) $t$ = 1.5 µs, c) $t$ = 1.8 µs, d) $t$ = 2.1 µs, e) $t$ = 2.4 µs

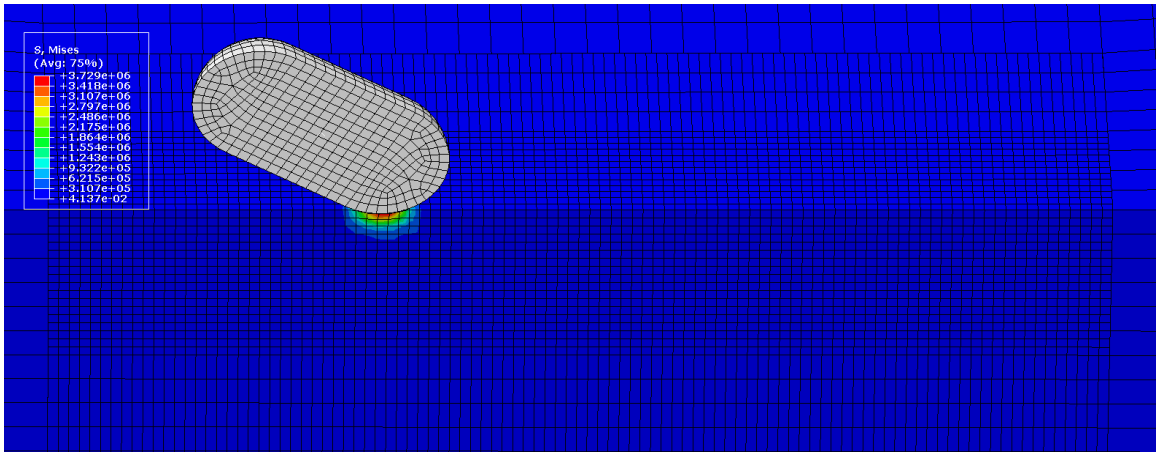


(a)

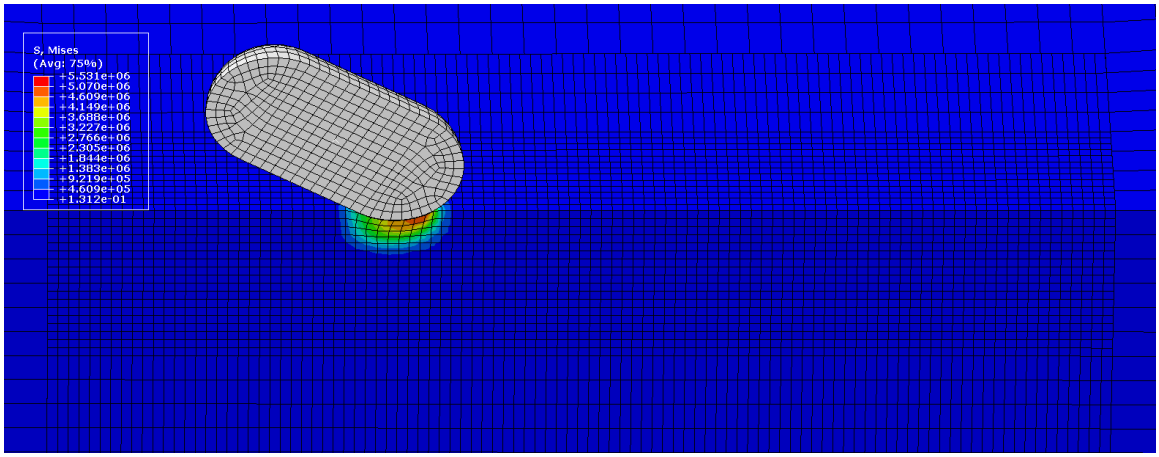
S, Mises
(Avg: 75%)
+5.531e+06
+5.070e+06
+4.609e+06
+4.149e+06
+3.688e+06
+3.227e+06
+2.766e+06
+2.305e+06
+1.844e+06
+1.383e+06
+9.219e+05
+4.609e+05
+1.312e-01

(b)

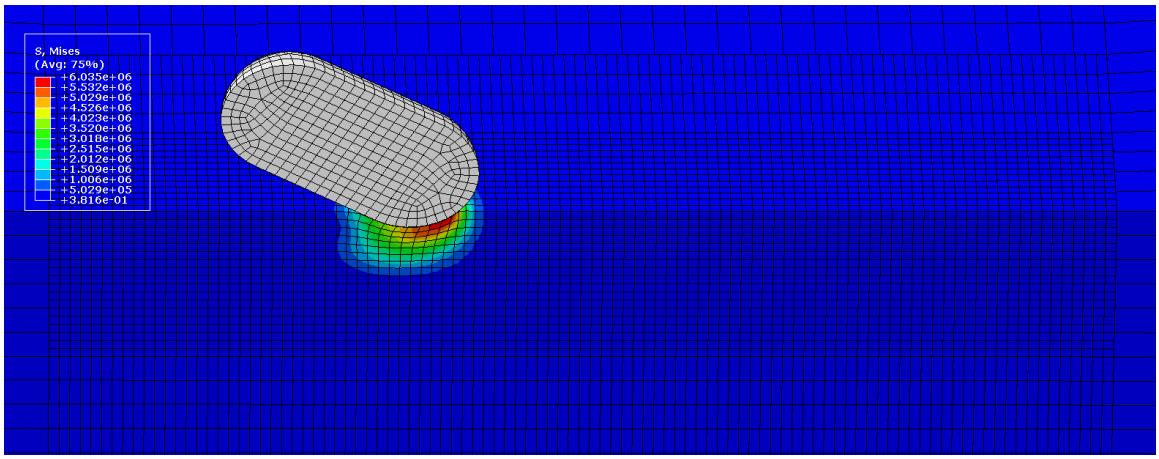
S, Mises
(Avg: 75%)
+6.035e+06
+5.532e+06
+5.029e+06
+4.526e+06
+4.023e+06
+3.520e+06
+3.018e+06
+2.515e+06
+2.012e+06
+1.509e+06
+1.006e+06
+5.029e+05
+3.816e-01

(c)

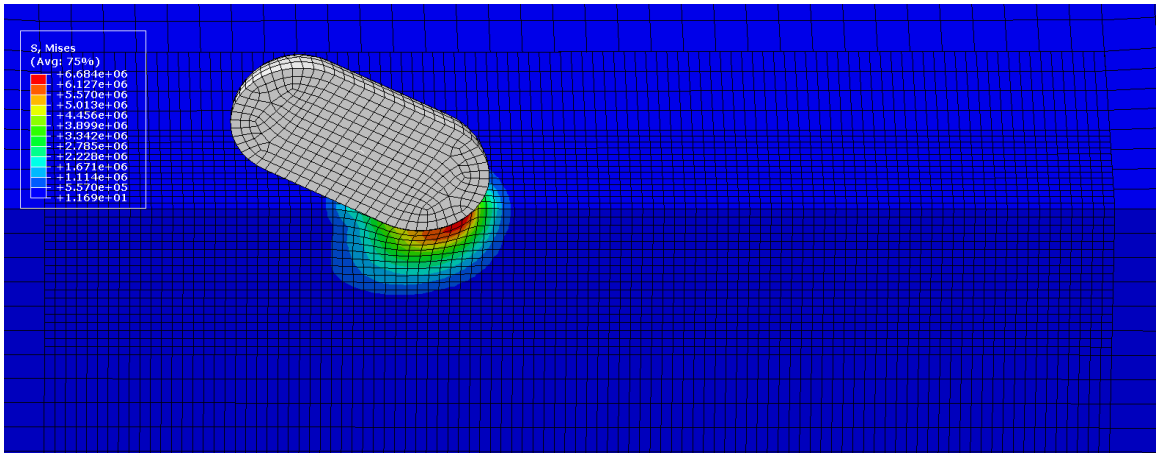
S, Mises
(Avg: 75%)
+6.684e+06
+6.127e+06
+5.570e+06
+5.013e+06
+4.456e+06
+3.899e+06
+3.342e+06
+2.785e+06
+2.228e+06
+1.671e+06
+1.114e+06
+5.570e+05
+1.169e+01

(d)

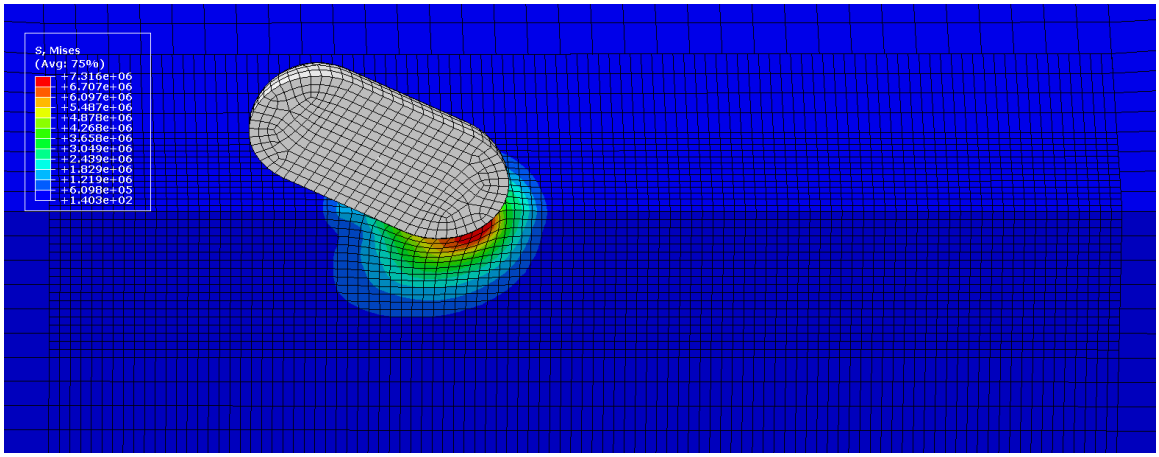


(e)

Figure 5-13 Produced stresses during the impact of a single particle with initial velocity of 50 m/s on 3000M-85A PU at 60ºC; a) $t$ = 1.2 µs, b) $t$ = 1.5 µs, c) $t$ = 1.8 µs, d) $t$ = 2.1 µs, e) $t$ = 2.4 µs

In contrast to the results obtained from experiments (see Fig. 4-9), the erosion rate of 3000M-85A at 22ºC was determined to be lower than that of the 3000-85A at 22ºC (see Table 5-1). The erosion rates determined by the model were not in agreement with the rates obtained from the experiments. This was due to the fact that the results presented in Table 5-1 incorporate only the effect of localized removal of material. However, in reality, detachment of larger asperities formed by the accumulation of residual strains up to failure was another material removal mechanism that was not taken into account in the result presented in Table 5-1. This was due to the limited number of impacting particles in the FE model. Conversely, as shown in Figs. 5-13 and 5-14, the area with residual strain in the 3000M-85A PU is larger than that of 3000-85A PU, suggesting that due to the impact of subsequent particles and increase in plastic strain up to the failure criterion, a larger volume of material will be removed from the model PU material.

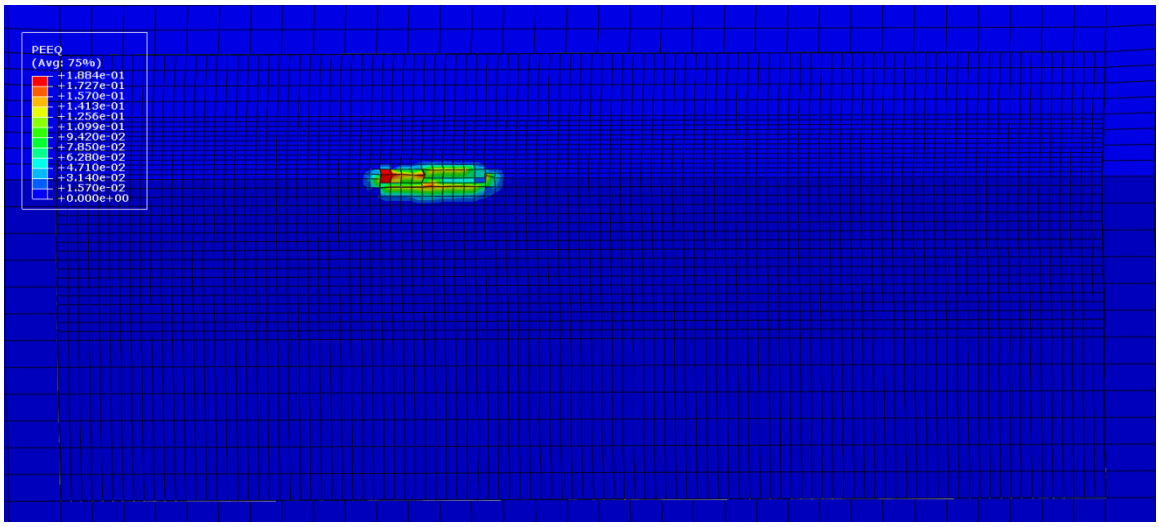
PEEQ
(Avg: 75%)
+1.884e-01
+1.727e-01
+1.570e-01
+1.413e-01
+1.256e-01
+1.099e-01
+9.420e-02
+7.850e-02
+6.280e-02
+4.710e-02
+3.140e-02
+1.570e-02
+0.000e+00

(a)

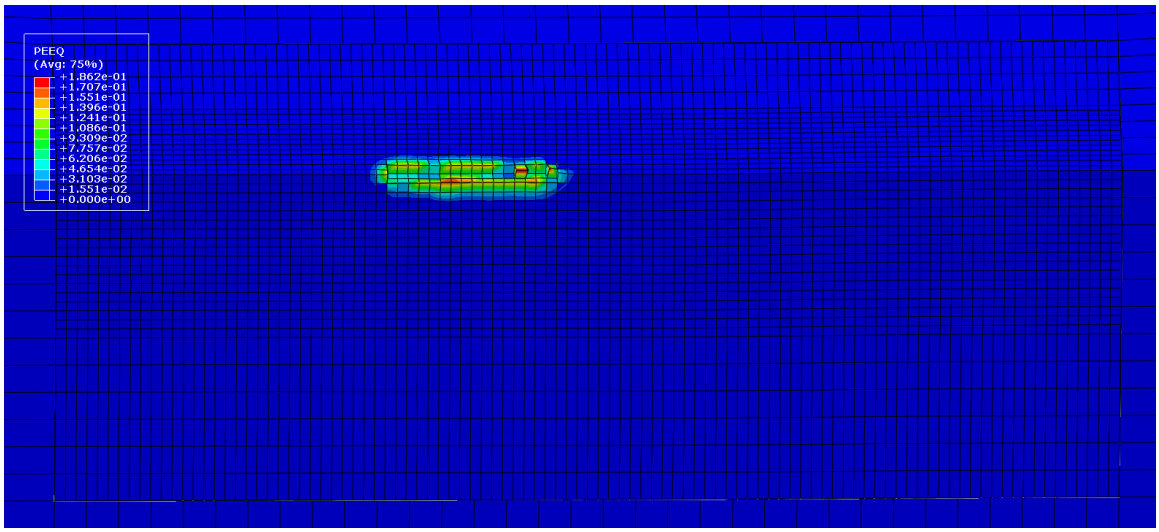
PEEQ
(Avg: 75%)
+1.862e-01
+1.707e-01
+1.551e-01
+1.396e-01
+1.241e-01
+1.086e-01
+9.309e-02
+7.757e-02
+6.206e-02
+4.654e-02
+3.103e-02
+1.551e-02
+0.000e+00

(b)

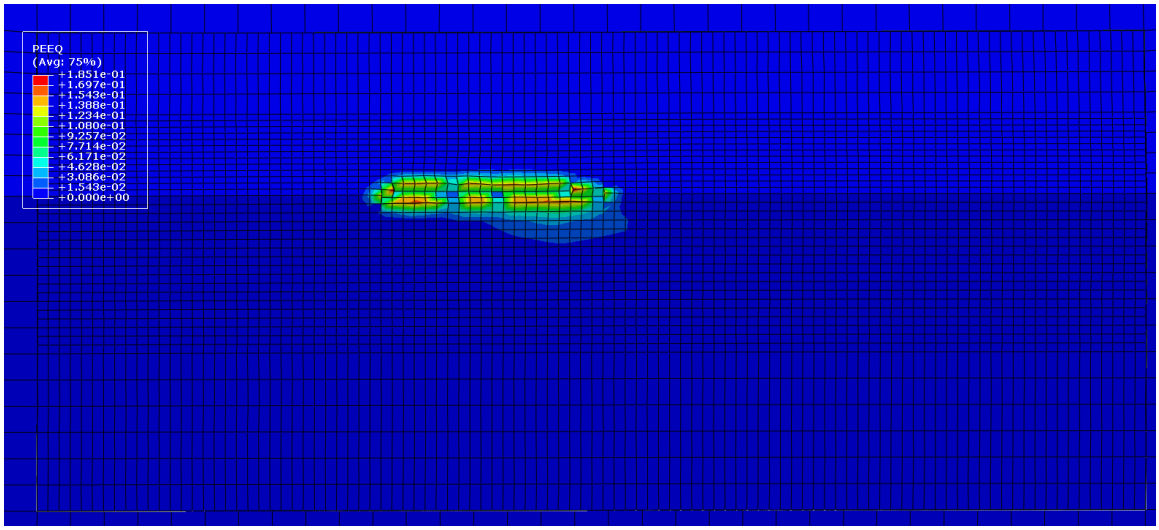


(c)

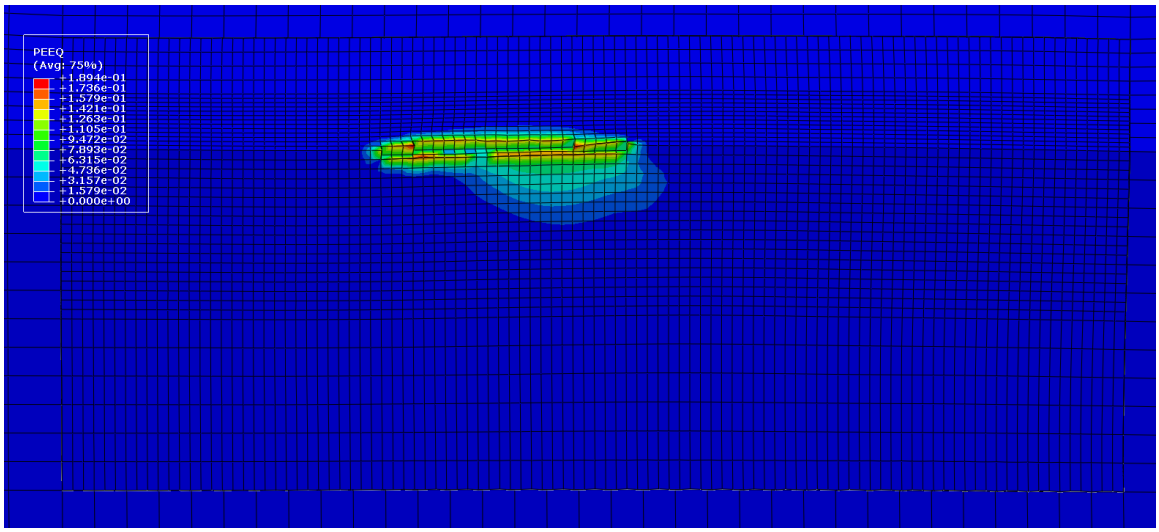


(d)

Figure 5-14 Equivalent plastic strain after impact of 10 erodant particles on 3000-85A PU at 22ºC with initial velocity of; a) 40 m/s, b) 50 m/s, c) 60 m/s, d) 73 m/s

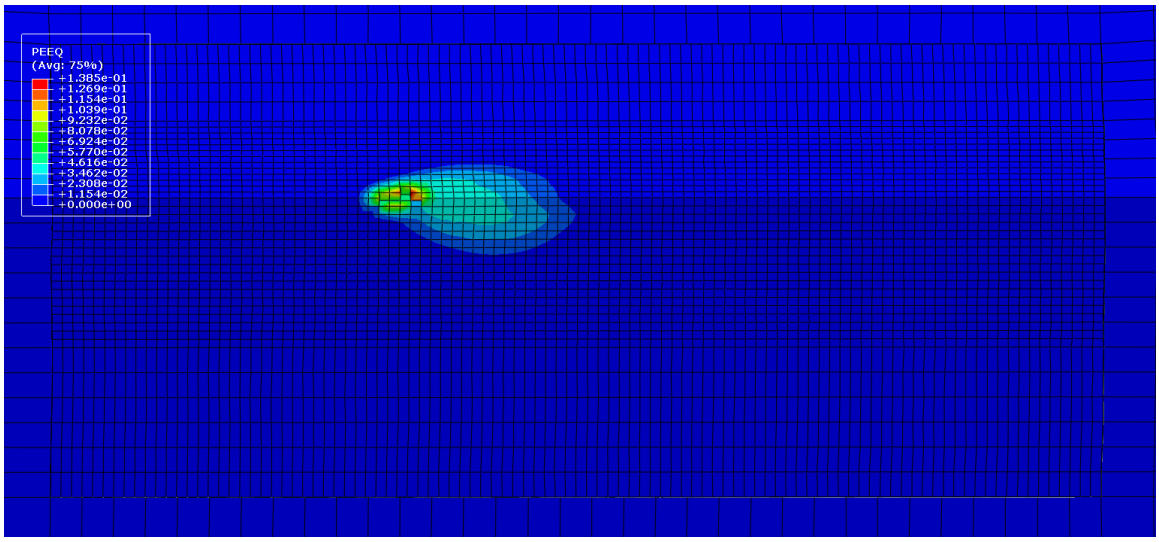
PEEQ
(Avg: 75%)
+1.385e-01
+1.269e-01
+1.154e-01
+1.039e-01
+9.232e-02
+8.078e-02
+6.924e-02
+5.770e-02
+4.616e-02
+3.462e-02
+2.308e-02
+1.154e-02
+0.000e+00

(a)

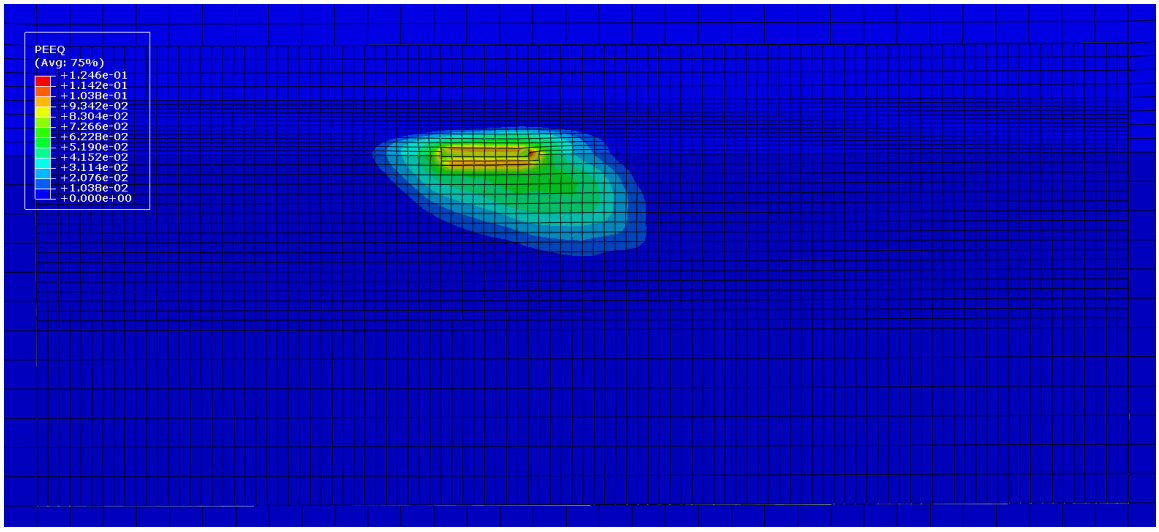
PEEQ
(Avg: 75%)
+1.246e-01
+1.142e-01
+1.038e-01
+9.342e-02
+8.304e-02
+7.266e-02
+6.228e-02
+5.190e-02
+4.152e-02
+3.114e-02
+2.076e-02
+1.038e-02
+0.000e+00

(b)

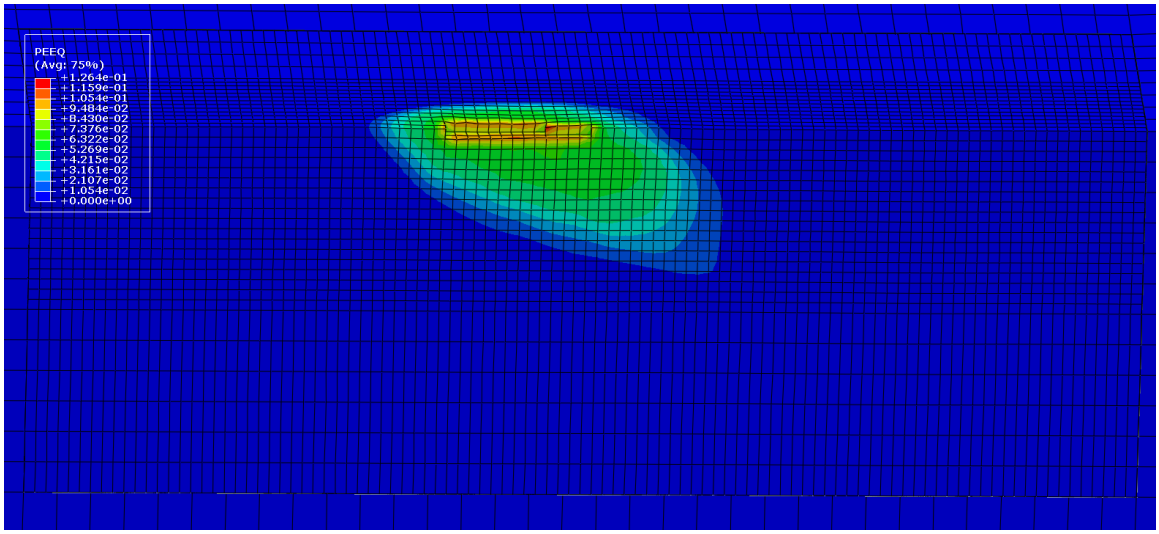


(c)

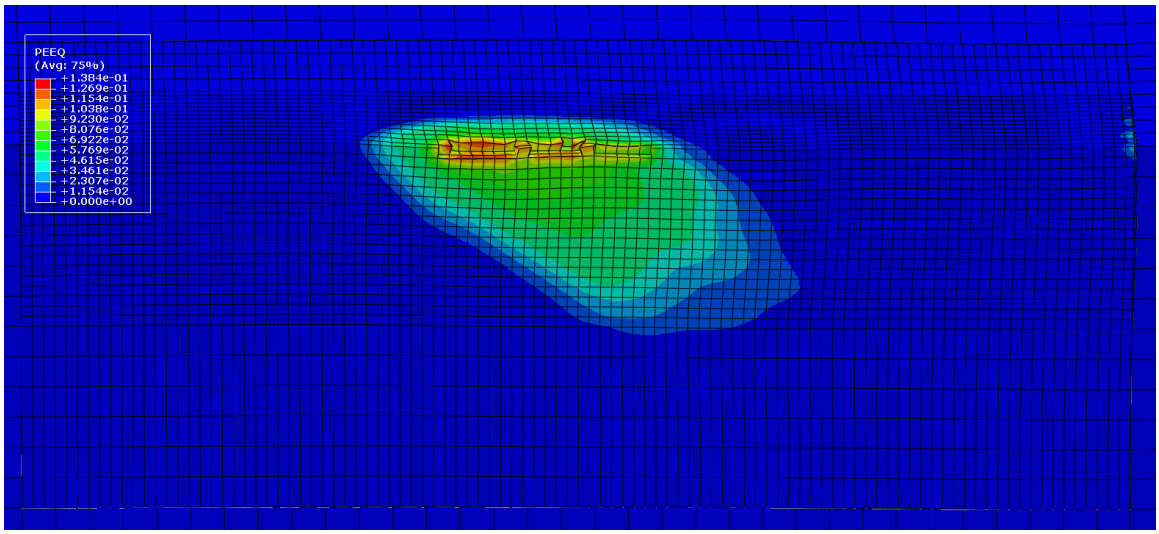


(d)

Figure 5-15 Equivalent plastic strain after impact of 10 erodant particles on 3000M-85A PU at 22ºC with initial velocity of; a) 40 m/s, b) 50 m/s, c) 60 m/s, d) 73m/s

### 5.2.4 Shortcomings of the Developed Finite Element Model

The erosion process, in general, is a complicated process involving more than one parameter that affects the final mechanism of material removal and, therefore, the erosion rate. The feasibility of employing the FE technique to model the solid particle erosion of PU

elastomers was studied. The FE model that was developed enabled the in-depth study of how the material ultimate strength, elongation at break, residual strain upon unloading, stress softening caused by Mullins damage, softness of the elastomer, and velocity of the erodant particles can contribute to the material removal mechanism and the final erosion rate of PU. In addition, the model further allowed for clarifying working temperature effects on the erosion of PU elastomers caused by impacting particles. On the other hand, the model failed to predict the correct erosion rate values mostly due to the assumptions that were made to simplify the physics of the problem to allow for the development of the FE model. Specifically, some limitations associated with assumptions are as follows.

- The FE model simulated the impact of particles with similar shape and dimensions while in reality, particles with different shapes, dimensions, and corner radii impact the PU surface (see Fig. 4-2). The shape of the erodant particles play an important role in the determination of the erosion rate, given that the irregular shape or roundness of the particle corners can affect the stresses produced, material removal mechanism, and, therefore, the erosion rate. In addition, due to the possible rotary motion of the erodant particles upon impact, the particles may collide with the surface of the PU with rounder corners, thus producing smaller stresses and, therefore, overall lower erosion rate.
- In the model, it was assumed that the erodant particles impact on a single spot and only impact of 10 particles was modeled. The assumption of the impact of the erodant particles on a single spot could have been one of the reasons for the overestimation of the erosion rate. On the other hand, in reality many particles impact the PU surface during the erosion experiment. The use of parallel processing techniques will be required to facilitate a simulation with a higher number of impacting particles. Furthermore, knowledge about the

distribution, frequency of the impact of particles and energy loss due to the particle in-flight time prior to impact are other parameters that should be taken into account when modeling the erosion process.

- Similar to previous studies [7, 90, 91], in the model, the removal of elements from the model upon reaching the failure criterion was assumed to represent the erosion of the surface. In fact, it was assumed that the removed elements were equivalent to material loss from the surface. This assumption led to the overestimation of the erosion rate caused by the impact of erodant particles. This was one of the major outcomes of this study showing that the assumption that can be made for FE modeling of the erosion process of ductile metals and brittle ceramics cannot be made for soft elastomers that experience large deformations upon impact. Improvement in the FE formulation such way that can model the failed elements as detached parts rather than deleting them from the model will be required to mitigate the overestimation of the material removal in the FE simulation.

# Chapter 6

# Conclusions

In this research program and thesis, the possibility of employing the flame spraying process for the metallization of PU substrates, as well as the possible influence of the fabricated coatings on wear resistance of PU elastomers was studied. Due to the heat sensitivity of PU elastomers, knowledge about the temperature distribution within the substrates was required. To that end, one of the primary objectives of this study were to develop a model capable of predicting the temperature distribution within a PU substrate during the flame spraying process. An average heat flux was employed by the model to predict the temperature distribution within the PU substrate. The model was solved analytically based on a Green's function approach and numerically by the finite volume technique. Good agreement was achieved between the experimental results and those predicted by the heat transfer model, and hence, the modeling approach was verified.

Another approach for prediction of the temperature distribution within the substrate based on solving the model with existence of an insulated surface on the back of the substrate was also studied. It was found that the model was valid for the period of time before the thermal wave arrives at the back surface of the substrate. Non-dimensionalized parameters were defined to find a parameter that can describe the time period in which the model was applicable. Based on the results obtained, it was found that the model was only valid for values of non-dimensionalized times (Fourier number) smaller than 0.4 and lacks sufficient accuracy beyond that point.

The developed model allowed for monitoring of the temperature distribution within the PU substrate during deposition of Al-12Si coatings. Al-12Si coatings were successfully deposited on PU substrates by employing the flame spraying process. The influence of pressure of air injected into the flame spray torch on the substrate temperature distribution and the corresponding effects on coating properties was thus studied. It was found that although increasing the air pressure lowered the temperatures of the flame and feedstock powder, the splats experienced a higher degree of deformation as a result of increase in velocity and impact of the particles with a stiffer substrate of lower temperature. Higher deformation of the splats led to better interlocking and, therefore, improved electrical conductivity. This suggests that the temperature distribution within the substrate during thermal spraying on elastomers is an important factor that, alongside with other parameters such as velocity and temperature of the impacting particles, can affect the properties of the deposited coating. It was further found that by increasing the air pressure from 135 kPa to 205 kPa, it was possible to decrease the stand-off distance from 215 mm to 150 mm and maintain a nearly constant temperature distribution within the PU substrate. Spraying at shorter stand-off distance of 150 mm led to deposition of a low-porosity coating with an electrical resistivity of as low as $0.9 \times 10^{-3}$ Ω-cm. The results of an XRD analysis indicated that the content of oxides was negligible and the predominant factor that account for the increased electrical resistivity of the coating, in comparison to that of the base Al-12Si material ($4.25 \times 10^{-6}$ Ω-cm), was likely the presence of pores in the coating as well as its lamellar microstructure.

The coatings were produced without any visible damage or deterioration of the PU substrate. Possible chemical or microstructural damage effects within the substrate were further assessed by conducting dynamic mechanical analysis with virgin and flame-exposed PU

samples. The storage modulus was selected as an indicator for comparison purposes, and it was found that the storage modulus of the flame-exposed samples increased insignificantly with respect to the virgin samples and no critical change in PU substrate properties in response to the flame spraying process was noticed.

The deposited metallic coating can affect the temperature distribution within the PU, and therefore, its resistance to wear. Consequently, knowledge of temperature effects on the wear behavior of PU elastomers was of interest. To that end, an erosion testing assembly for evaluating the wear resistance of PU elastomers at controlled temperatures was designed and developed. A cold gas dynamic spray system was used to enable the erosion tests. The velocity of the blast media was estimated by the use of an analytical model based on the flow of a compressible gas through the cold spray nozzle. The temperature distribution within the PU samples during the erosion tests was computed employing a heat transfer model based on a FE analysis. The model was validated by comparing the calculated temperature with the experimental data that was measured with a thermocouple. The calculated temperature distribution showed that the temperature in the to-be-eroded area was uniformly close to 60ºC and 100ºC for elevated temperature experiments.

The evaluation of the wear resistance of PU elastomers at controlled temperatures showed that the different PU elastomers do not generally exhibit similar behavior. Two of the tested PU elastomers showed improvement in erosion rate at 60ºC while the other studied elastomers exhibited an increase in erosion rate. At 100ºC, an increase in erosion rate for all studied PU elastomers was ascertained. The evaluation of the mechanical properties of the studied PU elastomers suggested that the improvement in erosion rate at 60ºC was due to an

improved ability of the material to regain its initial state following deformation. This behavior was studied by calculating the permanent set of the studied PU elastomers for cyclic loading. It was further found that although there is no simple relation between the ultimate failure stress/elongation at break and erosion rate, it is evident that elongation at break is one of the parameters affecting the final wear resistance and the morphology of worn surfaces. Besides, studying the effect of working temperature on erosion performance of PU elastomers allowed for a closer examination of erosion mechanisms for PU elastomers, and introduced plastic deformation, Mullins stress softening, ultimate failure stress and elongation at break as key parameters affecting the PU wear resistance.

A numerical model based on the finite element technique was developed to better understand the mechanism of material removal during solid particle impact on PU elastomers, and to study the effect of erosion testing temperature on the produced stresses. The FE model simulated the impact of 10 erodant particles at a single location on the substrate elastomer at controlled temperatures of 22ºC, 60ºC, and 100ºC. The results obtained from the FE model showed that at velocities higher than a critical value, the stresses that were produced upon the initiation of the impact were higher than the ultimate stress of the PU material, which led to the removal of elements that were in contact with the erodant particle. The model successfully demonstrated the importance of ultimate failure stress and elongation at break of the material as parameters affecting the erosion rate for velocities higher than a threshold. The model successfully simulated the mechanism of material removal as the accumulation of residual strains up to the detachment of larger pieces from the surface and provided further evidence for what was suggested as the erosion mechanism of PU elastomers. Evaluation of the surface morphology of the worn samples showed that the model was capable of predicting the

morphology of the formed asperities similar to those observed in SEM images taken from the top surface of worn samples. Moreover, the model showed that the Mullins damage caused by the impact of particles can facilitate the detachment of localized small fragments from the surface upon impact of subsequent particles. The evaluation of the surface morphology of worn samples supported the results obtained by the FE model and showed that the detachment of small fragments caused by cutting and gouging could have been another mechanism of material removal. While the FE numerical model allowed for an in-depth study of the erosion phenomenon of PU elastomers, the model failed to predict the correct values of erosion rates, which most probably is due to the assumptions that were made to simplify the model.

In previous studies of FE modeling of the erosion phenomenon of ductile metals and brittle ceramics, the removal of elements from the model upon reaching the failure criterion was assumed to represent the material removal from the surface. It was found in this study that this assumption led to the overestimation of the erosion rate caused by the impact of erodant particles. This was one of the major outcomes of this study showing that the assumption that can be made for FE modeling of the erosion process of ductile metals and brittle ceramics will overestimate the material removal for soft elastomers that experience large deformations upon impact.

From what was observed by experiments and numerical simulation of the erosion process caused by solid particle impact, it can be concluded that the softer PU elastomer can allow for a longer impact duration and, therefore, lower impact forces. On the other hand, the PU should have high elongation at break to ensure that its ultimate failure stress is high enough to prevent failure of the material upon impact of an erodant particle. In addition, the greater tendency of PU

to return to its initial condition with minimal plastic deformation and stress softening caused by Mullins damage upon loading are other parameters that are of interest for an ideal PU elastomer with maximum resistance to erosion.

Finally, based on the studied erosion conditions of PU materials, a deposited metallic layer may distribute heat effectively to mitigate localized high temperatures in a PU liner and resulting adverse effects on its wear resistance. Moreover, in case of employing PU liners with properties similar to the tested 3000 series PU elastomers, the coating may function as a heater to elevate the temperature of the PU liner and promote a lower erosion rate.

# Chapter 7

# Recommendations for Future Work

This research program has made significant contributions in the area of thermal spray deposition of metallic coatings on polymer-based substrates, development of heat transfer models for the determination of temperature distribution within a substrate during the spraying process, and analysis of the wear phenomenon of PU elastomers by experiments and numerical simulations. However, this work can be expanded and enhanced further, and several recommendations for future work can be given as follows:

- In the development and validation of the proposed heat transfer model for determining the temperature distribution within a substrate during the spraying process, no powder was deposited and it was assumed that the additional heat input from the molten and partially molten Al-12Si particles was negligible compared to the heat flux from the flame spray torch. The validity of this assumption was verified by experiments in this study. However, this assumption may not be valid for the case of deposition of powders with high melting temperatures such as nickel alloys. Although powders with high melting temperatures require higher torch heat fluxes, the amount of heat input from molten and partially molten particles may not be negligible when compared to the heat flux from the torch. To that end, further investigation is required to determine if the error induced by the assumption of a negligible influence of the powder on the temperature distribution of the proposed heat transfer model is reasonable when depositing powders with high melting points.

- In this study, a material similar to that of the sprayed powder was used to roughen the substrate as a part of surface treatment prior to the thermal spraying process. In other studies [18], roughening of the substrate by the addition of a material with low thermal conductivity such as garnet sand has been suggested to protect the polymeric heat sensitive substrate from the high temperatures of the thermal spraying process. The studies that have focused to study the effectiveness of this technique on reducing the temperature distribution within the substrate are limited. The model presented in this study can be extended to account for the effect of an added layer of material with low thermal conductivity on the top surface. An experimental assembly similar to what was employed in this study can be designed and installed to provide data as for the verification of the developed model.

- The electrical resistivity of the coating was found in this study to be approximately three orders of magnitude higher than the bulk sprayed material. Porosities and a lamellar microstructure of the coating were introduced as the possible sources of increased electrical resistance. The number of studies that have focused on finding a relation between the porosity and electrical resistance of thermally-sprayed coatings are limited. Thus, studying the effect of porosity and clearances between splats on the electrical resistance by experiments and modeling is suggested as one of the future extensions of this thesis research. The results from this work may provide information about the feasibility of employing of these types of coatings as structural health monitoring devices.

- It was shown in this study that the temperature distribution within the substrate during thermal spraying on elastomers is an important factor that, along with other parameters such as velocity and temperature of the impacting particles, can affect the properties of the deposited coating such as porosity, electrical resistivity, and deformation of the impacting powder particles. The changes in substrate softness as a result of different temperature distributions was found to be one possible factor affecting the deformation of molten and semi-molten droplets upon impact. The number of studies that have focused on evaluating the effect of substrate softness on the properties of the fabricated coatings are limited. An experimental study for thermal spray deposition of metallic coatings on elastomers with different softness is recommended as future work. Moreover, the number of studies that have focused on modeling droplet deformation on soft substrates are limited. Modeling of this process can provide greater insight in the deformation behavior of impacting droplets on soft substrates.

- In this study, an experimental assembly for erosion testing at controlled temperatures was designed and developed. The test assembly allowed for evaluating the effect of temperature on erosion rate and mechanism of material removal caused by solid particle impact. On the other hand, the mechanism of material removal of PU elastomers during abrasion wear may be different from that of the erosion caused by solid particle impact. To that end, the development of an abrasion testing assembly with controlled temperatures is suggested as a possible extension of this thesis work to study the effect of temperature on the abrasion resistance of PU elastomers and further investigate the mechanism of material removal during abrasion wear. The testing equipment may be

modified from the ASTM Standard G65 abrasion testing procedure [89] to incorporate the effect of temperature during the test. Similar to this work, a heat transfer model to determine the temperature for the area to be abraded may be developed. This study would assist with estimating the overall efficiency of PU liners against wear given that in many industrial applications, a combination of abrasive-erosive wear mechanisms can occur.

- The repeated deformation of PU by the impact of erodant particles and the friction forces between the impacting particles and the PU surface can lead to generation of heat and, therefore, temperature rise within PU during the erosion process. In this study, the data obtained from the thermocouple inserted 1.5 mm below the surface revealed that the temperature rise caused by the impact of erodant particles was negligible most likely due to the high heat transfer rate through convection and relative low feeding rate of the erodant particles. On the other hand, localized temperature rise close to the surface, within the micrometer range, may occur and may affect the mechanism of material removal. Design of an experimental setup that can allow for monitoring of the transient temperature rise of PU close to the surface during the impact of erodant particles and a study of the effect of the temperature rise on the material removal mechanism and produced stresses by modeling is recommended for future work. The results obtained from this study can provide greater insight on the wear mechanism of PU elastomers.

- The deposited metallic coatings on polymer-based structures can be employed as resistive (Joule) heating to function as heating elements [30, 31]. This thesis showed the feasibility of depositing conductive coatings on PU substrates and studied the effect of temperature

on erosion resistance of PU elastomers. However, in this thesis work, the effect of Joule heating on the temperature distribution of PU elastomers and its corresponding effect on the erosion resistance was not studied. Thus, deposition of a metallic coating on a PU substrate and evaluation of the erosion resistance of the PU while warming by Joule heating is suggested for future work. After fabrication of the metallic coating on the PU, another layer of PU may be fabricated on the metallic coating to confine the metallic coating within the layers of PU similar to what is presented in Fig. 1-2. Later, the erosion resistance of the PU-metallic coating system may be evaluated while warming it by resistive heating. The results from this research can provide insight in possible industrial applications of this type of heating and further evaluate the effect of heating on the wear resistance. Evaluating the effect of temperature on the adhesion strength of a PU-metallic coating structure can be considered another future research task.

- In this study, the mechanical properties such as ultimate failure stress, elongation at break and response of the PU material to cyclic loadings were evaluated at low strain rates. This thesis showed that the data obtained at low strain values correlates well with the observed erosion rate and the data obtained was ascertained to be a suitable input for a numerical model simulating the erosion process. The main advantage of acquiring the data at low strain rates is the simplicity of the testing setup that was used. However, the erosion caused by solid particle impact takes place at very high strain rates where the elastomer material response may be different from that at low strain rates. This thesis work can be extended to evaluate the relation between the stress-strain behavior obtained at high strain

rates and erosion rates at controlled temperatures. To that end, a testing apparatus capable of tensile testing at high strain rates will be needed.

- The FE model that was developed to simulate the erosion of PU caused by solid particle impact allowed for better understanding of (i) the rebounding of impacting erodant particles from the PU surface, (ii) the material removal mechanisms, and (iii) the material properties with the most significant effect on the erosion rate. However, the FE model failed to accurately predict the erosion rate quantitatively, most probably due to the assumptions that were made to simplify the problem. The following future works are suggested to further extend and modify the developed model:

  (a) Accurate determination of the erodant particle velocity profile and applying this profile in the FE model.
  (b) Use of parallel computer processing techniques to allow for modeling a larger number of erodant particles.
  (c) Presence of erodant particles with different sharpness and roundness on corners to study the effect of particle shape on the erosion resistance of PU elastomers.
  (d) Development of a new formulation for element removal upon reaching the failure criteria so that the failed elements remain in the model, as opposed to the element deletion technique employed in the present study.
  (e) Development and coding of a new material model that can account for both the viscoelastic behavior and plastic deformation, which is of interest given that in the

present study the Abaqus material model for viscoelastic behavior cannot be combined with isotropic hardening.

# References


[1] A. Al-Hamed, H.Y. Al-Fadhli, S. Al-Mutairi, B.S. Yilbas, M.S.J. Hashmi, J. Stokes, Investigation of HVOF thermal sprayed nanostructured WC-12Co mixed with inconel-625 coatings for oil/gas applications, WIT Trans. Eng. Sci. 78 (2013) 215-225.

[2] M.A. Zavareh, A.A.D.M. Sarhan, P.A. Zavareh, B.B.A. Razak, W.J. Basirun, M. CheIsmail, Development and protection evaluation of two new, advanced ceramic composite thermal spray coatings, $Al_2O_3$-40$TiO_2$ and $Cr_3C_2$-20NiCr on carbon steel petroleum oil piping, Ceram. Int., 42 (2016) 5203-5210.

[3] M.A. Zavareh, A.A.D.M. Sarhan, P.A. Zavareh, W.J. Basirun, Electrochemical corrosion behavior of carbon steel pipes coated with a protective ceramic layer using plasma and HVOF thermal spray techniques for oil and gas, Ceram. Int. 42 (2016) 3397-3406.

[4] H. Ashrafizadeh, F. Ashrafizadeh, A numerical 3D simulation for prediction of wear caused by solid particle impact, Wear 276-277 (2012) 75-84.

[5] P. L. Fauchais, J.V.R. Heberlein, M.I. Boulos, Thermal Spray Fundamentals From Powder to Part, Springer, New York, USA, 2014.

[6] P. Mertiny, K. Juss, and T. Bell, Corrosion and erosion resistant polymer composite pipe for oil sands hydrotransport, Proceedings of the NACE International Corrosion Conference and Expo, (2008) New Orleans, LA, USA, Paper # 08667.

[7] N. Zhang, F. Yang, L. Li, C. Shen, J. Castro, L. J. Lee, Thickness effect on particle erosion resistance of thermoplastic polyurethane coating on steel substrate, Wear 303(1–2) (2013) 49-55.

[8] J. Li, I. M. Hutchings, Resistance of cast polyurethane elastomers to solid particle erosion, Wear 135(2) (1990) 293-303.

[9] J. C. Arnold, I. M. Hutchings, The mechanism of erosion of unfilled elastomers by solid particle impact, Wear 138 (1990) 33-46.

[10] Y. Xie, J. Jiang, K. Y. Tufa, S. Yick, Wear resistance of materials used for slurry transport, Wear 332-333 (2015) 1104-1110.

[11] F. J. Martinez, M. Canales, J. M. Bielsa, M. A. Jimenez, Relationship between wear rate and mechanical fatigue in sliding TPU-metal contacts, Wear 268 (2010) 388-398.

[12] I. Clemitson, Castable Polyurethane Elastomers, Taylor and Francis Group, 2008.

[13] K. G. Budinski, Guide to Friction, Wear and Erosion Testing, ASTM International, West Conshohocken, PA, USA, 2007.

[14] S. W. Zhang, W. Deguo, Y. Weihua, Investigation of abrasive erosion of polymers, J. Mater. Sci. 30 (1995) 4561-4566.

[15] Z. Ping, L. Youwei, Y. Chengqing, L. Jian, Erosion behaviors of polymer coatings, Proceedings of CST2008 & ITS-IFToMM, Beijing, China, 2008, pp. 738-741.

[16] P. Mertiny, R. Popella, K. Juss, Manufacturing of large-scale polyurethane-lined FRP piping, Proceedings of the ASME 2011 Pressure Vessels & Piping Division Conference, (2011) Baltimore, Maryland, USA, Paper # PVP2011-57870.

[17] N. Huonnic, M. Abdelghani, P. Mertiny, A. McDonald, Deposition and characterization of flame-sprayed aluminum on cured glass and basalt fiber-reinforced epoxy tubes, Surf. Coat. Technol. 205(3) (2010) 867-873.

[18] R. Gonzalez, A. McDonald, P. Mertiny, Effect of flame-sprayed Al-12Si coatings on the failure behavior of pressurized fiber-reinforced composite tubes, Polym. Test. 32 (2013) 1522-1528.

[19] F. Robitaille, M. Yandouzi, S. Hind, B. Jodoin, Metallic coating of aerospace carbon/epoxy composites by the pulsed gas dynamic spraying process, Surf. Coat. Technol. 203(19) (2009) 2954-2960.

[20] J. Voyer, P. Schulz, M. Schreiber, Conducting flame-sprayed Al coatings on textile fabrics, J. Therm. Spray Technol. 17(4) (2008) 583-588.

[21] J. Voyer, P. Schulz, M. Schreiber, Electrically conductive flame sprayed aluminum coatings on textile substrates, J. Therm. Spray Technol. 17(5-6) (2008) 818-823.

[22] C.L. Beyler and M. Hirschler, Thermal Decomposition of Polymers, SFPE Handbook of Fire Protection Engineering, 3rd ed., P.J. DiNenno, Ed., NFPA, 2001.

[23] T.G. McNaughton, K.W. Horch, Metallized polymer fibers as leadwires and intrafascicular microelectrodes, J. Neurosci. Methods 70(1) (1996) 103-10.

[24] J. Siegel, V. Kotal, Preparation of thin metal layers on polymers, Acta Polytech. 47(1) (2007) 9-11.

[25] T. Duguet, F. Senocq, L. Laffont, C. Vahlas, Metallization of polymer composites by metalorganic chemical vapor deposition of Cu: Surface functionalization driven films characteristics, Surf. Coat. Technol. 230 (2013) 254-259.

[26] K.P. Gritsenko, Metal-polymer optical storage media produced by PECVD, Thin Solid Films 227(1) (1993) 1-2.

[27] L. Pawlowski. The Science and Engineering of Thermal Spray Coatings. 2nd ed. John Wiley & Sons, Ltd., New York, NY, USA. 2008.

[28] S. Kuroda, J. Kawakita, M. Watanabe, H. Katanoda, Warm spraying - A novel coating process based on high-velocity impact of solid particles, Sci. Technol. Adv. Mater. 9(3) (2008) 1-17.

[29] J.R. Davis, Handbook of Thermal Spray Technology, ASM International, Materials Park, OH, United States, 2004.

[30] A. Lopera-Valle, A. McDonald, Use of flame-sprayed coatings as heating elements for polymer-based composite structures, International Thermal Spray Conference 2015, Long Beach, CA, USA, 2015, pp. 1183-1190.

[31] A. Lopera-Valle, A. McDonald, Application of flame-sprayed coatings as heating elements for polymer-based composite structures, J. Therm. Spray Technol. 24(7) (2015) 1289-1301.

[32] An Introduction to Thermal Spray, Oerlikon Metco, Reproduced from http://www.oerlikon.com/ecomaXL/files/metco/oerlikon_Thermal_Spray_Brochure_EN5.pdf, June 2015.

[33] P. Fauchais, A. Vardelle, Heat, mass and momentum transfer in coating formation by plasma spraying, Int. J. Therm. Sciences 39(9-11) (2000) 852-870.

[34] P. Fauchais, G. Montavon, Thermal and cold spray: Recent developments, Key. Eng. Mat. 384 (2008) 1-59.

[35] R.W. Smith, R. Knight, Thermal spraying I: powder consolidation - from coating to forming, J. Minerals, Metals & Mater. Soc. 47(8) (1995) 32-39.

[36] A. McDonald, M. Lamontagne, C. Moreau, S. Chandra, Impact of plasma-sprayed metal particles on hot and cold glass surfaces, Thin Solid Films 514(1-2) (2006) 212-222.

[37] M.P. Dewar, A.G. McDonald, A.P. Gerlich, Interfacial heating during low-pressure cold-gas dynamic spraying of aluminum coatings, J. Mater. Sci. 47(1) (2012) 184-198.

[38] T. Schmidt, F. Gartner, H. Assadi, H. Kreye, Development of a generalized parameter window for cold spray deposition, Acta Materialia 54 (3)(2006) 729-742.

[39] P. Fauchais, M. Fukumoto, A. Vardelle, M. Vardelle, Knowledge concerning splat formation: An invited review, J. Therm. Spray Technol. 13(3) (2004) 337-360.

[40] A. Moridi, S. Hassani-Gangaraj, M. Guagliano, M. Dao, Cold spray coating: Review of material systems and future perspectives, Surf. Eng. 30(6) (2014) 369-395.

[41] T. Goyal, R.S. Walia, T.S. Sidhu, S. Samir, A review of coating technology processes and recent advancements, National Conference on Advances in Manufacturing Technology 2012, Chandigarh, India, 2012, pp. II -1-II -5.

[42] D.S. Therrien, A.G. McDonald, P. Mertiny, Temperature measurements of polymer composite flat plates coated with aluminum-12silicon, International Thermal Spray Conference 2012, Houston, TX, USA, 2012, pp. 1-6.

[43] F.N. Longo, Industrial guide - markets, materials, and applications for thermal-sprayed coatings, J. Therm. Spray Technol. 1(2) (1992) 143-145.

[44] P.C. King, A.J. Poole, S. Horne, R. de Nys, S. Gulizia, M.Z. Jahedi, Embedment of copper particles into polymers by cold spray, Surf. Coat. Technol. 216 (2013) 60-67.

[45] M.J. Vucko, P.C. King, A.J. Poole, M.Z. Jahedi, R. de Nys, Polyurethane seismic streamer skins: an application of cold spray metal embedment, Biofouling 29(1) (2013) 1-9.

[46] M.J. Vucko, P.C. King, A.J. Poole, C. Carl, M.Z. Jahedi, R. de Nys, Cold spray metal embedment: an innovative antifouling technology, Biofouling 28(3) (2012) 239-248.

[47] A.S.M. Ang, C.C. Berndt, A review of testing methods for thermal spray coatings, Int. Mat. Rev. 59(4) (2014) 179-223.

[48] A. Ganesan, J. Affi, M. Yamada, and M. Fukumoto, Bonding behavior studies of cold sprayed coating on the PVC polymer substrate, Surf. Coat. Technol. 207 (2012) 262-269.

[49] X. L Zhou, A. F Chen, J. C Liu, X. K Wu, and J. S Zhang, Preparation of metallic coatings on polymer matrix composites by cold spray, Surf. Coat. Technol. 206(1) (2011) 132-136.

[50] G.M. Nelson, J.A. Nychka, A.G. McDonald, Structure, phases, and mechanical response of Ti-alloy bioactive glass composite coatings, Mater. Sci. Eng. C 36 (1) (2014) 261-276.

[51] D.S. Therrien, Heat Transfer Analysis of Flame-sprayed Metal-polymer Composite Structures, University of Alberta, 2013. Dissertation.

[52] M.H.A. Malek, N.H. Saad, S.K. Abas, N.M. Shah, Thermal arc spray overview, International Conference on Manufacturing, Optimization, Industrial and Material Engineering, Bandung, West Java, Indonesia, 2013, pp. 012028-1-012028-11.

[53] A. Liu, M. Guo, M. Zhao, H. Ma, S. Hu, Arc sprayed erosion-resistant coating for carbon fiber reinforced polymer matrix composite substrates, Surf. Coat. Technol. 200(9) (2006) 3073-3077.

[54] A. Liu, M. Guo, J. Gao, M. Zhao, Influence of bond coat on shear adhesion strength of erosion and thermal resistant coating for carbon fiber reinforced thermosetting polyimide, Surf. Coat. Technol. 201(6) (2006) 2696-2700.

[55] E. Lugscheider, T. Weber, Plasma spraying--An innovative coating technique: Process variants and applications, IEEE Trans. Plasma Sci. 18 (6) (1990) 968-973.

[56] W. Huang, X. Fan, Y. Zhao, X. Zhou, X. Meng, Y. Wang, B. Zou, X. Cao, Z. Wang, Fabrication of thermal barrier coatings onto polyimide matrix composites via air plasma spray process, Surf. Coat. Technol. 207(2012) 421-429.

[57] A. Ganesan, M. Yamada, M. Fukumoto, The effect of CFRP surface treatment on the splat morphology and coating adhesion strength, International Thermal Spray Conference 2013, Busan, Yeongnam, South Korea, 2014, pp. 236-244.

[58] R. Beydon, G. Bernhart, Y. Segui, Measurement of metallic coatings adhesion to fibre reinforced plastic materials, Surf. Coat. Technol. 126(1) (2000) 39-47.

[59] S. Guanhong, H. Xiaodong, J. Jiuxing, S. Yue, Parametric study of Al and Al2O3 ceramic coatings deposited by air plasma spray onto polymer substrate, Appl. Surf. Sci. 257(17) (2011) 7864-7870.

[60] J. Affi, H. Okazaki, M. Yamada, M. Fukumoto, Fabrication of aluminum coating onto CFRP substrate by cold spray, Mater. Trans. 52(9) (2011) 1759-1763.

[61] M. Mellali, P. Fauchais, A. Grimaud, Influence of substrate roughness and temperature on the adhesion/cohesion of alumina coatings, Surf. Coat. Technol. 81(2-3) (1996) 275-286.

[62] W. Huang, Y. Zhao, X. Fan, X. Meng, Y. Wang, X. Cai, X. Cao, Z. Wang, Effect of bond coats on thermal shock resistance of thermal barrier coatings deposited onto polymer matrix composites via air plasma spray process, J. Therm. Spray Technol. 22(6) (2013) 918-925.

[63] R. Lupoi, W. O'Neill, Deposition of metallic coatings on polymer surfaces using cold spray, Surf. Coat. Technol. 205(7) (2010) 2167-2173.

[64] A. Ganesan, M. Yamada, M. Fukumoto, Cold spray coating deposition mechanism on the thermoplastic and thermosetting polymer substrates, J. Therm. Spray Technol. 22(8) (2013) 1275-1282.

[65] P.S. Ghoshdastidar, Heat Transfer, 2nd ed, Oxford University Press, New Delhi, India, 2012.

[66] L. PawŁowski, Temperature distribution in plasma-sprayed coatings, Thin Solid Films 81(1) (1981) 79-88.

[67] M. Floristan, R. Fontarnau, A. Killinger, R. Gadow, Development of electrically conductive plasma sprayed coatings on glass ceramic substrates, Surf. Coat. Technol. 205(4) (2010) 1021-1028.

[68] M. Gardon, A. Latorre, M. Torrell, S. Dosta, J. Fernandez, J.M. Guilemany, Cold gas spray titanium coatings onto a biocompatible polymer, Mater. Lett. 106 (2013) 97-99.

[69] F. Hugot, J. Patru, P. Fauchais, L. Bianchi, Modeling of a substrate thermomechanical behavior during plasma spraying, J. Mater. Process. Technol. 190(1-3) (2007) 317-323.

[70] Y. Chen, X. Liang, Y. Liu, J. Bai, B. Xu, Finite element modeling of coating formation and transient heat transfer in the electric arc spray process, Int. J. Heat Mass Transfer 53(9–10) (2010) 2012-2021.

[71] Y. Zhu, H. Liao, C. Coddet, Transient thermal analysis and coating formation simulation of thermal spray process by finite difference method, Surf. Coat. Technol. 200(16–17) (2006) 4665-4673.

[72] Y. Bao, T. Zhang, D.T. Gawne, Non-steady state heating of substrate and coating during thermal-spray deposition, Surf. Coat. Technol. 194(1) (2005) 82-90.

[73] T. Zhang, Y. Bao, D.T. Gawne, P. Mason, Effect of a moving flame on the temperature of polymer coatings and substrates, Prog. Org. Coat. 70(1) (2011) 45-51.

[74] S.C. Wu, H.O. Zhang, Q. Tang, L. Chen, G.L. Wang, Meshless analysis of the substrate temperature in plasma spraying process, Int. J. Therm. Sci. 48(4) (2009) 674-681.

[75] W.J. Mansur, C.A.B. Vasconcellos, N.J.M. Zambrozuski, O. C. R. Filho, Numerical solution for the linear transient heat conduction equation using an Explicit Green's Approach, Int. J. Heat Mass Transfer 52(3-4) (2009) 694-701.

[76] J. R. Monds, A. G. McDonald, Determination of skin temperature distribution and heat flux during simulated fires using Green's functions over finite-length scales, Appl. Therm. Eng. 50(1) (2013) 593-603.

[77] A. Grine, J. Y Desmons, S. Harmand, Models for transient conduction in a flat plate subjected to a variable heat flux, Appl. Therm. Eng. 27(2-3) (2007) 492-500.

[78] A. P Fernandes, P. F. B Sousa, V. L Borges, G. Guimaraes, Use of 3D-transient analytical solution based on Green's function to reduce computational time in inverse heat conduction problems, Appl. Math. Model. 34(12) (2010) 4040-4049.

[79] N. Sahoo, R. K Peetala, Transient surface heating rates from a nickel film sensor using inverse analysis, Int. J. Heat Mass Transfer 54(5-6) (2011) 1297-1302.

[80] Z. Wang, K. H Tan, Green's function solution for transient heat conduction in concrete-filled CHS subjected to fire, Eng. Struct. 28(11) (2006) 1574-1585.

[81] R. A. Beck, R. W. Truss, Effect of chemical structure on the wear behavior of polyurethane-urea elastomers, Wear 218(2) (1998) 145-152.

[82] I. M. Hutchings, D. W. T. Deuchar, Erosion of unfilled elastomers by solid particle impact, J. Mater. Sci. 22 (1987) 4071-4076.

[83] D. J. Hill, M. I. Kileen, J. H. O'Donnell, P. J. Pomery, D. St John, A. K. Whittaker, Laboratory wear testing of polyurethane elastomers, Wear 208 (1997) 155-160.

[84] N. M. Barkoula, J. Karger-Kocsis, Review Processes and influencing parameters of the solid particle erosion of polymers and their composites, J. Mater. Sci. 37(18) (2002) 3807-3820.

[85] F. J. Martinez, M. Canales, S. Izquierdo, M. A. Jimenez, M. A. Martinez, Finite element implementation and validation of wear modeling in sliding polymer-metal contacts, Wear 284-285 (2012) 52-64.

[86] S. W. Zhang, R. He, D. Wang, Q. Fan, Abrasive erosion of polyurethane, J. Mater. Sci. 36(20) (2001) 5037-5043.

[87] Y. S. Zuev, A. D. Chelmodeev, Effect of temperature and concentration of aggressive media on rubber wear in an abrasive flow, Polym. Mech. 4(1) (1968) 70-74.

[88] D. I. James, Abrasion of Rubber, Maclaren, London, England, 1967.

[89] ASTM Standard G65, Standard Test Method for Measuring Abrasion Using the Dry Sand/Rubber Wheel Apparatus, West Conshohocken, PA, United States, 2010.

[90] M.S. ElTobgy, E. Ng, M.A. Elbestawi, Finite element modeling of erosive wear, Int. J. Mach. Tools Manuf. 45 (2005) 1337-1346.

[91] P. Balu, F. Kong, S. Hamid, R. Kovacevic, Finite element modeling of solid particle erosion in AISI 4140 steel and nickel-tungsten carbide composite material produced by the laser-based powder deposition process, Tribol. Int. 62 (2013) 18-28.

[92] Z. G. Liu, S. Wan, V. B. Nguyen, Y. W. Zhang, A numerical study on the effect of particle shape on the erosion of ductile materials, Wear 313 (2014) 135-142.

[93] H. Zhang, X. Dong, Finite element analysis of multiple solid particles erosion in cermet coating, Surf. Coat. Technol. 262 (2015) 184-190.

[94] Y. F. Wang, Z. G. Yang, Finite element model of erosive wear on ductile and brittle materials, Wear 265 (2008) 871-878.

[95] N. Kumar, M. Shukla, Finite element analysis of multi-particle impact on erosion in abrasive water jet machining of titanium alloy, J. Comput. Appl. Math. 236 (2012) 4600-4610.

[96] S. Anwar, D. A. Axinte, A. A. Becker, Finite element modelling of abrasive waterjet milled footprints, J. Mater. Process. Technol. 213 (2013) 180-193.

[97] F.J. Martínez, M. Canales, J.M. Bielsa, M.A. Jiménez, Relationship between wear rate and mechanical fatigue in sliding TPU-metal contacts, Wear 268 (2010) 388-398.

[98] Y. Gong, Z. G. Yang, Y. F. Wang, Impact simulation on ductile metal pipe with polymer coating by a coupled finite element and meshfree method, J. Fail. Anal. Prev. 12 (2012) 267-272.

[99] W. Martienssen, H. Warlimont, Springer Handbook of Condensed Matter and Materials Data, Springer, Berlin Heideberg 2005.

[100] E. Sullivan, A. McDonald, Mathematical model and sensor development for measuring energy transfer from wildland fires, Int. J. Wildland Fire 23 (2014) 995-1004.

[101] K. D Cole, J. V Beck, A. Haji-Sheikh, Heat Conduction Using Green's Functions, 2nd ed. Taylor & Francis Group, New York,2011.

[102] A. Faghri, Y. Zhang, J. Howell, Advanced Heat and Mass Transfer, Global Digital Press, Columbia,2010.

[103] G. Nellis, S. Klein, Heat transfer, Cambridge University Press, New York, 2009.

[104] ASTM Standard D2240, Standard Test Method for Rubber Property-Durometer Hardness, West Conshohocken, PA, United States, 2010.

[105] R. Brandt and G. Neuer, Electrical resistivity and thermal conductivity of pure aluminum and aluminum alloys up to and above the melting temperature, Int. J. Thermophys. 28(5) (2007) 1429-1446.

[106] G. Wolinne, C. Harnisch, E. Héripré, S. Ruch, A. Salito, M. Jeandin, and L. Corte, Mechanical study of novel VPS-titanium coating on polyethylene substrates, J. Therm. Spray Technol. 24(1-2) (2015) 206-214.

[107] A. Boubakri, N. Hadder, K. Elleuch, and Y. Bienvenu, Impact of Aging Conditions on Mechanical Properties of Thermoplastic Polyurethane, Mater. Design 31 (2010) 4194-4201.

[108] H. P. Menard, Dynamic Mechanical Analysis: A Practical Introduction, 2ed ed., Taylor and Francis Group, 2008, p 148.

[109] ASTM G76, Standard test method for conducting erosion tests by solid particle impingement using gas jets, West Conshohocken, PA, USA, (2013).

[110] ASTM D638, Standard test method for tensile properties of plastics, West Conshohocken, PA, USA, (2014).

[111] R. C. Dykhuizen, M. F. Smith, Gas dynamic principles of cold spray, J. Therm. Spray Technol. (1998) 205-212.

[112] M. Grujicic, C.L. Zhao, C. Tong, W. S. DeRosset, D. Helfritch, Analysis of the impact velocity of powder particles in the cold-gas dynamic-spray process, Mater. Sci. Eng. A368 (2004) 222–230.

[113] U. Prisco, Size-dependent distributions of particle velocity and temperature at impact in the cold-gas dynamic-spray process, J. Mater. Process. Technol. 216 (2015) 302-314.

[114] H. Z. Li, J. Wang, J. M. Fan, Analysis and modelling of particle velocities in micro-abrasive air jet, Int. J. Mach. Tools Manuf. 49 (2009) 850-858.

[115] VV Mineral-Super Garnet Brochure, Retrieved from www.vvmineral.com/content/garnet-specification, March 2016.

[116] Abaqus Analysis User's Manual, Version 6. 13.

[117] L.M. Jiji, Heat Convection, second ed., Springer, Verlag Berlin Heidelberg, 2009.

[118] C. Prisacariu, Polyurethane elastomers-from morphology to mechanical aspects, Springer, Verlag/Wien, 2011.

[119] X. Jia, R. Ling, Two-body free-abrasive wear of polyethylene, nylon1010, expoxy and polyurethane coatings, Tribol. Int. 40 (2007) 1276-1283.

[120] M. Yahiaoui, J. Denape, J. Y. Paris, A. G. Ural, N. Alcala, F. J. Martinez, Wear dynamics of a TPU/steel contact under reciprocal sliding, Wear 315 (2014) 103-114.

[121] J. C. Arnold, I. M. Hutchings, Flux rate effects in the erosive wear of elastomers, J. Mater. Sci. 24 (1989) 833-839.

[122] R. J. K. Wood, Y. Puget, K. R. Trethewey, K. Stokes, The performance of marine coatings and pipe materials under fluid-borne sand erosion, Wear 219 (1998) 46-59.

[123] M. Takaffoli, M. Papini, Finite element analysis of single impacts of angular particles on ductile targets, Wear 267 (2009) 144-151.